UNIVERSITAT DE BARCELONA

New experimental techniques for axion searches in the RADES and BabyIAXO experiments

Cristian Cogollos Triviño

PhD Thesis

New experimental techniques for axion searches in the RADES and BabyIAXO experiments

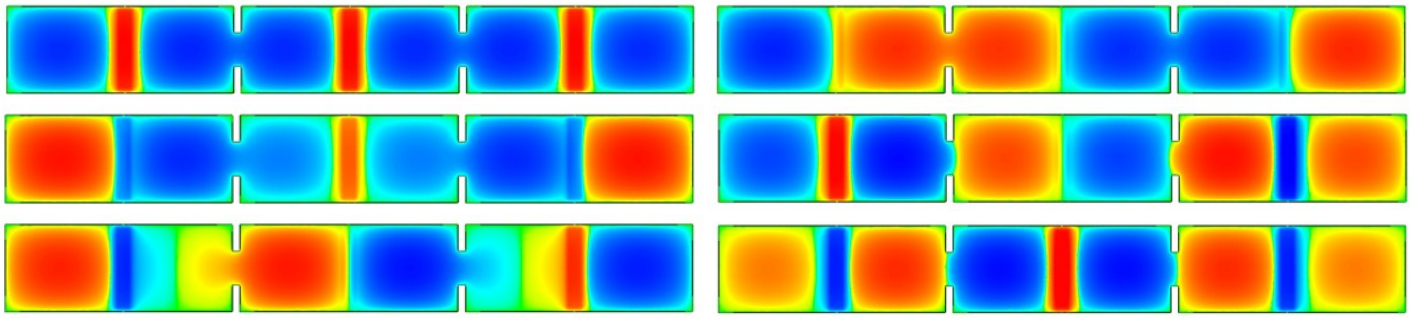

Author: **Cristian Cogollos Triviño**

Directors: **Eduardo Picatoste Olloqui**
Babette Döbrich

UNIVERSITAT DE BARCELONA

New experimental techniques for axion searches in the RADES and BabyIAXO experiments

Doctoral program in Physics

Author: Cristian Cogollos Triviño

Directors: Eduardo Picatoste Olloqui

Babette Döbrich

Tutor: Joan Soto Riera

UNIVERSITAT DE BARCELONA

Cristian Cogollos Triviño

Resum del treball de tesi

Títol: Noves tècniques experimentals per la búsqueda d'axions als experiments RADES i BabyIAXO.

Paraules clau: Física experimental, Matèria fosca, Física de les partícules elementals, Física d'astropartícules.

Els axions, i les denominades axion-like particles, són partícules elementals pseudoescalars que apareixen en diverses extensions del model estàndard de la física de partícules. Els axions foren proposats inicialment per explicar la simetria de paritat i conjugació de càrrega en les interaccions fortes. Però aquests bosons pseudo-Nambu-Goldstone també podrien ser la resposta a una de les preguntes més desconcertants de la cosmologia, el problema de la natura de la matèria fosca. Durant dècades s'han desenvolupat diferents experiments amb l'objectiu de detectar axions. El mètode més atractiu per detectar axions de matèria fosca es basa en el conegut com a inverse Primakoff effect i consisteix en la conversió d'axions en fotons en presència d'un camp magnètic molt intens. Els fotons produits en aquest procés poden ser detectats amb l'ús d'una cavitat resonant on l'energia associada a la conversió és enmagatzenada. Aquest tipus d'experiments centrats en la detecció d'axions que componen l'halo matèria fosca es denominen haloscopis. L'altre tipus d'experiment paradigmàtic el constitueixen els helioscopis, on l'objectiu consisteix en la detecció d'axions emessos a l'interior del Sól. A diferència dels haloscopis, on els axions se suposen freds i, per tant, el seu moment és menyspreable. Als helioscopis es tracten de detectar axions relativistes, amb una energia en l'escala dels keV. Els limits experimentals més precisos per a l'existència d'axions solars són els obtesos a l'experiment CAST al llarg dels últims anys. En el context actual, BabyIAXO es proposa com a una etapa experimental intermèdia al desenvolupament del International Axion Observatory (IAXO), un helioscopi de nova generació amb l'objectiu de detectar axions i axion-like particles amb una sensibilitat ordres de magnitud superior a la d'experiments anteriors, com CAST. El setup experimental de BabyIAXO consisteix en un imà amb un camp magnètic de 5 T, i dos forats de 10 m de longitud i 70 cm de diàmetre. La manca d'imans d'aquestes característiques el fan un candidat ideal per aprofitar a l'hora de desenvolupar cerques, no només d'axions solars, sinó també de matèria fosca.

Aquest treball de tesi compila tres contribucions experimentals diferediferents de cerques de axions, per a ambdós axions de matèria fosca i axions solars, dins els experiments RADES i BabyIAXO. El primer bloc comprén el treball desenvolupat en una proposta que aplana el camí per a cerques d'haloscopi a l'experiment BabyIAXO, en particular es proposa un conjunt de cavitats de 5 metres de llarg basades en l'experiència desenvolupada a l'experiment CAST. A la segona part s'exposa la car-

acterització i optimització del fons radioactiu produït per l'electrònica d'adquisició a l'helioscopi BabyIAXO. Aquests estudis es basen en mesures de la contaminació radioactiva dels components electrònics al laboratori subterrani de Canfranc i simulacions de decaïments radioactius. En la darrera part es presenta un marc general per tractar els ressonadors multicavitat ampliant la teoria desenvolupada per al primer prototip RADES, aquesta extensió teòrica permet dissenyar cavitats més estables per mesurar axions de matèria fosca. Basats en aquest formalisme per a ressonadors de microones, es van dissenyar, fabricar i caracteritzar dos nous prototips per la detecció de matèria fosca.

Abstract

Initially proposed as part of the solution to the strong CP problem of the Standard Model of particle physics, axions and axion-like particles appear on several Beyond Standard Model extensions. These pseudoscalar pseudo-Nambu-Goldstone bosons could also be the answer to one of the most puzzling questions on cosmology, the Dark Matter problem. For decades, searches have been performed for finding these elusive particles. The most promising of which deals with the conversion of axions into photons and their observation. Depending on the origin of these axions we can distinguish between two main kind of experiments, haloscopes (for dark matter axions) and helioscopes (for solar axions).

In this document we compile three different contributions to axion searches within the same framework that have been inside the scope of the thesis work during the last years. The first comprises the work developed in a proposal that paves the path for haloscope searches at BabyIAXO, in particular a set of 5 meter long cavities are proposed for covering the structures already used at CAST for axion searches. In the second part we expose the characterization and optimization of the radioactive background of the acquisition electronics for the BabyIAXO helioscope. In the last part a general framework for treating multicavity resonators is presented as an extension of the theory developed for the first RADES prototype, based on this idea two new prototypes were designed, manufactured and characterized.

Contents

1 Introduction

For centuries there has been no hunt as thrilling as the hunt for the unknown. The human being has always been captivated by the unknown, and in our quest for knowledge we have pushed the frontiers on research, not only to find answers but to be able to formulate the correct questions. One of the biggest unknowns in modern day physics is the nature of dark matter (DM). Lots of physicists have joined the hunt for DM in the last decades. But what would be of a hunter without the proper tools to do their job? In this thesis work I focused on developing a series of tools, both mathematical and experimental, and improved some of the ones already existing. These tools can be used by dark matter axion searches worldwide both present and future. Eventually I also took some time myself to borrow some of them and, together with the rest of the Relic Axion Detector Exploratory Setup (RADES) team, perform our own *dark matter hunt*, some results of which will be exposed here, some others still yet to come to light in the near future.

On this work we will be, almost constantly, discussing axions which are hypothetical particles relevant for testing hypothesis associated to beyond standard model (BSM) extensions, an also are one of the most viable cold dark matter (CDM) candidates due to the fact that they are effectively collision less being their only relevant long-range interaction gravitational.

The thesis is divided into two clearly differentiated experimental areas[1], the first being radio purity studies for improving solar axion searches and the second consisting in experimental developments for dark matter axion detection. This division of the material, is due to axion detection physics being a vast area where expertise from the most diverse disciplines in physics and engineering converge. We, as physicists, in general treasure face on approaches and specialization on carefully segmented problems. But the path to the discovery of new particles is not always a straight trail, and thus there are some contexts where we should not try pushing only on one front when our resources, even our dedication as individuals, can be judiciously split on different fronts to give us both a broader perspective and better experimental results. As applied to axion physics this means that the helioscope and haloscope approaches should go hand in hand, and as axion physicists we can profit the most by participating on both searches simultaneously.

There is a lot of material covered in this thesis regarding the fundamentals of

[1] Some would even argue three

experimental and theoretical axion physics, and even some nuclear physics found its way inside the document you are holding! As short as I wanted to keep the basics needed for following my work, it is impossible to dive in a subject already more than 40 years old, but which still is not part of the regular curricula, and expect to present the basics in a couple of pages. The philosophy when putting the pieces together has been to make it as self-contained as possible without getting lost on technicalities, since most of the literature can get extremely derivative. But on the other hand trying to stick to just presenting the fundamentals, leaving the extra flavors as references to be consulted, if in need of a broader perspective. The same approach has been taken regarding experimental results, only those results needed to follow the discussion or those original of this work are explicitly presented here. A more exhaustive treatment on axion detection experiments can be found on several references listed along the document and the reader is strongly encouraged to check them by themselves in order to get the full picture.

2

Dark matter and Strong CP problem

I will proceed in this section to introduce the dark matter existence and composition puzzles, and the strong Charge-Parity (CP) problem of quantum chromodynamics (QCD). These fundamental and apparently unrelated questions originated in two different areas of physics. But, even though unrelated on their origin, there exists the possibility for both to be solved on a really elegantly and straightforward way in one of the simplest extensions of the standard model (SM) of particle physics. Specifically, they could be connected to the addition of a new fundamental particle to the SM, a pseudoscalar pseudoNambu-Goldstone boson known as the axion[1].

2.1. Dark matter

Most of this thesis work revolves around the direct detection of axions and axion like particles (ALPs), which are regarded as *beyond standard model cold dark matter* candidates. So let us give some context in which clarifying all this terms before we advance any further.

2.1.1. ΛCDM cosmological model

The role of cosmology is describing the universe as a whole and studying the dynamics that command its evolution. It is an incredibly vast area which deals with the largest scales imaginable in nature, but sometimes requires a subtle and detailed understanding of the physics at infinitesimal distances and the interactions that govern the dynamics at those low scales.

In 1915 Albert Einstein published a series of seminal papers that would set the mathematical foundations for all cosmology to come until nowadays. General relativity (GR)- which belongs to the realm of classical field theories- provided us with a framework in which we can study the interplay between the geometry of space-time and matter/energy in all of its possible forms. In particular it has allowed us to explain in a straightforward manner the behavior of the universe at both galactic and extragalactic scales.

[1]Named after a detergent brand, since it would *clean* the strong CP problem.

On the other hand, trying to explain the phenomena at the shortest distances in Nature, in particular at atomic and nuclear scales. Physicists developed the standard model of particle physics, in the mathematical framework of the quantum field theory (QFT). The SM, usually regarded as the theory with the most accurate predictions in the history of humankind, was completed with the announcement of the experimental detection of the Higgs boson in 2013 [1]. This theory allows for the unification of electromagnetic and nuclear interactions with just a handful of fundamental parameters. All the matter ever detected, baryonic and leptonic matter, can be split into these fundamental building blocks. However, the possibility of matter sectors existing outside of the SM is not only possible but strongly motivated in most extensions of the SM to account for unexplained effects [2], this matter is often referred to as non-baryonic matter. On the next sections we will discuss extensions outside the standard model and the potential nature of some of this non-baryonic matter.

The current understanding for the large scale of universe we inhabit and its dynamical evolution is what we call the ΛCDM Model [3, 4]. This model has two main ingredients:

- Dynamics dictated by Einstein's equations of General Relativity
- A matter and energy content split into three different components [5]:
  - 5% Baryonic matter
  - 27% Cold dark matter (CDM)
  - 68% Dark energy (Λ)

The baryonic contribution comprises protons, neutrons, helium and, to a lesser extend, heavier nuclei. Cold dark matter, which will be discussed more in detail in subsection 2.1.2, refers to matter with an equation of state similar to that of baryonic matter, which is non-relativistic and has very weak interaction with light. The exact nature of dark matter is still unknown, and it will be addressed in section 2.1.3. Finally dark energy refers to an exotic fluid with the equation of state of vacuum energy which origin is not understood within the SM.

In this ΛCDM Model the universe originates at a singularity, the Big Bang, it expands during several epochs dominated by its different energy components. Passing by a particularly relevant era where cold dark matter drives matter accretion and large scale structure formation. Finally it reaches a stage of accelerated expansion driven by dark energy.

For both dark matter and dark energy: their origin, interactions and direct detection are still open problems in cosmology with a lot of activity within the physics community [6–9].

To be completely fair- even though this will be the only mention in this work- one should not leave out of this discussion the possibility of explanations outside General

Relativity, in what are generally called modified gravity theories. Most of this theories do not rely on the existence of dark matter and/or dark energy but explicitly modify the theoretical framework. For the interested reader a comprehensive and thorough summary can be found here [10].

2.1.2. Dark matter evidences

Until around the 1980s, dark matter searches would not become an active field of research. But it was already in the 1930s when the first observation pointing towards DM existence was performed [11]. When studying the dispersion velocities of nebulae in the Coma cluster, Fritz Zwicky found a clear inconsistency between the total mass of the cluster- as calculated applying the virial theorem- and the mass given by the mass-luminosity relation of the nearly thousand nebulae that conform the cluster. The dispersion velocity gave him a mass to luminosity ratio, $M/L \sim 500$, way above the value for other known systems, such as the Kapteyn solar system, with $M/L \sim 3$. However he did not postulate explicitly the existence of DM for solving this problem, instead he regarded it to the system not being stationary and to the need for larger time scales in order to virialize the system.[2] Nevertheless, modern techniques confirmed Zwicky's measurement independently, requiring some extra material content to account for the missing mass.

In the 1970s the measurement of flat rotation curves for many galaxies started by the works of Vera Rubin [12] gave stronger evidence towards the existence of dark matter. From Kepler laws one would expect the rotational velocity of galaxies to decrease as $1/\sqrt{r}$ when departing from its center towards the outer region. However, during the 1970s more and more measurements of spiral galaxies rotation curves where available [3], showing profiles such as the one in figure 2.1. This observations imply a constant velocity after a certain radius, which can be straightforwardly explained by the presence of a matter halo surrounding the galaxy, only perceived by us via gravitational interaction.

These two are evidences, together with others: luminosity/mass discrepancies in the Milky Way [14], the mass distribution of the Bullet Cluster merger [15] and the gravitational lensing from distant clusters [16]; point to the existence of dark matter on the scale of individual galaxies and clusters of galaxies. However, there are also evidences of the existence of dark matter on cosmological scales the most convincing being the fitting of cosmic microwave background (CMB) anisotropies [5].

In the early Universe the processes for production and disintegration of hydrogen were in equilibrium, until cosmic expansion cooled down the mean photon energy below $E_\gamma < 13.6\,\text{eV}$. This stage was reached around 380 million years after the Big Bang, and entailed the emission of an isotropic background of photons, which redshifted down to microwave wavelengths during expansion. In 1964 Arno A. Penzias

[2] In the same work he also proposed several alternative methods to measure cluster masses, one of them being gravitational lensing.

[3] A vast historical review, with a modern day perspective, can be found in [13]

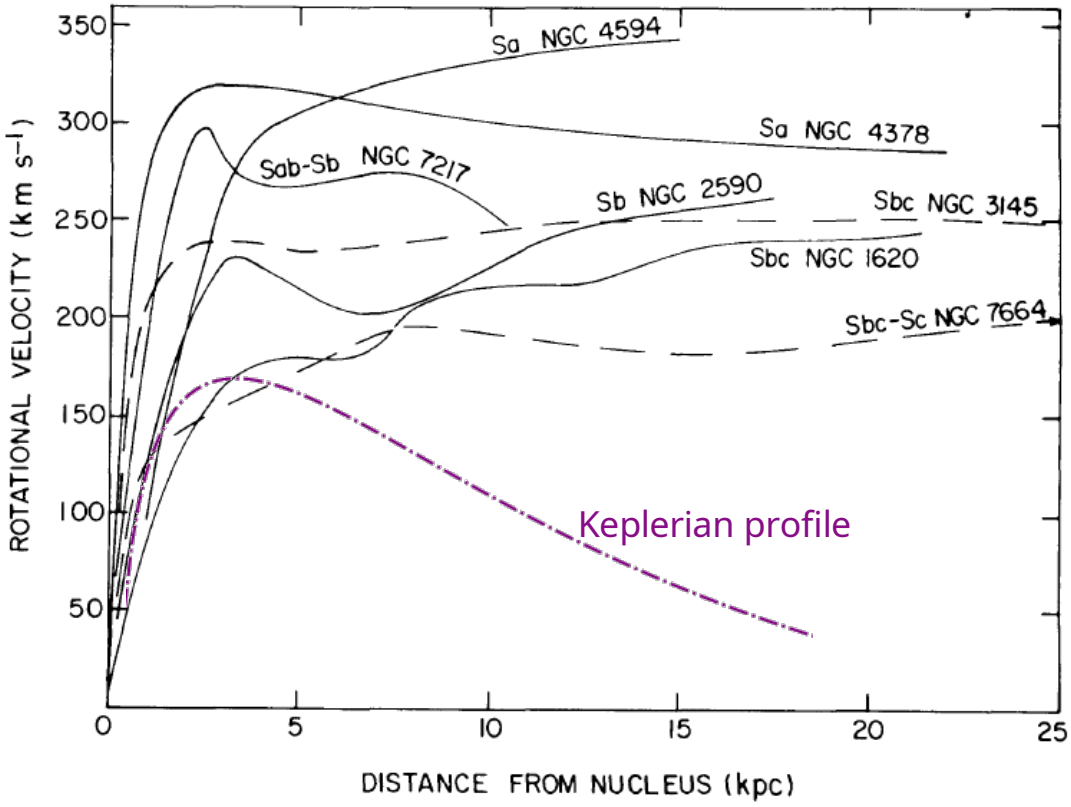

Figure 2.1.: Rotational curves for different galaxies, figure adapted from [12]. In purple (dashed-pointed) we show the prediction for an arbitrary halo of visible matter that follows Kepler's third law. The dependency of the rotational velocity as a function of the distance to the galactic center, clearly deviates from this behavior for all galaxies considered.

and Robert W. Wilson discovered the homogeneous component of this radiation, usually referred to as cosmic microwave background [17]. Later observations with higher precision performed by the COBE [18], WMAP [19] and Planck [5] satellite missions have detected a network of small anisotropies which are associated to photon emission in denser or more diluted regions. This structure in the CMB implies that the distribution of baryonic that matter at the time of emission was not homogeneous. Since matter and radiation were in equilibrium, random fluctuations in the baryonic matter distribution would be washed out on the present spectra. However, the presence of a dark matter component which does not couple to photons, but interacts gravitationaly would account for this structure formation. From these observations a dark mater energy density of 26.8% with respect to the total energy density of the universe is determined, its value being roughly five times higher than that of baryonic matter (4.9%).

2.1.3. Dark matter candidates

Some of the main characteristics of dark matter particles can be inferred from the observations previously mentioned. First that it has mass, and therefore interacts gravitationally with baryonic matter, second that it only interacts very weakly-if at all- via SM interactions. And finally that self-interactions are very limited too. Resulting in a gravitating fluid with essentially collisionless behavior.

Another main ingredient when studying dark matter candidates is the existence of a production mechanism in the early universe and its later evolution towards a non-relativistic state.

Different extensions of the standard model of particle physics introduce particles which could play the role of dark matter, the main candidates being:

- Axions [20] and ALPs [21]: Pseudoscalar pseudoNambu-Goldstone bosons arising in BSM physics, as a consequence of spontaneously broken global $U(1)$ symmetries. They have small masses (typically sub-eV) and feeble weak interactions. We will discuss them in detail in section 2.3, and some of their detection techniques are the main focus of this thesis work.

- Weakly Interactive Massive Particles (WIMPs) [22]: They are proposed in a very general way, and can appear as extension of the SM in different theoretical frameworks such as supersymmetric theories. The main requisites are that they interact very weakly with baryonic matter, and have a mass of the order of the electroweak scale ($10^2 - 10^3$ GeV). Another restriction, fixed by thermal production of the correct amount of DM, is that the self-annihilation cross-section to SM particles is of the order of the electro-weak (EW) scale too. Direct searches try to measure the scattering cross-section of these interactions with standard model particles. In general, this search is performed by looking at spontaneous nuclear recoils in a monitored medium. Most experiments use as a target, either a noble gas above its liquefying temperature, e.g. cryogenic Xenon at the XENONnT experiment [23]; or a very pure crystal at cryogenic temperature, as in the CRESST [24] and Cosinus [25] experiments.

- Massive hidden photons [26]: Gauge vector bosons of a $U(1)$ symmetry outside of the SM, they would mix kinetically with the standard model photon, but they would be not charged under SM interactions. They will be presented in more detail in section 2.4 and their detection in setups similar as those used for axion searches will be discussed in section 3.3.2.

- Primordial Black Holes [27]: Black holes formed in the early stages of the universe could contain the missing matter component while not contributing to the luminosity component of the dark matter halos. We will not be exploring it in this thesis, but some signals arising from primordial black holes could also be detected by using technologies developed for the detection of axion dark matter [28, 29].

- Sterile neutrinos [30–32]: Hypothetical right-handed neutrinos that are not charged under SM interactions which appear in several beyond standard model physics extensions [33]. They could have been produced in the early universe via mixing with SM neutrinos, decay of heavier particles or produced by interactions of dark sector particles at high energies. Sterile neutrinos with masses in the range of 1 keV to 1 MeV could be of special interest when considering their production in connection to the seesaw mechanism [34].

2.1.4. Dark matter halo

The exact distribution of dark matter- both at galactic and extragalactic scales- is still an open question. A lot of effort in the field is dedicated nowadays to topics connected with DM distribution, such as: improving simulations for large scale structure formation, dark matter self-interactions and its consequences and the analysis of the galactic halo DM profile based on observations [35–38].

If we restrict now to our galaxy- the Milky Way- the presence of DM is strongly motivated by experimental observations [14]. Nevertheless, the exact profile the halo adopts is still a hot topic. Current work from experimental observations and numerical simulations of galactic dynamics has provided us with simple models, that are used to estimate observational effects in direct detection experiments.

The basic model that fits most of the classical profile observations of the DM halo is the so called Standard Halo Model (SHM). It was proposed originally in [39] to provide a realistic model for extracting possible signals on direct detection experiments. The model is based on the flat rotation curves extracted for spiral galaxies [12]. The halo is assumed to be isotropic and spherically symmetric and exhibits a Gaussian velocity distribution for the DM particles, with a local circular velocity, $v_0 \approx 220\,\mathrm{km/s}$, measured for the solar system [40], which is connected to the velocity dispersion of the halo as $v_0 = \sqrt{2}\sigma_v$.

$$f(\mathbf{v}) = \frac{1}{N} \frac{e^{-\frac{|\mathbf{v}|^2}{2\sigma_v}}}{(2\pi\sigma_v^2)^{3/2}} \times \Theta(v_{\mathrm{esc}} - |\mathbf{v}|) \tag{2.1}$$

here N is a normalization factor, v_{esc} is the escape velocity which is estimated based on the halo model, and the Heaviside function $\Theta(v_{\mathrm{esc}} - |\mathbf{v}|)$ ensures that the distribution is only extended for the orbital radius of the galaxy.

The SHM agrees with several N-body simulations of galactic formation, however extensions to it have been proposed during the last years to account for anisotropies that do not fit properly on this simplified model, e.g. an elongated area of the velocity distribution measured by the *Gaia* mission [41]. An example of this extensions, that tries to account for these kind of anisotropies is the SHM++ [42]. It is in this context, that experiments which can have the sensitivity to probe the dark matter velocity distribution are crucial to measure this velocity components directly and understand their connection with structure formation.

Another hypothesis regarding the dark matter structure is the existence of the so called dark matter streams, similar to tidal streams [43]. These streams make reference to spikes in the velocity distribution that appear during galactic formation. In [44] a series of simulations of structure formation combining geodesic deviation and N-body equations of motion are presented. In their work, Vogelsberger and White found the possibility of modeling the six Milky Way halo profiles studied in the Aquarius project [45], as a combination of around 10^{14} dark matter streams from which the most massive 10^6 would account for almost half of the local dark matter density.

2.2. QCD and the Strong CP Problem

One of the most outstanding problems within the Standard Model of elementary particle physics is the so called Strong CP Problem, which deals with the understanding of why, apparently, quantum chromodynamics does not violate charge-parity symmetry [46, 47].

More particularly, this problem arises in QCD because, due to the existence of instanton solutions [48], a term of the form

$$\mathcal{L}_\theta = \frac{\theta}{32\pi^2} G^a_{\mu\nu} \tilde{G}^{a\mu\nu} \tag{2.2}$$

must be included in our Lagrangian, where

$$G^a_{\mu\nu} = \partial_\mu A^a_\nu - \partial_\nu A^a_\mu + g f^{abc} A^b_\mu A^c_\nu \tag{2.3}$$

and

$$\tilde{G}^{a\mu\nu} = \frac{1}{2} \epsilon^{\mu\nu\sigma\rho} G^a_{\sigma\rho} \tag{2.4}$$

A^a_μ being the gluon fields and f^{abc} the structure constants of the SU(3) group. The presence of this θ vacuum violates both $\mathcal{P}$ and $\mathcal{CP}$ symmetries. θ is not symmetric under chiral quark mass phase transformations and therefore it is not a QCD observable. However if we define $\bar{\theta}$ as $\bar{\theta} \equiv \theta - \arg\det \mathcal{M}_q$, where $\mathcal{M}_q$ is the quark mass matrix. We find $\bar{\theta}$ to be invariant, and therefore an observable which implies the presence of an explicit breaking of the $\mathcal{CP}$ symmetry mentioned.

One of the experimental consequences of the $\bar{\theta}$ term most studied is the existence of a neutron electric dipole moment of magnitude

$$|d_n| \simeq 2.4 \times 10^{-16} \bar{\theta}\, e\,\mathrm{cm} \tag{2.5}$$

where e is the electric charge of the electron [49].

The value of d_n can be studied experimentally [50], e.g. measuring Larmor precession under external magnetic and electric field conditions. Current and past experiments impose strong bounds for d_n, being the current limit [51]

$$|d_n| < 2.9 \times 10^{-26}\, e\,\mathrm{cm} \tag{2.6}$$

which implies an surprisingly small value for $\bar{\theta}$, i.e. $\bar{\theta} \lesssim 10^{-11}$.

There is no clear explanation yet of why $\bar{\theta}$ has such a small value, while it could have any value from 0 to π. Furthermore, the value of $\mathcal{M}_q$ is of the order of $\pi/3$ which implies a fine tuning of θ in order to cancel out the effect of $\mathcal{M}_q$. Explaining this apparent inconsistency, or fine tuning, of the Standard Model is what we are referring to when talking about solving the Strong CP Problem.

While there have been several solutions proposed since the Strong CP Problem was originally described [52–54], a particularly attractive one implies the introduction of an extra $U(1)_{PQ}$ symmetry (where the subindex PQ stands for the initials of the authors who first proposed this idea in the literature, Roberto Peccei and Helen Quinn [55, 56]).

In general terms we can sketch the Peccei-Quinn solution in the following steps. First it begins by introducing this extra $U(1)_{PQ}$ symmetry as a symmetry of the full QCD lagrangian, which is then spontaneously broken at a certain high energy scale f_a generating a pseudo Nambu-Goldstone boson, named the axion [57, 58]. The exact details on how this theory at higher energies is build and the new fields to be included are not fixed, and will condition the value of f_a, the axion mass and the couplings to different Standard Model particles. We will give a brief overview of the main models in the next subsections. Independently on how this spontaneous symmetry breaking (SSB) mechanism is implemented, it generates a term in the form $aG^a_{\mu\nu}\tilde{G}^{a\mu\nu}$ which is similar to the θ term in (2.2), but it is conceptually different.

Now a is a dynamical field and θ is redefined as

$$\theta = \frac{a}{f_a} \tag{2.7}$$

Excitations of this field a correspond to a new massive boson, the axion, and θ_0 can be understood as its vacuum expectation value (vev). In this context the Vafa-Witten theorem states that, in the absence of other CP-violation sources, the theta vacuum has an absolute minimum at $\theta_0 = 0$ [59]. Therefore, as a dynamical field, θ will relax to its minimum which corresponds to the CP conserving value $\theta_0 = 0$.

2.3. *The Axion Family*

In the previous section we explored the Strong CP Problem and one of its proposed solutions, the Peccei-Quinn mechanism. As we saw, this solution introduces a new pseudoNambu-Goldstone boson known as the QCD axion or, simply, axion. This new field gives us a contribution to the SM lagrangian

$$\mathcal{L}_a = \frac{1}{2}(\partial_\mu a)(\partial^\mu a) + a\frac{1}{f_a}\frac{g^2}{32\pi^2}G^a_{\mu\nu}\tilde{G}^{a\mu\nu} + \text{coupling terms} \tag{2.8}$$

Solving the Strong CP Problem is a common feature for all axion models, whereas

the coupling terms are dependent on the ultraviolet (UV) completion of the model, and therefore on how the $U(1)_{PQ}$ symmetry is implemented.

The original model proposed by Peccei and Quinn [55, 56] introduces two extra Higgs fields for absorbing the independent chiral transformations of up and down quarks, and their leptonic counterpart. This mechanism ensures that the full SM lagrangian is invariant under the new $U(1)_{PQ}$ symmetry. This symmetry transformation acts on a general set of coloured fermions $\{\psi_f\}$ and scalars $\{H\}$ for a given angle α as

$$\psi_f \to e^{iX_f\alpha}\psi_f \ , \ H \to e^{iX_H\alpha}H \tag{2.9}$$

where $\mathbf{X} = \{X_f, X_H\}$ is a vector with the $U(1)_{PQ}$ charges. The symmetry presents a color (and/or electromagnetic) anomaly, if the corresponding triangle anomaly diagrams weighted by the charges are non-zero. The coefficients for these electromagnetic and color anomalies, E and N, respectively are defined as

$$E = 2\sum_f (-1)^a X_f Q_f^2 \ , \ N = \sum_f (-1)^a X_f S_f^2 \tag{2.10}$$

where S_f are indices of the $SU_c(3)$ representation of the ψ_f fermions, and $a = \{0, 1\}$ for left-handed and right-handed fields, respectively.

For the original model proposed by Peccei and Quinn, the value of the axion decay constant f_a is of the order of the Higgs boson vacuum expectation value $f_a \sim v \simeq 250\,\text{GeV}$. However this axions have been already ruled out experimentally [20].

Aside from the original Peccei-Quinn proposal, one can add different fields on the complete lagrangian giving a whole range of different models, the main examples of these are the Kim-Shifman-Vainshtein-Zakharov (KSVZ) [60, 61] and Dine-Fischler-Srednicki-Zhitinsky (DFSZ) [62, 63] axion models. In them $f_a \gg v$ and, as a consequence, the mass of the associated axion is much smaller than in the case of the original Peccei-Quinn model. It is because of this that they are usually called invisible axion models.

In all three mentioned scenarios (PQ, KSVZ, DFSZ) the expansion of the second term in (2.8) generates a mass term for the axion

$$\mathcal{L}_m = \frac{1}{2}m_a^2 a^2 \tag{2.11}$$

and a coupling to photons

$$\mathcal{L}_{a\gamma} = \frac{1}{4}g_{a\gamma} a F_{\mu\nu}\tilde{F}^{\mu\nu} \tag{2.12}$$

where $g_{a\gamma}$ is the axion-photon coupling, $F_{\mu\nu} = \partial_\mu A_\nu - \partial_\nu A_\mu$ and its dual is $\tilde{F}^{\mu\nu} = \frac{1}{2}\epsilon^{\mu\nu\sigma\rho}F_{\sigma\rho}$.

Furthermore in the KSVZ and DFSZ models, m_a is related to the scale f_a by the

axion-pion potential in the following way [64]

$$m_a \approx \frac{10^{12}\text{GeV}}{f_a}\, 5.69\,\mu\text{eV} \tag{2.13}$$

In both models there is also a connection between the mass of the axion and the coupling to photons

$$g_{a\gamma} = \frac{\alpha}{2\pi}\frac{C_{a\gamma}}{f_a}\ ,\ C_{a\gamma} = \frac{E}{N} - 1.92 \tag{2.14}$$

where α is the SM fine structure constant and $C_{a\gamma}$ is the non dimensional coupling to photons.

The factor of -1.92 in (2.14) is a consequence of axion-meson mixing [65]. DFSZ axions- depending on model considerations- can have a value for E/N of either $8/3$ or $2/3$ [66]. While for the KSVZ model $E/N = 0$ and its generalizations can cover values over the range of $(5/3, 44/3)$ [67].

The combination of both (2.13) and (2.14) for QCD axion models defines a restricted region of the parameter space $(g_{a\gamma}, m_a)$ usually referred to as the QCD axion band. In figure 2.2 we present this region in the context of the most stringent experimental limits nowadays.

As it is out of scope of the current work and it does not add any additional phenomenology to the observational techniques developed in this thesis, we will avoid discussing the theory behind the different QCD axion models. However- for the curious reader- an exhaustive up-to-date treatment of them can be found in [64].

For the sake of completeness let us mention the general case of the so called axion like particles (ALPs). With this denomination, following the nomenclature in [69], we will refer to BSM particles with derivative couplings to matter, and an interaction with photons similar to (2.12). This family contains hypothetical pseudoscalar pseudoNambu-Goldstone bosons arising from SSB (like majorons [70] or familons [71]) and other particles created via superstring compactification [72]. In the context of this work we will consider ALPs to extend the physics case of our search outside of the QCD axion band without focusing in the particular details of their fundamental origin.

Axions and, more generally ALPs, are also involved in theoretical models that solve other open problems. For example, in [73], the fermion mass hierarchy problem is solved via Peccei-Quinn mechanism. We can find a way more ambitious example of this in the Standard Model-Axion-Seesaw-Higgs Portal Inflation SMASH model [74]. This model proposes a common theory able to solve the Strong CP Problem, explain the nature of dark matter, and reproduce a cosmological history where inflation, reheating and baryogenesis appear as natural processes of the evolution of the different particle species involved.

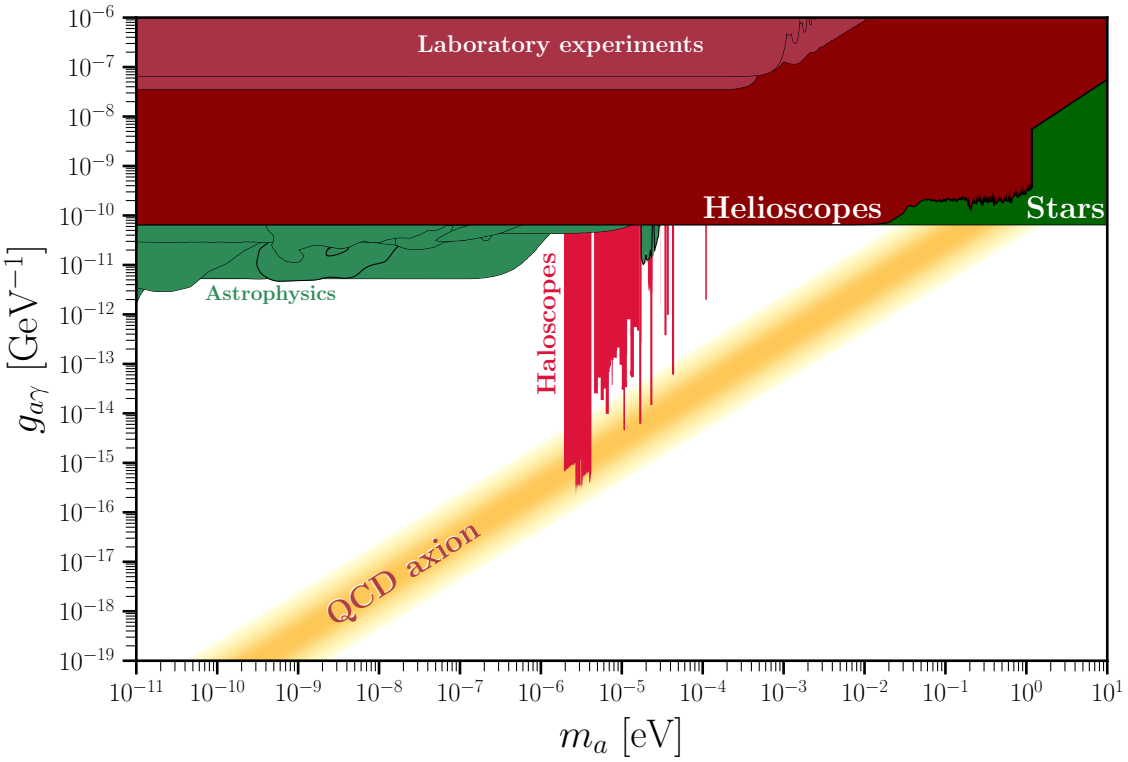

Figure 2.2.: Parameter space for axion-photon searches. The band of QCD axion models is plotted in yellow, together with different experimental limits. In laboratory experiments, axions are created in the lab via axion-photon conversion, helioscopes search for axions emitted from the Sun and haloscopes for axions in the dark matter halo. Limits depending on stellar or astrophysical phenomena are also shown. This simplified version of the parameter space has been adapted from [68].

2.4. Dark photons

In this section we will discuss another hypothetical particle that appears in BSM extensions, the dark photon. For a very didactic and complete treatment of phenomenology and experimental signatures we refer to the following lecture notes [75].

Even though outside of the axion and ALP family. Dark photons are a close relative when it comes to interactions with Standard Model particles. Because of this, most axion and ALP searches can also be regarded as dark photon searches, since a response in the detector would be triggered in the presence of either particle [69, 76–79]. We will motivate them briefly and introduce the basic theory needed to understand dark photon detection in the context of this work.

One of the most promising areas of physics beyond the Standard Model deals with the so-called dark sector, this concept refers to particles arising from unknown gauge field theories, which are *dark* in the sense of not being charged under the gauge groups already accounted for inside the SM. This does not mean they would

not interact with SM particles, since they could still mix via effective couplings, and interact gravitationally. From a formal perspective, we have been indeed discussing the dark sector during almost this whole section, since axion and ALPs are actually part of it.

The dark photon appears as the gauge vector boson of a new $U(1)$ symmetry inside the dark sector. Unlike the SM photon, the dark photon need not be massless, even though it could be. The existence of dark photons could have two main implications for dark matter:

- A very light massive dark photon could be a portion of the total relic DM abundance [80, 81].
- Both massive and massless dark photons could mediate self-interactions of fermion or scalar DM charged under the $U(1)$ group of the dark sector into consideration [82–84].

The massless case, even though important for dark sector phenomenology [85–87], does not couple directly to SM particles. Its influence can only be accounted via higher order operators (dimension higher than four), and it is effectively invisible in direct detection experiments as the ones described in this work.

The massive dark photon, can be detected directly in a laboratory setup due to its mixing with the SM photon,

$$\mathcal{L}_{\chi\gamma} = m_\chi^2 \chi X^\mu A_\mu \tag{2.15}$$

where m_χ is the mass of the dark photon, sometimes also called para-photon, A_μ, X^μ are the 4-potentials associated to the photon and dark photon, respectively, and χ is the coupling associated to the kinetic mixing of photons and dark photons [76].

The situation is fairly similar to that as for axions: in the given theoretical framework where dark photons are proposed as an extension of the Standard Model, several production mechanisms on energy scales corresponding to the early universe can be identified. Furthermore, later cooling can be easily implemented as the natural evolution of the field, allowing dark matter density estimations consistent with the current astrophysical observations [69, 88]. However, due to the fact that the dark photon is a vector boson, there exists the possibility of it to have a certain polarization, which generates a slightly different situation, for direct detection experiments, when compared with those searching for cosmic axions.

The main production mechanisms are fairly similar to those mentioned for cosmic axions:

- Misalignment mechanism [69]: A random initial field state oscillates around the potential minimum generating CDM dark photons.
- Quantum fluctuations during inflation [89]: Isocurvature perturbations in the early universe generate a vector field during inflation.

- Tachyonic instabilities [90]: ALPs, after inflation and reheating stages, could coherently transform into dark photons.
- Topological defects decay [91]: Dark photons are produced by the decay of Abelian-Higgs cosmic strings from a $U(1)$ spontaneously broken symmetry.

Depending on the production mechanism, dark photons will have different degrees of polarization nowadays. Misalignment mechanism and quantum fluctuations produce a dark matter dark photon background with a given polarization, usually referred to as the fixed polarization scenario. Tachyonic instabilities would generate a dark photon population with a given helicity that would evolve into a less coherent state after random scattering. Whilst the string decay case requires a dedicated calculation, and it can range from some degree of polarization to a state where all initial polarization information has disappeared completely, usually referred to as random polarization scenario. For completeness, and to show that dark photons are still an active field of research, we quote two recent publications pointing to very interesting phenomenology that could be studied in connection to dark photon dark matter and structure formation of halos [92, 93].

On the next section we will derive the observables for axion and ALPs based on axion-photon conversion, because of the similarity between axion-photon coupling and the kinetic dark photon mixing (2.15) we will generalize axion detection experiments to the dark photon case in a straightforward way.

3

Axions mathematical machinery

In this chapter we will introduce the mathematical treatment for the axion field. We will start analyzing the free axion field and its possible representations, and then we will study axion-photon coupling, or *axion electrodynamics*, which is one of the basics for dark matter axion detection (chapters 6 and 8).

Most of the steps that we will follow and the results we will show can be found in the literature, such as the classic paper by Sikivie [94] or more modern reviews like [95]. However we find it important to compile them here in order to make the notation clear and for having an organized and self-contained summary of the main results of axion detection physics, in which this thesis work is mostly based.

Unless specified otherwise, the expressions in this chapter are in natural units, i.e. $\hbar = c = 1$. For more information about the conventions and units assumed in this chapter, please review Appendix A.

Due to their direct applicability of the simulations developed in this work, most of the derivations in this chapter are adapted to a finite sized grid. However, only the main definitions of the discrete variables we use are included in this chapter. The derivations that lead to the change of continuous expressions (integrals) into equivalent sums is not explained here. We strongly encourage the reader to check Appendix A where this derivations can be found in order to familiarize themselves with the similarities and differences between the two cases.

3.1. Free axion field

As we studied in section 2, for any axion or ALP model we can write a free lagrangian in the form (2.12)

$$\mathcal{L}_a = \frac{1}{2}\left((\partial_\mu a)(\partial^\mu a) - m_a^2 a^2\right) \tag{3.1}$$

where a is the axion field, and m_a its mass. We will not address the ins and outs of the mass term and how m_a relates to the UV complete theory, where the $U(1)_{PQ}$ symmetry is restored. Therefore we will consider it to be a free parameter in our detection scheme.

Equation (3.1) corresponds to the usual Klein-Gordon lagrangian for a free scalar field. This lagrangian leads us to the differential field equation in position space,

$$(\partial_\mu \partial^\mu + m_a^2) a(\mathbf{x}, t) = 0 \tag{3.2}$$

The study of this equation is a traditional example for most QFT books such as [96] and [97]. We will detail a bit the different solution representations that we can have for the field a in both position and momentum space and their spectral decomposition. The focus will be on details that some times can be easily overlooked, like normalization of the Fourier expansions and the conditions derived from the field being real. This study will help us addressing different problems in the next sections which might be easier to connect to one decomposition or another.

The solution of (3.2) in a finite box of volume $V = L_x \times L_y \times L_z$ can be expanded in discrete modes as

$$a(\mathbf{x}, t) = \sum_{\mathbf{p}} \frac{1}{2} \left[a(\mathbf{p}) e^{-i(\omega_p t - \mathbf{p}\cdot\mathbf{x})} + a^*(\mathbf{p}) e^{i(\omega_p t - \mathbf{p}\cdot\mathbf{x})} \right] \tag{3.3}$$

where the wavenumber is related to the frequency by the usual dispersion relation, $\omega_p^2 = |\mathbf{p}|^2 + m_a^2$, and we use the following notation for the discrete $\mathbf{p}$

$$\mathbf{p}_{n_x,n_y,n_z} = 2\pi \left(\frac{n_x}{L_x}, \frac{n_y}{L_y}, \frac{n_z}{L_z} \right) \ , \ \{ n_i = 0, \pm 1, \pm 2, \dots \, ; i = (x, y, z) \} \ . \tag{3.4}$$

For completeness, we define the position vector $\mathbf{x}$ in a discrete grid as

$$\mathbf{x}_{n_x,n_y,n_z} = \left(n_x \frac{L_x}{N_x}, n_y \frac{L_y}{N_y}, n_z \frac{L_z}{N_z} \right) \ , \ \{ n_i = 0, 1, ..., N_i \, ; i = (x, y, z) \} \ . \tag{3.5}$$

where N_i are number the points of the grid on the different Cartesian axis.

For the rest of the chapter, and for clarity, sometimes we will display the indices n_x, n_y, n_z explicitly on the vectors. However, unless specified otherwise, all $\mathbf{x}$ and $\mathbf{p}$ vectors are to be understood as discrete. Therefore, for both position and momentum vectors, we will refer to $\mathbf{u}_{n_x,n_y,n_z} = \mathbf{u}_i = \mathbf{u}$ as representing the same, the difference being in the context where they are used.

By construction, $a(\mathbf{x}, t)$ is a real field and, therefore it is easy to modify (3.3) to express it in terms of real valuated functions

$$a(\mathbf{x}, t) = \sum_{\mathbf{p}} |a(\mathbf{p})| \cos\big(\omega_p t - \mathbf{p} \cdot \mathbf{x} + \arg(a(\mathbf{p}))\big) \tag{3.6}$$

Another important decomposition for the field, which we will mainly use, is the Fourier expansion on momentum space,

$$a(\mathbf{x}, t) = \sum_{\mathbf{p}} a(\mathbf{p}, t) e^{i\mathbf{p}\cdot\mathbf{x}} \tag{3.7}$$

considering that these are Fourier modes in momentum space, and imposing the fact that $a(\mathbf{x},t)$ has to follow the Klein-Gordon equation allows us to isolate the time evolution as,

$$a(\mathbf{p},t) = \frac{1}{2}\left[a(\mathbf{p})e^{-i\omega_p t} + b(\mathbf{p})e^{i\omega_p t}\right] \tag{3.8}$$

it is essential to remark that $a^*(\mathbf{p}) \neq b(\mathbf{p})$. In fact, to preserve $a(\mathbf{x},t)$ realness implies imposing $b(\mathbf{p}) = a^*(-\mathbf{p})$.

The other two field expansions relevant for our studies are the spectral decomposition of both $a(\mathbf{x},t)$ and $a(\mathbf{p},t)$, namely $a(\mathbf{x},\omega)$ and $a(\mathbf{p},\omega)$, respectively. These can be derived as the Fourier transform of the time varying fields.

Let us start with the position space representation,

$$a(\mathbf{x},\omega) = \int_{-\infty}^{\infty} a(\mathbf{x},t)e^{i\omega t}\mathrm{d}t \tag{3.9}$$

by direct substitution of (3.3) into (3.9) we get

$$a(\mathbf{x},\omega) = \sum_{\mathbf{p}} \frac{2\pi}{2}\left[a(\mathbf{p})e^{i\mathbf{p}\cdot\mathbf{x}}\delta(\omega-\omega_p) + a^*(\mathbf{p})e^{-i\mathbf{p}\cdot\mathbf{x}}\delta(\omega+\omega_p)\right] \tag{3.10}$$

where the 2π factor is kept for convenience and we have used the Dirac's delta distribution representation

$$\delta(\omega-\omega_p) = \frac{1}{2\pi}\int_{-\infty}^{\infty} e^{i(\omega-\omega_p)t}\mathrm{d}t \tag{3.11}$$

For completeness, let us mention the formula for moving from frequency domain back into time domain, with the correct normalization.

$$a(\mathbf{x},t) = \int_{-\infty}^{\infty} a(\mathbf{x},\omega)e^{-i\omega t}\frac{\mathrm{d}\omega}{2\pi} \tag{3.12}$$

If we perform exactly the same calculation as in (3.9) but using $a(\mathbf{p},t)$ it is easy to see that we reach

$$a(\mathbf{p},\omega) = \frac{2\pi}{2}\left[a(\mathbf{p})\delta(\omega-\omega_p) + a^*(-\mathbf{p})\delta(\omega+\omega_p)\right] \tag{3.13}$$

where we have made explicit use of the relation $b(\mathbf{p}) = a^*(-\mathbf{p})$

3.2. Field energy and velocity distribution

The study of the energy of the field is also a usual topic covered by field theory books [96,98]. We will start with the same approach, but we will focus our treatment in a way that it allows us to connect the momentum mode expansion with the velocity distribution and the dark matter density. This result, even though simple, sometimes is overlooked in QFT courses.

3.2.1. Energy momentum tensor

In field theory the natural generalization of momentum and energy conservation comes by the hand of what we call the energy-momentum tensor [96]. If the system under consideration is invariant under temporal and spatial translations both energy and momentum are conserved, as they are in classical mechanics. The energy-momentum tensor allows us to obtain the four different conserved quantities, that correspond naturally to energy and linear momentum components.

The energy-momentum tensor of a field ϕ can be constructed as

$$T^{\mu\nu} = \frac{\partial \mathcal{L}}{\partial(\partial_\mu \phi)}(\partial^\nu \phi) - g^{\mu\nu}\mathcal{L} \tag{3.14}$$

the connection with the energy and momentum density of the field being

$$\rho_E = \frac{1}{V}\int_V \mathrm{d}^3x\, T^{00} \tag{3.15}$$

$$\rho_{P_i} = \frac{1}{V}\int_V \mathrm{d}^3x\, T^{0i} \tag{3.16}$$

It can be easily shown that the Klein-Gordon lagrangian (3.1) is invariant under temporal and spatial translations, and therefore energy and momentum are conserved. In order to connect the energy density of the field to the density of modes with a defined momentum, we start by taking the T^{00} component of the energy-momentum tensor

$$T^{00} = \frac{\partial \mathcal{L}}{\partial(\partial_0 a)}(\partial^0 a) - \mathcal{L} = \frac{1}{2}\left(m_a^2 a^2 + (\partial_t a)^2 + (\nabla a)^2\right) \tag{3.17}$$

and expand the axion field (3.3) in momentum modes

$$\begin{aligned} T^{00} = \frac{1}{8}\sum_{\mathbf{p}}\sum_{\mathbf{q}} \Big[& (m_a^2 - \omega_p\omega_q - (\mathbf{p}\cdot\mathbf{q}))a(\mathbf{p})a(\mathbf{q})e^{-i\left[(\omega_p+\omega_q)t-(\mathbf{p}+\mathbf{q})\cdot\mathbf{x}\right]} \\ & +(m_a^2 + \omega_p\omega_q + (\mathbf{p}\cdot\mathbf{q}))a(\mathbf{p})a^*(\mathbf{q})e^{-i\left[(\omega_p-\omega_q)t-(\mathbf{p}-\mathbf{q})\cdot\mathbf{x}\right]} \\ & +(m_a^2 + \omega_p\omega_q + (\mathbf{p}\cdot\mathbf{q}))a^*(\mathbf{p})a(\mathbf{q})e^{i\left[(\omega_p-\omega_q)t-(\mathbf{p}-\mathbf{q})\cdot\mathbf{x}\right]} \\ & +(m_a^2 - \omega_p\omega_q - (\mathbf{p}\cdot\mathbf{q}))a(\mathbf{p})a^*(\mathbf{q})e^{i\left[(\omega_p+\omega_q)t-(\mathbf{p}+\mathbf{q})\cdot\mathbf{x}\right]}\Big] \end{aligned} \tag{3.18}$$

We can then use (3.15) and perform the sum over $\mathbf{x}$ to obtain a series of deltas in momentum space (A.5) which makes the sum over $\mathbf{q}$ immediate, leaving us with

$$\rho_E = \frac{1}{2}\sum_{\mathbf{p}} \omega_p^2 |a(\mathbf{p})|^2 \tag{3.19}$$

where we have used the dispersion relation $\omega_p^2 = m_a^2 + |\mathbf{p}|^2$.

The energy density ρ_E in (3.19) is then just a sum of energies of individual modes, each one carrying an energy $\omega_{\mathbf{p}}$. Therefore, $\frac{1}{2}\omega_p|a(\mathbf{p})|^2$ is the density of modes with a given momentum, i.e. the density of particles with momentum $\mathbf{p}$.

If we perform now a similar procedure for the momentum density ρ_{P_i} using the T^{0i} terms we arrive to the expression

$$\rho_{P_i} = \frac{1}{2}\sum_{\mathbf{p}} \omega_p p_i \left[|a(\mathbf{p})|^2 - \mathcal{R}e\{a(\mathbf{p})a(-\mathbf{p})\}\cos\big(2\omega_p t\big)\right] \tag{3.20}$$

For simplifying this last result we will consider that when measuring observables, we will always have a finite integration time T. This integration time, in general, will be long enough that the term oscillating with a frequency ω_p, with both positive and negative momenta. Moreover, since $a(\mathbf{p})$ and $a(-\mathbf{p})$ are independent the sign of the second term will average out when binning over momenta, resulting on a negligible contribution. Thus leaving us with

$$\rho_{\mathbf{P}} = \frac{1}{2}\sum_{\mathbf{p}} \omega_p \mathbf{p}|a(\mathbf{p})|^2 \tag{3.21}$$

We can interpret in this case the result found for $\rho_{\mathbf{P}}$ as the density of particles of momentum $\mathbf{p}$ times its momentum. there is a very straightforward interpretation for this result, i.e. each mode $a(\mathbf{p})$ contributes to the total momentum of the field only with its own momentum $\mathbf{p}$. This result will be crucial when connecting the velocity distribution of the field to the modes we can detect on our experimental setup.

We can express the velocity distribution of the axion field as the energy density expanded over different momentum modes and normalized to the total energy density

We will later need the spectral energy density of each mode, instead of the density of modes, which we can define as

$$f(\mathbf{v}) = \left.\frac{\frac{1}{2}\omega_{\mathbf{p}}^2|a(\mathbf{p})|^2}{\bar{\rho}_E}\right|_{\mathbf{p}=m_a\mathbf{v}} \tag{3.22}$$

where $\mathbf{v}$ is the velocity, and we normalize by the total energy density of modes $\bar{\rho}_E = \sum_{\mathbf{p}} \frac{1}{2}\omega_{\mathbf{p}}^2|a(\mathbf{p})|^2$.

Let us also study the time averaged energy density, over a period T, for a given position

$$\langle\rho_a\rangle_T = \frac{1}{T}\int_{-T/2}^{T/2} T^{00}(\mathbf{x}_0, t)\mathrm{d}t \tag{3.23}$$

if we take the expression (3.17), neglecting the gradient effects we can expand the energy density as

$$\langle\rho_a\rangle_T = \frac{1}{T}\int_{-T/2}^{T/2}\int_{-\infty}^{\infty}\int_{-\infty}^{\infty} \frac{m_a^2 + \omega\omega'}{2} a(\mathbf{x}_0,\omega)a^*(\mathbf{x}_0,\omega')e^{-i(\omega-\omega')t}\mathrm{d}t\frac{\mathrm{d}\omega\mathrm{d}\omega'}{(2\pi)^2} \tag{3.24}$$

we can integrate out the time using the delta relation provided in (3.11) and use the delta to solve the integral over ω', arriving finally to an expression that allows us to expand the energy density in frequency modes of the axion field

$$\langle \rho_a \rangle_T = \frac{1}{T} \int_{-\infty}^{\infty} m_a^2 |a(\mathbf{x}_0, \omega)|^2 \frac{\mathrm{d}\omega}{2\pi} \tag{3.25}$$

where we have also assumed the low momentum limit, for which $\omega^2 \approx m_a^2$.

3.2.2. Axions as dark matter candidates

Let us elaborate now on the connection of axions and the dark matter composition problem. Axions and ALPs fulfil three requirements that makes them promising candidates:

- Weakly interacting with SM particles, mostly with photons, electrons and baryons.
- Having nonzero mass
- Can be produced in the early universe in the observed amount by non-thermal mechanisms, rendering them cold enough.

Their interaction with baryonic matter appears from derivative couplings- most of which are model dependent- detailed derivations of them can be found in [64, 67]. However, without the need of digging into the details of these couplings, we can easily argue their weak order effects. All of these couplings are inversely proportional to the energy scale f_{PQ}, and therefore extraordinarily weaker than SM charged interactions.

In section 2.3 we already mentioned the existence of a mass term for axions. We will focus on how this mass contribution generates an energy density compatible with the one expected for dark matter.

The main production mechanisms considered for cosmic axions are vacuum realignment [99,100] and the decay of topological defects after the Peccei-Quinn phase transition [101]. In this context it is particularly relevant if the Peccei-Quinn symmetry is broken before or after inflation, since this conditions the value of the theta vacuum and its evolution inside our Hubble volume. Depending on which scenario we find ourselves in, the parameter space for axion searches might change.

If we assume axions to be produced during early stages of the universe evolution via misalignment mechanism and/or string decay (non-thermal production). Now the axion field can be regarded as classical, in the sense of being low in momentum and having a incredibly huge occupation number. The solution (3.6) in this case can be simplified into

$$a(\mathbf{r}, t) = a_0 \sin(m_a t + \delta) \tag{3.26}$$

Assuming now that the only contribution to the dark matter content of the universe is given by axions, then we can use (3.19) to obtain ρ_E and associate that value to that of the energy density of CDM in our halo, which has been experimentally measured by astrophysical observations [102].

$$\rho_E = \rho_{CDM} \approx 0.3\,\mathrm{GeV\,cm^{-3}} = 2.3 \times 10^{-6}\,\mathrm{eV}^4 \tag{3.27}$$

this and the relation $a_0 = \theta_0 f_a$, from section 2.2 leads us to

$$\theta_0 m_a f_a = \sqrt{2\rho_{CDM}} \approx 3 \times 10^{-3}\,\mathrm{eV}^2 \tag{3.28}$$

The value of the product $m_a f_a$ is constrained for QCD axion models, Eq. (2.13), and combined with (3.28), allows estimating the value of θ_0

$$\theta_0 \sim 5 \times 10^{-18} \tag{3.29}$$

which is way bellow the current limit of $\theta_0 \lesssim 10^{-11}$ imposed by neutron electric dipole moment (EDM) measurements (2.6).

Finally, we can write the contribution to the Universe energy density due to axions as found in [103] only as a function of parameters appearing in the theoretical axion model

$$\Omega_a h^2 = 0.5 \left(\frac{f_a}{10^{12}\,\mathrm{GeV}}\right)^{7/6} [\theta_i^2 - (\sigma_\theta)^2] \tag{3.30}$$

where θ_i is the misalignment angle, and σ_θ is its mean-squared deviation.

Post-inflationary scenario

In the case when the Peccei-Quinn symmetry is broken after inflation, we can take a democratic average of values in the our universe patch, $\theta_i = \frac{\pi}{\sqrt{3}}$ and neglect its deviation. Then (3.30) reduces to

$$\Omega_a h^2 \approx \frac{\pi^2}{6} \left(\frac{f_{PQ}}{10^{12}\,\mathrm{GeV}}\right)^{7/6} \tag{3.31}$$

Based on the observations of the *Planck* mission [5] we can use the limit

$$\Omega_a h^2 < 0.12 \tag{3.32}$$

to impose a bound on f_a for cosmological axions

$$f_a < 3 \times 10^{11}\,\mathrm{GeV} \tag{3.33}$$

which corresponds to masses of the QCD axion in the range

$$m_a > 2 \times 10^{-5}\,\mathrm{eV} \tag{3.34}$$

It is important to note that these results are for the particular scenario of QCD axions being the only dark matter constituents. Other models without that limitation, would reduce the value of Ω_a and move the minimum mass limit higher, squeezing parameter space of masses consistent with cosmological bounds.

A very important feature of the post-inflationary scenario is that the axion mass can be predicted by calculating the amount of CDM produced in the Big Bang. Recent studies of the decay of global cosmic strings [104] in the Early Universe point towards higher masses, specifically in the range $m_a \approx 95 - 450\,\mu\text{eV}$. However, as extensively discussed in that same work, there is still a lack of understanding and control of the systematic uncertainties present in such estimations that will require further examination before providing more narrow and reliable bounds.

Pre-inflationary scenario

If the Peccei Quinn symmetry is broken before inflation, the value of the θ_i is chosen randomly in different regions of the Universe. One of these patches, after inflation, corresponds to our observable universe and hence we cannot substitute the observed value of θ_i by an ensemble average as in the post-inflationary scenario.

Equation 3.30 is still valid, however the unknown value of θ_i in the region specific to out observable universe will play a role [105]. In this context measuring a dark matter axion signal would give us the initial value of θ but we cannot make a specific prediction for the expected axion mass m_a.

Another basic feature of the pre-inflationary scenario is that topological defects such as cosmic strings or domain walls produced in the cosmological phase transition are diluted immediately during inflation, and therefore do not contribute to the final axion density. And therefore only axions produced via misalignment mechanism are generally considered.

3.3. Axion-photon interaction

In this section we will introduce the coupling relevant for the experimental searches that will be explored in the next chapters. The existence of this coupling- as discussed in section 2.3- is independent on the particulars of the axion or ALP model into consideration, therefore it allows for some of the broadest searches in the mass space for all candidates. We will recover the well-known result from [94], however the derivation will be a bit different. In particular, in the description and factorization of the haloscope form factor will be done in a slightly different manner, that can be easily generalized for the combination of signals read by different detectors.

First of all it is important to note that the axion field will be treated as being externally sourced- with cosmic or solar origin- and thus we will still use the free lagrangian and its solution when describing it. Whereas for photons we will consider

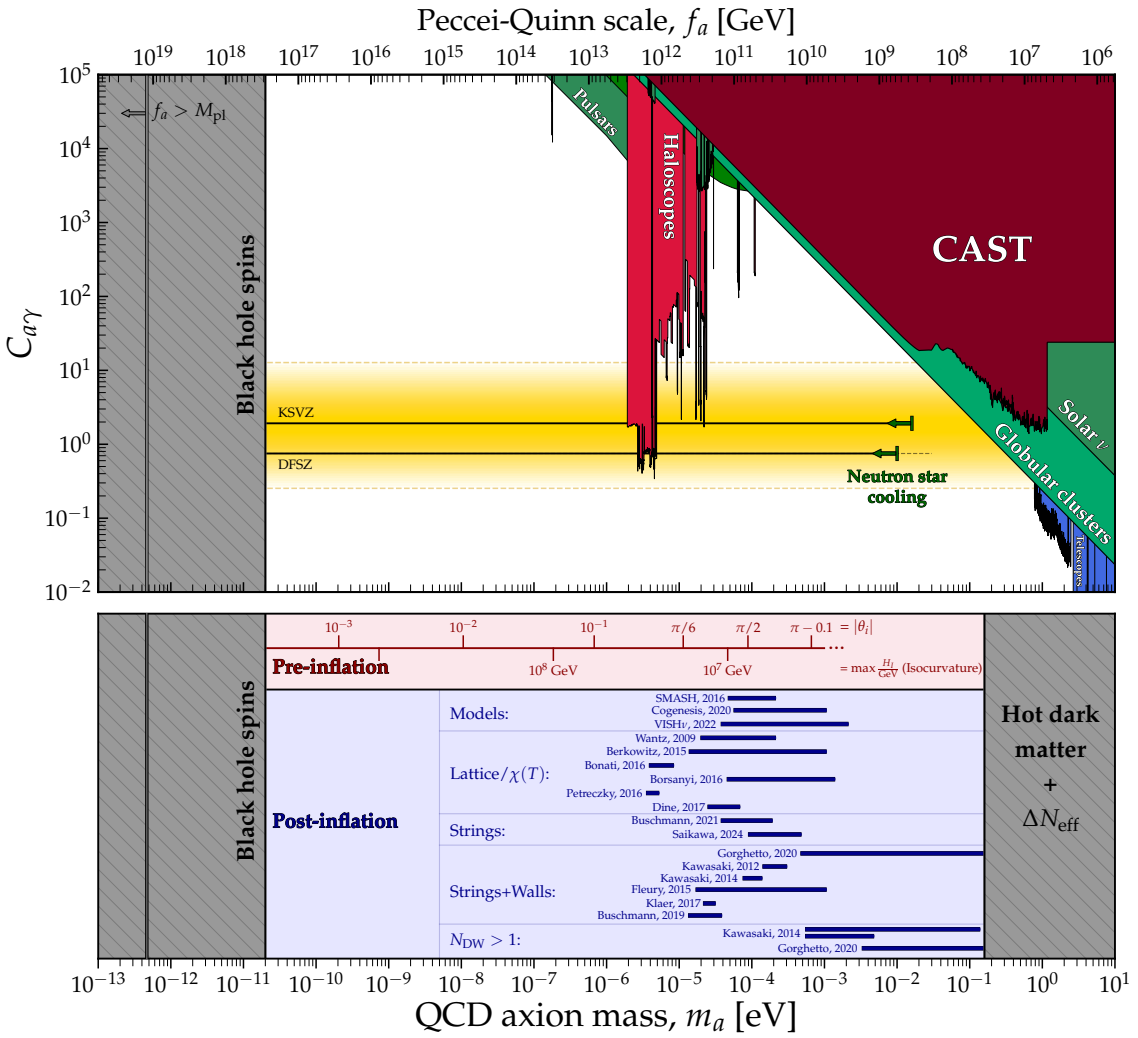

Figure 3.1.: Range of possible CDM axion masses spanned by different predictions, lower masses are bounded by black hole superradiance [106] and higher masses are restricted by axion-pion scattering in hot dark matter models [107]. For a modern approach on how to estimate the post-inflationary axion mass and an exhaustive compilation of previous works check [104]. The plot was generated using the code developed by Ciaran O'Hare [68], a full compilation of the references used for the limits plotted is available in the repository.

a lagrangian density comprised by two terms, one associated to the free field and an interaction term which we recall from equation (2.12)

$$\mathcal{L} = \mathcal{L}_\gamma + \mathcal{L}_{a\gamma} = -\frac{1}{4}F_{\mu\nu}F^{\mu\nu} - \frac{1}{4}ag_{a\gamma}F_{\mu\nu}\tilde{F}^{\mu\nu} \tag{3.35}$$

This lagrangian brings us to a set of equations of motion for the photon fields **E** and **B**. Which can be seen as a modified version of Maxwell equations that accounts for axions as an electromagnetic field source, allowing even for the definition of

equivalent current and charge densities,

$$\begin{aligned} \nabla \cdot \mathbf{E} &= -g_{a\gamma} \mathbf{B} \cdot \nabla a \\ \nabla \times \mathbf{B} - \dot{\mathbf{E}} &= g_{a\gamma} (\mathbf{B}\dot{a} - \mathbf{E} \times \nabla a) \\ \nabla \cdot \mathbf{B} &= 0 \\ \nabla \times \mathbf{E} + \dot{\mathbf{B}} &= 0 \end{aligned} \tag{3.36}$$

As the axion field is so weakly coupled, we can solve this equations perturbatively, allowing us a to linearize them and relate Fourier modes of axion and electromagnetic fields.

We will focus now in the two main methods of direct detection of axions via axion-photon conversion.

3.3.1. Haloscopes: Dark mater axion conversion

In this context we will consider the source of our signal to be axions of cosmic origin, and thus produced via misalignment mechanism, decay of topological defects, etc. As discussed in section 3.2.2 this axion field will behave as Cold Dark Matter.

Microwave resonators

The output power of a signal generated via axion-photon conversion depends on the square of the coupling $g_{a\gamma}$, which is expected to be lower than $10^{-10}\,\text{GeV}$ for the QCD axion in the unexplored region of the parameter space (see figure 2.2). Traditional haloscopes try to compensate this low conversion rate by converting axion into electromagnetic radiation inside a microwave resonator.[1]

A microwave resonator is a structure that allows certain electromagnetic field configurations to resonate and coherently store energy in its interior. The dimensions defining the resonator (see figure 3.2) determine this set of resonant electromagnetic modes. Each one of this modes has associated a frequency, this frequencies depend on the order of the mode, on the physical dimensions of the resonator and its electromagnetic properties.

We will consider electric $\mathbf{e}_m$ and magnetic $\mathbf{h}_m$ field solutions of Poisson equation inside of the resonator,

$$\begin{aligned} \nabla^2 \mathbf{e}_m &= -\omega_m^2 \mathbf{e}_m, \\ \nabla^2 \mathbf{h}_m &= -\omega_m^2 \mathbf{h}_m, \end{aligned} \tag{3.37}$$

[1] A detail on wording: for the rest of the work, since there is no ground for confusion on this context, we will use indistinctly the words microwave resonator, resonator, resonant cavity and cavity. In the particular cases when we want to refer to open or dielectric resonators, it will be mentioned explicitly.

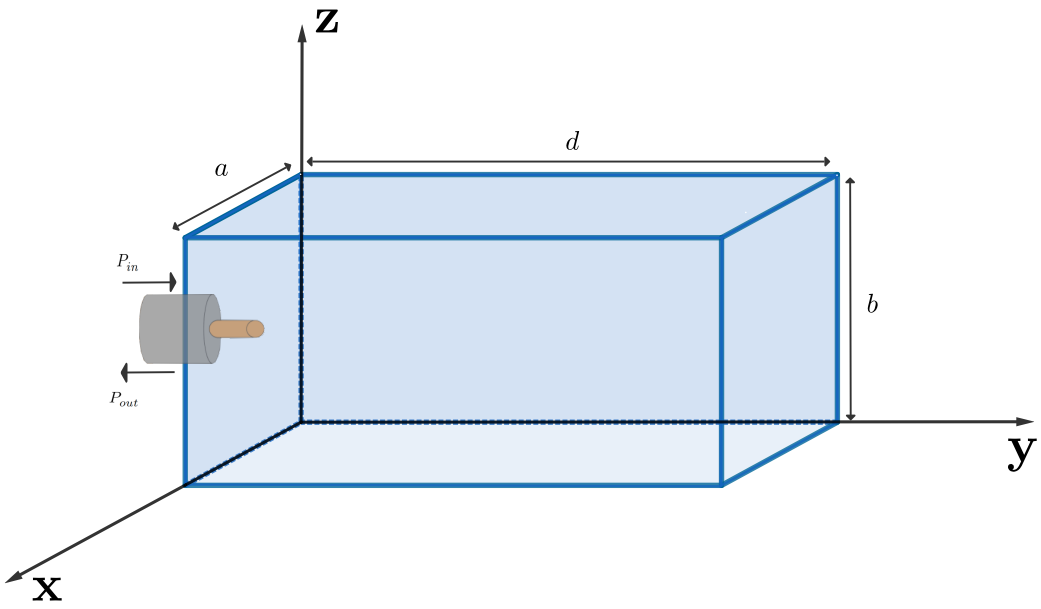

Figure 3.2.: Scheme of a rectangular resonator of dimensions a, b and d. The coaxial port on the left side of the structure allows the insertion and extraction of power from the resonator.

for clearly specifying the solution for this set of equations, we need to fix the boundary conditions of the system. Solving these equations implies finding the eigenvalues $(-\omega_m^2)$ and the eigenvectors ($\mathbf{e}_m$ and $\mathbf{h}_m$), which diagonalize ∇^2. This process is straightforward for resonators with a geometry that allows the Poisson equation to be separated[2], the typical examples of these coordinates are: rectangular, cylindrical and spherical. For geometries where the equations cannot be separated, this decomposition must still exist, since it only relays on a linear function expansion. However, obtaining this modes analytically will be impossible in most cases. One of the typical approaches in those situations is to consider a separable geometry, and approximate the one under study as a perturbation of it, this allows obtaining approximated modes as a combination of the ones that solve the separable variables problem.

To completely define the modes we need to impose the normalization condition for the fields inside the volume of the cavity, V_c,

$$\begin{aligned} \frac{1}{V_c}\int_{V_c} \mathbf{e}_m \cdot \mathbf{e}_n \mathrm{d}V = \delta_{mn} \\ \frac{1}{V_c}\int_{V_c} \mathbf{h}_m \cdot \mathbf{h}_n \mathrm{d}V = \delta_{mn} \end{aligned} \tag{3.38}$$

[2]For the curious reader: In 3 dimensional space, there exist *only* 11 different geometries for which we can separate this previous system of partial differential equations into a set of ordinary differential equations. One of the most comprehensive, yet accessible treatments of this topic can be found in Morse and Feshbach classical book [108]

We will focus now on a study of an arbitrary electric field $\mathbf{E}(\mathbf{x}, t)$ inside of the cavity, using the set of resonant electric modes that we have obtained, a similar process can be performed in order to study arbitrary magnetic fields $\mathbf{H}(\mathbf{x}, t)$ in terms of the magnetic modes. However as it does not add anything to the discussion at hand we will omit it.

Because $\mathbf{e}_m$ is a complete basis of the space of functions into consideration, we can expand any real function inside the cavity as a linear combination of these modes, in particular we will use this to decompose an arbitrary electric field in the following manner

$$\mathbf{E}(\mathbf{x}, t) = \sum_m E_m(t)\mathbf{e}_m(\mathbf{x}) \tag{3.39}$$

furthermore, we can separate each of the field amplitudes $E_m(t)$ in its spectral components to get

$$\mathbf{E}(\mathbf{x}, t) = \sum_m \left[\int_{-\infty}^{\infty} E_m(\omega)e^{-i\omega t}\frac{\mathrm{d}\omega}{2\pi}\right]\mathbf{e}_m(\mathbf{x}) \tag{3.40}$$

In the context of resonant cavity searches, we are concerned about the case where the axion electrodynamics equations from section 3.3 can be simplified neglecting local gradients of the axion field. This approximation is always acceptable as long as the volume of the detection setup is below the scale determined by the de Broglie wavelength of the axion

$$\lambda_{dB} = \frac{1}{p} \tag{3.41}$$

If we restrict ourselves to consider axions to be main contributors to dark matter, the value of p can be assumed to be given by the velocity dispersion of the halo DM distribution as discussed in section 2.1 and therefore $p = m_a v_{DM}$. Based on this, for every mass we can compute the scale where this approximation is applicable

$$L < \frac{1}{p} = 1.5\,\mathrm{km}\left(\frac{1\,\mu\mathrm{eV}}{m_a}\right) \tag{3.42}$$

The simplified equations we obtain in this case are

$$\begin{aligned} \nabla\cdot\mathbf{E} &= 0 \\ \nabla\times\mathbf{B} - \dot{\mathbf{E}} &= g_{a\gamma}\mathbf{B}\dot{a} \\ \nabla\cdot\mathbf{B} &= 0 \\ \nabla\times\mathbf{E} + \dot{\mathbf{B}} &= 0 \end{aligned} \tag{3.43}$$

To obtain an equation where we can make use of (3.37) we can apply the relation $\nabla^2\mathbf{E} = \nabla(\nabla\cdot\mathbf{E}) + (\nabla\times\dot{\mathbf{B}})$, which leads us to

$$\nabla^2\mathbf{E} - \ddot{\mathbf{E}} = g_{a\gamma}(\dot{\mathbf{B}}\dot{a} + \mathbf{B}\ddot{a}) \tag{3.44}$$

For the rest of the haloscope discussion we will introduce another important ingredient. In this kind of setup a strong external and static magnetic field will always be present, and therefore we will drop the $\dot{\mathbf{B}}$ term, keeping only the contribution that couples the time-varying axion field to the external magnetic field $\mathbf{B}_e$.

Expanding $\mathbf{E}$ in cavity modes, applying the spectral decomposition from (3.40) and using the relation (3.38) to project over an orthonormal mode $\mathbf{e}_m$, we find

$$(\omega^2 - \omega_m^2)E_m(\omega) = -g_{a\gamma}\omega^2 \sum_{\mathbf{p}} a(\mathbf{p},\omega)\frac{1}{V_c}\int \mathbf{B}_e \cdot \mathbf{e}_m(\mathbf{x})e^{i\mathbf{p}\cdot\mathbf{x}}\mathrm{d}^3x \tag{3.45}$$

For convenience we will define the following geometric factor for each of the cavity modes under consideration

$$\mathcal{G}_m(\mathbf{p}) = \frac{1}{V_c B_e}\int_{V_c} \mathbf{B}_e \cdot \mathbf{e}_m(\mathbf{x})e^{i\mathbf{p}\cdot\mathbf{x}}\mathrm{d}^3x \tag{3.46}$$

as we argued before $\frac{1}{|\mathbf{p}|}$ will always be much larger than $|\mathbf{x}|$ for the haloscopes into consideration, and therefore we can approximate the geometric factor for $\mathbf{p}$ as

$$\mathcal{G}_m(\mathbf{p}) \approx e^{i\vec{p}\cdot\mathbf{x}_0}\mathcal{G}_m \tag{3.47}$$

where $\mathbf{x}_0$ is the position of the setup and $\mathcal{G}_m$ is the value of the geometric factor assuming $|\mathbf{p}| = 0$

Putting all these pieces together we can write the spectral decomposition of the amplitude for each electric mode excited by the axion field as

$$E_m(\omega) = -ig_{a\gamma}B_e\mathcal{G}_m Q_m \mathcal{R}_m(\omega)a(\mathbf{x}_0,\omega) \tag{3.48}$$

where $\mathcal{R}_m(\omega)$ is the response function of the cavity for a given mode, defined as

$$\mathcal{R}_m(\omega) = \frac{i}{Q_m}\frac{\omega^2}{\omega^2 - \omega_m^2 + i\omega\Gamma_m} \tag{3.49}$$

and $Q_m = \frac{\omega_m}{\Gamma_m}$, the quality factor of the resonator for a given mode m, has been introduced to normalise the response function to 1 at the center of the resonance.

When coupling the cavity to an external acquisition system we can treat the signal contribution of each mode of the electric field to be

$$S_m(\omega) = \mathcal{R}_{\mathrm{DAQ}}(\omega)E_m(\omega) = -i\omega g_{a\gamma}B_e Q_m \mathcal{G}_m \mathcal{R}(\omega)\sum_{\mathbf{p}} a(\mathbf{p},\omega)e^{i\mathbf{p}\cdot\mathbf{x}_0} \tag{3.50}$$

where we have defined a response for the acquisition system, $\mathcal{R}_{\mathrm{DAQ}}$. For simplicity, we will assume it as independent on the mode topology, i.e. no x dependency. Most systems can have a complex structure for $\mathcal{R}_{\mathrm{DAQ}}$ when a broad range of frequencies is considered. However, unless specified otherwise, we will assume that the response of our system is uniform inside of a given frequency band and zero outside of it.

This conditions can be realized experimentally by restricting the acquisition band to a region where the response of the system is linear, the broadness of which will depend on the system quality, and imposing a band-rejection filter for the rest of the frequency spectra.

If we were interested only on the spectral decomposition of the axion-photon conversion signal in our setup we could stop here. However, in the haloscope searches developed in RADES we only have access to the average power extracted from the cavity, and therefore we need a couple of steps more.

Given the spectral decomposition $E_m(\omega)$ it is straightforward to recover the time domain behavior of the electric modes sourced by axion-photon conversion

$$E_m(t) = \int_{-\infty}^{\infty} E_m(\omega) e^{i\omega t} \frac{\mathrm{d}\omega}{2\pi} = i g_{a\gamma} B_e \mathcal{G}_m Q_m \int_{-\infty}^{\infty} \mathcal{R}_m(\omega) a(\mathbf{x}_0, \omega) e^{i\omega t} \frac{\mathrm{d}\omega}{2\pi} \quad (3.51)$$

Given $E_m(t)$ we can now compute the density power accumulated inside the resonant structure in a time cycle T

$$\frac{U_m}{V_c} = \left\langle |E_m(t)|^2 \right\rangle_T = \frac{1}{T} \int_{-\frac{T}{2}}^{\frac{T}{2}} \mathrm{d}t \int_{-\infty}^{\infty} \frac{\mathrm{d}\omega}{2\pi} \int_{-\infty}^{\infty} \frac{\mathrm{d}\omega'}{2\pi} E_m(\omega) E_m^*(\omega') e^{i(\omega-\omega')t} \quad (3.52)$$

by taking T to be sufficiently long, we can integrate out t to get a $\delta(\omega - \omega')$ and obtain the following expression for the accumulated power

$$U_m = \frac{V_c}{T} \int_{-\infty}^{\infty} |E_m(\omega)|^2 \frac{\mathrm{d}\omega}{2\pi} = \frac{V_c g_{a\gamma}^2 B_e^2 \mathcal{G}_m^2 Q_m^2}{T} \int_{-\infty}^{\infty} |\mathcal{R}_m(\omega)|^2 |a(\mathbf{x}_0, \omega)|^2 \frac{\mathrm{d}\omega}{2\pi} \quad (3.53)$$

As seen in section 3.2, the integral of all the spectral components of the axion field is connected to the average dark matter energy density in a straightforward manner (3.25). Taking that approximation and assuming a flat response for the cavity around the resonance frequency we assume a flat response for the cavity around the resonance frequency ($|\mathcal{R}_m(\omega)|^2 \approx 1$) we get a simple expression for the cavity power based on experimental and theoretical parameters

$$U_m = g_{a\gamma}^2 V_c B_e^2 \mathcal{G}_m^2 Q_m^2 \frac{\rho_{\mathrm{DM}}}{m_a^2} \quad (3.54)$$

Finally we want to evaluate the fraction of power extracted from the cavity, for this we write the output power as a fraction of the total energy of the cavity, parameterized with a loss parameter Γ_{out}. The total losses of the cavity for a given mode will then have two contributions $\Gamma_m = \Gamma_{\mathrm{cav}} + \Gamma_{\mathrm{out}}$, where Γ_{cav} refers to the dissipation of energy on the cavity walls. If we define now a coupling coefficient κ based on the ratio between the energy extracted and the total energy losses $\kappa = \frac{\Gamma_{\mathrm{out}}}{\Gamma_m}$ we arrive to the following expression for the signal power

$$P_s = \kappa g_{a\gamma}^2 V_c B_e^2 \mathcal{G}_m^2 Q_m \frac{\rho_{\mathrm{DM}}}{m_a} \quad (3.55)$$

This is one of the main expressions we will need for our haloscope studies, because of its relevance in connection to the experimental setup and the observed power, we will translate it into SI units

$$P_s = 8.47 \times 10^{-22}\,\mathrm{W}\frac{\kappa}{0.5}\left(\frac{g_{a\gamma}}{2\times 10^{-16}\mathrm{GeV}^{-1}}\right)^2 \frac{1\,\mu\mathrm{eV}}{m_a}\left(\frac{B_e}{2\,\mathrm{T}}\right)^2 \frac{V}{10^3\,\mathrm{l}}\,\frac{Q}{3\times 10^5}\,\frac{C}{0.63} \tag{3.56}$$

where we have introduced the usual definition of the geometric factor found in the literature, i.e. $C = \mathcal{G}_m^2$, and some standard benchmark parameters. These particular values will be discussed in chapter 6 as being associated to our haloscope proposal for BabyIAXO.

When measuring a signal out of a system as the one considered, we are not interested on the signal power itself, but on the ratio between the signal and the noise baseline, i.e. the Signal to Noise Ratio (SNR). The noise power for a setup such as the one into consideration can be easily estimated by using Dicke's radiometer equation [109]

$$P_N = T_{\mathrm{sys}}\Delta\nu \tag{3.57}$$

where T_{sys} quantifies the noise temperature of the setup, as a combination of both the cavity and the receiving system, and $\Delta\nu$ is the frequency bandwidth where the detector operates. For a given axion bin width this noise temperature, introducing again benchmark parameters can be computed in SI units as

$$P_T = 6.7 \times 10^{-20}\,\mathrm{W}\frac{T_{sys}}{6\,\mathrm{K}}\frac{3\times 10^5}{Q_a}\frac{m_a}{1\,\mu\mathrm{eV}} \tag{3.58}$$

where Q_a makes reference to the natural width of the axion line shape.

After an integration time T, and assuming the background to be Gaussian we consider the thermal noise baseline as given by the Johnson-Nyquist formula [110]

$$\sigma_N = \frac{P_N}{\sqrt{\Delta\nu T}} \tag{3.59}$$

The signal to noise ratio is therefore the quotient

$$\mathrm{SNR} = \frac{P_s\sqrt{\Delta\nu T}}{P_N} \tag{3.60}$$

with this expression in mind we can now estimate which is the sensitivity we can reach in $g_{a\gamma}$ for a given set of experimental parameters over the axion mass region in which the haloscope into consideration performs its search.

$$g_{a\gamma}^2 = \frac{S/N\,T_{sys}}{\kappa\rho_{\mathrm{DM}}B_e^2QVC}\left(\frac{m_a^3}{tQ_a}\right)^{\frac{1}{2}} \tag{3.61}$$

3.3.2. Haloscope techniques for dark photons

It is fairly straightforward to mimic the detection scheme developed in the previous section, to obtain a similar setup for the direct detection of relic massive dark photons on a haloscope. As it is shown in [76], where limits are recast for several axion search experiments into the massive dark photon phase space.

As we already mentioned in section 2.4, the lagrangian of a massive dark photon brings a kinetic mixing term with SM photons into the theory. If we consider then photons and dark photons at the same time the full lagrangian reads

$$\mathcal{L} = -\frac{1}{4}F_{\mu\nu}\tilde{F}^{\mu\nu} - \frac{1}{4}X_{\mu\nu}\tilde{X}^{\mu\nu} + eJ^{\mu}_{\mathrm{EM}}A_{\mu} + \frac{m_{\chi}^2}{2}\left(X^{\mu}X_{\mu} + 2\chi X^{\mu}A_{\mu}\right) \tag{3.62}$$

where $X^{\mu} = (X^0, \mathbf{X})$ is the 4-potential for the dark photon field, $X_{\mu\nu} = \partial_{\mu}X_{\nu} - \partial_{\nu}X_{\mu}$ is its corresponding stress-energy tensor, m_{χ} is the mass and χ its coupling to SM photons. It does not add much to the current discussion to redo here the derivation for the power step-by-step as we did for axion-photon conversion[3]. We will just quote the result one can usually find on the literature for haloscope dark photon searches [76] and discuss its implications.

For a resonant cavity, as the ones discussed in the previous section for axion detection, the presence of dark photons would generate a signal of the form

$$P_{\chi} = \kappa \mathcal{G}_{\chi} Q V \rho_{\mathrm{DM}} \chi^2 m_{\chi} \tag{3.63}$$

where dark photons are assumed to be the only contribution to dark matter, and ρ_{DM} is the local dark matter density and a geometric factor has been introduced

$$\mathcal{G}_{\chi} = \frac{\left(\int \mathbf{E}\cdot\mathbf{X}\mathrm{d}V\right)^2}{\frac{V}{2}\int\left(\mathbf{E}_m^2 + \mathbf{B}_m^2\mathrm{d}V\right)} \tag{3.64}$$

it is important to note that on this expression, E_m and B_m are just the electric and magnetic fields of the cavity modes.

Although a clear parallelism can be drawn between this result and what we found for axion-photon conversion, there are a couple of important differences worth mentioning:

- Dark photon to photon conversion will happen naturally without the need of a magnet. Furthermore, the sensitivity will not be affected by an external magnetic field neither for better, nor worse.
- The fact that dark photons are vector bosons makes this kind of experiment strongly dependent on polarization and orientation of the cavity with respect to movements along the galactic dark matter halo.

[3] There are indeed some interesting features on the calculation that arise from the fact that we are dealing now with a vector boson with a kinetic coupling, instead of a pseudoscalar with a derivative coupling on the photon. The interested reader is invited to check [69, 111] for a detailed derivation.

- The dependence on the mass of the dark photon for the signal output power is linear, as opposed to inversely linear in the axion case.

With these considerations in mind, if one obtains exclusion limits for axions in a resonant cavity experiment. Those can be rescaled into the equivalent ones for the dark photon case just by taking the axion power signal (3.55) and doing the substitution

$$g_{a\gamma}B = \chi m_{\chi}|\cos\theta| \tag{3.65}$$

where we have introduced the angle θ between the dark photon field and the vertical axis of our experiment, i.e. $\cos\theta = \mathbf{X}\cdot\hat{\mathbf{z}}$.

The introduction of $\cos\theta$ is of particular relevance for experimental observations. Two main scenarios are specifically motivated from a cosmological perspective [69]:

- Unpolarised dark photons: In this case the contribution for long time measurements would be in the form of an average value of $\langle\cos\theta\rangle^2 = \frac{1}{3}$
- Fixed polarisation: There is a preferred direction and only its projection on the $\hat{\mathbf{z}}$ axis contributes.

In the second case the possible range for $\cos\theta$ goes from the worst case scenario ($\mathbf{X}\perp\hat{\mathbf{z}}$), which one would naively expect to give zero signal, to the best one ($\mathbf{X}\parallel\hat{\mathbf{z}}$). However, it can be shown that timing information and earth rotation can help improve unfavorable situations on the polarized case to also approach the value of $\langle\cos\theta\rangle^2 = \frac{1}{3}$ [76].

3.3.3. Multi cavities formalism

The energy band at which classic cavity experiments have searched for axions, with enough sensitivity to reach the QCD axion band, comprises the range from 1μeV to 4μeV roughly. The paradigmatic example for resonant cavity haloscopes is the Axion Dark Matter eXperiment (ADMX) [112], where a cylindrical cavity is immersed in a strong magnetic field and axion DM should be converted into photons that excite a particular mode of the cavity. From (3.55) we can easily read that the volume of our resonant cavity will be directly connected to the sensitivity of the experiment. For experiments like ADMX, going to higher masses means designing a structure that resonates naturally at higher frequencies, and therefore building a resonator with a smaller radius. The direct consequence of this change on the dimensions of the detector is the reduction of the volume and thus systematically lower sensitivities, reaching a point where it is unfeasible to maintain a setup that allows for data taking.

There are several approaches for going into higher frequencies abandoning the traditional idea of cavity resonators, such as the use of dielectric resonators [113] or dish antennas [114]. However, another possible approach of still using resonant cavities is to implement geometries where the volume of the resonator is composed

of smaller cavities that fix the frequencies of the modes of the full structure. Different proposals have explored this possibility in the last years [115–117]. We will summarize first the formalism we developed at the RADES experiment for treating a resonant structure comprised of smaller resonant cavities, or sub-cavities [115].

The formalism presented in section 3.3.1 for axion photon conversion inside a resonant cavity can be applied independently of its geometry. Furthermore, it can be generalized also for structures consisting on an array of sub cavities coupled by irises.

Let us come back to one of the main results from section 3.3.1, i.e. the expression of the electric field induced on a resonant cavity via axion-photon conversion (3.48). And, for the rest of the discussion let us select one mode, in particular the one that couples maximally to the axion, namely E_1. From now on, even though we will be referring to E_1, we will drop the sub index for the sake of simplifying notation.

If we have a structure of identical cavities connected with irises one after another we could apply (3.48), and modify it slightly to account for the influence of neighboring cavities. For this purpose we introduce a linear coupling term of the form $K_{ij}E_j$ to relate the amplitude of the field of connected cavities

$$(\omega^2 - \omega_i^2 + i\omega\Gamma_i)E_i(\omega) = \sum_j K_{ij}E_j(\omega) + g_{a\gamma}B_e a(\mathbf{x}_i, \omega)\mathcal{G}_i \tag{3.66}$$

where we have substituted the response of the cavity in terms of the frequency, using (3.49) and the sub index i makes reference not to the electric field mode but to the cavity into consideration, in general we will be interested in cavities arranged along one direction and therefore the sum will only have two terms. But with this expression we could even consider more complex geometries, for example, spreading the cavities on a plane.

We can rearrange the terms and obtain a matrix equation of the form

$$(\omega^2\mathbb{1} - \mathbb{M})\bar{E} = -g_{a\gamma}B_e\omega^2 a_0\bar{\mathcal{G}} \tag{3.67}$$

Where the matrix elements $(\mathbb{M})_{ij}$ are defined as

$$(\mathbb{M})_{ij} = \tilde{\Omega}_i^2\delta_{ij} + (1 - \delta_{ij})K_{ij} \tag{3.68}$$

$\bar{E}$ and $\bar{\mathcal{G}}$ are column vectors with the electric field amplitude and geometric factor for the different cavities respectively, and $\tilde{\Omega}_i$ accounts for frequency behavior close to the resonance for each cavity

$$\tilde{\Omega}_i^2 = \omega_i^2 - i\omega_i\Gamma_i \tag{3.69}$$

The attentive reader will have noticed we dropped the axion field spatial and spectral dependence, taking $a(x_i, \omega) \approx a_0$. This, as discussed in section 3.2.2, for dark matter monochromatic axions is a good approximation. In the particular case

of a structure of N cavities placed consecutively along a line, (3.68) becomes the tridiagonal matrix

$$\mathbb{M} = \begin{pmatrix} \tilde{\Omega}_1^2 & K_{1,2} & 0 & ... & 0 & 0 \\ K_{2,1} & \tilde{\Omega}_2^2 & K_{2,3} & ... & 0 & 0 \\ 0 & K_{3,2} & \tilde{\Omega}_3^2 & ... & 0 & 0 \\ 0 & 0 & K_{4,3} & ... & 0 & 0 \\ \vdots & \vdots & \vdots & \ddots & \vdots & \vdots \\ 0 & 0 & 0 & ... & K_{N,N-1} & \tilde{\Omega}_N^2 \end{pmatrix} \tag{3.70}$$

With these tools in our hands the only thing left to do is to fix an operational frequency, associated to the axion mass band at which we want to look with our experiment. And study the couplings within the different cavities that can give us the best sensitivity.

In [115] this system was thoroughly studied, in the case N identical cavities separated by identical irises, i.e. $\tilde{\Omega}_i^2 = \tilde{\Omega}^2 \; \forall i \; K_{ij} = k < 0, \forall i, j$ and found an analytical solution for the eigenvalues and eigenvectors of (3.67)

$$\mathbf{e}_i = \frac{1}{\sqrt{(1+N)/2}} \begin{pmatrix} \sin\left(\frac{i\pi}{N+1}1\right) \\ \sin\left(\frac{i\pi}{N+1}2\right) \\ ... \\ \sin\left(\frac{i\pi}{N+1}N\right) \end{pmatrix} \quad , \quad \tilde{\omega}_i = \tilde{\Omega}_q + 2k\cos\left(\frac{i\pi}{N+1}\right) \tag{3.71}$$

The main result from that work is the fact that the system exhibits a collective behavior that can be understood as a combination of each one of the cavities resonating in its fundamental mode, but combined with the rest with different phases for different eigenmodes of the full structure. This behavior can be clearly seen in Fig. 3.3, where for each one of the modes, the cavities resonate either completely in phase or with opposite phases (with possible differences in the relative amplitude of the field among them), the only exception being cavities where the field is forced to be zero because of symmetry.

The conclusion we found in [115] was that a prototype such as the one displayed in Fig. 3.6 under the effect of a strong magnetic field oriented along the z direction would allow for axion detection with an effective conversion volume equivalent to the sum of all the sub cavities. But on a mass range given by, roughly, the frequency of the fundamental mode of the sub cavities. Which would therefore allow to access much higher masses than a single cavity with dimensions equivalent to those of the whole system.

3.3.4. Multi cavity manufacturing

The value of the coupling, k, between the consecutive cavities can be calculated for any cavity and iris pair in the following way [118]: A set of two identical cavities

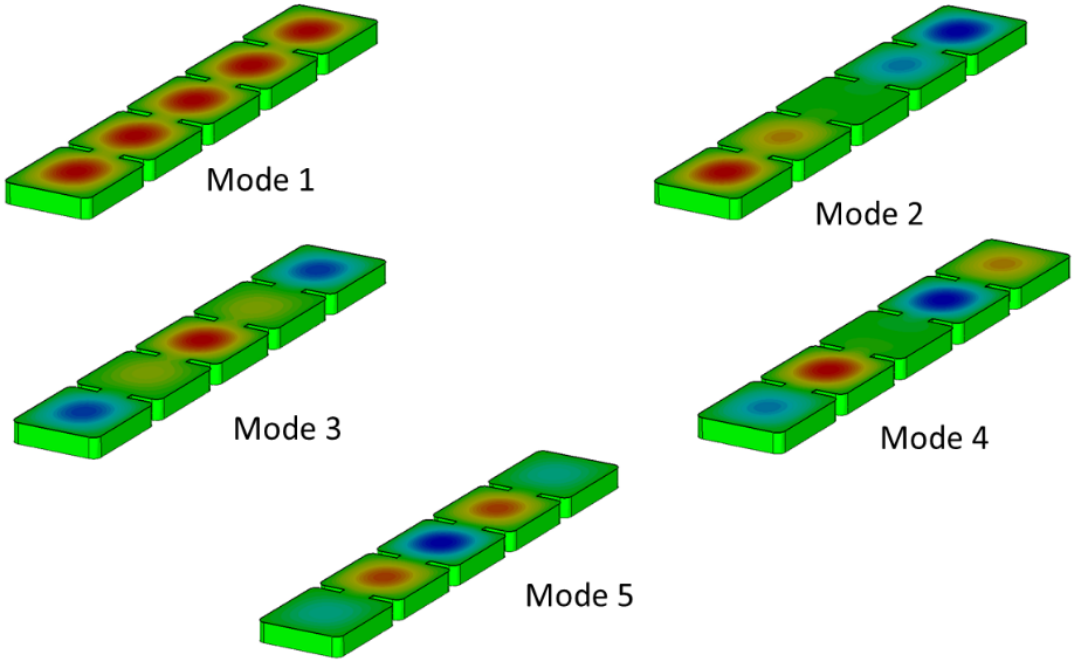

Figure 3.3.: Electric field pattern, z-component, of the 5 resonant modes for the structure described in Fig. 3.6, the color gradient red to blue represents the orientation of the field ranging from positive to negative. The first mode, which we also denominate fundamental mode, would display a perfect alignment of the E-Field with respect to an external static B-Field along the vertical axis.

connected by the iris under study are simulated. First we impose 'Perfect Electric Conductor' conditions on the iris, this will give us a fundamental mode frequency of the system f_e, the same procedure is repeated but imposing 'Perfect Magnetic Conductor' conditions this time on the iris, and the frequency f_m is obtained. With these two values, the coupling coefficient can be obtained as

$$k = \pm \frac{f_e^2 - f_m^2}{f_e^2 + f_m^2} \tag{3.72}$$

the $+$ sign corresponds to inductive irises, while the $-$ to capacitive irises. The physical difference between capacitive and inductive irises can be seen in figure 3.4. When modeling a microwave filter each cavity is treated as a RLC circuit coupled to its neighbors. The terms inductive and capacitive therefore make reference to the coupling between different circuits to be mediated by either inductance or capacitor contribution.

Since there is a connection between f_e, f_m and the dimensions of the cavities and the irises, one would expect that a relation can be extracted for k as a function of those same parameters. However, we have been unable to identify an expression, neither fully analytical nor approximate, connecting the structure dimensions and the irises coupling. For obtaining such an expression one needs to characterize the

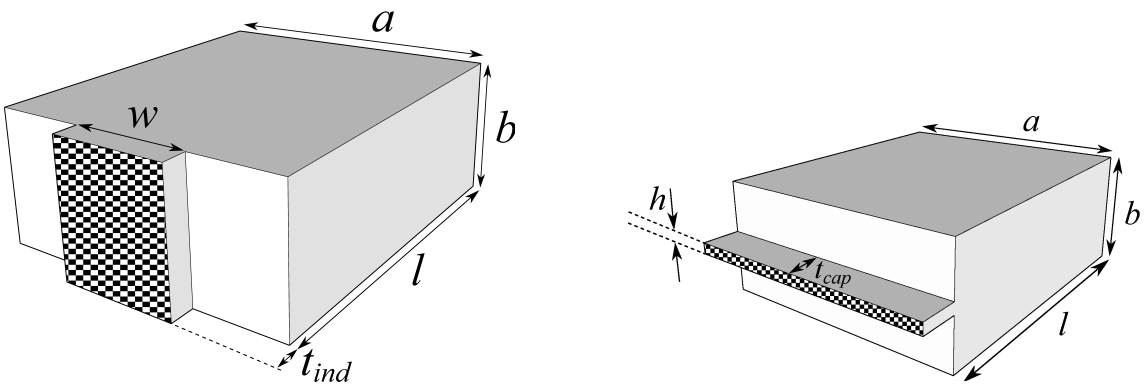

Figure 3.4.: Geometry of the cavities with inductive (left) and capacitive (right) irises. The parameters a, b, l determine the resonant frequency of the cavity, while the values of w and h govern the coupling between cavities. The smooth surface is the external conductor, the inside volume is vacuum and the checked area represents the irises (holes) that connect consecutive cavities.

direct influence of the boundary conditions on the fundamental mode frequency. It is unclear how the dependency on the physical dimensions can be factorized outside of the integral equations associated to this calculation, or if this is even possible without very specific assumptions for the geometry of the structure. A more detailed study of these expressions is envisioned as a future development for a better understanding of the underlying theory of the formalism presented here.

For the manufacturing process of a structure where all irises are either capacitive or inductive, see figure 3.5, one can proceed as follows:

- A block of metallic material is milled, resulting in a structure composed by consecutive sub cavities and irises.
- A lid made out of the same material is milled to close the structure.
- If needed, both parts are coated by a higher conductivity metal deposition.

Some complications arise when one targets at manufacturing a system that combines both kind of irises, since such a structure cannot be easily manufactured as a full solid piece and a lid. Specific examples about this process and the consequences regarding Q factor degradation is discussed in 8.3.1 when considering prototypes that alternate inductive and capacitive irises.

3.3.5. RADES First prototype

The first axion dark matter run performed by the RADES group took place in 2018 as part of the CAST-RADES haloscope search. And, after a thorough analysis, the results were published in 2020 [119].

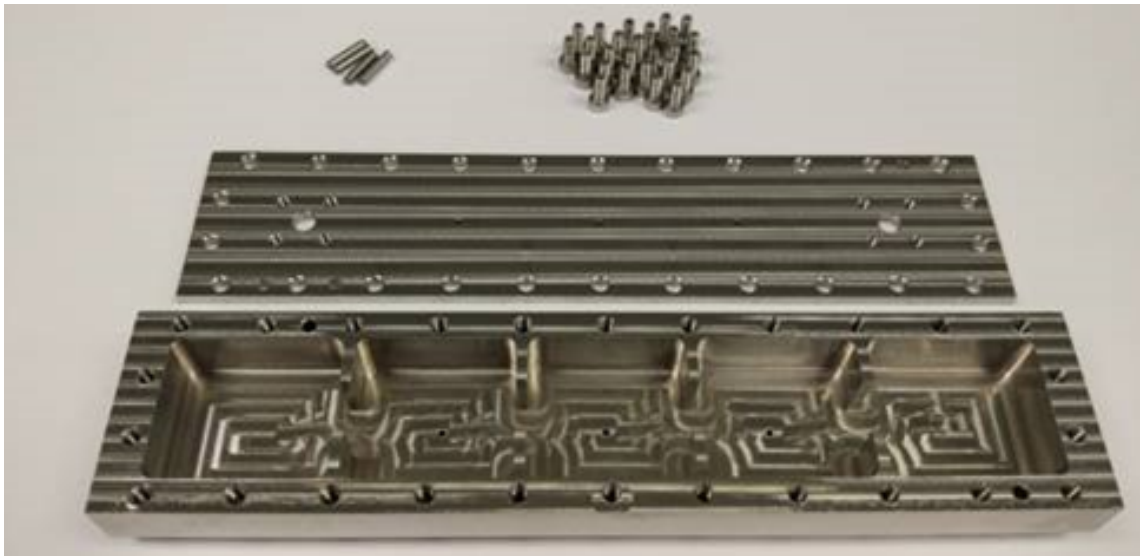

Figure 3.5.: Multi cavity prototype based on a 5 cavities all-inductive irises design. It was manufactured in stainless steel 316L, and later copper coated for the CAST-RADES experiment [115].

For the data taking, the prototype designed in [115] was placed inside one of the CAST magnet bores. The detection volume (see Fig. 3.6) consisted on a resonant structure segmented into five sub cavities. The dimensions of the sub cavities where chosen to fix the resonance frequency of the fundamental mode around 8.428GHz which corresponds to an axion mass of 34.64μeV and the value of coupling between cavities, k, was chosen to keep the modes as much separated as possible without losing the resonating mode structure. An optimization process was performed on CST Microwave Studio with the maximization of the figure of merit $\mathcal{G}^2QV$ as the goal function, and the final dimensions, compiled on Table 3.1, were fixed for the structure to be manufactured. It was built on stainless steel and a copper coating was applied to improve the quality factor.

The resonant frequency of the fundamental mode, and the desired value of the coupling k give a restriction on both the values of the cavity length, and the iris width L_i and W_i respectively. The value of W_i is the same for all irises. While the value of L_i is the same for all internal cavities on the system, and has to be slightly corrected for the cavities on the extremes to account for them only having one iris instead of two. The values of a and b, cavity width and height, are arbitrary and were chosen for convenience to match a radio-frequency engineering standard, namely the dimensions of WR-90 rectangular waveguides. The value of iris length, t, is also arbitrary and was fixed to accommodate to manufacturing restrictions.

Once the resonant structure was manufactured, we tested its behavior, measuring the frequency on the first mode and its quality factor with a vector network analyzer. A deviation of $\sim 3\%$ in the value of the fundamental mode frequency was found, which was well in accordance with the associated manufacturing tolerances. However, the loaded quality factor measured experimentally $Q_L \approx 16000$ was a

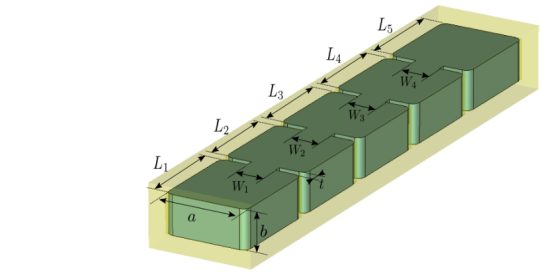

Figure 3.6.: Design of the CAST-RADES prototype. The system consists on 5 sub cavities coupled by irises, with the dimensions specified on Table 3.1.

Dimension	Length (mm)
a	22.86
b	10.16
$L_1 = L_5$	26.68
$L_2 = L_3 = L_4$	25.00
W	8.00
t	2.00

Table 3.1.: Dimensions of the CAST-RADES prototype at cryogenic temperature, $T = 2$K.

factor 2.5 lower than expected from simulations. This was assumed as associated to two manufacturing defects:

- A smaller residual resistivity ratio of the copper coating than expected, due to its anomalous skin effect and other imperfections in the coating,
- The horizontal cut in the cavity, separating the lid from the main structure, which was not included in the simulations.

This reduction of the quality factor lowered the sensitivity of the prototype but did not have a strong impact in the value of the figure of merit. The cavity was installed inside of the CAST magnet, as displayed on the scheme in Fig. 3.7. For extracting the signal a critically coupled port was implemented in order to maximize the output power without perturbing the resonance of the fundamental mode. Another port was implemented for testing and characterizing the system, this one under-coupled for minimizing the effect on the noise temperature of the system.

The data acquisition system (DAQ) consisted on two different stages:

- Analogue Part: Amplifies the signal and down-converts it to a band centered around 140MHz which can be easily read by an Field Programmable Gate Array (FPGA)
- Digital Part: Composed by an FPGA that digitizes the signal, computes its Fast Fourier Transform (FFT) and integrates up to 0.44739 s of acquisition time. Before sending the data via Ethernet to the acquisition computer.

After several days of continuous data acquisition, the data was analyzed in order to search for the presence of an axion signal on the band under observation.

The analysis procedure follows the guideline established by the HAYSTAC exper-

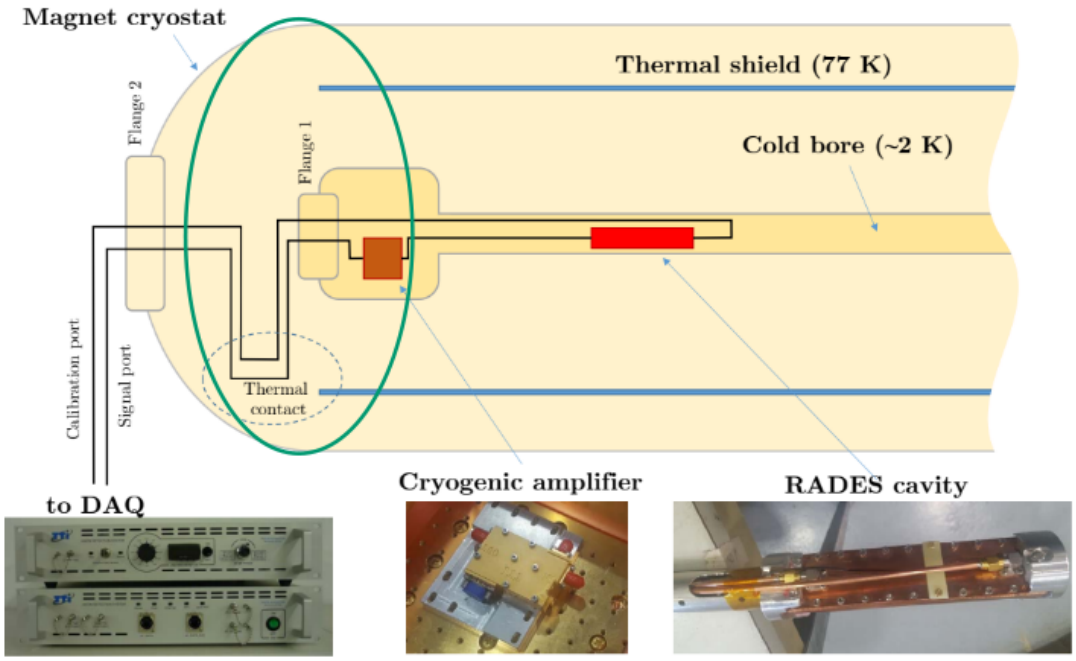

Figure 3.7.: Schematic of the CAST-RADES setup in 2018. The resonant cavity is placed inside one of the bores of the CAST magnet, refrigerated down to 2K. The signal from the system is extracted via a coaxial cable that goes into a cryogenic amplifier of 55dB and out of the cryostat into our data acquisition system. Image taken from [115]

iment (Haloscope At Yale Sensitive To Axion CDM) [120]. We will not describe the details, even though they played an extremely important role on the proper characterization of the system, but they are not of particular relevance for this work. This analysis was one of the main parts of the PhD work developed by Dr. Sergio Arguedas Cuendis at CERN. For a exhaustive treatment of this subject, the reader is encouraged to check the paper where we presented our results [119]. An even more detailed discussion, for those interested, can be found on Dr. Argueda's thesis [121].

The result of the data taking was an exclusion limit for axions in the mass range $34.6738\,\mu\text{eV} < m_a < 34.6771\,\mu\text{eV}$ and axion-photon couplings down to $g_{a\gamma} \gtrsim 4 \times 10^{-13}\text{GeV}^{-1}$.

This first implementation of the RADES approach to axion searches allowed us to show the feasibility of a resonant multi-cavity prototype and obtaining exclusion limits on a region not explored before. We had already acquired a lot of expertise on the path since the idea was born, and with that experience we could identify a series of points to improve on future setups.

3.3.6. Helioscopes: Solar axion conversion into photons

We want to turn our attention now to the detection of axions originated at the Sun. The basic mechanism for producing axions inside the inner core of the Sun, is via Primakoff effect (photon-axion conversion), this process takes place for all QCD axion, and ALPs models.

In [122] the general case of low-mass boson production via two-photon vertex coupling was studied. In particular, the rate of production for Primakoff axions inside the solar plasma was derived

$$\Gamma\left(\gamma_t \to a\right) = \frac{g_{a\gamma}^2 T k_{\mathrm{D}}^2}{16\pi}\left[\left(1+\frac{k_{\mathrm{D}}^2}{2\omega_t}\right)\ln\left(1+\frac{2\omega_t}{k_{\mathrm{D}}^2}\right)-1\right] \tag{3.73}$$

where $g_{a\gamma}$ is the axion-photon coupling, T is the solar plasma temperature, k_{D} is the Debye-Hückel wave number of the electrons, and ω_t is the frequency of the converted photon, in the rest frame.

Now, if one combines this rate of production, with the thermal photon bath in the sun, the flux of axions traveling towards the Earth and integrates over the solar model for the inner core [123] the axion flux per energy can be calculated. Quoting the general result found in [124] where E is in keV

$$\frac{\mathrm{d}\phi_a}{\mathrm{d}E} = 6.02\times10^{10}\,\mathrm{cm}^{-2}\,\mathrm{s}^{-1}\,\mathrm{keV}^{-}1\left(\frac{g_{a\gamma}}{10^{-10}\mathrm{GeV}^{-1}}\right)^2 E^{2.481}e^{-E/1.205} \tag{3.74}$$

In the case of non-hadronic axion models (the most famous being the DFSZ model), there is also the possibility for them to be produced via the so called ABC reactions [125], see figure 3.8a for the Feynman diagrams describing these processes. The name of these ABC processes stands for: Atomic axio-recombination, Atomic axio-deexcitation, axio-Bremsstrahlung, and Compton scattering, based on the equivalent SM interactions. In this context axions would couple at tree level to electrons and therefore these effects would be dominant, when compared to Primakoff conversion (see figure 3.8b).

Considering that Primakoff conversion is common for all axion an ALPs models, it is a safe approach to consider only the Primakoff spectra (3.74) when searching for solar axions. In the case of detecting a signal, and depending on the sensitivity of the detector, one could extract model dependent information, like the axion mass [126] or the $g_{a\gamma}$, g_{ae} couplings [127].

Having summarized the production mechanism we proceed to focus now on the acquisition setup for these solar axions. The main experiments proposed for the exploration of the solar axion flux are the so called helioscopes. The basic idea was proposed originally- together with haloscopes- in Sikivie's seminal paper [94]. It consists on the conversion of solar axions via inverse Primakoff effect in presence of a strong magnetic field, see figure 3.9 for a sketch of the helioscope setup.

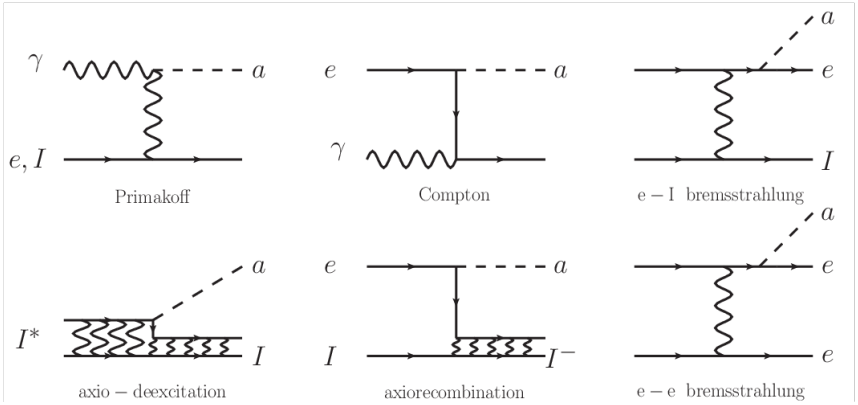

(a) Feynman diagrams for the Primakoff and ABC processes responsible for solar axion production [125].

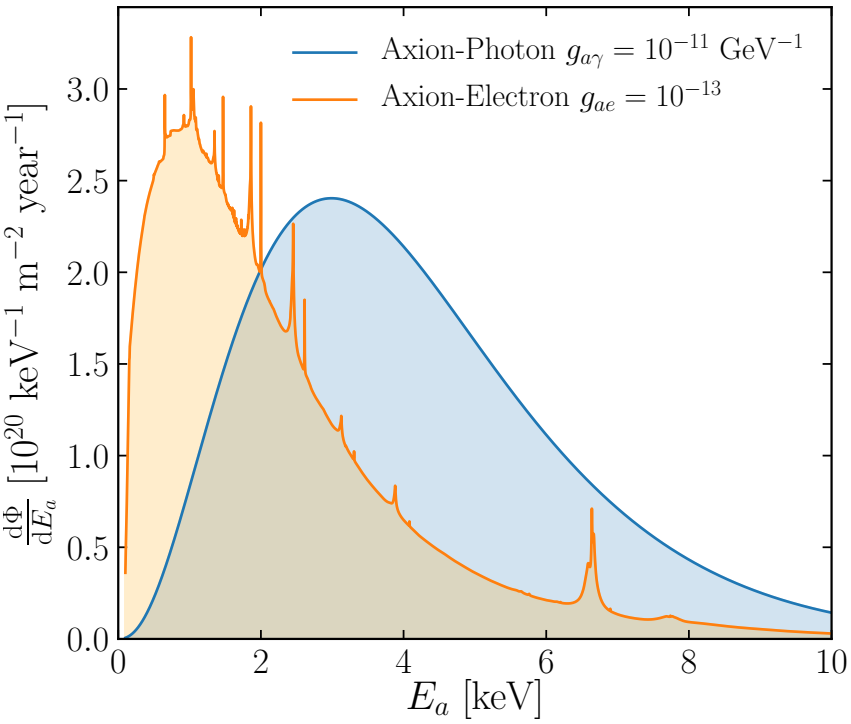

(b) Solar axion flux expected in non-hadronic models from Primakoff conversion and ABC processes . Values of the couplings $g_{a\gamma} = 10^{-11}\text{GeV}^{-1}$ and $g_{ae} = 10^{-13}$ have been assumed for the comparison [126].

Figure 3.8.: ABC Processes in axion to electron conversion.

The axion-photon conversion probability for relativistic axions inside of a magnet for a setup like the one sketched in figure 3.9, can be computed [129] as

$$P_{a\gamma}(E_a) = \frac{g_{a\gamma}^2 B^2}{4\left(q^2 + \frac{\Gamma^2}{4}\right)}\left[1 + e^{-\Gamma L} - 2e^{-\Gamma L/2}\cos\left(qL\right)\right] \tag{3.75}$$

where L is the length of the magnet, Γ is the x-ray damping of the media inside the

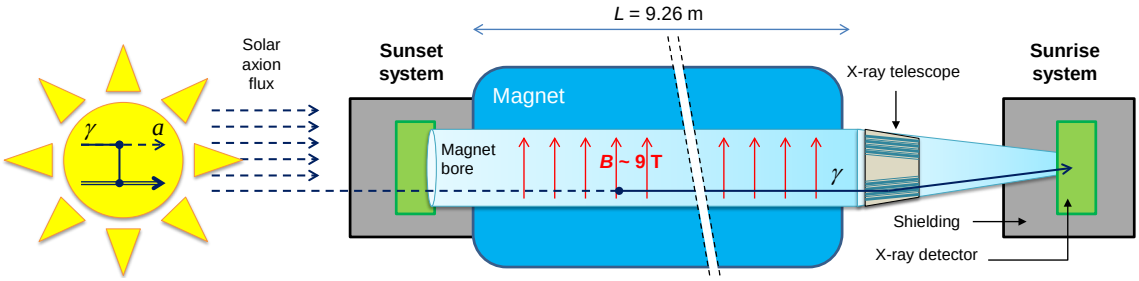

Figure 3.9.: Sketch of an axion solar telescope or helioscope. The solar axion flux crosses a intense transverse magnetic field where axion-photon is expected. Photons generated via inverse Primakoff effect result on focalized X-rays on the detector central spot. Figure extracted from [128].

magnet bore, and the momentum transfer, $q = q(E_a)$, carries the energy dependence

$$q(E_a) = \frac{\left|m_\gamma^2 - m_a^2\right|}{2\omega} \tag{3.76}$$

where $m_\gamma = \sqrt{\frac{4\pi\alpha n_e}{m_e}}$ is the refractive photon mass, with n_e being the number density of electrons for the inner media and m_e the electron mass.

There are three main experimental parameters that condition (3.75), i.e. L, n_e and Γ. If we consider the case where the inner media is vacuum, then $n_e = 0 \rightarrow m_\gamma = 0$, $\Gamma = 0$ and the probability of axion to photon conversion adopts the simplified expression

$$P_{a\gamma}(E_a) = \left(\frac{g_{a\gamma}BL}{2}\right)^2 \left[\frac{\sin\left(qL/2\right)}{(qL/2)}\right]^2 \tag{3.77}$$

and therefore, for the case where $qL \ll 1$, the conversion will be enhanced due the effect of a resonance. In the particular case of the CERN Axion Solar Telescope (CAST) magnet, $L \approx 10$m which allows detection up to masses of around $m_a \approx 10^{-2}$eV, in figure 3.10 one can see this behavior when going to higher masses with a given helioscope length in a vacuum phase. From equation (3.75) is easy to see, that one way for modifying the setup in order to be sensitive to higher masses is to introduce a buffer gas in the magnet bore. The buffer gas, changes the value of q allowing for higher values of qL without the need to increase the magnet length. The exclusion limits of such a search can also be seen in figure 3.10 for the particular case of the ^{3}He and ^{4}He runs performed in CAST during the years 2005 to 2011 [130–133].

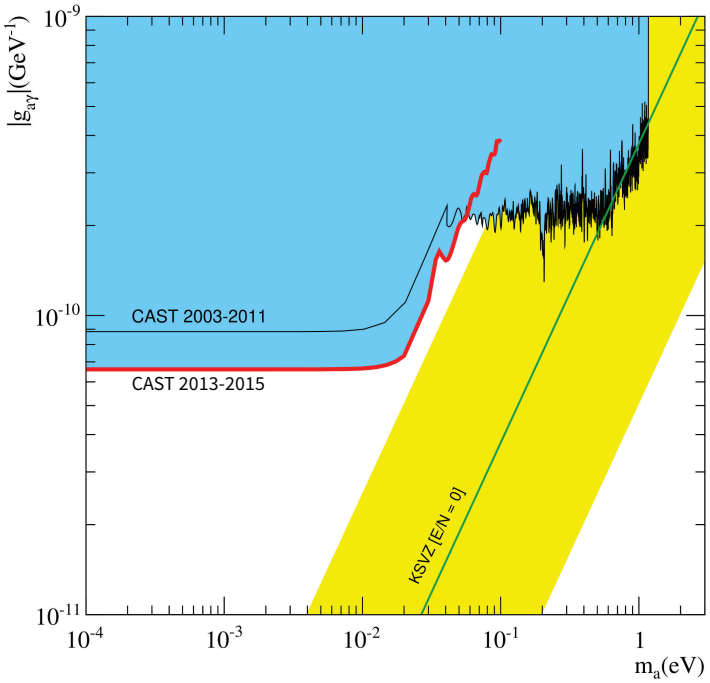

Figure 3.10.: Exclusion limits on the mass vs axion-photon coupling parameter space imposed by the consecutive CAST runs. In red the last run, with an improved sensitivity due to the use of x-ray focusing optics, one can see how the sensitivity drops after a certain mass, given by the magnet length. The previous runs, in blue, are less sensitive but can reach higher masses due to the presence of a buffer gas in the magnet bore [134].

4

Gaseous detectors in rare event searches

In this chapter we will take a momentary detour from axion physics to summarize the basics of gaseous ionization detectors, and the usual background sources for such a detector. This chapter is thus intended as a short compilation of the main ideas and vocabulary that we will need when studying the electronics contribution to the BabyIAXO background model in chapter 7.

The search for solar axions in the BabyIAXO helioscope [135] is part of the so called rare event searches. As rare event searches we consider experiments where we try to measure phenomena with an expected very low detection rate, what is considered "very low" might change depending on the experiment considered in particular, but in general we are talking about signal events on the order of one in billions or even less frequent. This searches constitute a pivotal aspect of experimental physics nowadays, particularly in the realm of particle and astroparticle physics, with Dark Matter searches being some of the most well-known [136–139].

In the context of these searches, a particular kind of gaseous detectors, namely Time Projection Chambers (TPCs) offer several advantages, including high spatial resolution, precise particle tracking capabilities, and the ability to operate in high-rate environments [140]. These features provide us with a detection environment in which all sources generating background events can be characterized very well, and their contributions properly discriminated.

Finally, we will also introduce the REST-for-Physics framework, a software based on ROOT that has been developed and extensively used for detector simulations in the context of the IAXO collaboration [141].

4.1. Fundamentals of gaseous detectors

The main ideas about gaseous detectors are typically discussed in most particle detection books, the recollection I make in this section is mostly based on [142], which is one of the well established references for experimental particle physicists. And [143], which focuses on gaseous detectors, and provides an in-depth treatment of the current state of the art.

Gas ionization detectors are a class of particle detectors commonly used in particle physics, nuclear physics, and radiation detection. These detectors operate based on the principle of ionization of gas molecules by incident radiation or particles. When ionizing radiation interacts with the gas within the detector volume, it creates ions and free electrons through collisions with the gas contained in the vessel. Gas ionization detectors offer advantages such as high sensitivity, fast response times, and the ability to detect a wide range of radiation types and energies.

The planar ionization chamber can be regarded as the simplest theoretical implementations of the gas ionization detector concept, see figure 4.1a. In it, a neutral gas is enclosed in a chamber with two parallel plates on opposite walls. A voltage difference ΔV is applied between these plates, i.e. the anode and the cathode. The presence of the gradient of a potential generates an homogeneous electric field in the direction perpendicular to the electrodes. In a setup with these characteristics, external radiation will interact with gas molecules (primary interaction) and generate ion-electron pairs which will be accelerated in opposite directions until collected in the electrodes, electrons in the anode and cations in the cathode.

The detector developed by Ernest Rutherford and Hans Geiger in the beginning of the XX century is considered the first implementation of a gas ionization detector [144]. The philosophy is exactly the same as the planar ionization chamber, but implemented on a cylindrical geometry. Thus, the detector consists on a hollow cylinder containing a gas and a thin metal wire inside, coaxial to the cylinder. The voltage difference is applied between the internal and external conductors, and a radial electric field is generated in the interior of the cylinder.

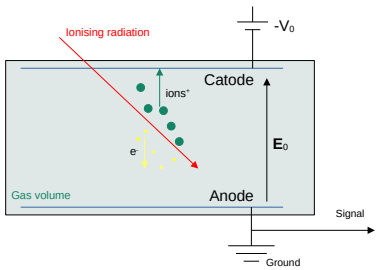

(a) Basic scheme of a planar ionization chamber, only primary events with electron-cation pairs generation are displayed.

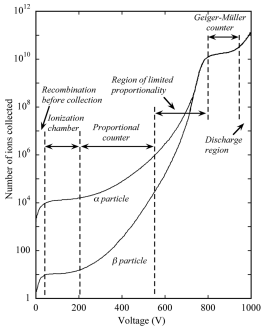

(b) Different operation regimes of a proportional counter as a function of the bias voltage applied to the external electrodes [143]. The detector response to α and β radiation as a function of the the applied voltage is plotted.

Figure 4.1.: Planar ionization chamber operation and general performance of gas ionization detectors.

The real potential of these kind of detectors is reached when increasing the bias

voltage on the electrodes, this increases the electric field giving extra acceleration to the cation-electron pairs (figure 4.1b). This extra energy makes the electrons (cations) trigger further ionization in the gas while traveling towards the anode (cathode), thus increasing the charge collected in the electrodes. In the voltage range where the detector is operated, this amplification of the initial signal is proportional to the charge released in the primary interaction, and therefore allows the reconstruction of the energy for the initial interaction. In this detector, even if the initial energy is small, the final signal would be high enough for being easily detected. Together Hans Geiger and Walther Müller later perfected this device [145], designing a proportional counter that allowed the detection of single electrons released in the initial interaction.

Electron drift

One of the main phenomena appearing in gaseous detectors, already mentioned above, is the so called charge drift. This effect refers to the movement of the charged particles towards the electrodes, i.e. electrons toward the anode and positive ions toward the cathode.

Electrons originated by the initial interaction acquire a constant acceleration towards the anode, the dynamics of the electrons is governed by this acceleration and by the constant elastic collisions with the atoms they encounter along the path. In this regime they get successively dispersed acquiring the average drift velocity [146]

$$\mathbf{v}_e = \frac{e}{2m_e}\mathbf{E}\tau \tag{4.1}$$

where e is the electron charge, m_e its mass, $\mathbf{E}$ is the external electric field and τ is the mean time between collisions. The collision cross-section is different for different gases and can be strongly dependent on the electric field applied. In particular, when the energy gained by the electrons approaches that of the electrons bound in the gas molecules inelastic collisions start dominating the dynamics of the electron drift. It is for these reasons that the drift velocity has to be studied for the particular gas and electric field. These simulations are implemented by software packages as Magboltz [147], and we will made use of them when characterizing the response of the detector in BabyIAXO to external radiation.

The larger mass of the ions in comparison to the electrons, generates one of the main differences between electron and ion drift. The mobility of the cations is way lower and chemical reactions with the rest of the gas might have to be taken into account. For this reason and because we will only analyze the signal derived from the electrons measured at the anode, we will skip discussing the case for ion drift.

Charge multiplication and final signal

As the external field strength E increases, electrons are able to further ionize gas molecules along their path towards the anode. This usually results in a chain reaction when the secondary electrons generate further ionization themselves. This phenomenon is referred to as electron avalanche and is the main ingredient of the signal amplification in a gaseous detector.

In the 1930s Shockley [148] and Ramo [149] showed that the signal measured by the detector for the electrons reaching the electrode is given by

$$I = e\frac{\mathbf{v}_e \cdot \mathbf{E}}{V} \tag{4.2}$$

where e is the electron charge, $\mathbf{v}_e$ is the velocity of the electrons reaching the anode, $\mathbf{E}$ is the electric field in the vicinity of the electrode and V is its voltage, this relation is known as the Shockley-Ramos theorem.

In a first approximation, as we apply higher fields the signal generated at the anode increases. In a more realistic picture, different regimes of operation for gaseous ionization detectors as a function of the magnitude of the voltage applied can be observed, see figure 4.1b. In the initial region, usually labeled as the *recombination* regime, most of the ions and electrons recombine together before reaching the electrodes. On the *ionization chamber* range, most of the initial pairs reach the electrodes. But it is not until we reach the *proportional counter* energy range, that the avalanche effect generates a response in the anode proportional energy deposited in the gas by the primary event. After this range large charge densities are created surrounding the electrodes and the proportionality effect is lost eventually. At even higher voltages, a final plateau (the *Geiger-Müller* region) is reached where the ionization collected at the electrodes is independent of the initial energy, as its name suggest, this is the range where Geiger-Müller counters operate which allows very precise event counting resolution while compromising completely energy resolution. At even higher voltages the gas undergoes self-ionization due to the electric field and arc discharges are constant, limiting the detection performance completely.

The objective with most of these detectors is therefore to operate in a regime where the signal amplification is maximum, while avoiding arc discharges. However, depending on the application, energy resolution can be disregarded, in order to optimize counting performance.

4.1.1. Time Projection Chambers

Let us center our attention now around one of the modern gaseous detectors broadly used in collider physics and rare event searches, the time projection chamber. There are two main points motivating this section, first it will helps us describe the setup with a TPC implemented on the phase I of the solar axion search at CAST [150],

and second it will serve as a first step for understanding the context in which the Micromegas detector is developed and implemented.

Time projection chambers are gaseous detectors designed, not only to count events, but to precisely track the paths of charged particles. TPCs operation is based on the use of a long distance drift chamber, as the ones described previously, in combination with a more elaborated system of electrodes that allows obtaining both spatial resolution and time information about the avalanche. Based on this measurements the initial event can be characterized in a more detailed way than with proportional counters, and detailed information about the initial energy and trajectory can be extracted.

The principle of operation for TPCs was established with the development of the multi-wire proportional chamber (MWPC) in 1968 by Georges Charpak and his team at CERN [151]. This invention, figure 4.2a, remains nowadays a basic part in most particle physics experiments, and granted Charpak the Physics Nobel prize in 1992. In a MWPC an array of many closely spaced anode wires are placed between two cathode planes, which generates an electric field topology as the one in figure 4.2b. Accelerated electrons in the avalanche get trapped in the different regions defined by the consecutive anode wires. These regions can be read and amplified independently and provide detailed special resolution in the direction perpendicular to the anode plane. In most MWPC two of this detectors are stacked one after another with the anode planes aligned perpendicularly to obtain 2D information.

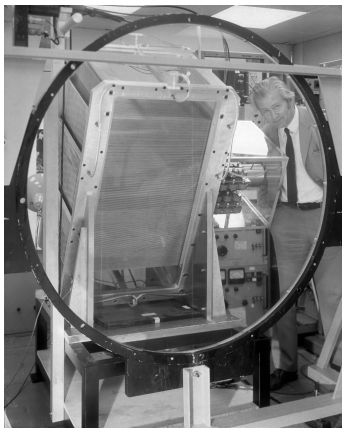

(a) Georges Charpak standing by a Multi-Wire Proportional Chamber at CERN in 1973 [152].

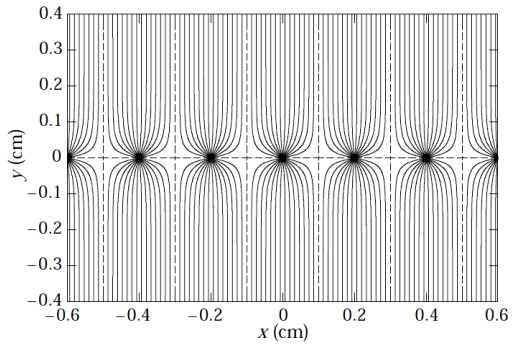

(b) Typical electric field distribution generated inside of a TPC. The array of anodes generates a series of consecutive regions that behave as independent proportional counters [153].

Figure 4.2.: Multi-Wire Proportional Chambers and TPCs

The general TPC design, figure 4.3, follows the MWPC idea and incorporates temporal information by measuring the drift time, in case of correlating the detection of electrons and ions this measurement can be absolute, otherwise it will be relative to the avalanche itself. The time evolution of the signal is obtained by recording the charge distribution on the readout pads at successive instants. By measuring

the drift times and positions of the ionization signals on the readout plane, TPCs can reconstruct the three-dimensional trajectories of charged particles with high precision.

We can summarize the main parts of a typical TPC to be

- Gas Volume: A large gas-filled volume typically enclosed in a chamber. The gas serves as the medium for particle ionization. Different gases can be chosen based on factors such as its density, ionization properties, and ability to provide a uniform electric field.
- Electric Field: A uniform electric field is established within the gas volume, by applying high voltages to the cathode located at one end of the chamber. This electric field causes electrons produced by particle interactions to drift through the gas towards the readout plane.
- Readout Plane: The readout plane is equipped with a grid of sensitive detectors, such as wires or electronic pads, that record the arrival times and positions of the ionization electrons as they reach the plane. The spatial distribution of ionization signals along with their drift times provide information about the trajectory of the charged particle that triggered the avalanche.

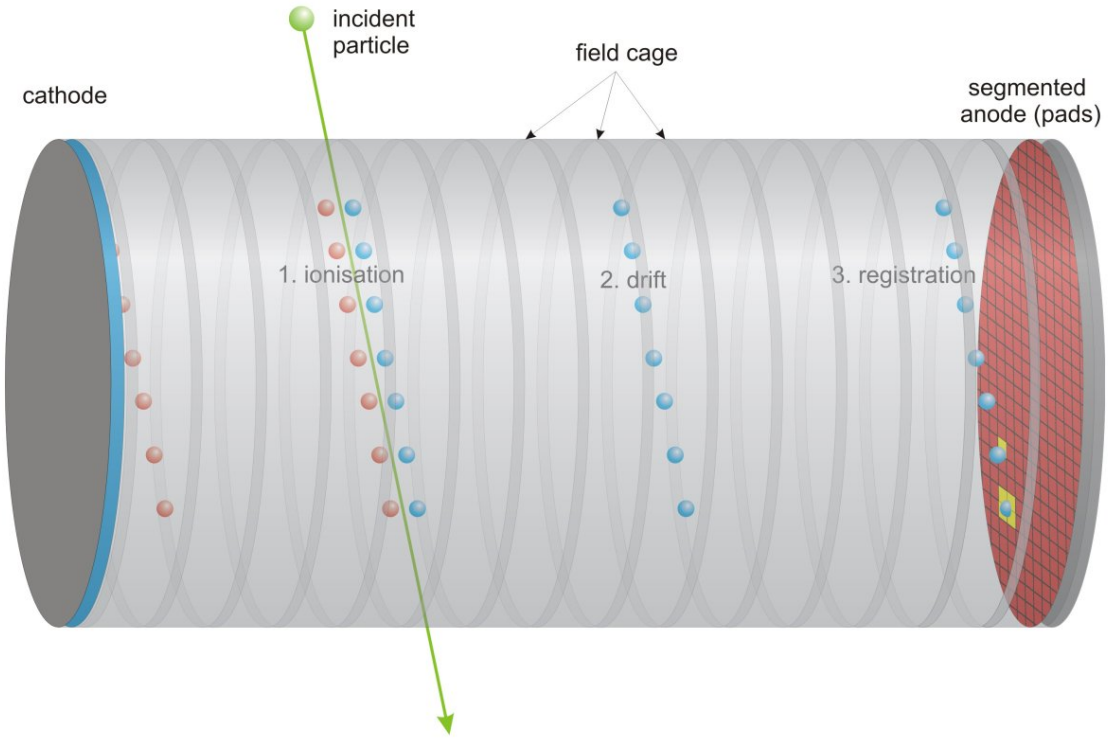

Figure 4.3.: Schematic side view of a time-projection chamber. The electrons travel to the anode, where the readout plane is located, while the positive ions travel towards the cathode. The external field cage, at high voltage homogenizes the electric field, in a similar manner as in the MWPC case [154].

4.1.2. The MICROMEGAS detector

In 1996 a considerable advance was achieved in the field of parallel plate detectors with the development of the MIcro-MEsh-GAseous Structure detector technology in the group of Ioannis Giomataris at Saclay [155]. These detectors, usually abbreviated as Micromegas (MM), introduce the use of a micro-engineered segmented anode on a TPC for substantially increasing the amplification of the signal, while maintaining the original topology of the cathode, figure 4.4a.

A schematic depiction of the operation for a Micromegas detector is shown in figure 4.4b. A first voltage difference is set between the drift cathode and the anode. A second cathode, in the form of a surface with micro-meter sized holes is placed at a distance of $\sim 100\,\mu$m with respect to the TPC anode, and a a high voltage is applied between them. In this kind of setup free electrons liberated in the drift region are accelerated towards the anode. Once they arrive close to the micromesh they are guided through the gaps, following the lines of very high electric field between the micromesh and the anode, and collected in the pads or strips present in the anode. The electric field in the amplification region, is in general 10 or 50 times higher than the one present in the drift volume, this generates an enormous amplification which, combined with the detailed spatial resolution of the pads or strips in the anode, provides great track reconstruction capabilities.

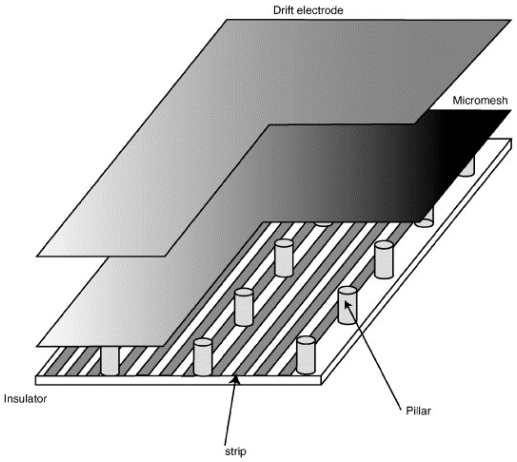

(a) Scheme of a micromegas parts. A drift volume is defined by a drift cathode and the micromesh. The micromesh acts as a cathode for the detector anode, which presents a series of pads or strips that collect the signal. The system is assembled on top of an insulating substrate and support pillars are placed to ensure the mechanical stability of the mesh.

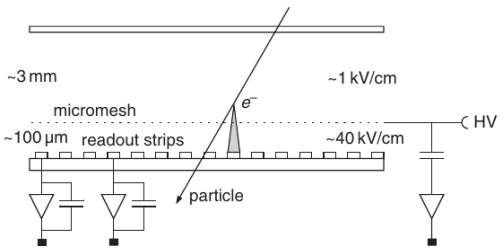

(b) Representation of an event crossing a MM detector. The ionizing particle generates electrons which travel through the drift region, until reaching the micromesh and entering the amplification region. This amplification generates a powerful avalanche effect and hit information is collected by a pad or a set of strips with very fine spatial resolution.

Figure 4.4.: Micromegas structure and basic operation [155].

Aside from the high signal amplification one can achieve in comparison to other detectors, one important advantage of using Micromegas detectors for rare event searches is its high radiopurity. The detector is only made of highly pure materials, in particular kapton and copper. The activity of MM was screened at Canfranc Underground Laboratory by using high purity germanium spectrometry techniques [156]. These measurements were performed in the context of the TREX-DM experiment which also requires a extreme low background environment for operation. The results showed levels of activity as low as $30\,\mu\text{Bq/cm}^2$ for Th and U and $\sim 60\,\mu\text{Bq/cm}^2$ for ^{40}K. Even though the MM detectors under study were not developed taking any extra precaution on material purity, just because of their composition, these values are at the level of those quoted for photomultipliers very carefully manufactured for rare event searches, like the ones employed at the XENON experiment [157]. The conclusions of these studies allows us to safely neglect the background contribution of the Micromegas detector in our system, since they are in general orders of magnitude below the natural background we would expect coming for most other sources.

4.2. The REST Framework

The REST-for-Physics (Rare Event Searches Toolkit for Physics) framework [158] is a software, which has been mainly developed by the Nuclear and Astroparticle Physics group at the University of Zaragoza, inside of the IAXO Collaboration but also in association to other experiments for low background detectors in which the group is involved like TREX-DM or PandaX-III [159, 160].

We will describe now briefly the main ideas behind the REST framework while focusing on a user oriented approach, in particular when studying the background generated for radioactive decays. Therefore, we will avoid getting into the technical details behind the software. For the readers interested on a developer focused approach, we refer to the detailed account of the underlying classes and the framework infrastructure that can be found here [141].

4.2.1. Steps for background simulations

Background simulations in REST follow three differentiated steps:

- Defining the geometry of the detector
- Running a Montecarlo event generation for the given background source
- Reconstructing the signal for the energy deposited in the detector

The first step relays mostly in translating the geometry of the detector into an XML-based language, the second step employs a sub-package that integrates Geant4

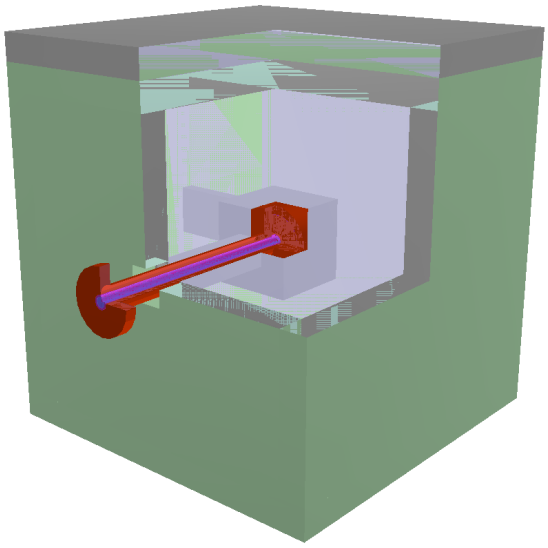

Figure 4.5.: Geometry of the IAXO-D0 detector as implemented in REST, by means of its GDML description. For a detailed description of the components see section 7.3.1

[161] in REST and the last one comprises the simulation of a series of physical processes programmed in ROOT [162].

4.2.2. Geometry implementation

The implementation of the geometry under study is made using markup language, in particular, Geometry Description Markup Language (GDML) [163]. GDML is a language developed at CERN for the description of detector geometries in a general way that allows both ROOT and Geant4 to interpret and implement the shapes and materials of the different parts of the detector: the gas volume, the copper strips, the lead shielding, etc. GDML allows the definition of complex solids by performing addition, intersection or subtraction operations between them; or even looped definitions for cases such as multi-cell structures or arrays of detector strips.

The material description of the geometry implemented serves two main purposes. First, it is used for the associated density and mass of the different volumes of the detector. But it also serves the purpose of registering the atomic number and the atomic mass of the nuclei that conform the material, which will be used later on in the code when the simulation of interactions with radiation are considered.

One last reason that makes GDML useful is how easy it is to show a given geometry, by using ROOT viewer classes, an example of a detector geometry is shown in figure 4.5.

4.2.3. RESTG4

The restG4 package integrates Geant4 simulations in the REST framework, which makes it an invaluable tool for background simulations in gas detector experiments. This package allows simulating the passage of particles through matter, as implemented in Geant4, i.e. for a given source it returns the energy deposits on the different areas of the detector geometry under consideration. The initial sources cover a vast range, from external fluxes of particles (neutrons, muons, photons, etc.) to radioactive decays either inside of the detector itself (intrinsic contamination) or outside (environmental radiation). The result of running a restG4 simulation is a TRestRun containing a series of TRestEvents

This package simulates the initial event generation and it is intrinsically connected to the physical processes to be taken into account, both in the particle emission and in the interactions with the different detector materials. For this simulations a series of so called *physics lists*, containing the main processes of interest, are selected. In order to simplify the simulations, it is advisable to select the main physic lists to be taken into account depending on the particles and energies under study. This processes are separated in terms of interactions, e.g. hadronic or electromagnetic, and in terms of the energy scales involved: low energy, UV regime, etc.

The main parts of a restG4 configuration file are

- Metadata and variables: Containing information about the simulation and data paths.
- Detector geometry: Specified in GDML, as described in section 4.2.2.
- Event generator: A description of the emitter with the nature of the source, its location and its angular distribution.
- Recorded data: Information to be stored after the simulations for each event.
- Physics lists: List of files containing the physical processes of interest to be considered in the simulations.

4.2.4. REST Processes

The last part of a REST simulation, as described in Sec. 4.2.1, deals with the performance of a series of analysis steps that allows us to extract the track reconstruction of either data generated with restG4, and signals measured by the detector during a data taking campaign. This analysis steps are defined as **REST Processes**. Hereunder there is a review of the main analysis processes in REST which are of interest for our studies. For the readers interested in the code structure, the actual RML code can be found in Appendix B.

TRestGeant4AnalysisProcess:

It provides observables associated directly with the energy deposits in the setup and allows for fast discrimination of irrelevant events, e.g. events triggering other active volumes but not the gas volume. It also provides information for the next analysis steps.

TRestElectronDiffusionProcess:

Evolves the energy deposited into particular points of the gas emulating the drifting of the signal. The nature of the gas mixture inside the copper chamber is very relevant in this part, since it conditions the drift velocity. For our study we assumed a mixture of 98% Argon and 2% isobutane.

TRestG4toHitsProcess:

Converts the energy deposits (TRestG4Event) into hits (TRestG4tHit). The correspondent TRestG4Hit objects contain the spatial, energy ant time information of the final interactions on the detector mesh for each initial TRestG4Event.

TRestHitsAnalysisProcess:

Computes a series of observables associated to the final energy deposits on the detector. This process is crucial for the background discrimination, since it can give us information about the spatial distribution of energy for a given event, and therefore allow us to separate events that can have an axion to photon conversion origin, from those that are associated to radioactive decays or cosmic muons crossing the gas volume off-axis.

TRestHitsToTrackProcess:

This REST process reconstructs the track in the gas volume associated to a given TRestHitEvent. This event can be either the result of a restG4 simulation or part of an actual data taking performed with the detector. Since the detector resolution is finite, possible multi-valuations on the reconstruction could appear, and therefore the TRestTrackEvent obtained after this processed could not fit exactly the event simulated by restG4, or the cascade in the gas detector in the case of real data.

TRestTrackReductionProcess:

The purpose of this process is to reduce the amount of tracks by adding together hits which are closer than a certain threshold. The reason behind the application of this process is to reduce the computational load of the simulations.

TRestTrackPathMinimizationProcess:

Recovers the minimum path between different hits inside of a same track. In our case this process does not modify much the results, but we keep it for tests in the reconstruction process and accelerating code performance.

TRestTrackReconnectionProcess:

Refines the physical track description of the particle showers in the detector, after applying path minimization. This process is required for physical consistency in case the previous one is applied.

TRestTrackAnalysisProcess:

As the other **AnalysisProcesses**, it allows us to compute a series of observables which contain physical information relevant for the study of the events, in this particular case, those observables are associated to the tracks of energetic particles reconstructed from a set of hits. This process, together with TRestHitsAnalysis-Process, contain most of the information required in order to characterize the background for a given source. In particular, it allows us to how similar background and signal events are, based on a series of physical observables.

4.2.5. Analysis observables

The different REST processes produce a set of physical observables that describe the events simulated and, ultimately, the response one would expect in the detector. From all the observables available in the REST simulations we will enumerate those which will be of special relevance to discriminate potential axion-photon conversion events from background. For the enumerated observables, the index i makes reference to the single hits in the detector, and the sums are over all of the hits in a single event.

- **Total energy**: Sum of all the energy deposits for a single event

$$E = \sum_i E_i \tag{4.3}$$

- **Mean position**: Weighted mean of the event, for the x, y and z coordinates.

$$\bar{x} = \frac{1}{E}\sum_i x_i E_i\,; \quad \bar{y} = \frac{1}{E}\sum_i y_i E_i\,; \quad \bar{z} = \frac{1}{E}\sum_i z_i E_i \tag{4.4}$$

- **Energy variances** σ^2: Variance of the energy distribution along the different axis

$$\sigma_j^2 = \frac{1}{E}\sum_i E_i(\bar{j} - j_i)^2, \quad j = x, y, z \tag{4.5}$$

  And in the xy plane

$$\sigma_{xy}^2 = \frac{1}{E}\sum_i \left[E_i(\bar{x} - x_i)^2 + E_i(\bar{y} - y_i)^2\right] \tag{4.6}$$

  These observables are specially relevant for characterizing the spreading of the event. Specifically, σ_{xy} gives information about the spot size on the detector plane for a given event, and σ_z^2 gives information about its temporal distribution.

- **xy sigma balance**: Calculated based on the variances found for the x and y axis. This balance informs us of how spread the event is between the two directions.

$$\text{Balance}(\sigma_x, \sigma_y) = \frac{\sigma_x - \sigma_y}{\sigma_x + \sigma_y} \tag{4.7}$$

- **Skewness** γ: Third moment of the energy distribution. Specially interesting for the estimation of asymmetry of the energy distribution of the event.

$$\gamma_{xy} = \frac{1}{E\sigma_{xy}^3}\sum_i \left[E_i(\bar{x} - x_i)^3 + E_i(\bar{y} - y_i)^3\right] \tag{4.8}$$

$$\gamma_z = \frac{1}{E\sigma_z^3}\sum_i E_i(\bar{z} - z_i)^3 \tag{4.9}$$

5

IAXO and BabyIAXO experiments

In this chapter we will discuss one of the main experiments under development for axion detection in the world. Namely, the International Axion Observatory (IAXO). We will start by briefly reviewing the paradigmatic example for last generation solar axion telescopes: the CERN Solar Axion Telescope (CAST). However, CAST did not only set an example as a helioscope but as a facility for broad axion and ALP searches, including solar axions, dark matter axions and even chameleons.

After reviewing CAST we will present the IAXO proposal and its first stage demonstrator, BabyIAXO, which is currently in development and is expected to be built and operated in the next few years.

5.1. Helioscopes: From first to last ... for now.

In 1992, following the proposal of solar axion conversion into photons in the interior of a strong magnet (see section 3.3.6), a first demonstrator of this principle was constructed in Brookhaven with the collaboration of Rochester and Fermilab, giving the first experimental exclusion limit for solar axions associated to direct detection, with just a few hours of data taking [164].

Five years later, in 1997, Sumico- a second axion helioscope at the University of Tokyo- tracked the Sun searching for axion-photon conversion for five days [165]. After being upgraded it was operated for another two runs, one in 2000 [166] and another from December 2007 through April 2008 [167].

The third generation axion helioscope, CAST, was originally proposed in 1999 [168]. After being successfully approved it underwent a commissioning phase that culminated in May 2003 when it started its first data taking campaign that would last 6 months, until November 2003 [169].

The original set up of the CAST experiment consisted on a 9.0 T LHC decommissioned dipole magnet with two separate bores and a total magnetic volume of $\sim 240\,\mathrm{Tm}^3$. It was mounted on a structure that allowed for sun tracking during sunrise and sunset. The sunrise was followed by a Time Projection Chamber (TPC) placed at the end of one of the bores, whereas the sunset was monitored by a Micromegas (MM) detector in one of the bores [170] and a combination of X-ray

focusing optics with a Charge Coupled Device (CCD) inside the other [171, 172].

After this first phase the experiment was upgraded several times continuing to run with different detectors and configurations [124, 130–133, 150, 170, 172–174] until its final discontinuation in 2021. The culmination of the CAST solar search was published in 2017 in *Nature* [134] and placed the strongest limits for solar axions up to the 1 eV scale. Three years after its discontinuation, the analysis of the last dataset was completed and the final limits updated [175].

In figure 5.1 we compile the regions excluded consecutively by the mentioned helioscopes, they account for more than 25 years of experimental research in several groups worldwide. During their lifetime these experiments also served as an environment in which several technologies found application and evolved. This technologies being rooted in fields as diverse as low background detectors, X-ray optics, cryogenics, superconducting magnets, etc.

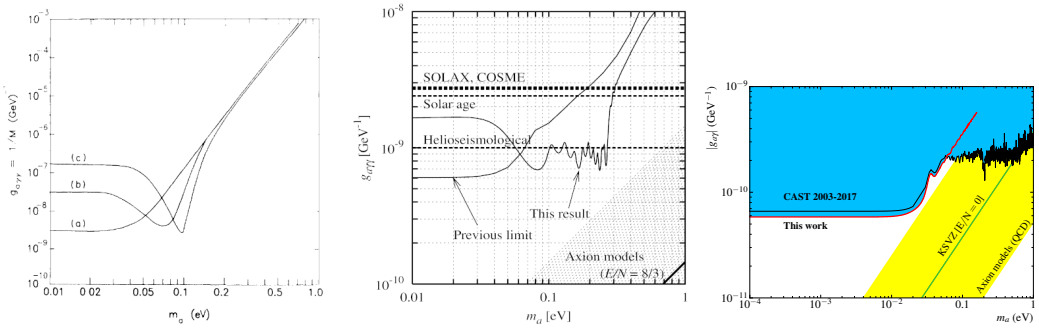

(a) Solar RBF (b) SUMICO (c) CAST

Figure 5.1.: Axion mass vs axion-photon coupling parameter space. The three different subfigures depict the regions excluded by the Rochester-Brookhaven-Fermilab (RBF)(a), SUMICO (b) and CAST(c) helioscopes. Over the course of these three generations of helioscopes the refinement of the technique has allowed to an increase of the sensitivity in $g_{a\gamma}$ of up to 3 orders of magnitude.

5.2. The CAST multi-detector paradigm

During the last stages of the CAST data taking, in the year 2017, the first RADES and CAPP cavities were installed inside of its magnet [176]. In this context, the CAST experiment became the first helioscope in the world to run simultaneously a haloscope search by using the same magnet. In the following years up to three different experimental setups would operate in parallel to the solar detectors:

- The CAST-RADES axion haloscope: Multi cavity haloscope experiment searching for DM axions with a mass of around 34.67 µeV [119].

- The CAST-CAPP axion haloscope: High frequency haloscope operating in the band from 19.74 μeV to 22.47 μeV [177].
- The Kinetic WISP (KWISP) sensor: An opto-mechanical force sensor for the detection of chameleons, ALP candidates that could constitute Dark Energy [178].

Because of its connection with this thesis work, we will discuss more in detail the CAST-RADES setup in section 3.3.5, however let us take this occasion to remark briefly the results of both RADES and CAPP searches at CAST, during their data takings in 2018 [119], and 2019-2021 [177] respectively. In figures 5.2 and 5.3 one can see the success of both experiments when probing different areas of the axion-photon coupling phase space.

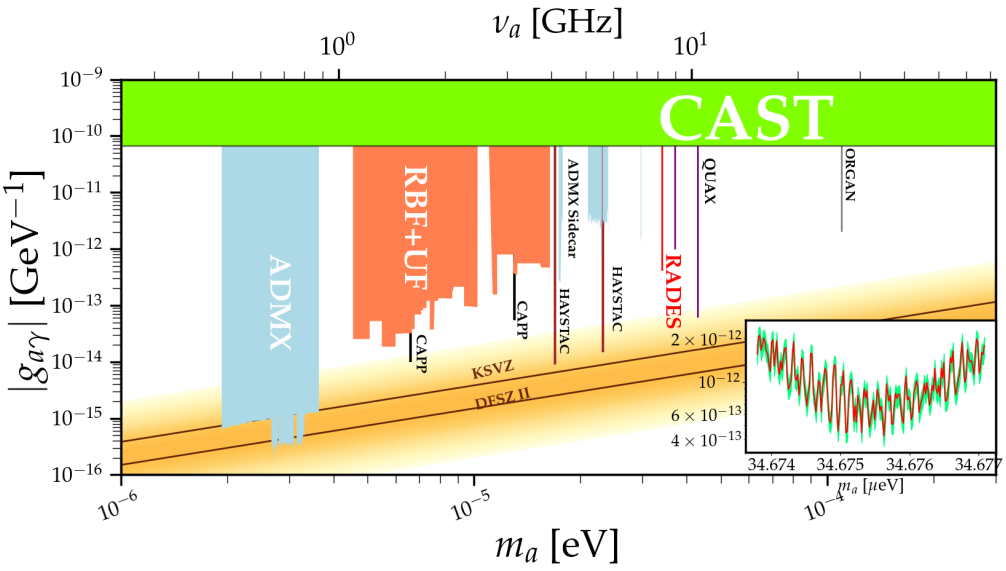

Figure 5.2.: Parameter space for axion-photon coupling. In red we mark the RADES exclusion limits for a mass range of $34.738 - 34.6771\,\mu$eV up to a 95% CL. This limits were obtained after the data taking of 2018 at CAST [119]. Other results for haloscope experiments are shown in the same region: ADMX [179–181], RBF [182], UF [183], CAPP [184, 185], HAYSTAC [186, 187], QUAX [188, 189] and ORGAN [190].

The KWISP experiment searched for the chameleon stream coming from the Sun [178]. Chameleons are hypothetical ALPs that could behave as Dark Energy and help understand completely the ΛCDM model [191, 192]. The setup of the KWISP experiment consisted on a Michelson interferometer with a membrane sensitive to incoming chameleons. This particles, if present, would deform the membrane and generate a distinct interference pattern [193]. After the data taking during 2017 no significant signal was found and a limit of 80 pN was placed for the chameleon force exerted over the membrane. Which can be translated in the exclusion limits for matter (β_{m}) and photon coupling (β_γ) displayed in figure 5.4.

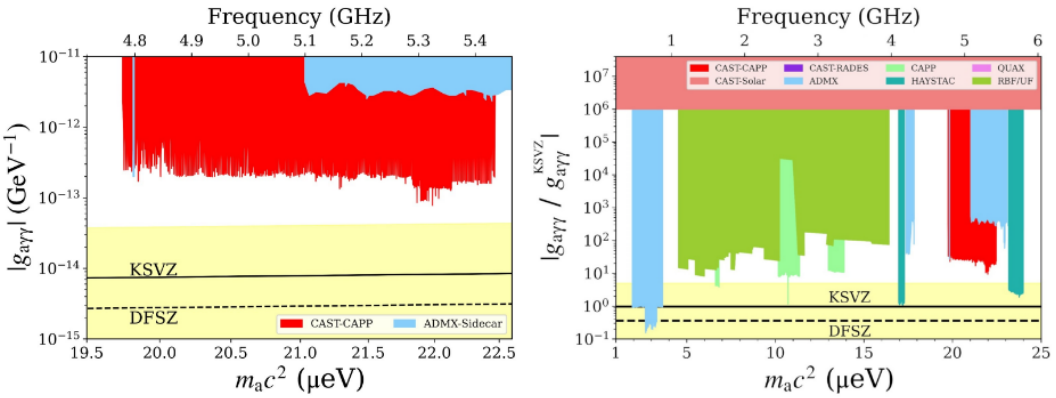

Figure 5.3.: Parameter space for axion-photon coupling (left) and parameter space for an axion-photon coupling normalized with respect to KSVZ axion coupling to photons (right). Both plots show the results of the CAPP-CAST experiment, in red, in the context of other haloscope searches [177].

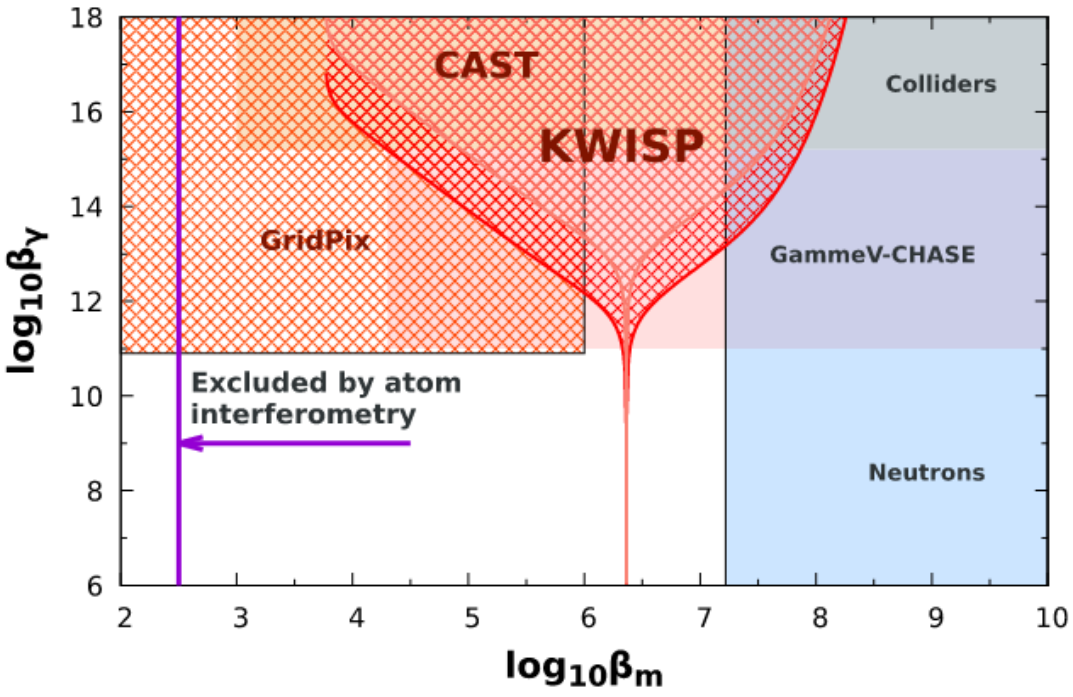

Figure 5.4.: Exclusion limits for chameleons imposed at CAST by the KWISP experiment after the data taking of 2017 [178]. The previous limits imposed by CAST are shown, these were based on chameleon-photon conversion explored with SDD [194] and GridPix [195] detectors.

In light of the results for CAST, and its different setups already presented, it is straightforward to argue how an experiment such as a helioscope can be extremely useful also for searching for bosonic dark matter or even more exotic ALPs, like

chameleons. This environment of research, covering different theoretical topics and experimental technologies, allows for cooperation to surpass technical challenges, and at the same time it provides a common ground for enriching phenomenology discussions, that ultimately broaden the physics case of the collaboration. It is because of this experience with similar setups that we strongly believe IAXO, as the main successor of CAST, should keep this broad approach to axion physics in mind from the beginning.

5.3. IAXO proposal

In 2013 the International Axion Observatory (IAXO) letter of intent (LOI) was submitted to CERN [196], in it the proposal of a 4th-generation helioscope was presented, see figure 5.5. IAXO would be an axion helioscope designed to search in both parameter spaces $g_{a\gamma}$ and g_{ae}, reaching regions currently unexplored. Its conceptual design and operational description is inherited from the design of previous helioscopes, but its sensitivity in $g_{a\gamma}$ could increase a factor of 20 in comparison to its direct predecessor, CAST.

The design consists on an enhanced version of the helioscopes presented in section 5.1, featuring:

- A superconductor NbTi 8-coil toroidal magnet with a nominal value of $B = 5 - 6\,\mathrm{T}$
- Eight magnetized conversion bores with a cross section of $A = \mathrm{m}^2$ and $L = 20\,\mathrm{m}$ in length.
- X-ray optics based on NASA's NuStar [197] and ASTRO-H [198] x-ray telescope optics.
- Ultra-low background x-ray detectors, in particular Micromegas detectors as the one implemented in CAST.

The sensitivity increase, when compared with CAST, is due mostly to its larger magnetic volume. Even though the nominal value for the magnetic field is lower, $5-6\,\mathrm{T}$ when compared to value of 9 T of the CAST magnet, the size and amount of bores increases dramatically the conversion probability for axions into photons. Other improvements, like a dedicated optics system, and detectors with better energy resolution also contribute to increase the sensitivity and the overall physics potential of the telescope.

The IAXO helioscope has the potential to study axion and ALP models strongly motivated. The increase in sensitivity- when compared to previous helioscopes- would allow to probe a region deeper inside of the QCD axion band and explore particularly motivated theoretical models [199]. Some very interesting and promising aspects of axion and ALP physics lay in regions that could be probed by IAXO [200].

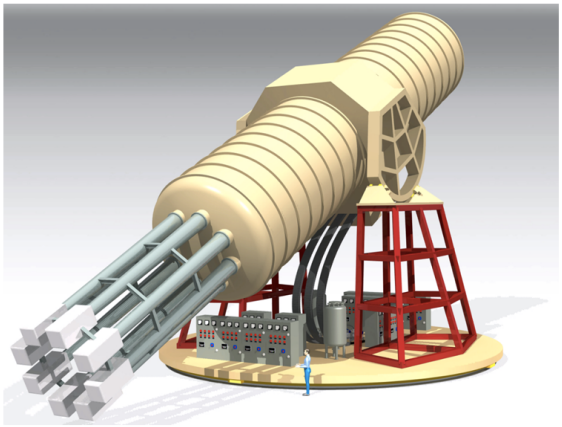

Figure 5.5.: Schematic depiction of the proposed IAXO telescope [196]. The central part comprises a cryostat with eight magnet bores, each one with a separate x-ray optics system. The cryostat rests on a supporting frame with a rotation system that allows for solar tracking.

Significant examples of these regions, displayed in figure 5.6, contain : Axion driven inflation [201], stellar cooling anomalies hints [202] and the high energy (HE) photon transparency of the Universe [203].

5.4. BabyIAXO proposal

As a first step towards the construction of IAXO, in 2017 a demonstrator was conceived inside of the collaboration to be build at operated in the following years at Deutsches Elektronen-Synchrotron (DESY) facility in Hamburg. This intermediate experiment, named BabyIAXO, was reviewed positively by the Physics Review Committee (PRC) at DESY in May 2019, endorsing unanimously its approval [204]. As a consequence, construction of the BabyIAXO telescope is currently under progress and it is expected to start taking data at DESY in the next 5 to 10 years.

BabyIAXO was conceived with two main goals in mind:

1. As a proof of principle for the technologies and experimental techniques involved in IAXO.

2. To be a next generation helioscope capable of imposing new limits, competitive with respect to the current ones, in particular those imposed by CAST.

3. Covering specially motivated regions of the parameter space: axion driven inflation [201], stellar cooling anomalies hints [202], and HE photon transparency of the Universe [203].

Let us stress the second point since, as we will see, the operation of BabyIAXO itself is backed by a strong physics case [200], even if one were to disregard the construction of IAXO.

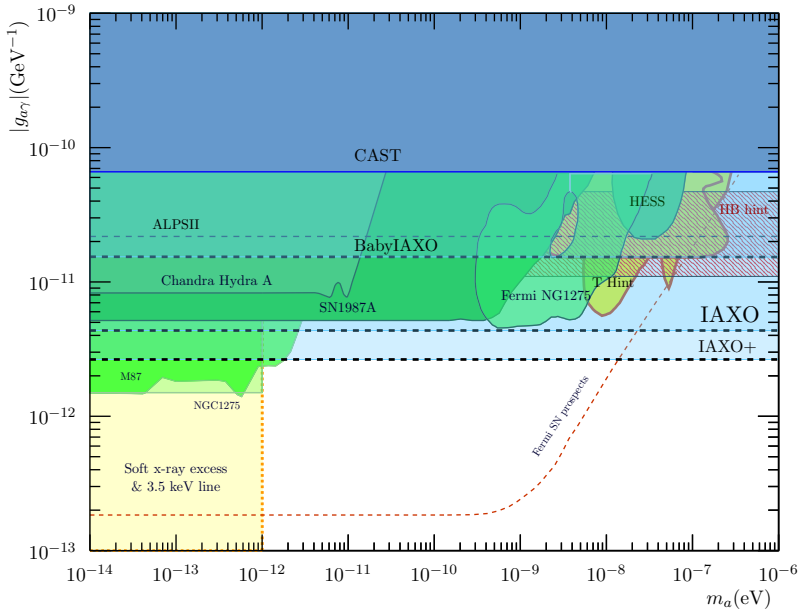

(a) Low masses region of the phase space. In combination with the sensitivities, astrophysical hints and observations are shown.

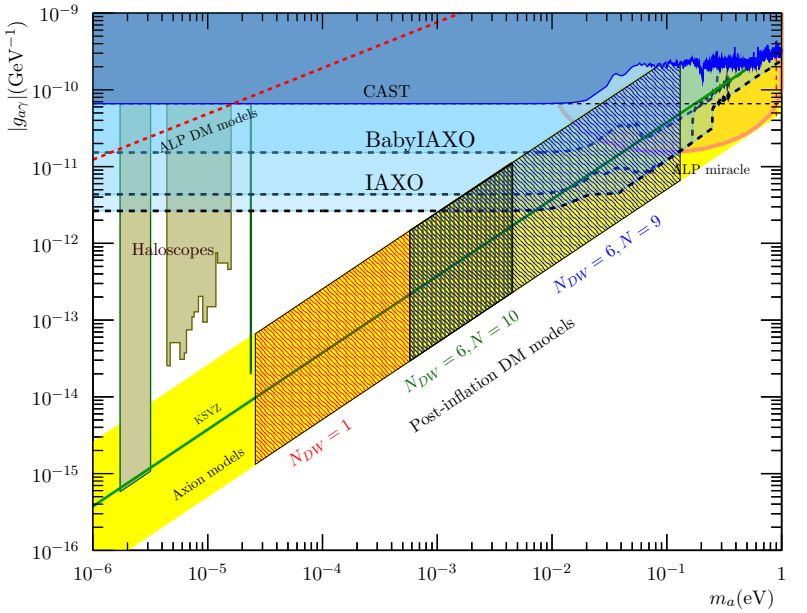

(b) Higher masses region of the phase space, covering masses way above the reach of conventional haloscopes.

Figure 5.6.: Close-up of specially motivated areas of the IAXO and BabyIAXO sensitivity reach in the axion-photon coupling phase space.The band labeled *HB hint* corresponds to observations of anomalous cooling of horizontal branch stars. The *T hint* region is motivated from the unexpected high transparency for HE. At relatively high couplings and high masses, the *ALP Miracle* region appears, in it the axion potential could be responsible for inflation in the early universe. All of these regions could be probed almost completely by the IAXO experiment.

There are three main ingredients on the BabyIAXO design that will be of particular relevance for us in the rest of this work, these are: the magnet, the optics and the detectors. Let us now summarize them briefly. However, the interested reader is strongly encouraged to check the conceptual design [135] in order to get the full picture.

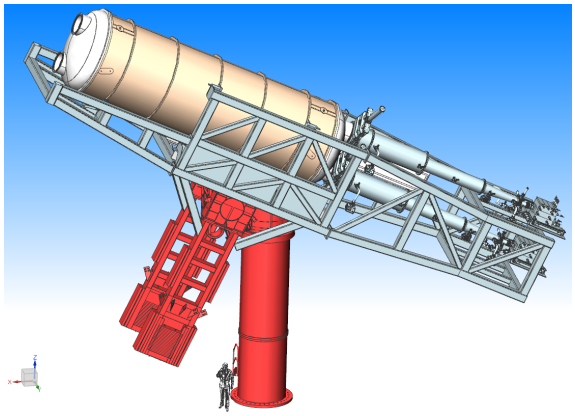

Figure 5.7.: Schematic of the BabyIAXO telescope design [135]. A cryostat containing a dipole magnet with two bores comprises the main part of the structure. The two bores contain dedicated x-ray focusing systems and a box-like structure for containing the detectors is envisioned. The cryostat rests on a rotating structure, similar to the main tower of a Cherenkov Telescope Array (CTA) Medium-Sized Telescope (MST) [205].

5.4.1. Magnet

BabyIAXO will feature a double coil magnet of superconducting Nb-Ti Rutherford cable. This magnet design allows having two cylindrical bores, 10 m in length and 0.7 m in diameter running in parallel (see figure 5.8a), with a magnetic field structure inside of them similar to that of a dipole magnet. The magnet figure of merit (MFOM) is defined as the magnetic volume of the telescope, and therefore is given by

$$\mathrm{MFOM} = \int_V |\mathbf{B}(\mathbf{r}) \cdot \hat{\mathbf{z}}|^2 \mathrm{d}V \tag{5.1}$$

where $B(\mathbf{r})$ is the magnetic field inside of the magnet bores, $\hat{\mathbf{z}}$ is the vertical direction, and the integral is taken for the full magnetized volume V. In the case of the CAST magnet, this figure of merit is $\mathrm{MFOM}_{\mathrm{CAST}} = 20.83\,\mathrm{T}^2\mathrm{m}^4$, while for IAXO this value is in the range of $\mathrm{MFOM}_{\mathrm{BabyIAXO}} = 232 - 326\,\mathrm{T}^2\mathrm{m}^4$, with a peak magnetic field along the bores center of $B = 2\,\mathrm{T}$.

For operation, the superconducting Nb-Ti coils have to be refrigerated down to 4.2K using external cryocirculators, while embedded on a cryostat as the one shown in figure 5.8b. One main difference with the CAST magnet is the fact that the inner volume of the bores is not refrigerated. For the solar axion search this is not an issue, since axion propagation and conversion will happen regardless and there will be no

relevant background effects arising from thermal noise when detecting x-ray photons from Primakoff conversion. However, in the case for dark matter axion searches the temperature of the bores is of the uttermost relevance, since it will strongly limit the signal to noise ratio one can obtain. It is because of this that the installation of resonant cavities for dark matter searches inside the BabyIAXO magnet requires the implementation of an extra cryostat, the design of which will be discussed in section 6.1.

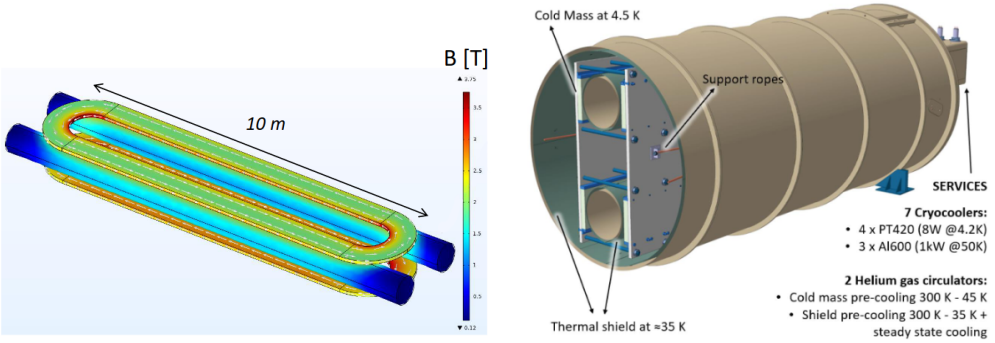

(a) Schematic of the BabyIAXO magnet layout. It is conformed by two superconducting race-track coils of Aluminum-stabilized Nb-Ti, with counter-flowing current, and two metallic inner bores.

(b) 3D schematic of the BabyIAXO cryostat envisioned for refrigerating the superconducting coils. The cold mass at 4.5 K is in thermal contact with the coils in order to achieve superconductivity, whereas the inner bores are kept outside of the cryogenic volume.

Figure 5.8.: Schematics of the magnet envisioned for the BabyIAXO telescope. [206]

In the magnet design we find the first relevant contribution to prepare the grounds for building IAXO in the future. The coil structure has been chosen in a way, that its design can be partially re implemented on an eight coil configuration, as shown in figure 5.9. This eight coil toroidal configuration would be the one needed when constructing the IAXO magnet. The assembly of the coils will be different but the cable production and coiling processes would be very similar if not identical, allowing for a substantial reduction of price and time in the production of one of the most expensive parts of the experiment.

5.4.2. Optics

Solar axions should reach the BabyIAXO magnet traveling in a similar fashion to a plane wave coming from the Sun, and once inside the magnet they would be converted into x-ray photons that propagate along the magnet bore all the way towards the detectors located at the end. In this type of setup one can consider placing an x-ray focusing system at the end of each bore in order to concentrate the incoming signal into a small region of the detector and thus boost the signal-to-noise ratio. This approach was followed in the CAST experiment and allowed

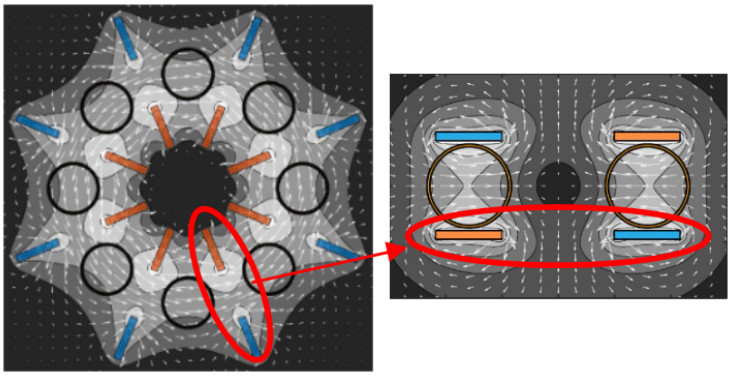

Figure 5.9.: IAXO (left) and BabyIAXO (right) coil configurations. The packing of the superconducting cables in pairs is similar, which allows for testing the production procedure in the BabyIAXO prototype. However, the complete coil distribution differs, corresponding to a toroidal magnet for IAXO and a dipole for BabyIAXO [206].

for a reduction of the background of more than 2 orders of magnitude [207], when performing its second vacuum phase run between 2013 and 2015 [134].

Based on the experience with CAST, in the BabyIAXO experiment the use of an x-ray focusing system is considered as a fundamental part of the basic design. The basic operating principle of the x-ray focusing optics relays in the total external reflection of keV-range photons over two consecutive sets of reflective mirrors, see figure 5.10. The first set of mirror consists of a series of coaxial paraboloids, followed by a second set of coaxial hyperbolic mirrors. The x-rays entering the system are focused on a focal plane after being reflected on both sets of mirrors. This configuration of mirrors is usually refer to as Wolter-I configuration.

For the BabyIAXO telescope, two different focusing optic systems (figure 5.11) have been proposed, one for each bore:

- Custom x-ray telescope: Brand new optics system, based on NuSTAR telescope layout as an inner core with an added external ring of cold-slumped glass [209, 210].
- XMM flight-spare x-ray telescope [211]: Two XMM Newton telescope modules, property of ESA, are available for commissioning and installation.

The custom x-ray optics are still on development but the steps for construction and characterization are clear. The inner core of the optics relies on technology extensively used during the last decades on existing infrastructure, i.e. the NuSTAR telescopes. The manufacturing procedure for the outer layers has been demonstrated to be feasible and a detailed review can be found in [210]. This optic is optimized for focusing photons originated in inverse Primakoff conversion inside of the BabyIAXO magnet, which are associated to axions produced in the solar disk. For this it features a focal length of 5 m, a pass band from 1-10 keV and a field of view of 2.9 mrad.

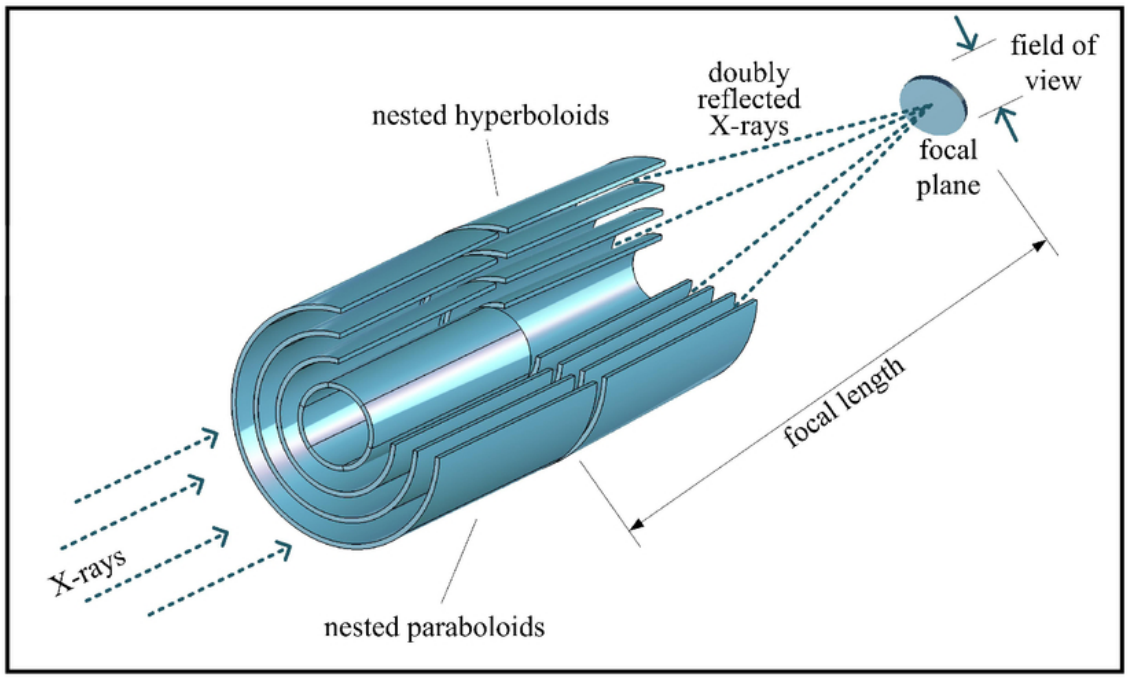

Figure 5.10.: Scheme of the operating principle for a x-ray telescope with a Wolter-I mirror configuration [208].

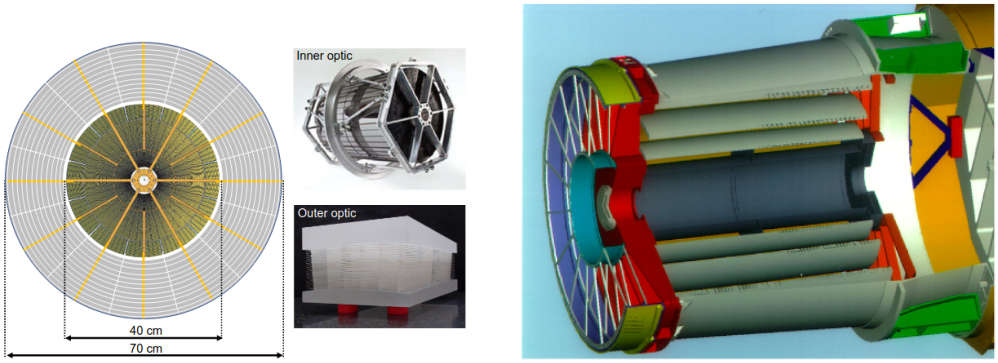

(a) Custom optics layout for BabyIAXO. An inner hexagonal structure for mounting the system is surrounded by an outer multilayer corona of cold-slumped glass.

(b) Model of the XMM Newton flight spare telescope. 58 layers of nickel coated with gold comprise the optic structure with a total mass approximately 4 times larger than the custom optics design.

Figure 5.11.: Schemes of the two optic systems proposed for BabyIAXO. A first one custom made (left) and a spare XMM Newton telescope currently in storage at MPE's PANTER X-ray Test Facility in Neuried, Germany [135].

On the other hand, the use of the XMM flight-spare optics system as an out of shelf solution seems very promising, both because of their availability and suiting characteristics. As part of the ongoing collaboration with MPE's PANTER X-ray

Test Facility a characterization and calibration protocol is being developed. The main difference with the custom x-ray telescope is a focal length of 7.5 m, and it would reduce the total effective area covered by the telescope by 30%, which in this kind of prototype is judged as not having a substantial effect.

5.4.3. Detectors

The natural technology to be considered as the baseline solar axion detection in BabyIAXO are Micromegas detectors. These detectors already showed an outstanding performance when operated in the CAST experiment [134], and the addition of more advanced muon veto systems and radio pure electronics could push their background level even lower.

The goal for detectors in the context of BabyIAXO is to prove the viability of operation at a background as low as, at least, $10^{-6}\text{counts}\,\text{keV}^{-1}\,\text{cm}^{-2}\text{s}^{-1}$ [196]. For this, specific detector technologies- Micromegas and others- are under study. Furthermore, active and passive shielding techniques are expected to be implemented regardless of the detector choice, e.g. the IAXO-D0 prototype displayed in figure 5.12. In section 7 we will discuss the required passive shielding and the filtering techniques taken into account to minimize the effect of the radioisotope contamination of the acquisition electronics.

For the passive shielding a 20 cm thick lead box will contain both the detector and the electronics reducing the environmental radiation levels to those already present on the CAST experiment.

Aside from the passive shielding an active system has to be implemented to reduce the cosmic rays contribution. The current prototype under study to serve this purpose, is a multi-layer veto system covering a total of almost 4π solid angle around the detector. It is conformed by a set of 57 veto panels and it allows for cosmic muon and neutron detection and signal discrimination.

As of today, the current background achieved on surface for the IAXO-D0 detector is $6.3 \times 10^{-7}\text{counts}\,\text{keV}^{-1}\,\text{cm}^{-2}\text{s}^{-1}$. This result is expected to be improved even further by optimizing the X-ray calibration data and updating the background cuts accordingly. Another improvement could come from better characterization of cosmic neutron sources, which could help developing better topological cuts, more information about background cuts will be discussed on section 5.5.

In the context of expanding the detection technologies implemented in BabyIAXO, up to five different detectors- aside from Micromegas- have been proposed as viable candidates for different solar axion runs, and are being developed by institutes inside the IAXO collaboration. The technologies considered in its conceptual design [135] are the following :

- GridPix [212] : Consists of a Micromegas mesh deposited on top of a pixelated readout chip. Allows single electron detection and was installed and operated

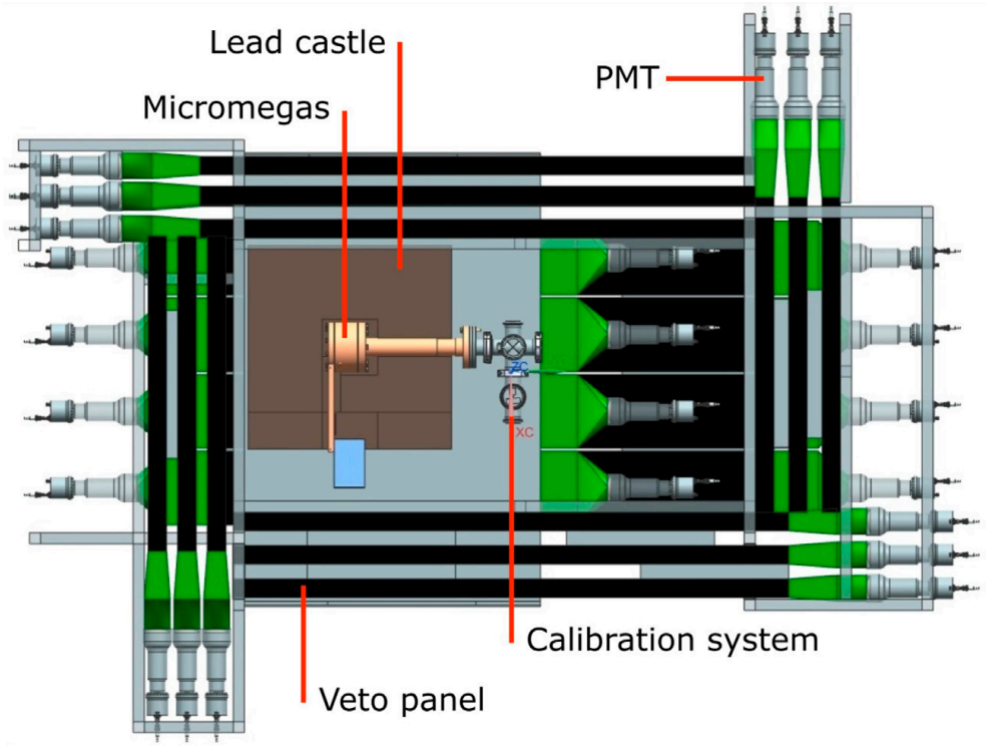

Figure 5.12.: Schematic view of the IAXO-D0 detector prototype as seen from above. The copper vessel containing the micromegas detector is surrounded by a lead cube for passive shielding of 55 cm sides, and a muon veto system for active shielding. The muon veto is composed by 57 scintillator panels disposed in three layers around the lead shielding in order to achieve 4π solid angle coverage.

during the 2014-2015 CAST data taking campaign. Achieving a background level of around $10^{-5}\,\mathrm{counts\,keV^{-1}\,cm^{-2}s^{-1}}$ [195].

- Silicon drift detectors (SDDs) [213] : Very high x-ray detection efficiency. A demonstrator for the BabyIAXO and TRISTAN experiments has been designed by collaborators working at the Technische Universität München (TUM). This demonstrator was recently tested in the Canfranc Underground Laboratory, showing a background level of $4.7 \times 10^{-6}\,\mathrm{counts\,keV^{-1}\,cm^{-2}s^{-1}}$, which- even already promising- is expected to be improved after further study.

- Metallic Magnetic Calorimeters (MMCs) [214] : Dispersive detectors operated at ultra-low temperatures (<100 mK) and available for soft x-rays detection. A first measurement of the background, performed on surface facilities and without a veto system giving preliminary estimation of $10^{-5}\,\mathrm{counts\,keV^{-1}\,cm^{-2}s^{-1}}$, however more studies are under development for improving background performance and the coupling of the system to the BabyIAXO optics.

- Neutron transmutation doped detectors (NTDs) [215] : Widely used as thermometers in cryogenic rare event searches. The interest in BabyIAXO is targeted on coupling them to Germanium crystals and operating them as bolome-

ters. These devices have shown high energy resolution (∼0.2–0.4 keV FWHM at 5.9 keV x-rays of ^{55}Fe) and its operation tested at underground facilities displaying a background on the order of 10^{-6} counts keV^{-1} cm^{-2}s^{-1} [216,217].

- Transition edge sensors (TESs) [218] : Single photon counting detectors, operated for x-ray imagining in ultra-low temperature conditions (20-100 mK). They are currently used in Dark Matter experiments such as CRESST [219]. An important advantage of these detectors is the flexibility of the material and the possibility of manufacturing them out of radiopure materials. However proper background studies are still yet to be performed.

This would conclude the review of detector technologies for solar axions at BabyIAXO. However, as we already saw when summarizing CAST operation, an experiment with these characteristics allows for a very much wider search. The most motivated extension in this context is the inclusion of an axion DM search in the context of BabyIAXO. Based on the expertise developed in the CAST-RADES experiment a proposal from the RADES group has been already prepared and submitted. It will be dissected on section 6 and, as a matter of fact, the BabyIAXO-RADES initiative is part of the Conceptual Design of BabyIAXO as presented in [135].

5.4.4. Sensitivity

BabyIAXO will be not only a demonstrator of the technologies relevant for the construction an operation of the full IAXO experiment, but it will also allow for a solar axion search. In fact, the BabyIAXO experiment- as one can see in figure 5.13- will cover a vast part of the parameter region which has not been explored yet by other experiments.

The sensitivity reach of the BabyIAXO helioscope surpasses by one order of magnitude the best results in the field, obtained by the CAST collaboration [134]. It is of particular relevance the chance that BabyIAXO will give us to cover axions in the QCD band, an area difficult to reach for both previous helioscopes and haloscopes. Furthermore- since its detection is based on solar axions- it does not depend on the axion being a sensitive part of the dark matter density, as haloscopes do. During a buffer gas run, such as the one performed in CAST [131, 132], it could also enter the region for QCD axions of masses between 70 and 250 meV, a region particularly motivated by stellar cooling anomalies [220].

The physics case of BabyIAXO in general overlaps the one to be covered by IAXO [200], up to some extent. The main difference being the possibility of IAXO to test hypothetical ALPs and axions down to lower couplings. The regions of interest of the parameter space for IAXO discussed in the previous section, are also partially covered by BabyIAXO, as shown in figure 5.6.

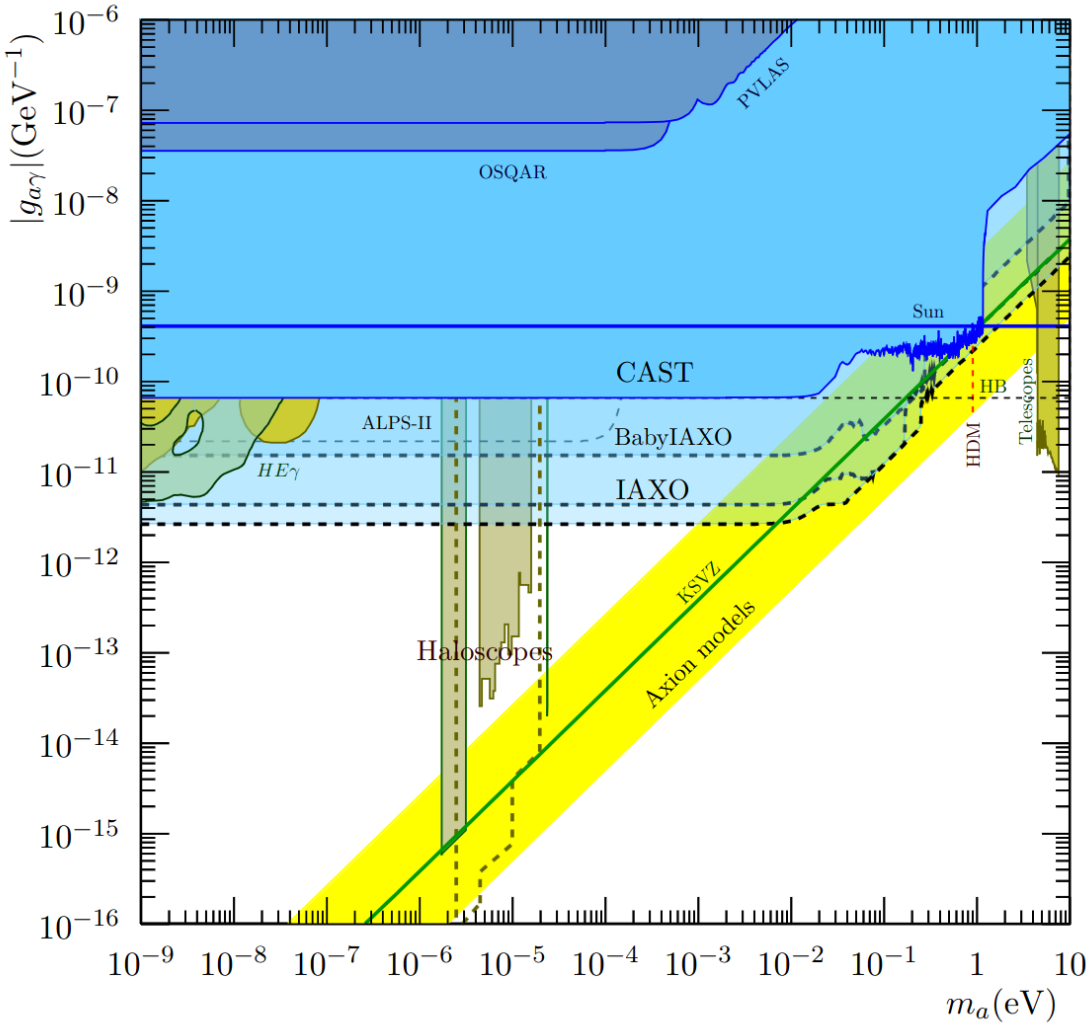

Figure 5.13.: Mass vs axion-photon coupling parameter space. The regions accessible for the IAXO and BabyIAXO helioscopes are shaded. The previous limits for solar axions, imposed by CAST are shown in light blue. The excluded regions for the laboratory experiments OSQAR and PVLAS are marked in dark blue, and the prospects for the future ALPS-II experiment are shown in dashed blue. Other experimental areas- relevant for dark matter axions- are shown, i.e. the regions excluded (solid green) and projected (dashed green) for current and future haloscopes, for more details regarding the haloscope region see figure 6.12. The region for QCD axion models is highlighted in yellow.

5.5. IAXO-D0 original background model

The IAXO-D0 prototype is the first detector considered for solar axion detection at the IAXO helioscope [221]. It features a micromegas detector inside a copper vessel coupled to the beamline with a radiopure copper pipe. More detail about the

IADO-D0 geometry will be given in chapter 7, in particular in section 7.3.1 when discussing the radiopure electronics background model.

Prior to this work a series of studies were performed at the University of Zaragoza in order to properly characterize the background of the IAXO-D0 detector. The complete study of the environmental and detector background- not including the detection electronics- was performed by Dr. Elisa Ruiz Chóliz in her PhD thesis [222]. Here we review the different components of this background. In particular it will be very important to understand the topological cuts that later on were also applied to our study of the electronics contribution.

After the characterization of x-ray events simulated in REST for the IAXO-D0 detector a series of discrimination cuts were developed. In particular, the topology of these events was studied, allowing to extract the overall x-y distribution of counts in the detector after the gas amplification, see figure 5.14. Based on this one can select a region for each magnitude that allows for maximum detection efficiency while properly discriminating events that come from other sources. The selected values for the topological cuts are compiled in table 5.1, while the distribution of the events with respect to those cuts is illustrated on figure 5.14. The descriptions of the energy distribution observables, and how they are calculated, are in section 4.2.5. They include the variance at the detector plane σ^2_{xy}, the z variance σ^2_z which contains information about time spread for the event, the balance between σ_x and σ_y, the skewnesses γ_{xy} and γ_z that characterize asymmetry of the distributions. x and y origins are set at the center of the detector, while the z origin is set at the center of the gas volume of the detector.

A final fiducial cut, d_w, defined as the event distance to the detector wall is applied in order to eliminate all events spreading outside of the detector center.

Variable	Cut value
$\sigma^2_{xy}(\mathrm{mm}^2)$	[0,2.6]
$\sigma^2_z(\mathrm{mm}^2)$	[0,0.55]
$\frac{\sigma_x-\sigma_y}{\sigma_x+\sigma_y}$	[-0.15,0.15]
γ_{xy}	[-0.5,0.5]
γ_z	[-1.12,1.12]
$d_w(\mathrm{mm})$	[17,30]

Table 5.1.: Acceptance regions for x-ray events. The main observables have been filtered based on simulations to obtain maximum acceptance in the 2 to 6 keV region [222].

These cuts allow for extracting events that are centered around the focal spot of the x-ray optics, as one would expect for axion-photon conversion in the interior of the IAXO magnet. Furthermore, only events which are symmetric and round-like are kept, which is also a main characteristic of the cascades corresponding to properly focused x-rays. The efficiency of the cuts when accepting x-ray events is strongly dependent on the energy of the x-ray, for this reason they have been optimized in

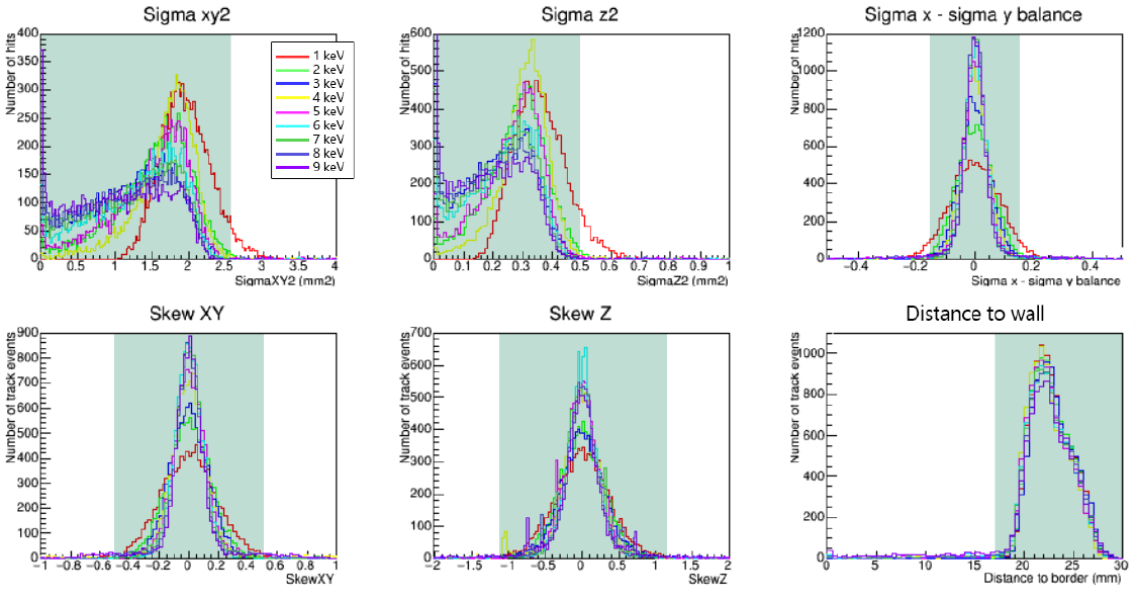

Figure 5.14.: Observables used for background discrimination. The curves show the distribution for x-rays of different energies and the shadowed region is the area of event acceptance [222].

order to be most accurate when describing events on the region from 2 to 6 keV, in table 5.2 we list the efficiency for x-ray events with different initial energies. The optimized region was chosen because the axion flux peaks for an energy of 3keV and the spectra extends mainly from 1 to 7 keV

Energy keV	Efficiency (%)
1	76.05 ± 0.87
2	91.98 ± 0.96
3	89.47 ± 0.95
4	90.34 ± 0.95
5	89.44 ± 0.95
6	87.47 ± 0.94
7	86.10 ± 0.93
8	84.71 ± 0.92
9	78.44 ± 0.89

Table 5.2.: Efficiency of the cuts for x-rays of different energies with their statistical uncertainties [222].

The performance of this energy cuts has been studied also on experimental data. For a first run [222] with a ^{109}Cd source of x-rays the efficiency found for events around the 8 keV fluorescent peak of copper was $\sim 90\%$. However in a later characterization using a ^{55}Fe source [223], an efficiency of only 49.8% was found for x-ray events. This second set of measurements was done by studying the 5.9 keV line of ^{55}Fe. The low efficiency can be explained because of noisy spots in the readout

caused by several dead strips of the detector. This noise affects directly the topological separation of the charge deposits and hence the symmetric energy distribution expected in the detector readout plane.

5.5.1. External background

We refer to external sources for the background when discussing both environmental radio activity and cosmic rays. For the CAST experiment, due to its location being on the earth surface, no overburden is considered for cosmic radiation. The BabyIAXO telescope planned location is the HERA South Hall at DESY, where up to 15 m of shielding could be considered for cosmic radiation. However, it is unavoidable that the detectors of BabyIAXO pass below the access shaft during sun tracking. This limitation, and the development of technologies suitable for the IAXO telescope, which is expected to operate at ground level, makes us consider for BabyIAXO a background model without overburden.

The different contributions studied in this context were:

- Cosmic muons: Direct cosmic that reach the detector. One of the main sources, with a contribution on the order of $10^{-3} - 10^{-4}$counts keV^{-1} cm^{-2}s^{-1} as the raw background estimated for the CAST setup, based on the one observed during data taking [134]. Application of the topological cuts allows for a reduction of this background component down to the order of 10^{-6}counts keV^{-1} cm^{-2}s^{-1}. Furthermore, the implementation of a simple veto system with just one layer has shown the possibility of reducing a factor of 2 in the number of counts. A full 4π veto shielding system is currently being tested and the goal of 10^{-7}counts keV^{-1} cm^{-2}s^{-1} for the background is expected to be reached under these conditions.

- Cosmic neutrons: Neutrons generated mainly in the atmosphere due to interactions with cosmic radiation. This radiation source is one of the most penetrating in the setup and can be particularly relevant due to cascades generated inside the lead shielding. In simulations it is estimated to be of the order of 10^{-5}counts keV^{-1} cm^{-2}s^{-1}, and therefore another of the main contributions to the background if cuts and veto system are not included. The implementation of both background control tools allows to reduce these counts down to around $10^{-6} - 10^{-7}$counts keV^{-1} cm^{-2}s^{-1}.

- Cosmic gammas: Similar to cosmic neutrons, they are emitted after cosmic rays interact with matter in the atmosphere. In this case, only high energy gamma radiation will reach the detector, while the rest will be easily stopped by either the building or the lead shielding of the detector. They are not a source of background as strong as the other cosmic sources discussed before, but the simulations have to be compared with experimental data since they are very dependent on models for cosmic radiation distribution.

- Environmental gammas: Produced naturally by materials inside the building. They are simulated based on measurements of environmental radiation at the site, their contribution is estimated to be marginal, and can be easily lowered by improving the detector shielding.

5.5.2. Intrinsic background

When working on conditions of ultra low background, the sensibility of the detectors to radioactivity is so elevated that its own components start to become troubling emitters of radiation. These sources were studied by Cristina Margalejo Blasco on her master thesis work at the University of Zaragoza [224] allowing to characterize the intrinsic background of the detector itself, they can be separated into three main contributions.

- Detector radioactivity: The presence of certain radioactive isotopes on the different pieces that conform the detector generates an extra background that can be troubling for detector performance if the materials are not selected carefully for the manufacture procedure. For the assessment of this contribution, the activity of the different components with which the detector is build was measured at Canfranc Underground Laboratory, then radioactive decay simulations were performed. This simulations included different sub-series of the decay chains of ^{238}U, ^{235}U and ^{232}Th, the radionuclides ^{40}K, ^{60}Co and ^{137}Cs and the ^{210}Pb present in the lead bricks used to shield the detector against external radiation. This background contribution was estimated to be $\sim 2 \times 10^{-7}\,\mathrm{counts\,keV^{-1}\,cm^{-2}s^{-1}}$ with the current materials, similar to the background level of an equivalent setup characterized experimentally at Canfranc Underground Laboratory [225]. It is important to note that one has to be very careful when considering upgrades to the detector, since substituting these radiopure materials for others could change drastically this very low background.

- Ar gas radioactivity: The argon gas present on the detector naturally contains ^{39}Ar isotopes which will decay triggering signal cascades inside of the gas volume, and ultimately appearing as events in the mesh of the detector. A natural concentration of ^{39}Ar [226] was assumed for the volume of the TPC and simulations were performed to register the events on the detector. The background found for this contribution is on the order of that for the detector radioactivity. However, the events in general tend to spread across the full gas volume, and therefore the topological cuts allow for a reduction of even one order of magnitude in the amount of events.

- Radiogenic neutrons: Neutron emission from Uranium isotopes present on the detector shielding. The ^{238}U activity in the lead shielding has been measured to be of 0.33 mBq/kg. Simulations were performed to characterize this component of the background, and a total contribution on the order of $10^{-14}\mathrm{counts\,keV^{-1}\,cm^{-2}s^{-1}}$ in the IAXO energy region of interest was found,

which was ruled negligible. However, neutrons produced in (α, n) reactions from the radioactive chains were not taken into account, a more detailed study taking them into consideration would be in order to completely characterize this background component.

In table 5.3 we compile the values of the background simulated for all the components mentioned- with and without topological cuts-, assuming a simple veto system as the one originally proposed in the IAXO-D0 detector. The total background after the topological cuts is 1.51×10^{-6}counts keV^{-1} cm^{-2}s^{-1} which is an improvement when compared with the CAST case. However, this result is still one order of magnitude away from the desired value of 10^{-7}counts keV^{-1} cm^{-2}s^{-1}. Currently a new and more advanced veto system is being tested with a full 4π solid angle coverage which could allow to shield properly the detector against cosmic rays which are the main source of background at the moment. Improvements are still in development, however, it has already been shown that the background can be easily reduced up to one order of magnitude for most relevant contributions.

Origin	Contribution before cuts	Contribution after cuts
Cosmic muons	$< 5.19 \times 10^{-8}$	$< 3.97 \times 10^{-8}$
Cosmic neutrons	8.1×10^{-6}	5.5×10^{-7}
Cosmic gammas	5.9×10^{-7}	4.17×10^{-7}
Environmental gammas	4.8×10^{-8}	$< 2.24 \times 10^{-8}$
Radiogenic neutrons	7×10^{-14}	2.55×10^{-14}
Detector radioactivity	$< 6.39 \times 10^{-7}$	$< 4.56 \times 10^{-7}$
Ar gas radioactivity	1.71×10^{-7}	1.03×10^{-8}
Total	9.8×10^{-6}	1.51×10^{-6}
Goal	-	1×10^{-7}

Table 5.3.: Different background contributions to the IAXO-D0 prototype before and after applying the energy rejection cuts, units in (counts keV^{-1} cm^{-2}s^{-1}). The different sources cover cosmic, environmental and intrinsic backgrounds, the only known source missing being the electronics radioactivity. Some of the lowest contributions could not be properly quantified, due to low statistics, and instead upper limits are given [222].

In [222] a data taking campaign was performed at ground level with the IAXO-D0 detector. In it a ^{109}Cd source was used as an x-ray emitter, in order to compare the simulation results previously discussed with data acquired experimentally. In this run a background of $(2.1 \pm 0.2) \times 10^{-6}$counts keV^{-1} cm^{-2}s^{-1} over the activity of the source was found experimentally, well in agreement with the results found in simulations. A more recent data taking with a ^{55}Fe source and an improved active veto system for cosmic rays yielded a background level of $(8.52 \pm 1.22) \times 10^{-7}$counts keV^{-1} cm^{-2}s^{-1} [223]. However, as mentioned in the beginning of the section when discussing the energy cuts, the efficiency of the cuts for this data

taking was only 49.8%, a more detailed study of the energy cuts and the active vetoing is under development.

6

Haloscope technologies for BabyIAXO

The BabyIAXO experiment is expected to start taking data on solar axions in the next few years. Following the path paved by the multi-detector approach to axion searches already implemented at CAST in the last decade, it is natural to propose a haloscope search by using the BabyIAXO magnet. This proposal was formally made by the RADES group due to our close interaction with the IAXO collaboration and, consequently, it is part of the Conceptual Design of BabyIAXO [135].

The BabyIAXO magnet operating as a helioscope is expected to track the Sun, but in the case of a haloscope setup installation we consider it remaining stationary, in parking position. This search could be also performed during solar tracking, as in CAST. But for the sake of simplicity we will not discuss it here since it introduces some design challenges that can obscure the basics of our haloscope setup. This chapter follows my work on the estimation of the sensitivity and data taking strategies published in the proposal [227]. In it an LC resonator experiment following the BASE experimental setup [228] is also proposed.

6.1. Cryostat design

As mentioned when reporting on the design of BabyIAXO in section 5.4, the current design for the magnet does not consider the possibility of having the inner volume of the magnet bores in cryogenic conditions, however the cryogenic environment is mandatory for an axion DM search. And thus the resonant cavities we propose would be inserted together with a dedicated cryostat. For simplicity and compatibility with the solar search this setup is planned to be installed on one of the BabyIAXO bores on the opposite side of the x-ray detectors.

Additionally, the dedicated cryostat provides us with a controlled testing environment where we can properly characterize the full system in, almost, data taking conditions, the only difference being the magnetic field. In figure 6.1 we show the cryostat designed for the RADES setup in BabyIAXO, which was developed by Marc Siodlaczek as part of his master thesis [229] at the CERN cryolab.

The complete cryostat is separated into three main parts at different tempera-

tures: a first stage at room temperature inside a vacuum chamber, an intermediate temperature stage for the thermal shield and the low temperature stage containing the cold mass and the thermalization plate. The system, a dry cryostat, consists on a set of cryocoolers and a closed helium circulation loop. The resonant cavities inside the BabyIAXO bore are surrounded by a thermal shield and sustained by a support structure made out of G10 epoxy-fiberglass. Ball transfer units on the structure enable the insertion of the support structure, the thermal shield, and the resonators into the bore. The cavities and the thermal shield are cooled by small cooling pipes that are brazed onto the surface and in which supercritical helium is circulated. A 30 layer Multi-Layer Insulation (MLI) blanket covers the thermal shield and a 10 layer MLI blanket protects the cavities.

The radiofrequency (RF) equipment, tuning actuators, cryogenic amplifiers, etc. are placed inside an auxiliary box with the rest of the equipment for the cooling system. The parts that need low temperature environment from the RF system, like the cryogenic amplifier and the testing lines, are placed in a separated vacuum chamber and cooled by the same system via thermal contact with a copper plate.

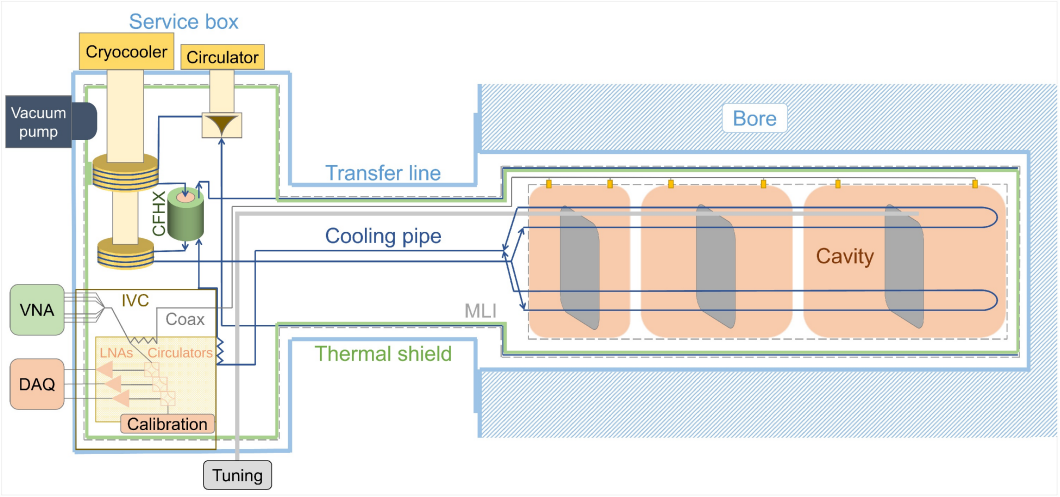

Figure 6.1.: Cryostat designed for the haloscope setup of the BabyIAXO telescope. Image extracted from [227]

During the design of the cryostat, numerical simulations were made for estimating the heat load for the different parts and the total heat load of the system was assessed. For this it was taken into account the thermal radiation of the surfaces inside the bore (which was shown to be the dominant effect), the heat load through the coaxial cables and the tuning rods and the solid heat conduction of the support structure for the cryostat. For the estimation of this heat load, the MLI model from Riddone [230] is applied and multiplied with an application factor, which considers the MLI performance for complex surface geometries with multiple degradation points. This approach provides an indicative value for the heat load and determines the relation between heat load and steady-state cavity temperature. Based on these simulations the heat load was minimized, for a system with a 50 K thermal shield

temperature, and a 4.5 K low temperature stage, a detailed derivation of the heat load and the optimization process can be found in [229].

The estimation of the total heat loads for a system with a thermal shield at 50 K and bore at 4.5 K corresponds to 37.3 W at 50 K and 1.69 W at 4.5 K. Of the total 37.2 W, 30.2 W occur in the bore and 7.1 W in the service box at 50 K. Analogously, 1.38 W and 0.31 W at 4.5 K can be assigned to the heat load in the bore and the service box, respectively. The origin of the heat loads at the service box and bore are presented in Table 6.1.

Source	Heat load 50 K (W)			Heat load 4.5 K (W)		
	Service box	Bore	Total	Service box	Bore	Total
Radiation / MLI	3.3	29.3	32.6	-	1.31	1.31
Coaxial cables	2.4	-	2.4	0.18	-	0.18
Support structure & IVC	1.0	0.9	1.9	0.06	0.05	0.11
Electrical equipment	0.1	-	0.1	0.07*	-	0.07*
Tuning system	0.3	-	0.3	-	0.02	0.02
Total	7.1	30.2	37.3	0.31	1.38	1.69

Table 6.1.: Summary of heat loads in steady state at the two temperature levels of the cryostat. The heat load values, the sources and the locations of their occurrence are specified.

As a result of this study a cooling system was proposed. It consists of two Cryomech® PT420 cryocoolers [231] connected in series, one Stirling Cryogenics® Noordenwind cryogenic circulator [232], one counter-flow heat exchanger specifically produced by the CERN Cryolab, cooling pipes with an inner diameter of 4 mm, and a helium flow rate of 0.5 g/s at 20 bar absolute pressure.

According to the specifications of the system described, it is possible to reach a cavity temperature of 4.6 K and a temperature of 4.8 K for the calibration, mixing and pre-amplification RF equipment. However, for sensitivity estimates we will take a conservative value of $T_{\mathrm{sys}} = 6\,K$ based on the base temperature experimentally achieved for a simpler system in [229]. Another constraint taken into account in the optimization was to ensure a maximum temperature gradient of 1 K for the resonant cavities installed inside of the cryostat, in order to minimize the effect on the conductivity and thus on the quality factor of the resonator. A study of the effect of such a temperature gradient is envisioned but has not been done yet.

6.2. Haloscope setup

6.2.1. Single cavity design

The BabyIAXO telescope is equipped with a dipole magnet composed of two flat racetrack coils of 10 m and two parallel cylindrical bores of 70 cm in diameter. In figure 6.2 we show the magnetic field distribution on a section of one of the bores. It shows a mainly vertical direction, with slight deviations when approaching the surface of the bore. For sensitivity calculations the exact magnetic profile is used, however, for the general discussion we will assume it to be completely oriented in the vertical direction, i.e. $\mathbf{B}_e = |\mathbf{B}_e|\hat{z}$.

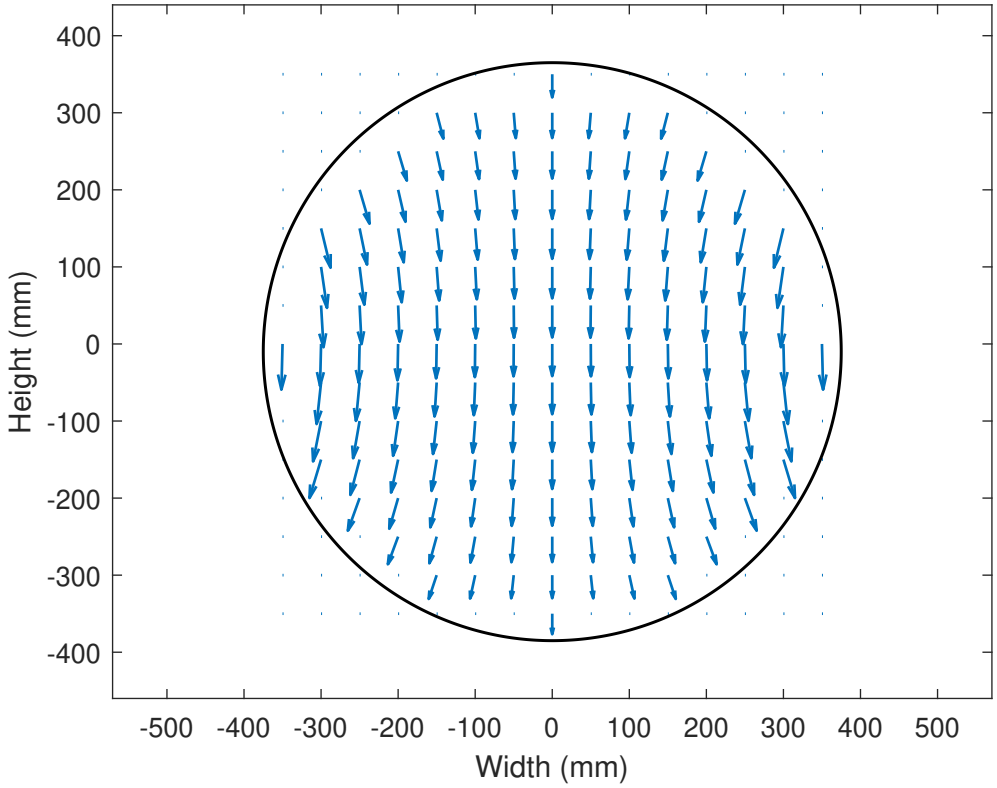

Figure 6.2.: Magnetic field profile of a transverse section inside one of BabyIAXO bores.

A first setup idea for a haloscope inside the BabyIAXO bore can be a long cylindrical cavity, 60 cm in diameter and 10 m long. If we consider axions converted under the influence of a magnet with a field distribution such as the one shown in figure 6.2, the mode that would maximally couple to them on a cylindrical geometry would be the TE_{111} mode. This can be easily seen in figure 6.3 where we display the E-field for that particular mode on an arbitrary cylindrical cavity, the pattern on a transverse section roughly matches that of the B-field for the magnet, and therefore maximizes the geometric factor C.

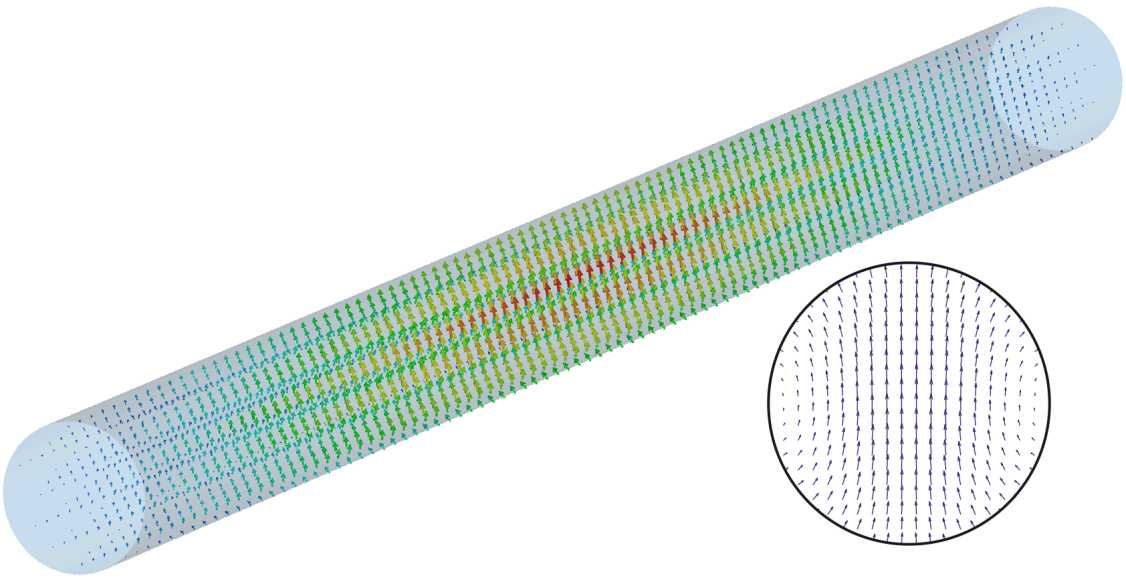

Figure 6.3.: Electric field for the TE_{111} mode of a cylindrical cavity. A transverse section detail is shown on the right.

The resonant frequency and the unloaded quality factor for the TE_{nml} modes of a cylindrical resonator, depend on the dimensions of the cavities and the electromagnetic properties of the inner material, general expressions for these magnitudes are usually found in most textbooks (e.g [233])

$$f_{\mathrm{TE}_{nml}} = \frac{c}{2\pi\sqrt{\epsilon_r}}\sqrt{\left(\frac{p'_{nm}}{R}\right)^2 + \left(\frac{l\pi}{L}\right)^2} \tag{6.1}$$

$$Q_{0\mathrm{TE}_{nml}} = c\sqrt{\frac{\pi\mu_0\sigma}{f_{\mathrm{TE}_{nml}}}}\frac{\left(1-\left(\frac{n}{p'_{nm}}\right)^2\right)\left(p'^2_{nm}+\left(\frac{l\pi R}{L}\right)^2\right)^{\frac{3}{2}}}{2\pi\left(p'^2_{nm}+\frac{2R}{L}\left(\frac{l\pi R}{L}\right)^2+\left(1-\frac{2R}{L}\right)\left(\frac{nl\pi R}{p'_{nm}L}\right)^2\right)} \tag{6.2}$$

where R and L are the radius and length of the resonator, n, m, l, label the azimuth, radial and axial modes respectively, ϵ_r is the relative permittivity of the inner media of the cavity, σ is the conductivity of the resonator walls, μ_0 is the vacuum permeability, c is the speed of light, and p'_{nm} is the m-th root of the derivative of the Bessel function of order n, J_n.

Using these equations, for a resonator as the one displayed in figure 6.3 with a fixed inner radius $R = 59$ cm and assuming the typical value for the conductivity of copper at 2 K $\sigma = 2 \times 10^9$ S/m, we find the behavior for $f_{\mathrm{TE}_{111}}$ and Q_0 plotted in figures 6.4 and 6.5, respectively, for a varying length up to the maximum available inside the BabyIAXO bore $L = 10$ m.

Uncertainties in the conductivity of copper could have relevant influence in the value of the quality factor. From our experience in previous prototypes, one of the main concerns is the anomalous skin effect of copper at cryogenic temperatures

which can alter the residual resistivity ratio (RRR), saturating the conductivity at higher temperatures and not allowing the system to reach the expected theoretical value. The worst values we found for copper coated resonators, with respect to the expected value, had a reduction of 5% for the conductivity, which is the value we will take for the uncertainty in σ.

Another uncertainty in the quality factor of the resonator could come from a temperature gradient of the structure, which would have an impact in the conductivity. As mentioned when presenting the design of the cryostat, a temperature gradient $\nabla T \sim 1\,K$ for each resonator length is feasible with the correct choice of cryocoolers. From the literature one can extract that temperature gradients of 5 K around 4 K have minimal effects (a maximum of 1%) in the conductivity of most pure copper and copper alloy samples [234], with RRR below 3000. Since in our previous prototypes we have always had a RRR below 100 we would expect this effect to be minimal when compared to the uncertainty on the conductivity appearing from surface and oxidation effects.

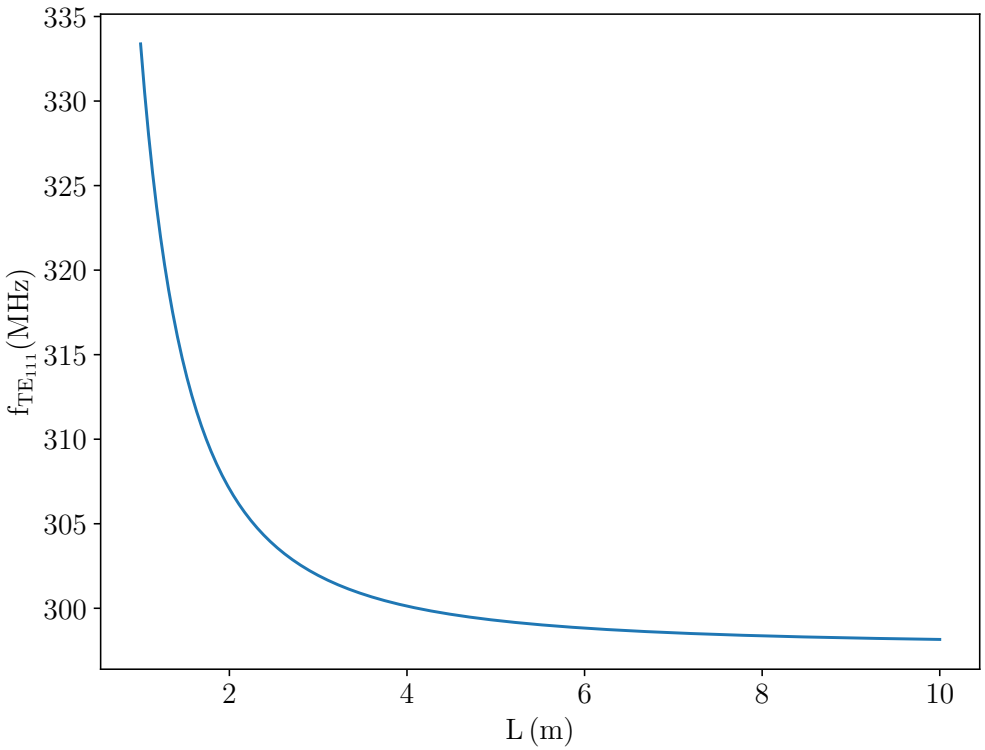

Figure 6.4.: Simulated resonant frequency for the TE_{111} mode of the cavity under study with a fixed value for the radius, $R = 59\,cm$, and increasing values of the length L.

For a cylindrical resonator filling completely the volume of the BabyIAXO magnet we would have an unloaded quality factor $Q_0 = 3.13 \times 10^5$, a volume $V = 2.731\,m^3$ and a geometric factor $C = 0.69$, which provides a figure of merit $FoM = Q_0 V C =$

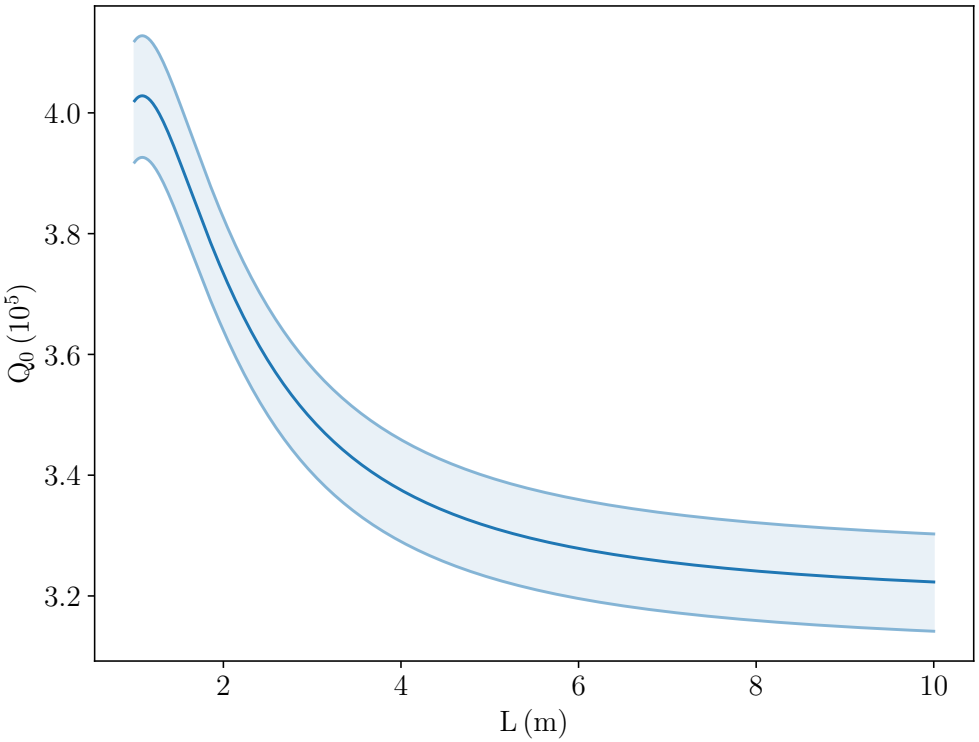

Figure 6.5.: Unloaded quality factor for the TE_{111} mode of the cavity under study with a fixed value for the radius, $R = 59\,\text{cm}$. After peaking for an optimal value for shorter lengths it decreases for increasing values of the resonator length L. The shaded area represents the uncertainty for Q_0 assuming a 10% symmetric uncertainty for σ at 4 K, specially relevant when considering quality factor degradation. However, higher values of RRR can be obtained for copper coatings with minimal skin effect and therefore conductivities above $\sigma = 2 \times 10^9\,\text{S/m}$ could also be attained.

$1.48 \times 10^5 \text{m}^3$ for the resonant frequency $f_{\text{TE}_{111}} = 298.2$ MHz, which corresponds to an axion mass of $1.42\,\mu\text{eV}$.

6.2.2. Multiple cavities

However the kind of elongated cavity described previously would have two main problems: the first would be the appearance of mode clustering close to the desired mode, making difficult the coupling to it while tuning the resonant frequency. The other main problem would be the implementation of the tuning mechanism itself, if we consider the most simple approach- two rotating metallic plates- the large size of the plates needed compromises the use of most piezoelectric actuators available, that can properly fit the bore. Even if we were able to set such a system, it would

be strongly sensitive to misalignment and possible bending of the tuning plates.

The next natural approach is to consider installing two or more smaller cavities during each data taking. For the sake of simplicity we will consider filling the whole volume of one bore with two cavities. Following this philosophy one can easily generalize this approach to an arbitrary number of cavities, the main price to pay in that case is an increased complexity of the acquisition system. When introducing more than one cavity, we need to flatten slightly the upper and lower parts of the cylindrical geometry, in order to properly fit all the cables inside the bore (see figure 6.6). However, this change does not modify much the characteristics of the mode of interest, see table 6.2 for a comparison between one 10 m cylindrical cavity and two 5 m quasi-cylindrical cavities combined coherently.

Parameters	Cylindrical	2 Quasi-cylindrical
$f_{\mathrm{TE}_{111}}$ (MHz)	298.2	303.8
V (m^3)	2.731	2.394
$Q_0(\times 10^5)$	3.13	2.97
C	0.69	0.63
$FoM(10^5\mathrm{m}^3)$	1.48	1.06

Table 6.2.: Difference in the main electromagnetic parameters for the TE_{111} mode of the resonator for the cylindrical and quasi-cylindrical case. In the cylindrical case a length of 10 m and an inner radius of 59 cm are assumed. While in the quasi-cylindrical the cavities are 5 m long, separated 8 cm with 0.5 cm thick walls.

6.2.3. Tuning mechanism

The most direct way to implement a tuning mechanism in a cylindrical cavity, such as the one displayed in figure 6.6, is by inserting one or more metallic plates and rotating them in order to modify the resonant frequency of the mode of interest. In the case of our design we considered the introduction of two parallel plates along the cavity axis, and rotating them around the same axis. The system and the tuning performance for an arbitrary sized cavity can be seen in figure 6.7.

With a set of four cavities as the ones described, we can cover the range from 1 to 2 μeV or, more specifically, the range from 253 MHz to 469 MHz (see table 6.3).

In figure 6.9 we show the performance of the mode of interest for the tuning range if each one of the cavities, this performance was simulated in CST Microwave Studio. One important study which is still missing for estimating the behavior of this system is the influence of waviness in the tuning plates surface and their misalignment from the perfectly parallel configuration. Based on our experience on the surface homogeneity tolerances that could be attained at workshops for other prototypes, and their low relevance in perturbing the geometry of TE_{111} modes waviness does not seem as a contribution that could be of high concern. However,

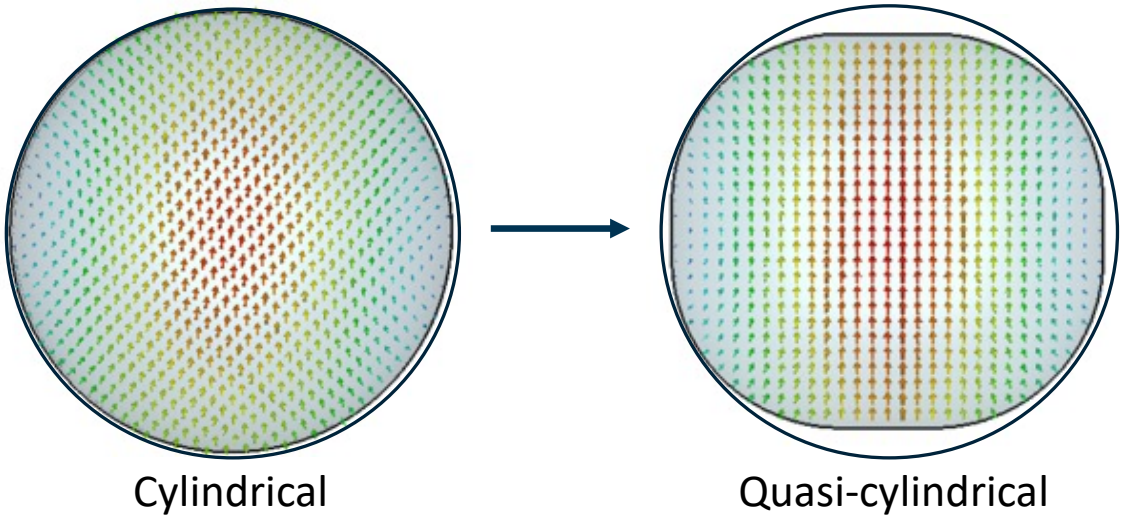

Figure 6.6.: Comparison between the E-field of a cylindrical waveguide profile and the one for the quasi-cylindrical design considered for the BabyIAXO-RADES prototypes.

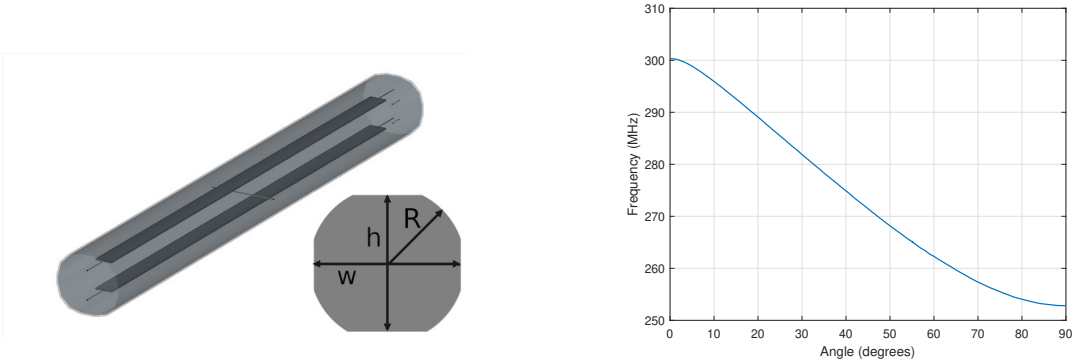

Figure 6.7.: On the left we display the geometry of one of the quasi-cylindrical cavities with a pair of rotating plates for tuning, the detail shows the design parameters: width (w), height (h) and corner radius (R). On the right we plot how the resonance frequency for the TE_{111} mode is displaced by rotating the inner plates for the first cavity in table 6.3.

Width (mm)	Height (mm)	Corner radius (mm)	w_p (mm)	V (m^3)	Tuning range (MHz)
560	504	220	150	1.195	252.8 - 300.3
492.3	443	220	125	0.876	300.3 - 351.6
430	387	180	95	0.682	351.2 - 395.2
355	319.5	140	95	0.475	392.2 - 469.3

Table 6.3.: Dimensions for the four quasi-cylindrical cavities considered for covering the 1-2μeV mass band inside the BabyIAXO magnet. The length of all cavities is 5 m. The tuning plates length and thickness are 4.5 m and 10 mm, respectively and their width is w_p.

deviations from the perfectly parallel model could have significant effect on the energy stored by the resonant modes, reducing the Q_0 in very extreme cases to a 25% of its nominal value. The study of this behavior is computationally consuming and has only been estimated based on experimental results for misalignment of more complex structures, which leads us to conclude that the quoted value of 25% is a clear overestimation for this prototype. Deeper studies, both simulations and measurements, of this behavior are under development at the moment.

It is important to note that the tuning steps imply not only the rotation of the plates, but also the recalibration of the port coupling. The coupling is implemented by means of a loop probe, which couples coaxial modes to the magnetic flux through the loop. Rotating the loop modifies the magnetic coupling, and allows the variation between the regimes where the probe is critically-coupled, over-coupled and under-coupled. The degree of freedom to adjust this coupling becomes then the tilting angle of the magnetic probe with respect to the vertical axis.

Figure 6.8a illustrates the coupling tuning implementation with three different angles (0, 33 and 60 degrees) of the magnetic probe. The radius of the loop has been fixed to 90 mm for an over-coupled condition when the angle of the loop is 0 degrees (vertically aligned). As the angle of the loop is varied, Figure 6.8b shows that the critically coupled condition is achieved for 33 degrees. For higher angles, an under-coupled condition is obtained as seen also in Figure 6.8b.

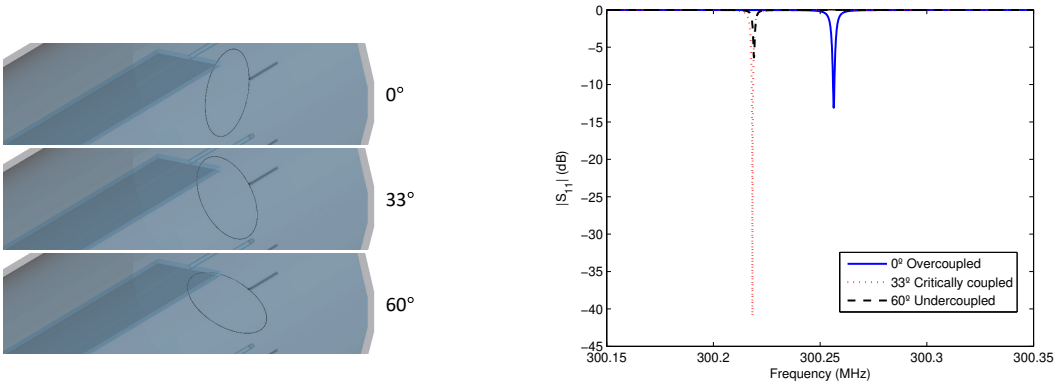

(a) (b)

Figure 6.8.: (a) Mechanical re-coupling by probe rotation for three different angles (0, 33, and 60 degrees), and (b) magnitude of the scattering parameter S_{11} for different angles of the magnetic probe.

The overall performance of the system under the action of the tuning mechanism is in the optimal range. Before starting to rotate the plates the form factor is maximum because of the structure optimization. Along the tuning range it drops but only down to a minimum of 30% in particular cases, and to an average value of around 10% while the quality factor remains roughly around the same value for the whole range.

A peculiarity one can also see in figure 6.9 is the presence of large drops on form

and quality factor due to mode crossing for particular configurations of the plates. However those are not significant as they only happen for very particular values of the frequency inside the tuning range. In any case, they should be compared with experimental values in order to reproduce the behavior in a real setup configuration.

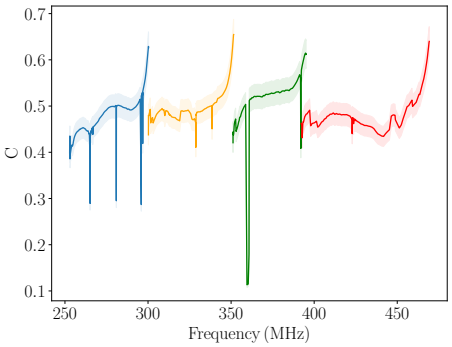

(a) Form factor

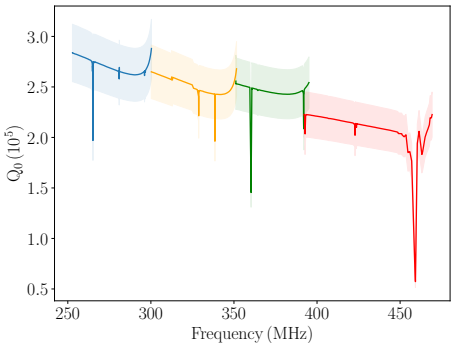

(b) Unlodaded quality factor

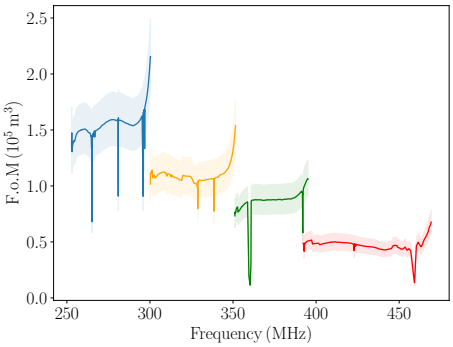

(c) Figure of merit

Figure 6.9.: Behaviour of the four different cavities when varying the frequency of the TE_{111} via rotation of two parallel metallic plates. The uncertainty of the form factor has been estimated to be around 5%, based tolerances simulations for previous prototypes. An uncertainty of 20% for the quality factor has been adopted, as discussed in the main text we consider this to be an overestimation based on simulations and previous prototypes.

6.2.4. Data taking strategy

With this set of four cavities, we envision two different scenarios depending on how we proceed with the data taking:

- **Parallel acquisition**: Two cavities designed for resonating at different frequencies taking data in parallel with two independent data acquisition systems.
- **Coherent acquisition**: Two identical cavities taking data in parallel with

their output power combined coherently, measured with a single data acquisition system.

For covering the desired band we would proceed with two data taking periods in the first scenario and four in the second one, the sketch of which can be found in figure 6.10. Seeing these data taking plans is easy to understand that in the parallel acquisition case we get double integration time for each frequency, whereas in the coherent acquisition case we get double the volume for each frequency.

Regarding sensitivity, and based on equation (3.61) it is simple to argue that the coherent acquisition scenario will yield a better result than the parallel one. Since the sensitivity in $g_{a\gamma}$ scales as $t^{\frac{1}{4}}$, whereas for the volume it scales as $V^{\frac{1}{2}}$.

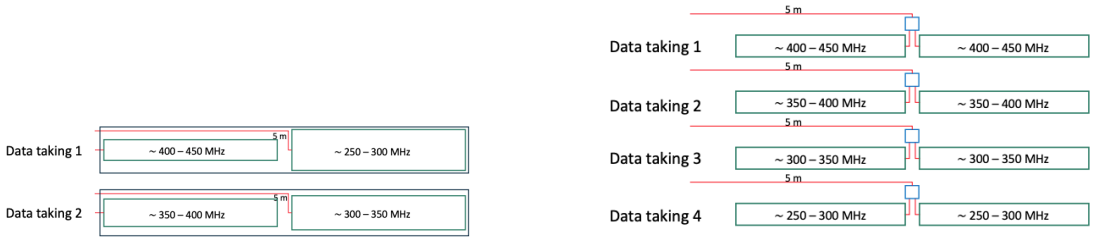

(a) Parallel acquisition scenario

(b) Coherent acquisition scenario

Figure 6.10.: Structure of the data takings scheduled for the parallel and coherent acquisition scenarios

Even if one can argue that the sensitivity reach of the coherent case will be systematically better, there are some technical details that have to be taken into account before deciding on one of the two detection schemes. A system with parallel acquisition, would be less technically challenging, since one only needs two acquisition systems taking data in parallel similar to the one we have already used in previous searches. In the coherent case only one data acquisition system is needed, however the setup is much more complex: we need to manufacture pairs of cavities as much identical as possible, tune them and couple them in a way they behave the most similar as possible in order to be able to properly combine their signal, we also need to provide the system with combiners for the pairs of cavities.

As of today, we are still investigating both approaches and simulating the behaviour of a system for coherent sum of cavities. This setup would not be only better performing, it also follows the basic philosophy we had in mind when building the first RADES prototypes, growing in volume and increasing the system resonant frequency by replicating smaller cavities.

6.3. Sensitivity estimates

With the general ideas for the setup mentioned in the previous section, we can now set a series of estimates on the sensitivity for axion and dark photon searches with

a haloscope inside the BabyIAXO magnet.

6.3.1. Axion sensitivity

Let us begin by taking the expression for the axion signal power (3.55) and re-scale it to the benchmark values of the RADES setup proposed for BabyIAXO in the previous section.

$$P_s = 8.47\times10^{-22}\mathrm{W}\frac{\kappa}{0.5}\left(\frac{g_{a\gamma}}{2\times10^{-16}\mathrm{GeV}^{-1}}\right)^2\frac{1\mu\mathrm{eV}}{m_a}\left(\frac{B}{2\mathrm{T}}\right)^2\frac{V}{10^3\mathrm{l}}\frac{Q}{3\times10^5}\frac{C}{0.63} \quad (6.3)$$

where we have assumed a dark matter energy density of $\rho_{DM} = 0.45\,\mathrm{GeV/cm^3}$. We can also introduce the $C_{a\gamma}$ adimensional coupling for QCD axions as

$$C_{a\gamma} = \frac{g_{a\gamma}}{2\times10^{-16}\mathrm{GeV}^{-1}}\frac{\mu\mathrm{eV}}{m_a} \quad (6.4)$$

and express the signal power as

$$P_s = 1.1\times10^{-22}\mathrm{W}\frac{\kappa}{0.5}\left(\frac{C_{a\gamma}}{0.36}\right)^2\frac{m_a}{1\mu\mathrm{eV}}\left(\frac{B}{2\mathrm{T}}\right)^2\frac{V}{10^3\mathrm{l}}\frac{Q}{3\times10^5}\frac{C}{0.63} \quad (6.5)$$

We can also introduce the experimental parameters in the noise temperature formula (3.57) to obtain

$$P_T = 6.7\times10^{-20}\,\mathrm{W}\frac{T_{\mathrm{sys}}}{6\mathrm{K}}\frac{3\times10^5}{Q_a}\frac{m_a}{1\mu\mathrm{eV}} \quad (6.6)$$

where we have used the relation between the natural width of the axion and the frequency dispersion $Q_a = \frac{\omega_a}{\Delta\omega_a}$, and we have taken a conservative value of $T_{\mathrm{sys}} = 6\,\mathrm{K}$.

We can use these expressions to set the region sensitive to an axion signal over the background with a confidence level of 90%. In figure 6.11 we show this region in the global context of axion searches. For our estimation we have assumed a data taking of around 400 days. This data taking time is split on either two or four periods as sketched in figure 6.10, depending on the scenario we consider. For simplicity we only plot the result obtained in the coherent acquisition scenario, for the parallel case there is an 10% reduction on the sensitivity reach.

It is interesting also to show these results on the context of haloscope searches, in figure 6.12 one can see how this resonant cavities installed in the BabyIAXO magnet would allow to target the region between $1\,\mu$eV and the lowest masses reached by ADMX, an area still unexplored by other experimental setups.

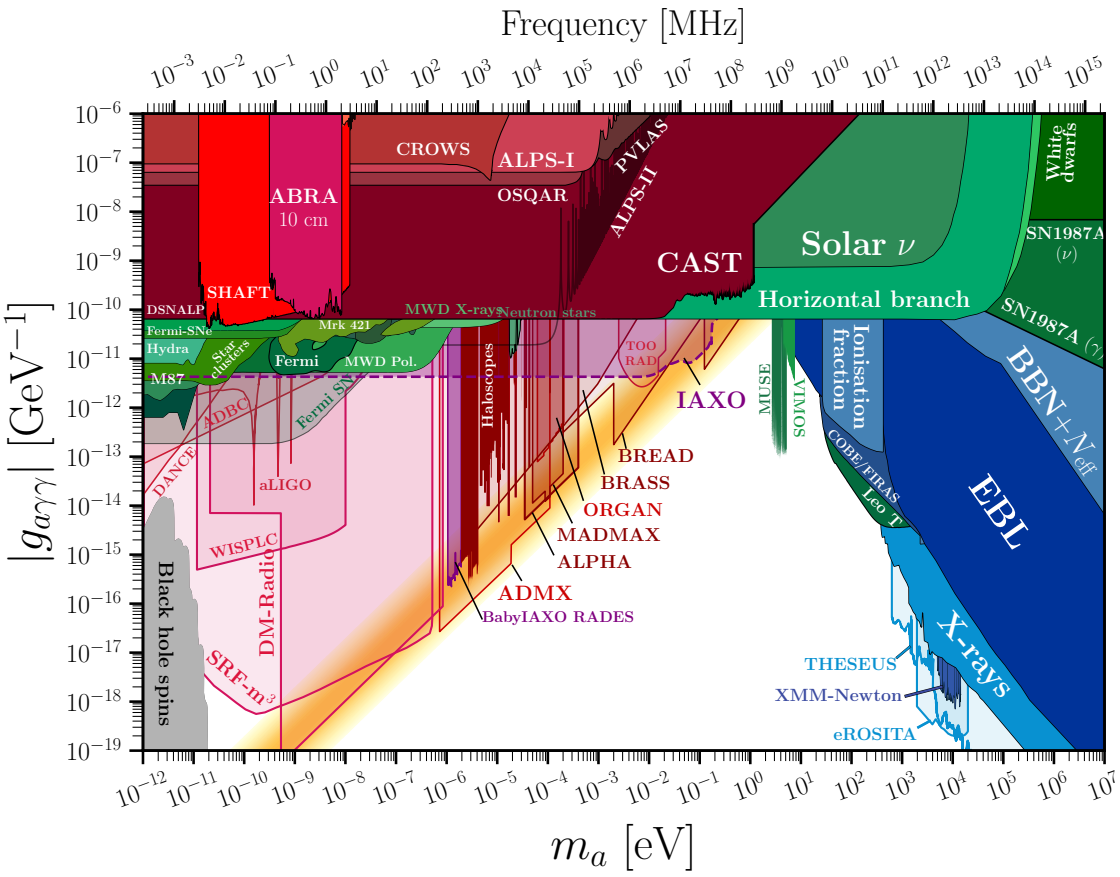

Figure 6.11.: Prospect in sensitivity for an axion search performed by a haloscope prototype placed inside of the BabyIAXO telescope, labeled as BabyIAXO RADES on the plot. Existing limits and prospected sensitivity from selected experiments are also shown, see [68].

6.3.2. Dark photon sensitivity

The interest on the dark photon search in this case is particularly motivated since, even before commissioning the magnet for BabyIAXO, the cavities and the cryostat could be operated independently in a first physics data taking campaign.

Following the approach exposed on section 3.3.2, we can recast the axion limits into limits for dark photon detection. For this simple estimate we will consider the case of unpolarized dark photons and we will not take into account orientation effects for the setup. However, as argued in [76], in most scenarios this can be considered a reasonable estimate for dark photon sensitivity.

In figure 6.13 we show the sensitivity estimates we find for the dark photon case. These are very competitive limits when compared to other haloscope experiments

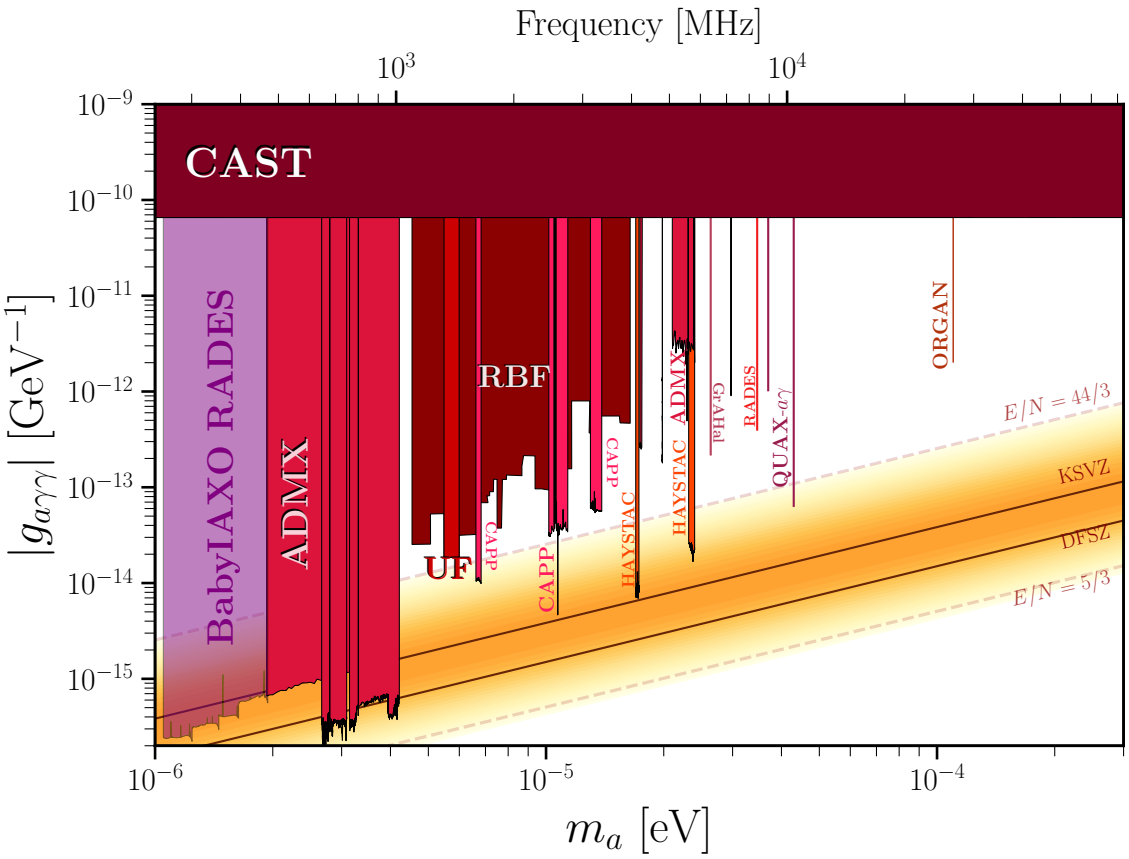

Figure 6.12.: Zoom in of 6.11 in the region of interest for cavity haloscopes. We display the prospect in sensitivity for an axion search performed by a haloscope prototype placed inside of the BabyIAXO telescope, labeled as BabyIAXO RADES on the plot. Results for other haloscope searches are shown, plot adapted from [68].

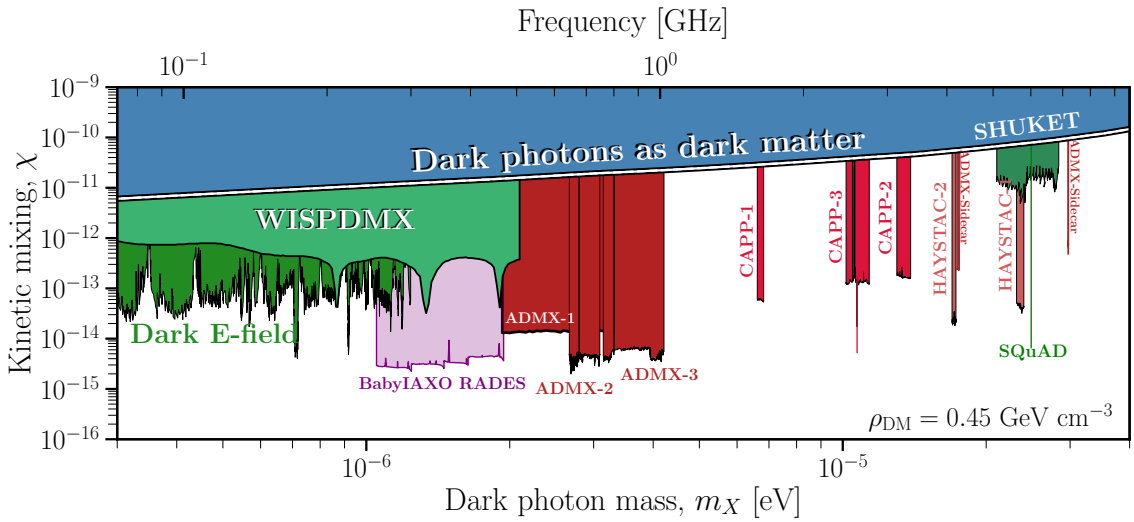

Figure 6.13.: Prospect in sensitivity for a dark photon search performed by a haloscope prototype placed inside of the BabyIAXO telescope, labeled as BabyIAXO RADES on the plot. For this estimation a non polarized cold dark matter halo was assumed, plot adapted from [68].

7

Electronics radio purity assessment for BabyIAXO

In this chapter we analyze the electronics that will process the Micromegas signal in the IAXO-D0 prototype, originally proposed for the IAXO telescope, but also adopted for BabyIAXO later. We start by presenting the front-end and back-end electronics, then we review the activity of the components of the front-end system and the simulations performed for characterizing their influence on the detector background. Finally we discuss the inclusion of these results on the complete background model for BabyIAXO. The screening and simulations associated to the radioactive background generated by the front-end cards (FECs) being one of my contributions developed during my PhD thesis work.

One of the main goals of the detector upgrades planned for BabyIAXO is to improve the lowest background level achieved by a Micromegas (MMs) detector, i.e. the one measured for the last run performed at CAST: 10^{-7}counts keV^{-1} cm^{-2}s^{-1}. However it is important to remark that the figure of merit when comparing the different detectors at BabyIAXO also takes into account the detector efficiency, ϵ

$$f_{\mathrm{D}} = \frac{\epsilon}{\sqrt{b}} \tag{7.1}$$

where the background b is normalized per area, time and energy bin. Based on this figure of merit, the criteria for selecting viable candidates to perform as BabyIAXO detectors relies on increasing x-ray detection efficiency while, at the same time, suppressing and discriminating background events.

7.1. Micromegas detector and electronics board design

From all the different detectors discussed in 5.4 we will now focus our study on the electronics system for reading out the Micromegas detector, mainly because of its suitability for x-ray detection with an extremely low background (see section 4.1). As mentioned previously, this particular detector gave outstanding results on the solar axion search performed at CAST [134] and for that it was selected as the main detector technology for both IAXO and BabyIAXO.

The electronics proposed for BabyIAXO and the TREX-DM experiments [235] is an evolution of the Application-specific integrated circuit for Generic Electronic system for TPCs (AGET) [236] implemented in previous experiments like CAST [170]. This new version of the electronics is denominated Second Step AGET (STAGE) and it introduces a modular and flexible approach for general purpose readout systems in small to medium size gaseous detectors designed at IRFU, CEA Saclay. The system layout, depicted in figure 7.1, also includes a spark protection circuit composed by a series of capacitors and high resistivity resistors. The 240 channels of the Micromegas readout detector active area will be connected to 4 Single STAGE Front-End Cards (SAFEC) containing one STAGE chip each. The output of the four SAFEC will be connected to the Back-End Card (BEC) which will include the ADC and an FPGA to control the system. Lastly, the BEC will communicate with a remote DAQ PC via a standard Gigabit Ethernet link and, optionally, it would receive global clocking and triggering information from a central Trigger and Clock Module (TCM).

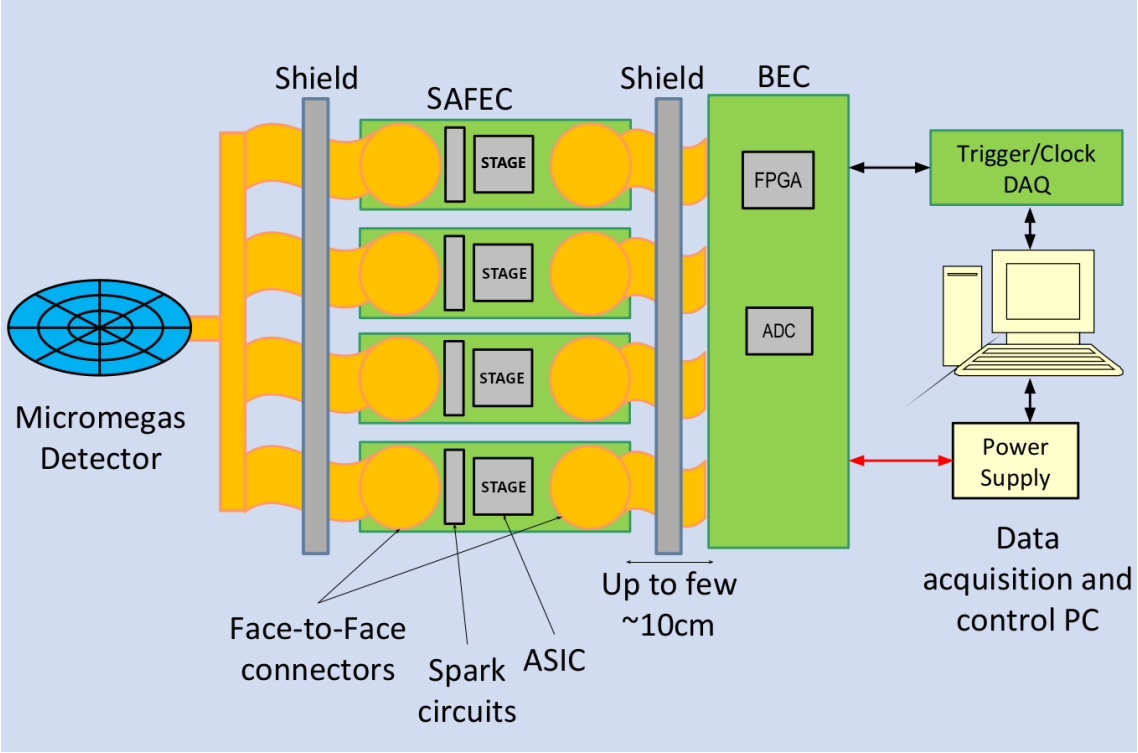

Figure 7.1.: Scheme depicting the acquisition chain. The Micromegas detector inside the copper vessel, after a small shielding stage, is directly connected to a series of Front-end acquisition cards. The signal is amplified and reaches the front-end electronics for digitization of the signal, outside of a bigger lead shielding stage. The front-end electronics are connected to a computer for data recording and trigger input.

In order to reduce the effects on noise and lower signal threshold, the SAFEC is expected to be placed as near as possible to the detector, at least, at mid distance inside the shielding, between the detector and BEC. For that, it is planned to minimize the radioactive impurities by selecting its components and a kapton based

board. Some of the components needed include capacitors, resistors and diodes for a spark protection circuit and the STAGE coupling capacitors. The radiopurity of these components was studied, and will be treated in detail in the following sections. In the case of the STAGE chip, in order to avoid the packaging material, the possibility of using naked chips and wire bond them directly to the board is being investigated. Lastly, the connectors are based on customized solutions in which two kapton PCBs are simply put in "face-to-face" (FtF) contact, without solder or intermediate connector pieces, developed and tested in the University of Zaragoza in the context of previous low-background Micromegas applications.

The SAFEC PCB is represented in figure 7.2. The FtF connectors cover almost one third of the extremes of the board each, one on the upper part and the other in the lower part, for the Micromegas and FEC connections, respectively. All the components are placed in the remaining central zone.

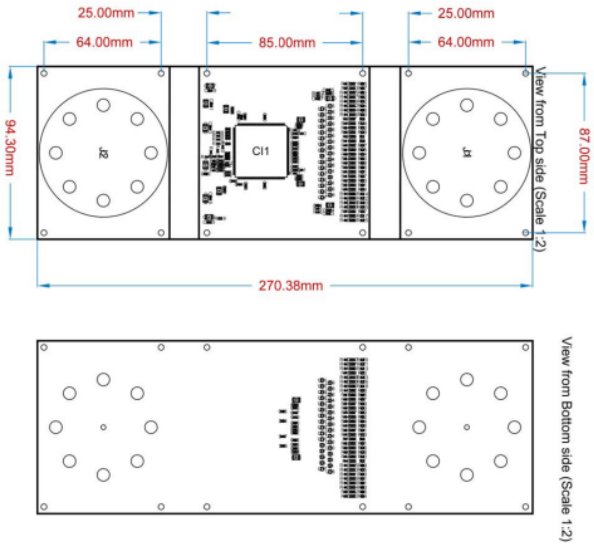

Figure 7.2.: Scheme for the SAFEC. The electronics components are placed in the central area of the card, while the extremes are used for the face-to-face connectors.

The Front-End Card consists of three distinct zones. At the ends, it features the FtF radiopure connectors based on direct contact with the Limandes (flexible boards made of Kapton and copper to connect to Micromegas and BEC), which are separated from the central zone by a flexible area to facilitate proper mechanical coupling to the support structure. The central zone encompasses all the necessary components for capturing the signal from the Micromegas sensor, primarily the AGET and passive components such as decoupling capacitors and some termination resistors. Additionally, spark protection circuits are included to prevent damage to the STAGE inputs.

The full list of components that conform the board is compiled in table 7.1.

Component	Quantity	Mass (mg per unit)	Product Reference
STAGE chip	1	2740	-
10 Ω resistors	83	4	CRCW060310R0JNEAC
100 MΩ resistors	64	4	HVC0805T1006JE
Diodes	64	5	BAV99W.115
220 pF ceramic capacitors	64	4.7	06035A221JAT2A
100 nF ceramic capacitors	64	5.5	0603YC104KAT2A
Tantalum capacitors	14	28.2	06035A221JAT2A

Table 7.1.: Electronic components constituting the FEC cards.

7.2. Components activity

7.2.1. Activity estimation

It is very important to perform precise measurements of the activity of all the components placed close to the detector, as much as the detector parts themselves. Since the components will be placed inside of the lead shielding and close to the detector, the SAFEC have to be taken into account as a source of background for the experiment. In particular because the different electronic components are not radiopure, and the decays of the contaminating elements present on them will trigger the detector.

As the first step in order to quantify the effect these boards might have on the background, we started by measuring the activity of diodes, resistors, capacitors and the STAGE chips. These measurements were made by Susana Cebrián and the team of the Canfranc Underground Laboratory [237], between August 2019 and November 2020. They were performed via gamma ray spectroscopy using high purity Germanium detectors. It is important to note that this is a non destructive technique, which allows to install the exact same batches that have been tested. The downside for this procedure is that, for components with very low activities, larger quantities and exposure times are needed in order to properly characterize them. Due to the low activity and mass of some components, their activity could not be quantified, in those cases a 95.45% C.L was derived by following Currie's criteria [238, 239]. In any case, this has to be understood as a good sign since it means that some of the components were not that much radioactive as we could have naively expected before measuring them.

For determining the activities of each sample, the components under study were placed on top of a low background germanium detector, see figure 7.3. After an exposure time between 7 and 70 days, depending on the activity of the batch under study, the resulting data was analyzed. For the analysis, a setup was implemented in Geant4 including the germanium detector and a thin cylinder on top of it reproducing the sample distribution (as seen in figure 7.3) with the estimated density of the components under study. Using this simulated configuration the activities of

different radioactive isotopes were fit to the spectra measured by the detector.

When measuring the activities of isotope decay chains, specifically for ^{232}Th and ^{238}U the activities of upper and lower parts of the chain were extracted, assuming secular equilibrium for certain parts, such as the ^{226}Ra partial chain for ^{238}U. There is a caveat here though, it could be that some isotopes inside partial chains like the ones mentioned are out of equilibrium. One specific case is the decay of ^{210}Pb isotopes as part of the ^{238}U decay chain, this isotope also appears naturally after exposition to ^{222}Rn in storage facilities. Its bremsstrahlung peak at 46.54 keV could have a significant effect in the energy spectra in our region of interest, $1 - 10\,\mathrm{keV}$. However, due to the absence of measurable gamma radiation the activity of that partial chain it is not feasible to quantify its activity with the germanium detectors employed at Canfranc Underground Laboratory. In the specific cases were there is suspicion of extra ^{210}Pb contamination α spectroscopy is used in order to determine its activity, but this requires extra exposition time and detailed measurements which were not performed for the electronic components.

As a side note let us point that precisely determining the activities of superficial ^{210}Pb is one of the main goals of the AlphaCAMM detectors which are currently under development at Zaragoza in order to characterize the background of the TREX-DM experiment [240], but with the idea in mind of using them for other experiments, such as IAXO and BabyIAXO. In this context, future measurements of the ^{210}Pb activity for the electronics and the rest of the parts of the detector are envisioned, specially if background inconsistencies are found in the BabyIAXO experiment when compared with the estimated background model in simulations.

For some samples the density was known, however for most of them it was not. In those cases it was assumed homogeneous and its value estimated based on the volume and weight of a single component. The densities of the components measured range from $2\,\mathrm{g/cm^3}$ to $9\,\mathrm{g/cm^3}$. The influence of varying the density was studied but it showed no substantial effect, mainly because the size of the components provides almost no self-shielding, most of them have a volume $\sim 1\,\mathrm{mm^3}$. To compensate this an other experimental uncertainties a conservative value of the 30% is assumed for the simulated efficiency of the detector.

One of the main results that was found on these measurements is that the metallic parts of the electronics, mostly copper based but also the Ta capacitors and Ge resistors were not that much contaminated as the ceramic or encapsulated components. This was expected since the production of encapsulating materials is not performed with the preservation of isotopic purity in mind, but just to adapt to certain thermal and electrical conditions. Most of the components considered cannot be operated without encapsulation but the most contaminated in general can be substituted by others more suited, there is a particular exception which can be implemented without encapsulation, the STAGE chip, this will be discussed in the following subsection.

I proceed now with the summary of all the activities measured for the different components of the FEC.

Figure 7.3.: Sample containing 500 capacitors placed on top of a low background Ge detector for activity screening.

7.2.2. STAGE chip

The main component of the SAFEC is the STAGE chip that processes the signal coming out of the Micromegas mesh. The fact that there is not much choice of STAGE chips that perform equivalently, makes it also one of the most strict limitations when modifying the electronics board in order to improve its radio purity.

A sample of 50 non-functional chips provided by CEA was screened. They are reported as LQFP 160 pin chips. Each unit has a mass of 2.74 g and dimensions $2.8 \times 2.8 \times 1.4\text{mm}^3$ for the package and $8.8\text{mm} \times 7.8\text{mm} \times 250\mu\text{m}$ for the silicon die. The exact composition of the chip was unknown, as it is not detailed on the data sheet, the substrate was assumed to be fr4 which is a typical epoxy substrate for similar chips, and the density was well reproduced by it.

In table 7.2 specific activity for the ^{232}Th and ^{238}U chains can be found and as for ^{40}K, ^{60}Co and ^{137}Cs decays. We label as ^{228}Th (combined) and ^{226}Ra (combined) the lower parts of the ^{232}Th and ^{238}U chains respectively.

Chain	Isotope	A (mBq/kg)	A (mBq/unit)
^{232}Th	^{228}Ac	58 ± 22	0.16 ± 0.06
	^{212}Bi	< 275	< 0.75
	^{212}Pb	213 ± 65	0.58 ± 0.18
	^{208}Tl	160 ± 37	0.44 ± 0.10
	^{228}Th (combined)	173 ± 32	0.47 ± 0.09
^{238}U	^{234}mPa	$< 3.2 \times 10^3$	< 8.7
	^{214}Pb	185 ± 41	0.51 ± 0.11
	^{214}Bi	171 ± 32	0.47 ± 0.09
	^{226}Ra (combined)	176 ± 25	0.48 ± 0.07
-	^{137}Cs	< 15	< 0.04
-	^{60}Co	< 13	< 0.04
-	^{40}K	303 ± 106	0.83 ± 0.29

Table 7.2.: Activity measurements for LQFP 160 pin chips. Based on a 50 components batch measured during 19.39 days at the Canfranc Underground Laboratory.

As we mentioned, there is not much chance to avoid the contamination present on the chip since there are not much possible substitutes on the market, however one option is to implement the chip without the encapsulation. This would require a special soldiering procedure- PCB direct bonding- which is under study at the moment. Chips without encapsulation were also measured and improved the background performance for up to 3 orders of magnitude, as displayed in table 7.3.

In any case, for the background assessment we used the data we have for the encapsulated chips since it will give us a more conservative limit for the background and because we still have no prototypes that implemented the chip without the encapsulation in the SAFEC board.

Chain	Isotope	A (mBq/unit)
^{232}Th	^{228}Ac	< 0.0072
	^{228}Th (combined)	< 0.0014
^{238}U	^{234}mPa	< 0.0059
	^{226}Ra (combined)	< 0.0027
-	^{40}K	< 0.0217

Table 7.3.: Activity measurements for non-encapsulated chips (0.35 microm AMS CMOs technology). Based on a 430 components batch measured during 9.20 days at the Canfranc Underground Laboratory.

7.2.3. Diodes

A sample containing 500 silicon switching diodes, supplied by Infineon, was analyzed ("Diode Array GP 100 V 150 mA SOT323" Ref. BAV99W.115). Each unit has a mass of 5 mg and dimensions $2 \times 1.5 \times 0.8\text{mm}^3$. They were placed on top of one of the germanium detectors for 73.23 days.

The simulations for connecting the background with the activity of different chains was performed considering a cubic box reproducing the sample dimensions. Only activities for isotopes on the ^{232}Th chain were quantified, for the rest upper limits were set, the complete results are complied in table 7.4.

Chain	Isotope	A (mBq/kg)	A (μBq/unit)
^{232}Th	^{228}Ac	487 ± 193	2.4 ± 1.0
	^{212}Bi	$< 2.3 \times 10^3$	< 11
	^{212}Pb	540 ± 181	2.7 ± 0.9
	^{208}Tl	623 ± 222	3.1 ± 1.1
	^{228}Th (combined)	573 ± 140	2.9 ± 0.7
^{238}U	^{234}mPa	$< 18 \times 10^3$	< 90
	^{214}Pb	< 720	< 3.6
	^{214}Bi	< 520	< 2.6
-	^{235}U	< 290	< 1.4
-	^{137}Cs	< 121	< 0.6
-	^{60}Co	< 91	< 0.5
-	^{40}K	$< 1.8 \times 10^3$	< 9.2

Table 7.4.: Activity measurements for Diode Array GP 100 V 150 mA SOT323. Based on a 500 components batch measured during 73.23 days at the Canfranc Underground Laboratory.

7.2.4. Resistors

As mentioned before there are two different kinds of resistors to be installed, one set of 10Ω and another with a resistance of 100MΩ.

The first sample was measured during 13.30 days and consisted on 150 SMD resistors of 100MΩ (HVC Series, Ref. HVC0805T1006JET) produced by Ohmite and supplied by Digi-Key. Each one of them weighing 4 mg and of dimensions $2.00 \times 1.25 \times 0.40\text{mm}^3$. For simulation purposes they were reproduced considering a disk replicating the sample distribution on top of the detector, and the composition was assumed to be mostly alumina ($\rho = 3.95\text{g/cm}^3$). The results can be found in table 7.5, the values obtained are at the same order as those of resistors analyzed for the TREX-DM [241] and NEXT [242, 243] experiments.

Chain	Isotope	A (Bq/kg)	A (μBq/unit)
^{232}Th	^{228}Ac	8.7 ± 3.3	35 ± 13
	^{212}Bi	19.2 ± 7.6	77 ± 30
	^{212}Pb	6.8 ± 2.2	27.3 ± 8.9
	^{208}Tl	5.6 ± 2.1	22.3 ± 8.4
	^{228}Th (combined)	6.7 ± 1.5	26.7 ± 6.0
^{238}U	^{234}mPa	< 194	< 777
	^{214}Pb	< 5.5	< 22
	^{214}Bi	5.1 ± 1.8	20.4 ± 7.3
-	^{235}U	< 1.7	< 6.6
-	^{137}Cs	< 1.2	< 4.8
-	^{60}Co	< 1.3	< 5.2
-	^{40}K	< 21	< 84

Table 7.5.: Activity measurements for SMD resistors of 100 MΩ (HVC Series, Ref. HVC0805T1006JE). Based on a 150 components batch measured during 13.30 days at the Canfranc Underground Laboratory.

Another sample was measured for 32.68 days, it contained 5000 10Ω resistors, reported as Lead-free Thick Film Rectangular Commodity Chip Resistors (Ref. CRCW060310R0JNEAC) produced by Vishay and supplied by Digi-Key. The dimensions of each unit being $1.6 \times 0.8 \times 0.45\text{mm}^3$ and weighing 4.05 mg. The data sheet describes the resistors as made of metal gaze on ceramic. Alumina was assumed for the material in the Geant4 simulations used for fitting the measurements. We report the results on table 7.6, the results are significantly lower than those found for the 100MΩ, in any case ones cannot substitute the others since both serve different purposes. However, they are also more radio pure than some equivalent ones which were measured in the context of the TREX-DM [241] and NEXT [242, 243] projects.

7.2.5. Capacitors

For the capacitors to be used in the SAFEC there are three different kinds depending on their purpose in the circuit: 220 pF, 100 nF ceramic capacitors and 10 mF tantalum capacitors.

We started by measuring the activity of the 220 pF ceramic capacitors, for it

Chain	Isotope	A (mBq/kg)	A (μBq/unit)
^{232}Th	^{228}Ac	218 ± 58	0.88 ± 0.23
	^{212}Bi	< 583	< 2.4
	^{212}Pb	239 ± 75	0.97 ± 0.31
	^{208}Tl	180 ± 63	0.73 ± 0.26
	^{228}Th (combined)	204 ± 48	0.83 ± 0.20
^{238}U	^{234}mPa	$< 7.5 \times 10^3$	< 30
	^{214}Pb	195 ± 49	0.79 ± 0.20
	^{214}Bi	244 ± 79	0.99 ± 0.32
	^{226}Ra (combined)	209 ± 42	0.85 ± 0.17
-	^{235}U	280 ± 69	1.13 ± 0.28
-	^{137}Cs	< 35	< 0.14
-	^{60}Co	< 26	< 0.11
-	^{40}K	< 575	< 2.3

Table 7.6.: Activity measurements for Lead-free resistors of 10Ω (Ref. CRCW060310R0JNEAC). Based on a 5000 components batch measured during 32.68 days at the Canfranc Underground Laboratory.

a sample of 500 units was prepared. The capacitors were tagged as C0G/NP0 Dielectric (Ref. 06035A221JAT2A), they were produced by AVX and supplied by Digi-Key. Each unit weighing 4.7 mg and measuring $1.6 \times 0.81 \times 0.9\text{mm}^3$. They were placed on top of one of the detectors for total of 6.98 days of data taking. Without the full composition of the capacitors available TiO_2 was assumed as it is typically used in ceramic capacitors manufacturing, the density being 4.2 g/cm^3 was also compatible with the considered units.

Specific activity and activity per unit is reported on table 7.7, high activity for ^{238}U and ^{232}Th chains was quantified. These values are way higher than those obtained for tantalum capacitors analyzed, both in this work and in the context of the NEXT [242, 243] experiment.

The second sample of capacitors analyzed consisted on 1000 units of multilayer ceramic capacitors of 100 nF, identified as 16 Volts, dielectric X7R capacitors (Ref. 0603YC104KAT2A) produced by AVX and supplied by Digi-Key. The mass and dimensions for each unit being 5.5 mg and $1.6 \times 0.81 \times 0.9\text{mm}^3$

The activity measured, registered in table 7.8, is significantly lower than the one found for the previous set of capacitors. And in the order of the results found for similar components studied for the NEXT [242, 243] experiment.

Finally a third set of capacitors was measured, this sample contained 500 tantalum capacitors of 10 μF, described as TCJ Series, Conductive Polymer Solid Electrolytic Chip Capacitors (Ref. TCJA106M010R0300). The mass of each unit being 28.2 mg and the dimensions $3.2 \times 1.6 \times 1.6\text{mm}^3$. The sample was measured for 6.76 days. No detailed information of the composition was available, and a mixture of C and MnO_2 has been assumed as for other tantalum capacitors in the market.

Chain	Isotope	A (Bq/kg)	A (mBq/unit)
^{232}Th	^{228}Ac	56 ± 11	0.264 ± 0.050
	^{212}Bi	< 95	< 0.45
	^{212}Pb	85 ± 26	0.40 ± 0.31
	^{208}Tl	66 ± 21	0.309 ± 0.098
	^{228}Th (combined)	74 ± 16	0.344 ± 0.076
^{238}U	^{234}mPa	$(0.89 \pm 0.35) \times 10^3$	4.2 ± 1.6
	^{214}Pb	$(1.11 \pm 0.24) \times 10^3$	5.2 ± 1.1
	^{214}Bi	$(0.87 \pm 0.15) \times 10^3$	4.07 ± 0.71
	^{226}Ra (combined)	$(0.94 \pm 0.13) \times 10^3$	4.40 ± 0.60
-	^{60}Co	< 3.6	< 0.017
-	^{40}K	< 43	< 0.20

Table 7.7.: Activity measurements for 220 pF ceramic capacitors (Ref. 06035A221JAT2A). Based on a 500 components batch measured during 6.98 days at the Canfranc Underground Laboratory.

Chain	Isotope	A (Bq/kg)	A (mBq/unit)
^{232}Th	^{228}Ac	2.15 ± 0.18	0.0118 ± 0.0010
	^{212}Pb	0.93 ± 0.12	0.00513 ± 0.00066
	^{208}Tl	1.22 ± 0.20	0.0067 ± 0.0011
	^{228}Th (combined)	1.01 ± 0.10	0.00556 ± 0.00056
^{238}U	^{234}mPa	< 24	< 0.13
	^{214}Pb	57.2 ± 4.2	0.315 ± 0.023
	^{214}Bi	49.9 ± 2.9	0.275 ± 0.016
	^{226}Ra (combined)	52.4 ± 2.4	0.288 ± 0.013
-	^{60}Co	< 0.15	< 0.00084
-	^{40}K	< 1.5	< 0.0083

Table 7.8.: Activity measurements for 100 nF ceramic capacitors (Ref. 0603YC104KAT2A). Based on a 1000 components batch measured during 33.13 days at the Canfranc Underground Laboratory.

The activity levels found for the ^{238}U and ^{232}Th chains are compiled in table 7.9, the results are way better than the ones found for the ceramic capacitors. However this was expected based on the data already available for other tantalum capacitors [242, 243].

7.3. Electronics background simulations

Having measured the activity of the different components that conform the electronics front-end cards, I proceeded with an analysis of the contribution to the background in the gaseous detector of the telescope. This study was initially performed for the IAXO-D0 prototype for the installation at the IAXO telescope, this

Chain	Isotope	A (Bq/kg)	A (μBq/unit)
^{232}Th	^{228}Ac	2.88 ± 0.55	81 ± 16
	^{212}Bi	4.7 ± 1.7	133 ± 48
	^{212}Pb	4.5 ± 1.4	128 ± 39
	^{208}Tl	3.42 ± 0.86	97 ± 24
	^{228}Th (combined)	3.89 ± 0.67	110 ± 19
^{238}U	^{234}mPa	< 22	< 621
	^{214}Pb	0.86 ± 0.29	24.3 ± 8.1
	^{214}Bi	0.80 ± 0.19	22.5 ± 5.3
	^{226}Ra (combined)	0.82 ± 0.16	23.0 ± 4.4
-	^{137}Cs	< 0.20	< 5.6
-	^{60}Co	< 0.13	< 3.7
-	^{40}K	< 2.4	< 67

Table 7.9.: Activity measurements for 10 μF tantalum capacitors (Ref. TCJA106M010R0300). Based on a 500 components batch measured during 6.76 days at the Canfranc Underground Laboratory.

first design is the one we will refer to as *IAXO-D0 geometry*. During the development of the thesis the BabyIAXO experiment was proposed and the IAXO-D0 prototype adopted for implementation, however some changes where made on the geometry of the detector system later on, in order to adapt it to mechanical limitations, this is the design we will denominate *IAXO-D1 geometry*. For this second design a new assessment of the electronics background was performed which was ultimately added to the other simulated sources, in order to consolidate the complete background model for BabyIAXO.

7.3.1. IAXO-D0 geometry

The original setup for the Micromegas detector of the IAXO telescope was named IAXO-D0, its initial geometry can be seen in figure 7.4. It was commissioned at University of Zaragoza during the first stages of the IAXO project development, between 2016 and 2018. The IAXO-D0 prototype was build using the IAXO pathfinder detector, previously implemented in the 2014-2015 CAST solar data taking campaign [207].

One of the main differences between the IAXO-D0 setup and the IAXO pathfinder, implemented at CAST, is the positioning of the electronic cards. In CAST, all the electronics were placed outside of the lead cube surrounding the Micromegas detector, which was proved to completely shield their background. However, in the case of IAXO the idea from the beginning was to segment the electronics into two parts, the front-end and the back-end. In that scenario with the objective of reducing the signal to noise ratio at the first electronics readout stage, the front-end cards would be placed inside the lead shielding, at an intermediate distance between the exterior of the lead castle and gas the chamber of the detector (figure 7.5).

(a) Cooper vessel containing the detector. The x-rays are expected to transverse the copper tube (oriented vertically in the figure) and the signal is sent via the readout strips (oriented horizontally).

(b) External lead shielding structure for the detector, the front-end electronics and the copper pipe. Also referred to as *lead castle*.

Figure 7.4.: IAXO-D0 prototype [135].

For properly studying the radioactive background we need to simulate sufficient events reaching the detector in order to capture their energy spectra. However most simulated events in this context, after generation and full processing, do not deposit energy on the detector. Therefore, the computational time until reaching sufficient statistics for several isotopes can easily increase up to months worth of simulations.

This situation increases in complexity when the emitters for the decays are considered to be distributed along a volume, and even more if simulating the decay chains step by step. It is because of this that we implemented a slightly simplified version of the SAFEC and the IAXO-D0 geometry in REST (see figure 7.6), and prepared a series of simulation files for full chain decays of the different isotopes present on the electronic components.

Some of the activities were quantified for single radioisotope decays, e.g. the case of ^{40}K for the STAGE chips. But most of the relevant background comes from the ^{232}Th and ^{238}U decay chains. However, in those cases secular equilibrium was assumed and the simulations simplified to full chain decays with the highest activity, which in some cases was even two orders of magnitude higher than other parts of the chain. In table 7.10 we quote the full chain activities we used for the different isotopes present on each of the electronic components. When implementing the

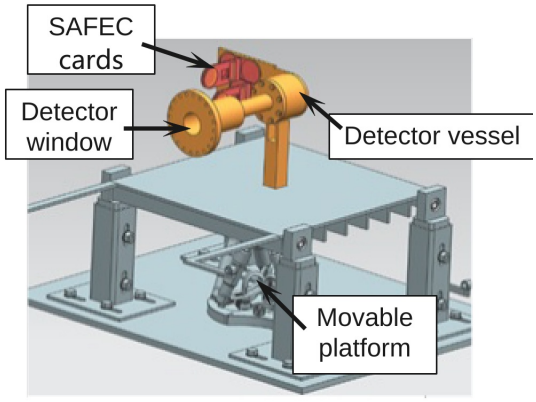

Figure 7.5.: Diagram of the IAXO-D0 detector prototype mounted on a supporting platform. A copper pipe connects the magnet beam line with the gas chamber of the detector, the Micromegas detector is located at the base of the gas chamber and the copper lines from the mesh are connected to four different SAFEC cards that operate as the front-end electronics. The system is enclosed by a lead shielding, not displayed on the image.

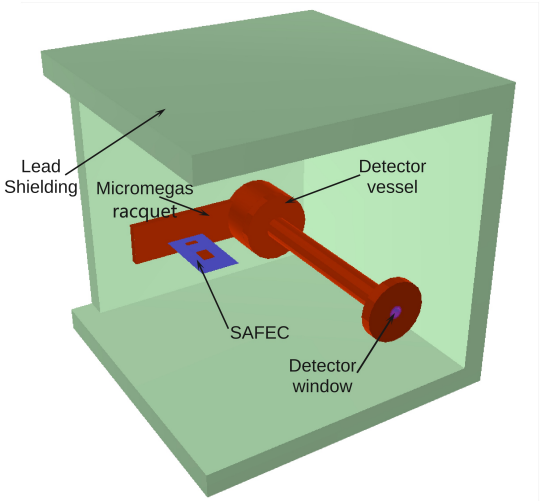

Figure 7.6.: View from above of the geometry implemented in REST. Includes the lead shielding (transparent in the picture) containing the vessel of the detector, the pipe connected to the telescope, the racquet and the SAFEC.

simulations, the 100 nF ceramic capacitors had not been measured yet, and they were treated as if the contamination was similar as to that of the 220 pF capacitors. In view of the higher activity displayed by the later this is consistent with obtaining an uper limit for the total background. From here on we will refer to this set of 128 capacitors as ceramic capacitors, and quote only the activity of the 220 pF ones.

Component	Units	^{40}K	^{60}Co	^{137}Cs	^{232}Th	^{235}U	^{238}U
100 MΩ resistors	64	84	5.2	4.8	77	6.6	777
10 Ω resistors	113	2.3	0.11	0.14	2.4	1.13	30
Ceramic capacitors	128	200	17	-	450	-	4200
Ta capacitors	14	8.3	0.84	-	12	-	130
Diodes	64	9.2	0.5	0.6	11	1.4	90
STAGE	1	830	40	40	750	-	8700

Table 7.10.: Activities considered for the different isotopes when simulating full chain decays based on the measured activities for each component of the electronics in μBq/unit. The ceramic capacitors with the most activity have been considered in order to obtain upper limits. The 10 Ω resistors are not considered since they are not part of the original board design.

Another of the simplifications considered when simulating radioactive decays was related to the distribution of the components on the SAFEC board. The volume of the STAGE was implemented and decays were randomly sourced at different points inside of it. For the rest of the components a generic volume was added on the region containing the components closest to the detector in the real geometry. In this way we ensured obtaining an upper limit for the number of events reaching the detector while simplifying event generation.

As described in section 4.2 the first step for our background simulations, once the geometry has been implemented, is to simulate the energy depositions in the gas inside the copper vessel. This is done by preparing a restG4 simulation file, an example of the different blocks in such a configuration file can be found in Appendix B for the particular case of a decay of ^{238}U originating on the capacitors of the SAFEC. Let us review how the relevant parameters and characteristics of the simulation are implemented in them:

Globals:

In this part of the code the global variables and parameters are defined. In particular, the path for the simulation directories and the main details that characterize the simulation, i.e. the isotope whose decay we want to study, the electronics component where the decay will start, and the amount of initial events to simulate per run.

TRestRun:

The first object in the restG4 simulation file is a TRestRun, it contains most of the information about the run, such as: the experiment, the type of simulation, the user running the script, etc. In the particular example discussed here, this object carries the information about the simulation being part of a background study for

the electronics of the BabyIAXO experiment.

TRestG4Metadata:

The main object inside a restG4 simulation file is the TRestG4Metadata, it contains the main parameters that will be passed to the Geant4 simulation run. In this case, the values for target step size and sub-event time delay are chosen in order to have resolution for the event evolution reaching the gas volume, without compromising the simulation time. The generator volume is assigned to match one of the sub-volumes in the geometry file, the emission is assumed isotropic and the energy is set to 0 to simulate radio active decays. Finally, the gas is set as the only sensitive volume since we will be interested in events that trigger a cascade inside the detector. Even though we will be ultimately interested in events reaching the detector in the 1-10 keV range, the recording range at this stage is set up to 5 GeV to account for events at higher energies that can end up triggering signals at lower energies after the gas drifting process. This value has been chosen rather arbitrarily to record most events, it could be optimized to reduce even further the amount of events recorded at this stage, but we did not find it necessary.

TRestPhysicsLists:

Finally, we have to add the physics lists that will be implemented in the Geant4 simulation. The usual hadronic and decay physics lists are added, both simulations including ARM or ICM events were considered and showed no significant difference. For choosing the electromagnetic physics list a series of studies where performed comparing the Livermore, Penelope and Standard lists. We found the Livermore and Standard libraries to give equivalent results, whereas when using Penelope some energy depositions where missing. Since we did not find any physical argument to accept one set of results or the others, we decided to stick to using the Livermore package since it gave us a slightly larger background for all the decay chains under consideration and therefore a more conservative limit, however this discrepancy only meant registering around 1% more events reaching the detector per each set of thousands of simulations. We suspect that other packages than Livermore could be implementing low energy cuts in the simulations which get rid of some relevant events in our energy region of interest, but a more detail case by case study would be in order to properly understand where these discrepancies could come from.

A first set of simulations allowed us to characterize the isotopes contributing the most to the background in the 1-10 keV region. As we will see later, the highest contribution was found to be that of ^{228}U, and therefore extra simulations were performed. In total, several million of radioactive decays were studied for each isotope (see table 7.11). For each one of these isotopes, the amount of hours of computational time was of the order of ten thousand. It is clear that the only way to perform these kind of studies in a reasonable time is to use some cluster computing

services. In our case most of the simulations were performed on the CERN lxplus [244] cluster during the year 2018 and using the supercomputing services of DESY at the National Analysis Facility (NAF) [245] from 2019 to 2022.

Isotope	Initial events (10^6)
^{40}K	180
^{60}Co	180
^{137}Cs	180
^{226}Ra	190
^{228}Ra	210
^{228}Th	180
^{232}Th	210
^{235}U	180
^{238}U	310

Table 7.11.: Initial events for the different isotope decay chains that have been simulated in REST.

After running the restG4 simulation files, the energy deposits on the gas coming from different isotope decays are obtained. The next step consists on running the restManager tool in order to reconstruct the events that would be measured on the detector as a consequence of these energy deposits.

For this procedure we prepared one first RML file (*G4processes.rml*) defining the processes to be performed in each step of the analysis was based on a general template available on REST-for-Physics [158], the description of the different processes and the associated observables can be found on section 4.2.

A configuration file was prepared for sequentially performing the steps defined in the *G4processes.rml* file. The steps for processing the background events discussed here, once the gas depositions have been simulated are the following:

1. Diffuse the energy deposits on the gas.
2. Transform the cascade into hits on the detector.
3. Reconstruct the equivalent track from the acquired hits.
4. Analyse the observables of the track.

An example of this code can be found in Appendix B, in particular for implementing the analysis steps of background studies originated from radioactive decays.

After the analysis we obtain a series of observables for each decay event we simulated, in figure 7.7 we show the distribution of some of this observables for 310 million initial events of ^{238}U decays. The combination of these observables for all the different isotopes simulated allows us to properly characterize the expected background due to the electronics radioactive contamination.

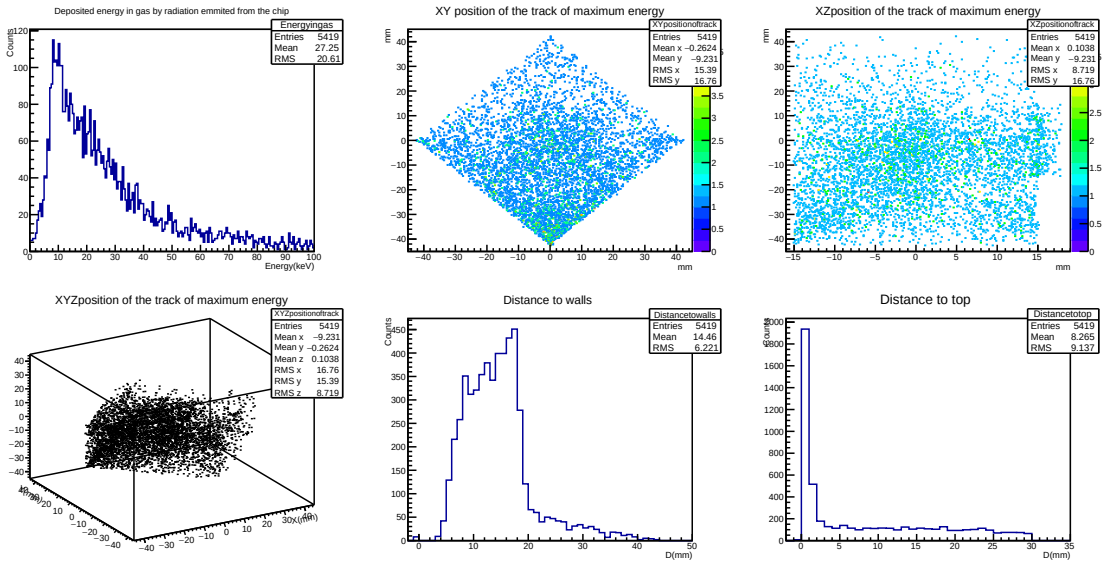

Figure 7.7.: Distribution of different observables for 310 million of initial events of ^{238}U full chain decays originated on the electronics board location.

For the total assessment of the background we weighted the spectra obtained for each isotope, taking into account the activity and the number of units for each component. After adding all the spectra together we obtained the background profile for the 1-10 keV range that we show in figure 7.8. Before applying any cuts, the total integrated background for the region of interest we find is:

$$\mathrm{E_{BG}} = 3.4 \times 10^{-7}\,\mathrm{counts\,keV^{-1}\,cm^{-2}s^{-1}}\,(\mathrm{No\,cuts})$$

which is already close to the level set as a goal for the IAXO-D0 prototype, $10^{-7} - 10^{-8}\,\mathrm{counts\,keV^{-1}\,cm^{-2}s^{-1}}$ as originally stated in the IAXO conceptual design [221].

One important feature of this spectrum comes to our attention when separating the contribution for each component. As it can be seen in table 7.12 the main contribution to the total background comes from the ^{238}U chain, in particular from the ceramic capacitors of 220 pF, which account in total for almost 90% of it. It is also interesting to note that no significant contribution was found from ^{137}Cs or ^{235}U contamination.

The ceramic capacitors found to be the ones contributing mostly to the background are difficult to substitute, since they have to be able to sustain voltages up to 600 V without risk of being conductive. Therefore, they cannot be substituted by smaller ones like the silicon capacitors, which were measured to be more radio pure. Other alternatives are being researched at the moment, but the equivalent capacitors measured in the context of the NEXT and TREX-DM experiments yielded the same results.

As mentioned before the background level of the electronics would be already at an acceptable level, however it can be improved by taking into account the cuts already developed for the rest of the background events (section 5.5). In figure 7.9

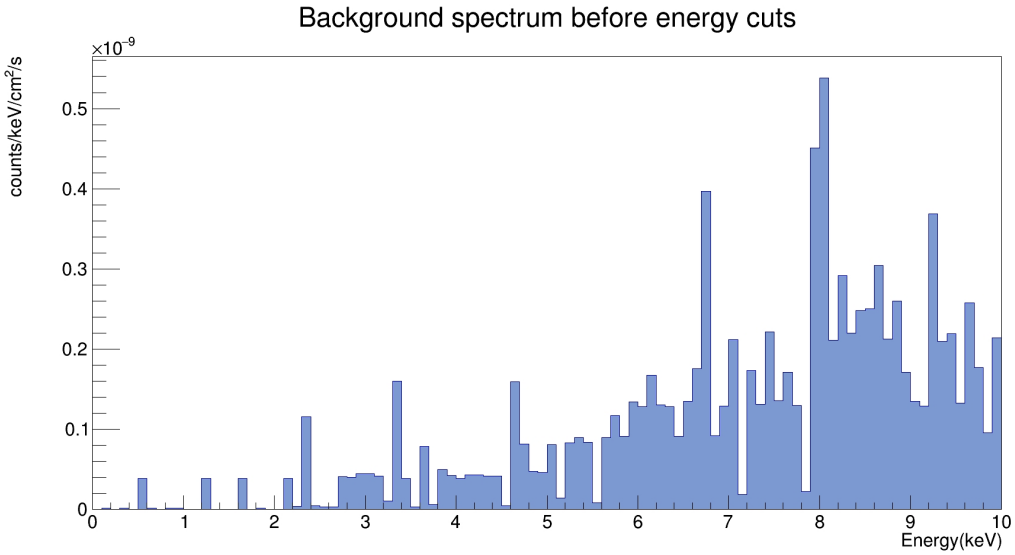

Figure 7.8.: Background spectrum for the range 1-10 keV as an effect of radioactive decays originated on the electronics boards.

Component	^{40}K	^{60}Co	^{232}Th	^{238}U	All isotopes
100 MΩ resistors	0.094	0.057	0.060	7.432	7.643
10 Ω resistors	0.005	0.027	0.003	0.503	0.538
Ceramic capacitors	0.450	0.397	8.909	80.08	89.84
Ta capacitors	0.019	0.022	0.036	1.524	1.602
Diodes	-	-	0.005	0.025	0.030
STAGE	0.004	-	-	0.342	0.372

Table 7.12.: Break down of the total background into the contributions coming from the different electronic components in %. More than 98% of the background is generated by the 220 pF capacitors and the 100 MΩ resistors together.

we can see how imposing the value of the cuts compiled in table 5.1 restricts the amount of events registered for ^{238}U decays.

After applying the cuts quoted previously to the complete background shown in figure 7.8 we obtain a severely reduced contribution, figure 7.10, and a total integrated background of

$$\mathrm{E_{BG}} = 3.5 \times 10^{-9}\,\mathrm{counts\,keV^{-1}\,cm^{-2}s^{-1}}\ (\mathrm{With\,cuts})$$

This level is lower than the total background measured for the IAXO-D0 prototype, with the electronics placed outside of the lead shielding, in screened conditions at Canfranc Underground Laboratory: $7 \times 10^{-8}\,\mathrm{counts\,keV^{-1}\,cm^{-2}s^{-1}}$.

One interesting comment is that the reduction of the background for the different components- when applying the energy cuts- is almost homogeneous, see table 7.14.

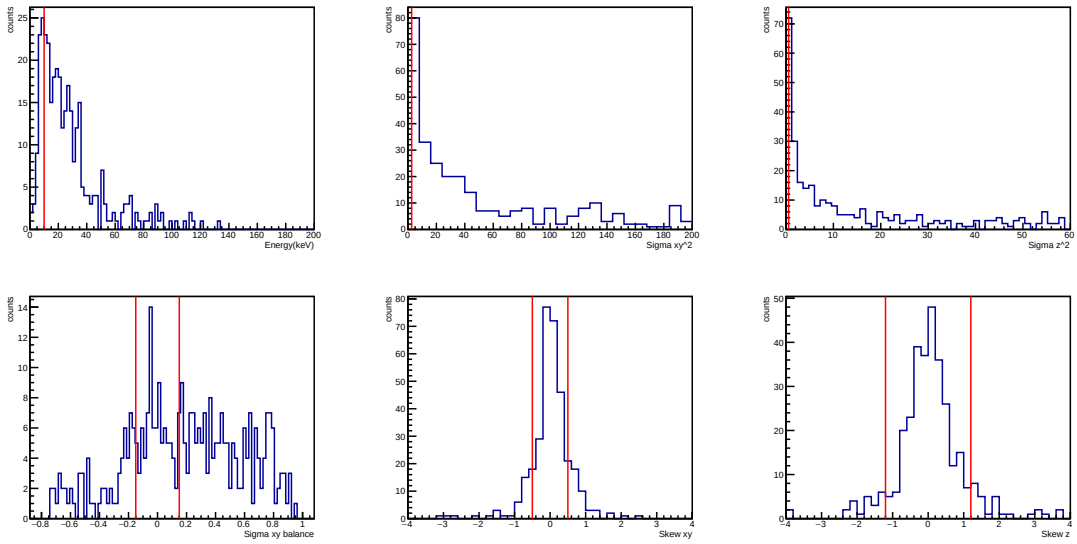

Figure 7.9.: Variables used for the energy cuts applied to background events. A file of ^{238}U decays with 70 million initial events was used for these plots.

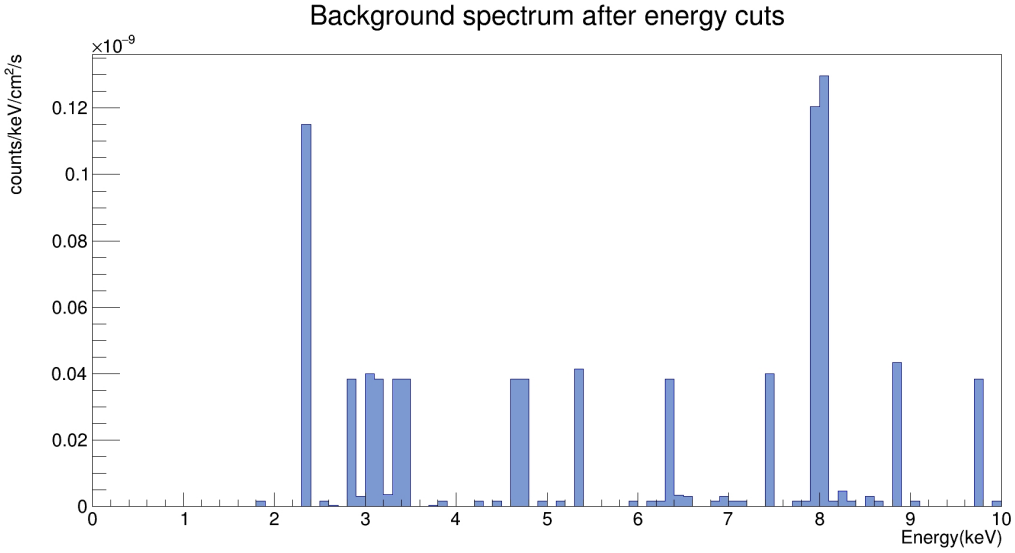

Figure 7.10.: Background spectrum for the SAFEC electronics after applying the energy cuts compiled in table 5.1.

This feature and the reduction of almost two orders of magnitude of the background contribution, makes the energy cuts developed for other sources also suited for the radioactive contamination of the SAFEC boards.

7.3.2. IAXO-D1 geometry

When BabyIAXO was firstly proposed as a demonstrator of the IAXO telescope, the IAXO-D0 prototype was immediately adopted as the detector to be implemented for

Component	^{40}K	^{60}Co	^{232}Th	^{238}U	All isotopes
100 MΩ resistors	0.113	0.076	0.060	7.324	7.467
10 Ω resistors	0.005	0.034	0.003	0.498	0.535
Ceramic capacitors	0.540	0.499	9.936	78.93	89.37
Ta capacitors	0.034	0.014	0.040	1.504	1.569
Diodes	-	-	0.006	0.024	0.030
STAGE	0.004	-	-	0.343	0.343

Table 7.13.: Break down of the total background into the contributions coming from the different electronic components in %, after the energy cuts have been applied.

Component	^{40}K	^{60}Co	^{232}Th	^{238}U	All isotopes
100 MΩ resistors	0.83	0.75	1.00	1.01	1.02
10 Ω resistors	1.00	0.79	1.00	1.01	1.01
Ceramic capacitors	0.83	0.80	0.90	1.01	1.00
Ta capacitors	0.56	1.57	0.90	1.01	1.02
Diodes	-	-	0.83	1.04	1.00
STAGE	1.00	-	-	0.99	1.08

Table 7.14.: Ratio of the different background component contributions before and after the energy cuts are applied.

the first physics run. However, due to restrictions on the total weigh of the supporting structure the lead shielding and the copper pipe that connects the gas chamber to the beam line had to be re-designed, giving place to the development of the prototype known as IAXO-D1. In this process the readout lines of the Micromegas detector were also changed and as a consequence the position of the front-end electronics modified. In figure 7.11 we show the technical diagrams depicting the new positioning of the electronic boards.

It is important to note that this rearrangement of the electronics was possible because the first assessment of the background yielded a positive result, and therefore approaching the FECs without compromising the background was judged feasible. However, this new positioning of the SAFEC boards implied the need for a re-assessment of the contribution of the electronics to the total background. Based on the results found for the IAXO-D0 prototype, i.e. ^{238}U accounting for almost 90% of the total background (see table 7.13), we decided to focus on simulating the effect of ^{238}U decays only for the IAXO-D1 prototype. These events being more prone to give us substantial statistics, than other decays.

The energy spectrum obtained after 10^9 simulations of ^{238}U decays was higher than the one found for the IAXO-D0 prototype, see figure 7.12. This increase was expected because the new placing of the electronics reduces substantially the volume of the lead shielding between the front-end cards and the gas volume of the detector. However, the integrated effect after applying the same cuts compiled in table 5.1, is still compatible with the limit set at Canfranc Underground Laboratory

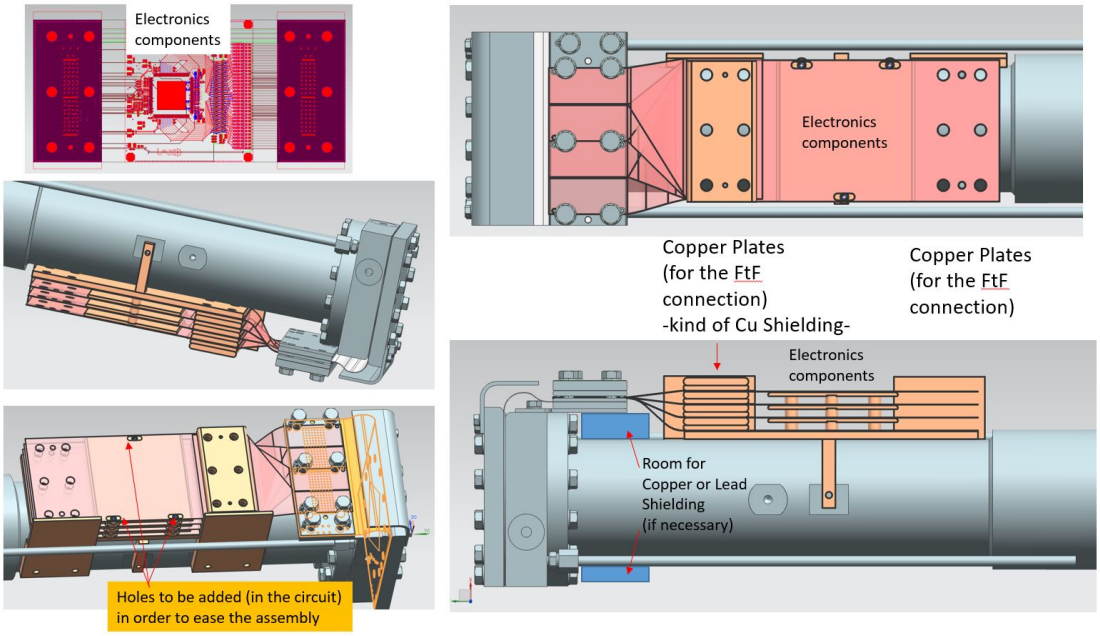

Figure 7.11.: Diagram of the positioning for the SAFEC cards on the current BabyIAXO detector prototype. The rest of the setup is similar to the IAXO-D0 prototype (fig. 7.5), but the copper lines coming out of the Micromegas follow the detector pipe from above connecting the mesh to four different SAFEC cards place right on top of the pipe. The possibility of adding a lead collar to shield the detector from the electronics is depicted.

of $7 \times 10^{-8}\,\mathrm{counts\,keV^{-1}\,cm^{-2}s^{-1}}$

$$\mathrm{E_{BG}} = 4.89 \times 10^{-9}\,\mathrm{counts\,keV^{-1}\,cm^{-2}s^{-1}}\ (\mathrm{IAXO-D1\ With\ cuts})$$

As mentioned before, in this background model only the contribution of ^{238}U was considered. A more complete study is currently under development as a natural continuation of this thesis work by measuring the contamination of the precise components to be placed in the final front-end cards. We can consider the result shown in this work as an upper limit for the background generated by the electronics where the components have been considered the most contaminated possible, some of them not being the ones that were selected finally for the cards.

7.3.3. Contribution to BabyIAXO background

The results presented in this section are included in a recent publication where the use of micromegas detectors for dark matter searches and their very low background is discussed [246]. For the case of the BabyIAXO experiment, a background of the order of $\times 10^{-7}\,\mathrm{counts\,keV^{-1}\,cm^{-2}s^{-1}}$ is usually quoted as the requirement for the

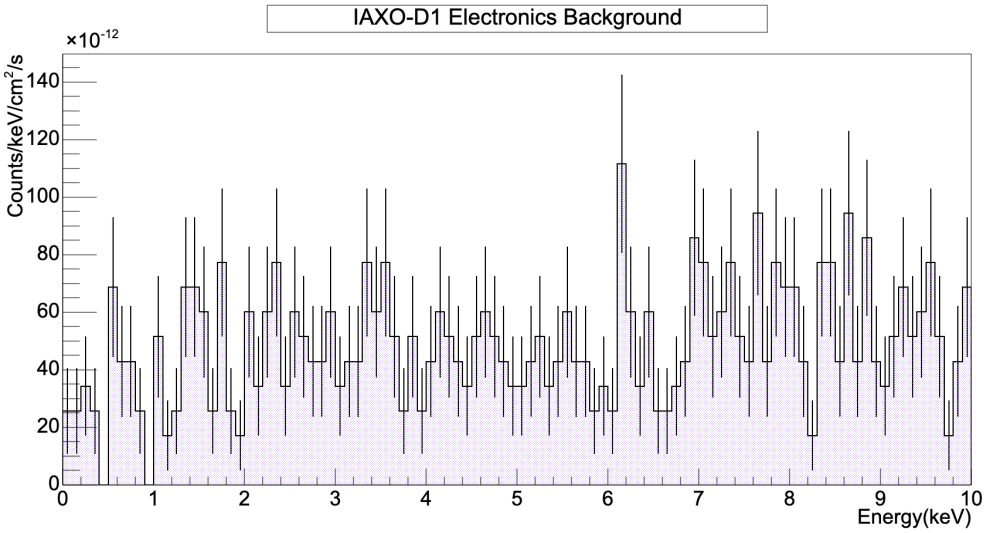

Figure 7.12.: Background spectrum for the SAFEC electronics in the IAXO-D1 prototype. Based in 10^9 simulations of ^{238}U radioactive decays, and applying the energy cuts compiled in table 5.1.

desired sensitivity. The result found for the background generated by the front-end electronics, after applying the same energy cuts used for other environmental signals, is already between one and two orders of magnitude better than the required one. And there are ways to explore the possibility of even improving this result, such as direct bonding of the AGET chip or the implementation of specific analysis cuts for the acquired signals.

The main limitation for reaching the low background required by the BabyIAXO and IAXO telescopes comes from the neutron events induced by cosmic rays in the lead shielding that surrounds the detector. They present a topology similar to the one associated to X-ray events, specially the ones producing secondary fluorescence in the innermost regions of the detector, and are therefore difficult to differentiate from solar axion events in the analysis. Different groups inside of the IAXO collaboration are currently working on the development of an active veto system for cosmic rays that allows the reduction of the background by tagging the events originated outside of the magnet, for more information see [246].

Before closing this chapter let us make one last comment regarding the background simulations performed and the code generated for running them. The simulation framework used for the background assessment- the REST framework- only allows for the study of gaseous detectors, however the way the simulations and the later analysis are performed the code we generated is fairly general and could be used for the electronics systems of other gaseous detectors proposed for BabyIAXO. Furthermore, the extension of REST to include other kind of detectors is currently under development. In the future maybe the effect of the electronics for SDDs, MMCs, etc. could be studied slightly modifying the codes presented here.

8

Multi-cell resonators for axion DM detection

In section 3.3.3 we introduced the use of multi cavity structures for the search of dark matter axions. Following the success of our first prototype with 5 sub-cavities as a proof of principle, we started the development of larger structures in order to reach competitive sensitivities at higher masses. Let us keep in mind the power generated from axion-photon conversion in a resonant cavity presented in 3.3.1, and define the figure of merit of our haloscopes as F.o.M. $= Q\mathcal{G}^2V$.

8.1. Steps towards improvement

Three different lines of action were chosen to work towards improvement in our setup:

1. Increasing the detection volume: The bigger the volume the higher the sensitivity.
2. Adding a tuning mechanism: Not knowing the exact axion mass, imposes the need of an experiment with a broader band than the one we developed initially.
3. Improving the Q factor of the overall structure: In the same fashion as the first point, a better quality factor can improve dramatically the sensitivity of the system.

In this work we focused on the increase of the detection volume of the system of sub cavities deployed at CAST. The other two points are out of the scope of this thesis, but there has been extensive work performed on those areas by other researchers on the RADES group. More information about the research lines currently under development in our group for studying the tuning and the Q factor can be found in [247].

Based on what we have discussed, it is simple to argue that increasing the volume of these kind of devices can be done without affecting the resonant frequency of the system, just by adding more sub cavities. This was the approach we took, and a couple of prototypes, with 19 and 30 cavities respectively, were designed. We will

discuss these prototypes in the next section.

When taking this approach, we realized that the system started to be less and less stable the more sub cavities were added. After reviewing the details of the formalism for coupling the system of sub cavities, we developed a new kind of prototype more stable against mechanical tolerances. This was done by designing a system for which the sign of the coupling of neighboring cavities is alternated from one pair of cavities to the next one. In section 8.3 we expose the details on how our formalism applies to this particular case and what it means from the radio-frequency design perspective.

8.2. Longer cavities

After the positive results from the first RADES data taking, the approach taken to increase the sensitivity of the experiment was to enlarge the detection volume by designing a structure composed by several more cavities than the previous one. And displace a bit the mass window of our search, not to overlap with the previous exclusion limit. In particular, the frequency at which the fundamental mode of the structure was located was $f = 8.187\,\mathrm{GHz}$ which corresponds to an axion mass of $m_a = 33.86\,\mu\mathrm{eV}$.

During the design process a series of simulations were performed in order to identify the behavior of the cavities and optimize the sensitivity of the experiment. During this stage a series of complications were identified when considering a system like the one under study with almost four times more cavities than the original prototype.

8.2.1. Mode overlap

Mode overlap happens when two consecutive resonant modes start getting closer and closer in frequency, see figure 8.1, until their tails begin to overlap. In general, this translates into an effective drop on the quality factor of the resonance into consideration and can generate a system in which the desired mode under study cannot store energy properly. The extreme case of this situation would be having degenerated modes, i.e. two or more modes resonating at the exact same frequency, this case is, in general, only associated to particular symmetries of the system and was not a problem in our case, even though it constrains the proportions for a, b and L in each sub cavity. In figure 8.1 one can also see that two modes have merged, since we can only identify 18 peaks (instead of the 19 expected). Based on finite elements simulations performed with CST Microwave Studio of the E-Field of the fundamental mode, in particular after computing the geometric factor, we can assure the 'axion mode' is not the one merged and therefore this would not affect our sensitivity to axions.

It is easy to understand how this mode overlap appears as a side effect of the

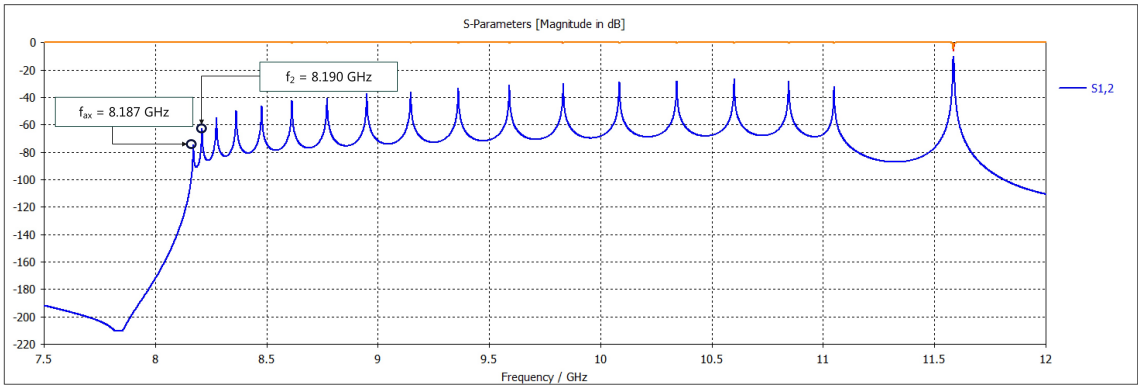

Figure 8.1.: Simulation of the reflection and transmission parameters for the 19 sub cavities structure as a function of frequency in cryogenic conditions. The filter-like behavior, with up to 19 modes, associated to the prototype can be seen. The lowest mode, labeled f_{ax}, corresponds to the one coupling maximally to the axion field, while f_2 is its closest neighbor.

addition of cavities in our system in a straightforward manner. For each cavity we add to the system, it acquires a new resonant mode, but the width of the frequency band along which this modes are distributed does not depend on the number of cavities but, small corrections aside, on the dimensions of the sub cavities themselves.

This imposes a strong restriction on the amount of cavities you can add to the system, for a given search mass before the frequency band gets crowded and mode overlap starts being critical. This intuitive result was confirmed by simulations, where we found that the lower the experiment goes in masses, the wider the band will be, and thus the less mode overlap there will be. This correlation imposes a limit on our approach to axion detection for much higher frequencies, in particular for masses above $50\,\mu$eV $\sim$ 12 GHz, we expect this mode overlap to compromise detection for structure volumes in the order of those considered here.

An optimistic comment is in order here: even though it is true that in the case under study we found this mode overlap to be very limiting when growing in volume, we expect this issue to have a milder effect on structures with higher Q values for the fundamental mode. This assumption is backed by simulation results showing that the narrower the resonance, the more one has to move away from the resonant frequency before the field distribution of the next mode starts appearing in the simulation.

To show how this mode distribution changes, we can look at the particular case of interest- the 19 cavities structure- and compare the spacing of the frequencies of the fundamental mode f_1 and its first neighbor f_2, with the situation we had for the 5 cavities structure. In the new structure we found this spacing to be $(f_2 - f_1)_{19\text{cav}} = 3\,\text{MHz}$, almost then times lower than the value for the 5 cavities resonator: $(f_2 - f_1)_{5\text{cav}} = 25\,\text{MHz}$. Now, to evaluate how relevant this is we can compare it with a couple of experimental parameters, in particular the Q value of the structure and the data acquisition system bandwidth.

The quality factor for the first resonance, as found on simulations, is $Q = 42711$. Which is roughly in the same scale as the quality factor for the 5 cavities structure ($Q = 40386$). This Q factor can be understood as the ratio between the resonant frequency and the value at which the extracted power drops significantly (a factor of $1/e$ equivalent to $\approx 37\%$ loss in energy). With that value for the quality factor, and the frequency of the resonant mode under consideration we can estimate the sensitive band to be

$$Q = \frac{\omega_r}{\Delta\omega} \rightarrow (\Delta\omega)_Q = \frac{8.187\,\text{GHz}}{42711} = 0.2\,\text{MHz} \tag{8.1}$$

this range broadly covers the lineshape of an axion signal in that range of masses, which would spread in around 10 kHz. This value of $(\Delta\omega)_Q$ is also 15 times lower than the distance between f_{ax} and its first neighbor, which leads us to conclude that the field pattern will not be influenced by the neighboring mode. This result is a more quantitative way of expressing the comment about the Q factor and mode overlap in the previous couple of paragraphs. In fact, a really bad case of mode overlap would in general be perceived as dramatically reducing the quality factor due to the smoothing of the ripples on the cavity response, which is not the case here.

With the previous argument one could think that the problem is solved and there is nothing to worry about. But, there is a subtle issue that can avoid detection at first sight that has to do with the data acquisition system and the analysis procedure.

As mentioned in the previous section where we described the CAST-RADES setup, our data acquisition system consists of two stages giving us a measuring band of 12 MHz. When performing the analysis to search for a signal in our data, we take sets of integrated spectra for the full acquisition band and we try to fit them to a combination of Gaussian noise convoluted with a Lorentzian function, which is given by the fundamental mode, and centered on f_1. If we have another resonant mode in that 12 MHz region, this white noise estimation for the full band becomes significantly more complicated, since we cannot provide an analytical fit to the structure behavior. In the case of having several modes inside the measuring band we have to fit the different resonances independently and try to construct a proper model for how the background behaves with that amount of modes present. One can always restrict the band under consideration for the analysis just to be centered around the fundamental mode and therefore not influenced by the neighboring modes, this solution would be ideal in the case of a flat response of the system, which is not what we have in our system. For properly characterizing how our DAQ behaves and remove the background we need to widen the analysis band as much as possible. Therefore we have to choose between a more complicated fit that combines several modes or narrowing our window, thus preventing us from using out of resonance data when studying the noise of the system. In our case we focused on keeping an analysis window as big as possible, while not including neighboring modes in our model. Further studies of more complex spectral responses have been envisioned in our group for the future.

8.2.2. Geometric factor stability

After fixing the dimensions of the prototype two mechanical workshops were contacted for manufacturing the structure. They gave us the specifications for the manufacturing process and the precision they could achieve on the cavity dimensions, for a stainless steel based prototype, which we would later copper coat in order to increase the quality factor.

Based on the precision given by the workshops we performed a tolerances study to survey how the figure of merit could be affected by this deviations from the ideal case simulated. The procedure for these studies being as follows: we consider the ideal case and vary every dimension of the structure adding a random number extracted from a normal distribution with a standard deviation σ_{err} corresponding to the error provided by the manufacturers. We run the simulation on CST that gives us the values of the resonant frequency, the geometric factor and the quality factor, f, $\mathcal{G}$ and Q respectively, and we study how they are distributed.

Another relevant study would be associated to correlated effects, for example, deviations from perfect parallel alignment within the two halves of the structure. For multi cavity structures with all inductive irises misalignment has been studied in the RADES group both in simulations and experimentally when researching tunable haloscopes [248], in extreme cases it has shown to be the main reason for deteriorating both the quality and form factor of the structure. However, the deviations from the ideal case that can arise from two halves slightly misaligned, e.g. different screw lengths on different halves introduce around 5% to 8% uncertainty in form factor, and around 1% in quality factor. When considering structures with sizes as the ones described here, $\sim 10\,\text{cm}$ long, and the machining tolerances offered by the CERN workshop the contribution of the manufacturing process to deviations from the parallel case is negligible when compared with the ones coming from the assembly process discussed previously. As we will see later, for structures where not all irises are inductive this effect can be larger, and therefore a more detailed study would be in order.

For the particular case of the 19 cavities prototype, we used the best precision the manufacturers offered us, $\sigma_{\text{err}} = 30\,\mu\text{m}$, for having a bound on the best possible scenario. In figure 8.2 one can see the geometric factor of the fundamental mode of this multi cavity structure for the different realizations performed in this tolerances studies. If we compare the geometric factor with the mean value of this simulations we find it drops by a factor of 14%. Let us remark that the value of the ideal case is indeed an upper bound for $\mathcal{G}$, meaning that the optimization procedure has indeed converged to the best case, as expected. The value of the quality factor and the fundamental mode frequency we found them to be more stable and are not added to the discussion for simplicity.

This reduction on $\mathcal{G}$ translates in a direct drop on the figure of merit, which could be regarded as not that much relevant, if it was only of order 10% independently on the amount of cavities, but it is easy to check that the larger the amount of cavities

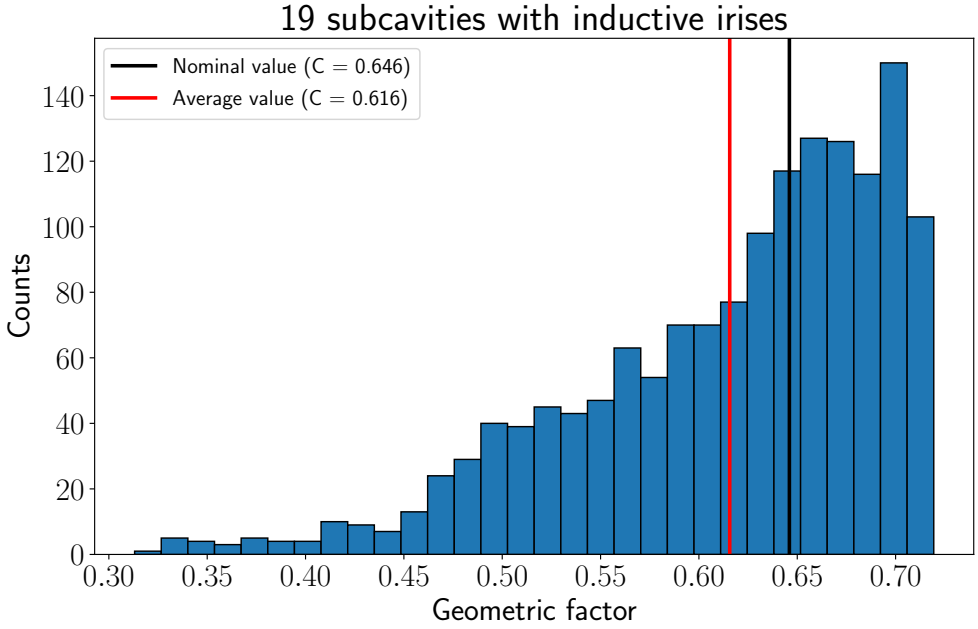

Figure 8.2.: Histogram with the geometric factor of the 19 cavities prototype, resulting from 1500 simulations varying all dimensions of the sub cavities and irises according to a normal distribution with $\sigma = 30\mu$m.

the more pressing this issue becomes. We can, for example, compare with the 5 cavities case assuming the same manufacturing error, see figure 8.3. By increasing from 5 cavities to 19, the deviation from ideal to the mean value of $\mathcal{G}$ has increased drastically, i.e. from 0.4% we go up to 14%. . As we discussed in chapter 3, decreasing the geometric factor impacts directly in the sensitivity of our search, since the power extracted from axion-photon conversion is proportional to $\mathcal{G}$.

Even though a structure as the one studied in this section could still perform a proper axion search, under the conditions exposed so far. One of our main goals was to have a procedure for obtaining prototypes that can easily go to higher frequencies, and in light of these results we found it troubling to continue growing in volume by adding cavities with the same irises as we had originally envisioned.

8.3. Alternated irises cavities

The content of this section follows mainly the developments shown in [249] for a cavity haloscope with alternated irises.

After we found about the mode overlap and the instability of the geometric factor showed by the prototypes discussed on the previous section, we decided to address it without completely changing our multi cavities approach to axion haloscopes. Let us go back to our formalism to see where this problem is coming from and how can we

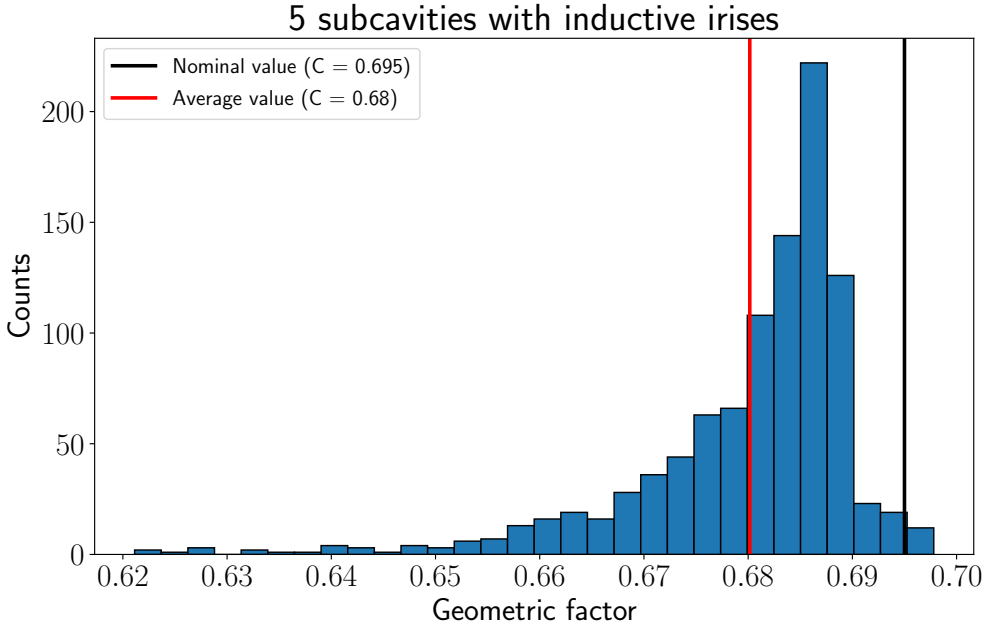

Figure 8.3.: Histogram with the geometric factor of the 5 cavities prototype, resulting from 1000 simulations varying all dimensions of the sub cavities and irises according to a normal distribution with $\sigma = 30\mu$m.

obtain properly scalable prototypes without compromising sensitivity or stability.

In section 3.3.3 we introduced our formalism for multi cavity haloscopes. One of the main ingredients of this approach is the coupling matrix for the different sub cavities, expression (3.68). As we showed, if we assume a 1 dimensional prototype, where cavities are connected sequentially, with a coupling coefficient $K_{ij} = K < 0$. This matrix can be easily diagonalized, and the resulting eigenstates interpreted as modes where all the cavities resonate coherently. The eigenvalue corresponds to the frequency at which this mode resonates and the eigenvector gives the de-phasing of the field between cavities.

In the particular case mentioned above, the eigenstate with the lowest frequency, ω_1, would couple maximally to the electric field originated from axion-photon conversion. The rest of the modes, being orthogonal, would not couple at all or couple somehow marginally. In this context, it is of particular interest then to look at the spacing between the first and second modes in frequency, ω_1 and ω_2, respectively. From equation (3.71), we can extract

$$\omega_2 - \omega_1 \sim K \left(\cos\left(\frac{2\pi}{N+1}\right) - \cos\left(\frac{\pi}{N+1}\right) \right) \tag{8.2}$$

In order to keep the notation simple we will assume the case where the number of cavities N is even, all of the results we will find can be generalized for the case where N is odd [249], however there is not a conceptual difference between both cases.

In general we are interested on producing structures with the largest value of N possible in order to increase the detection volume maximally. But it is easy to see that in this configuration, the limit for large N means that the first and the second mode frequencies will approach each other at a rate

$$\omega_2 - \omega_1 \propto K \frac{1}{(N+1)^2} \tag{8.3}$$

this means that moving from the original 5 cavities RADES prototype unto the 19 cavities one will reduce the spacing between ω_1 and ω_2 a factor of 0.1 already. For even longer cavities this would make the multi cavity approach almost useless.

To bypass this problem, some observation of the spacing between ω_i and ω_{i+1} for the different modes can already give a possible solution. In particular, if one redoes the previous study but for the central modes ($N/2$ and $N/2+1$) the following behavior can be found for large N

$$\omega_{\frac{N}{2}+1} - \omega_{\frac{N}{2}} \propto K \frac{1}{(N+1)} \tag{8.4}$$

which now only decreases linearly with N and not quadratically.

The main question now is: is there a way to build a prototype for which the axion couples maximally not to the minimum frequency but to the central one? The answer is yes, in fact there could be several ways to couple to this central mode by judiciously tuning the different couplings, we will discuss now the simplest one.

Let us consider a multi cavity system as the one in section 3.3.3 and, for simplicity, assume a structure with an even number of cavities and when referring to the central mode we will be discussing the mode $N/2+1$, since this will be the case for the prototypes discussed later[1]. We start by considering the original tridiagonal matrix of the system, once diagonalized its eigenvalues and eigenvectors are found to be

$$\lambda_i = 1 + 2k\cos(\beta_i) \quad , \quad \beta_i = \frac{\pi i}{N+1} \tag{8.5}$$

$$(e_i)_q = \frac{\sin(q\beta_i)}{\sqrt{(N+1)/2}} \tag{8.6}$$

where the q index numbers the different cavities. Given this set of vectors, if one implements a transformation in the form $\tilde{\mathbf{e}}_i = P\mathbf{e}_i$, it is trivial to see that $\tilde{\mathbf{e}}_i$ has to be an eigenvector of the transformed matrix $\mathbb{M} = P\mathbb{M}_{\text{ind}}P^{-1}$. We can translate our problem now into finding a transformation P such that $P\mathbf{e}_{\frac{N}{2}+1} = \mathbf{e}_1$.

Checking the behaviour of $\mathbf{e}_{\frac{N}{2}+1}$ one can see that it changes sign every two cavities, now we can easily choose P to be a diagonal matrix with signs alternating in a way

[1]The N-odd structure is a bit more tricky and does not add much to the discussion here, the interested reader can find the differences in our paper [249]

that the product $P\mathbf{e}_{\frac{N}{2}+1}$ gives a vector with all the cavity modes oriented in the same direction.

$$P = \text{diag}\left\{1, -1 - 1, 1, 1, -1, -1, ...\right\} \tag{8.7}$$

Using this transformation now we can write the new coupling matrix as

$$\mathbb{M} = P\mathbb{M}_{\text{ind}}P^{-1} = \begin{pmatrix} \tilde{\Omega}^2 - K & K & 0 & ... & 0 & 0 & 0 \\ K & \tilde{\Omega}^2 & -K & ... & 0 & 0 & 0 \\ 0 & -K & \tilde{\Omega}^2 & ... & 0 & 0 & 0 \\ 0 & 0 & K & ... & 0 & 0 & 0 \\ \vdots & \vdots & \vdots & \ddots & \vdots & \vdots & \vdots \\ 0 & 0 & 0 & ... & K & 0 & 0 \\ 0 & 0 & 0 & ... & \tilde{\Omega}^2 & -K & 0 \\ 0 & 0 & 0 & ... & -K & \tilde{\Omega}^2 & K \\ 0 & 0 & 0 & ... & 0 & K & \tilde{\Omega}^2 - K \end{pmatrix} \tag{8.8}$$

By construction, this matrix has the same eigenvalues as $\mathbb{M}_{ind}$ while the original eigenvectors, $\mathbf{e}_i$ are transformed under P into the new ones $\tilde{\mathbf{e}}_i$, adopting the following general expression

$$(\tilde{e}_i) = (-1)^{s(q)} \frac{\sin(q\beta_i)}{\sqrt{(N+1)/2}} \quad , \quad s(q) = \text{floor}\left(\frac{q}{2}\right). \tag{8.9}$$

There were two important points for exchanging structures with all couplings being negative, inductive, by structures that alternated positive and negative couplings, capacitive and inductive respectively. The first was the spacing in frequencies between the axion coupled mode and its closets neighbors. We have already shown how this new design gives us the coupling to the maximally spaced set of modes inside the frequency band of operation.

The second reason for adopting this new system was the search of a structure for which the sensitivity to mechanical tolerances was minimized, and therefore having a more robust design for increasing in size without compromising the figure of merit of our haloscope. Let us show briefly how coupling to the central mode can also help solving this issue.

We will consider Gaussian deviations from the original design parameters, these deviations will happen naturally in the manufacturing process due to imperfections appearing from either the extrusion procedure or the copper coating. Specifically, we vary independently the three dimensions of all the single sub cavities, all the irises and the thickness and length of both coaxial ports. Surface roughness is assumed homogeneous, which is consistent with the uncertainty of the copper coating being between more than one order of magnitude lower than the tolerances of the machining process.

If we allow variations of the resonant frequencies for the different cavities and the couplings, these can be treated as adding $\delta\Omega_q^2$ and δK_{ij}^2 to the diagonal and off-diagonal elements, respectively. We will denote this variations as $\delta\mathbb{M}$ and analyze how the eigenvalues and eigenvectors of the system are modified.

In a first order approximation the eigenvalues, which correspond to the modes frequencies, will change as

$$\delta\lambda_i = (\mathbf{e}_i)^T \delta\mathbb{M}(\mathbf{e}_i) \tag{8.10}$$

if the errors are Gaussian, a linear order correction will have a zero mean value and a variance such as

$$\left\langle (\delta\lambda_i)^2 \right\rangle = \sum_{q=1}^{N} \left\langle (\delta\Omega^2)^2 \right\rangle (e_i)_q^4 + \sum_{q=1}^{N-1} \left\langle \left(\delta K_{q,q+1}\right)^2 \right\rangle (e_i)_q^2 (e_i)_{q+1}^2 \tag{8.11}$$

where we have assumed a one dimensional filter. This result is obviously equivalent for all possible filters with cavities connected sequentially and allows us to compare the fundamental mode of the all inductive irises structure with the central mode for the alternating design

$$\left\langle (\delta\lambda_1)^2 \right\rangle = \frac{3}{2N}\left((\delta\Omega^2)^2 + (2\delta K)^2\right) \tag{8.12}$$

$$\left\langle \left(\delta\lambda_{\frac{N}{2}+1}\right)^2 \right\rangle = \frac{1}{2N}\left((\delta\Omega^2)^2 + (2\delta K)^2\right) \tag{8.13}$$

where the change in the sign of δK between the two expressions does not play a role since δK appears squared in both cases. This means that the central mode frequency is $1/\sqrt{3}$ less sensitive to mechanical tolerances than the first one. This result, added to the fact that the neighbors of the central mode are more spaced, motivates even more its use for avoiding mode mixing and miss identification problems.

Studying the variation now for the eigenvectors can give us an idea of how modes will be distorted, changing the coupling to the axion mode

$$\delta\mathbf{e}_i = \sum_{j\neq i} \frac{(\mathbf{e}_j)^T \delta\mathbb{M}(\mathbf{e}_i)}{\lambda_i - \lambda_j}\mathbf{e}_j = \sum_{j\neq i} \frac{(\mathbf{e}_j)^T \delta\mathbb{M}(\mathbf{e}_i)}{2k(\cos\beta_i - \cos\beta_j)}\mathbf{e}_j \tag{8.14}$$

as in the eigenvalues case, linear order contributions for Gaussian errors will average to zero. The denominator on (8.14) shows clearly how neighboring modes dominate the variance and the perturbative expansion for successive orders. Computing the variance and the quadratic order correction involve cumbersome calculations the exact result of which do not play a relevant role on the analysis. However we can already argue that the effect of other modes, as we increase N will become more and more extreme for the fundamental mode of our structure, since mode spacing decreases following $1/N^2$. While for the central mode this influence will be more moderated, since the spacing to its closets neighbors decreases as $1/N$.

An example of an structure with alternated irises can be seen in figure 8.4, in particular that of a system consisting in 6 cavities of arbitrary dimensions. If one

studies the modes appearing in this structure with a finite element software, such as CST Microwave Studio, is easy to check that for the central mode, $n = 4$, the alignment between the external vertical magnetic field and the electric field of the cavity is parallel for all the cavities, as displayed in figure 8.5.

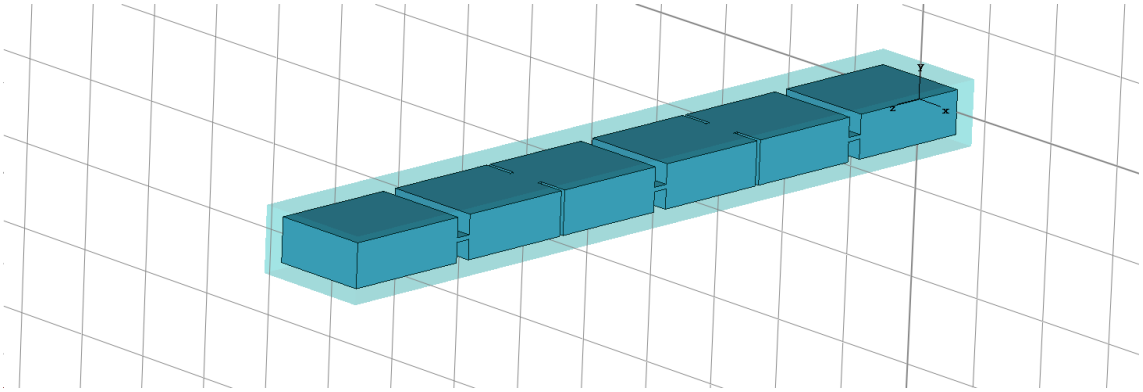

Figure 8.4.: Multi cavity structure designed by alternating inductive and capacitive irises between consecutive cavities.

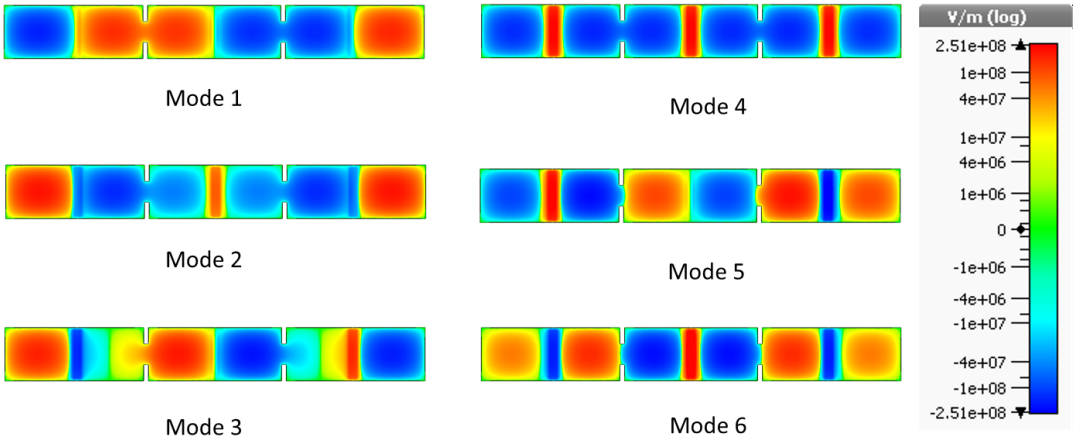

Figure 8.5.: E-field for the resonant modes of a full structure composed by 6 rectangular cavities connected with alternated irises.

8.3.1. 6 cavities prototype manufacture

Before constructing a structure that could compete in volume with the 19 cavities proposed prototype, we decided to test the alternated irises option in a manageable way, by designing and manufacturing a 6 cavities structure. The design dimensions were fixed based on the simulations shown in section 8.3. First, a resonance frequency was chosen which fixed the single cavities dimensions, we chose a value of $f = 8.5$GHz. The main reason for this value was to maintain a prototype with dimensions close to the one we already used before, while at the same time displacing

the search band a bit. After fixing the single cavity dimensions, we adopted a value for the coupling k similar as the one we had for the original RADES prototype, based on its good performance. With the value of k we computed the physical dimensions of the irises, as explained in the last part of 3.3.3. Finally, we run an optimization of F.o.M. $= Q_0 \mathcal{G}^2 V$ in CST Microwave Studio where we allowed the dimensions of cavities and irises to vary. After which the dimensions were fixed to the values displayed in table 8.1. The complete structure can be seen in figure 8.6.

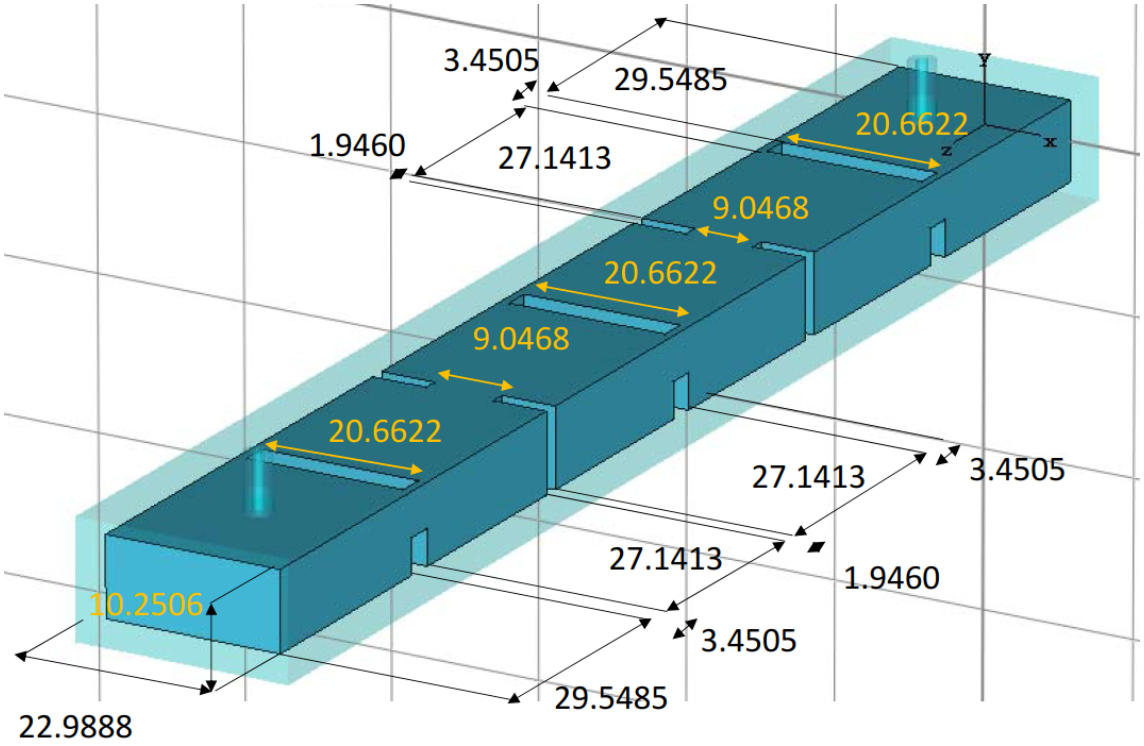

Figure 8.6.: Design of the 6 cavities alternated irises structure manufactured in 2019.

Parameter	Size (mm)
Cavity width (a)	22.860
Cavity height (b)	10.160
Length external cavities (l_{ext})	29.400
Length internal cavities (l_{int})	27.000
Inductive iris width (w)	8.900
Inductive iris thickness (t_{ind})	2.000
Capacitive iris height (h)	1.000
Capacitive iris thickness (t_{cap})	3.500
Capacitive iris gap (g)	1.100

Table 8.1.: Physical dimensions of the 6 cavities alternated irises prototype proposed. The notation follows that of figure 8.7, with l_{ext} making reference to the length of the cavities on the extremes of the array and l_{int} to the length of the rest.

When transitioning from the theoretical design, displayed on figure 8.4 to the

actual prototype to be manufactured, one important change has to be included. The capacitive irises have to be slightly modified and a gap appears between the iris and the cavity wall, see figure 8.7. This is due to constraints on the extrusion procedure performed on the manufacturing process. The influence of this change on the coupling coefficient k was simulated, see figure 8.8. The coupling for the same value of h is systematically lower in the quasi-capacitive case, but as long as we can identify the correlation between h and k that is not a problem

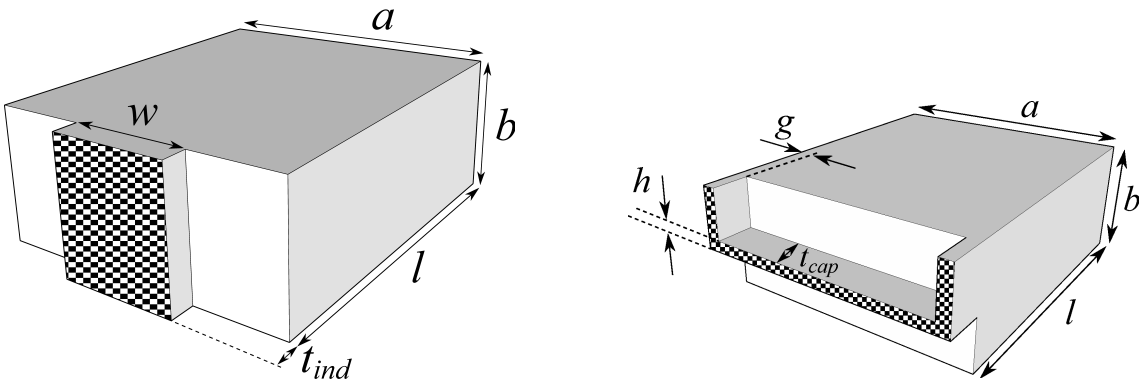

Figure 8.7.: Geometry of the inductive (left) and capacitive (right) irises. The inductive case is similar to the theoretical model discussed in the previous section, while the capacitive has a gap g that makes the coupling deviate a bit from the ideal case, check figure 8.8 for a comparison of the coupling with and without gap. Smooth surfaces represent external conductor while the inner volume and the checked surfaces are vacuum.

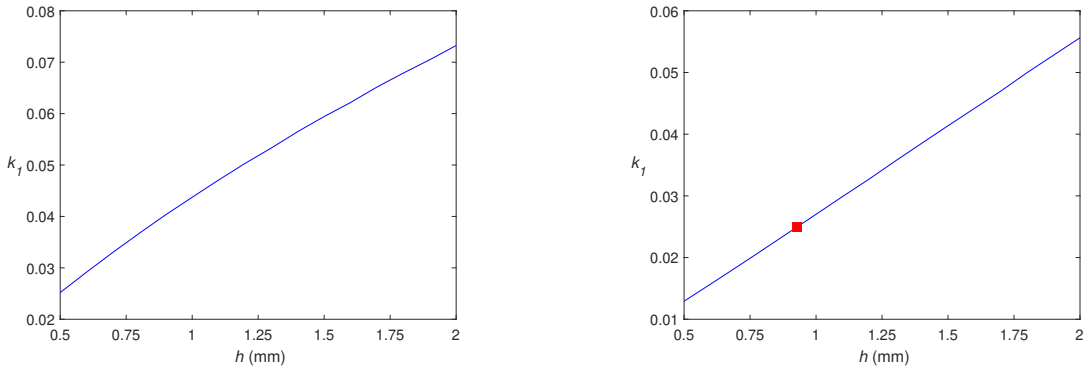

Figure 8.8.: Simulated value of the coupling coefficient k changing the iris width. On the left we can see the behavior of an ideal capacitive iris, while on the right we have the situation of a capacitive iris with a gap of $g = 1.1\,\mathrm{mm}$, in both cases the iris depth is $t_{\mathrm{cap}} = 3.5\,\mathrm{mm}$. The red point on the right plot marks the value of k chosen for the design and its respective h value.

After agreeing on the production of this haloscope we performed a Monte Carlo study of the effect of manufacture tolerances in order to evaluate the effect on the geometric factor, for this we prepared 600 realizations of the structure with the dimensions varying slightly according to a normal distribution with $\sigma = 30\,\mu\mathrm{m}$, the

distribution of values we found for $\mathcal{G}$, plotted in figure 8.9. Results in a more stable that the one found for the a structure with all inductive irises. From this results we conclude that the behavior of this structure is more robust, not dropping more than a 10% form the nominal value in the worst case scenario.

However, some unexpected behavior catches our eye, a different peak with a higher $\mathcal{G}$ value appears outside of the optimized region. We do not have a clear explanation for this behavior, however varying the sizes of the gaps in the sides could induce extra modes. It could be signaling that a more optimized structure can be achieved by allowing the structure not to be periodical. In any case we did not find a systematic correlation between higher $\mathcal{G}$ values and particular geometric configurations. A more detailed study of the theoretical model and the connection between the physical dimensions and the couplings would be in order to clarify this issue.

Even though we did not reach a satisfactory explanation for this behavior it is important to note that this result, in case of being physical, would only contribute to improve the average value of our figure of merit. All in all, the results of this tolerances studies allowed us to show that this structure is more stable than the all inductive one, this can be easily seen when comparing figure 8.9 to figure 8.2.

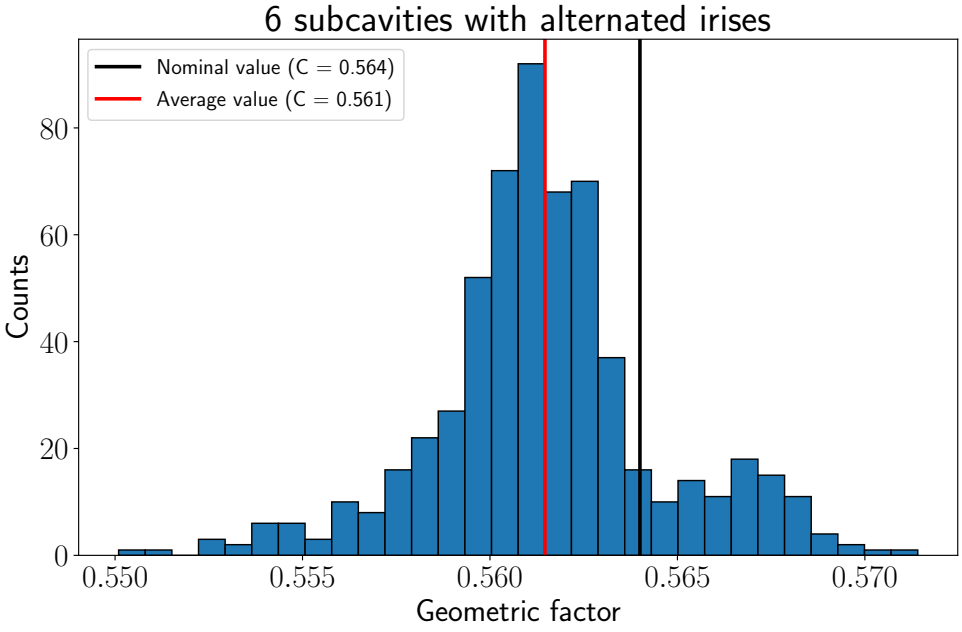

Figure 8.9.: Histogram with the geometric factor resulting from 600 simulations varying all dimensions of the sub cavities and irises according to a normal distribution with $\sigma = 30\,\mu$m.

As the structure used on the 2018 data taking, the cavity was manufactured in stainless steel at the Institute of the Technical University of Valencia. The prototype was also built in two pieces, a lower part with the sub cavities and irises structure and an upper lid to close it, see figure 8.10. Later a 30 µm copper coating was applied at CERN in order to improve the quality factor of the prototype. After completing this

stages the prototype was characterized at room temperature and its mode structure was found to have the predicted topology, in figure 8.11 we show how the electrical response of the cavity. However, a consistent deviation toward lower frequencies was found for the first four resonant modes with respect to simulations, this behavior has not been understood yet. It could arise from the mode perturbation introduced by the gap modifying the capacitive irises.

The experimental value found for the resonant frequency of the fourth mode, the one that couples to the axion field maximally, was $(f_{\mathrm{ax}})_{\mathrm{exp}} = 8.462\,\mathrm{GHz}$ which showed a relative deviation of 0.2% from the theory prediction $(f_{\mathrm{ax}})_{\mathrm{theo}} = 8.483\,\mathrm{GHz}$, which is in agreement with the 1% deviations expected from mechanical tolerances.

The port coupling was later studied by setting a given inner conductor and outer dielectric length according to simulations, these dimensions were varied until attaining critical coupling at room temperature. We followed the usual way for ensuring critical coupling in RF engineering applications, which relies on measuring the S_{11} parameter of the system and checking that the circle representing the resonance of interest in the Smith Chart passes through the center [250].

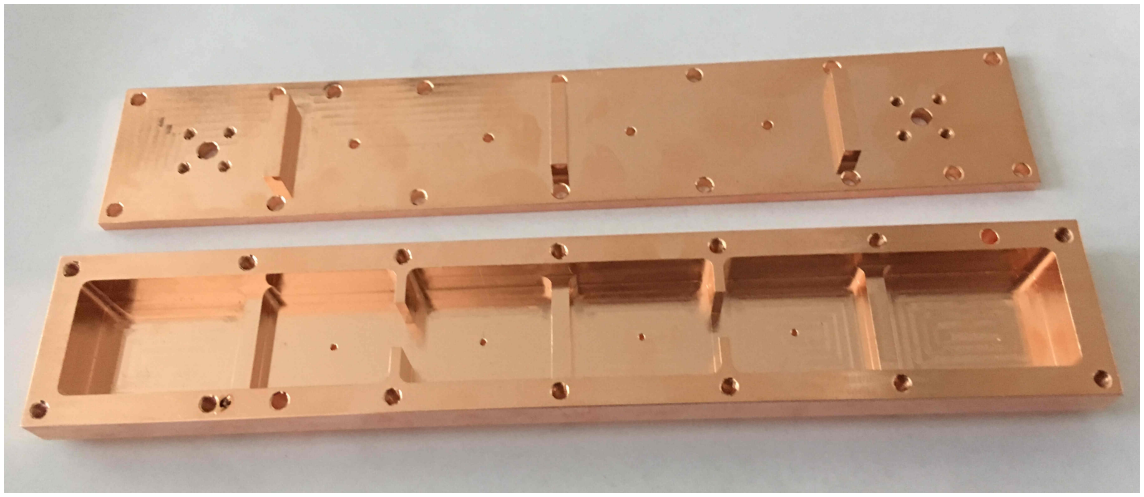

Figure 8.10.: Photo of the opened copper-coated 6-cavities alternating prototype. The top-plate has the upper halves of the capacitive irises, while the lower piece has the sub cavities and the rest of the irises structure. The big holes at the outermost edges of the are used for the placement of the RF antennas, and the small holes in the sub cavities are venting holes for evacuating the air inside of the resonator.

The resonator was introduced in one of the cryostats at the CERN cryolab and characterized at 2 K, see figure 8.12. The cooldown was monitored which allowed observing the two first modes overlapping and identifying the mode coupling to the axion as the third peak in the spectra, $f_{\mathrm{ax}} = 8.412\,\mathrm{GHz}$. This deformation and the extra attenuation, when compared to 8.11, can be explained mostly because critical coupling ($\beta = 1$) for the first port could not be achieved, only a value of $\beta = 0.44$, much under-coupled. On top this, extra RF lines which could not be calibrated were present in comparison to the setup used in room temperature. The main problem

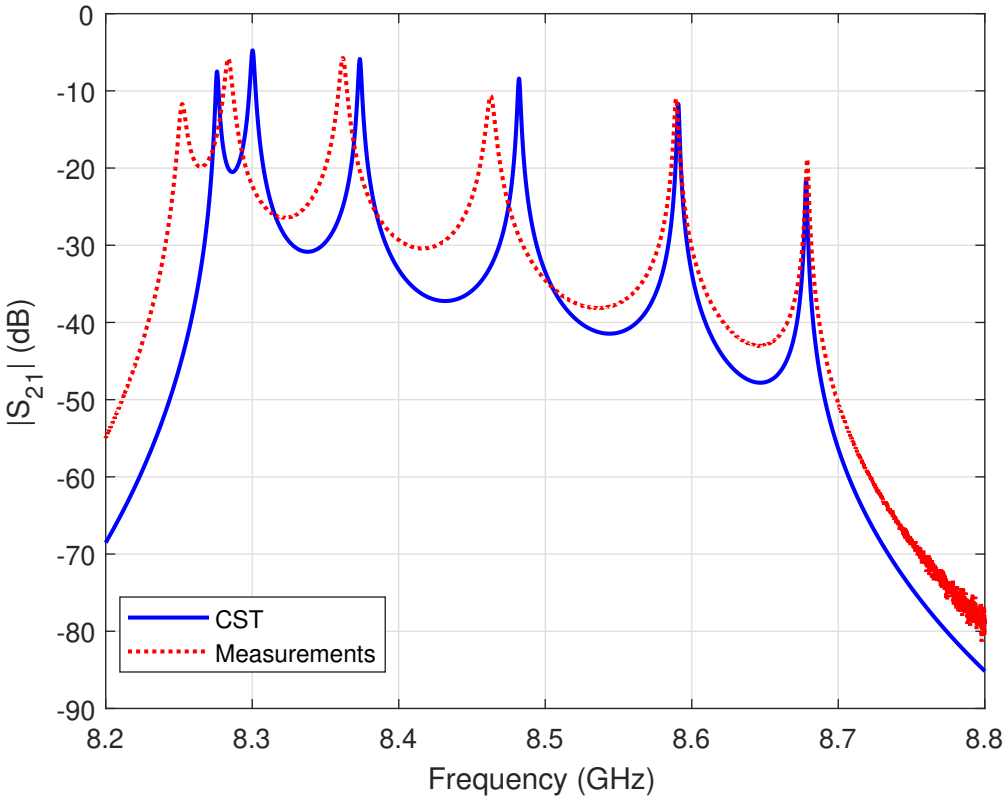

Figure 8.11.: Comparison between the simulated S_{21} scattering parameter of the alternated irises prototype and the value measured for the manufactured structure, at room temperature.

encountered, however, was a severe decrease in the value for the unloaded quality factor. From a value predicted on simulations of $(Q_0)_{\text{theo}} = 6000$ to a measured value of $(Q_0)_{\text{exp}} = 1252$.

After discovering this discrepancy several tests performed with the 6 cavities structure finding that the lid of the multiple cell structure was twisted and the presence of a slope between the outer and inner parts of the resonator. The CERN workshop helped in the untwisting of the lid to improve the electrical contact, which improved the Q_0 value up to 1600, still far from the desired value, but showing that the twisted cover lid had a big contribution for reducing the quality factor of the structure. A gap between the lid and the cavity was also found and 36 new screw holes were added to the original 14 in order to improve electrical contact, in figure 8.13 we show how the performance changed, even though the coupling for the fourth mode was reduced, the unloaded quality factor improved up to a value of $(Q_0)_{\text{exp}} = 2640$, still below the expected value, $(Q_0)_{\text{theo}} = 6000$.

The aperture between the lid and the cavities was simulated in CST but the results were not conclusive. It is important to note that in this kind of simulations the precision is crucial for properly capturing the radiative behavior of the gap.

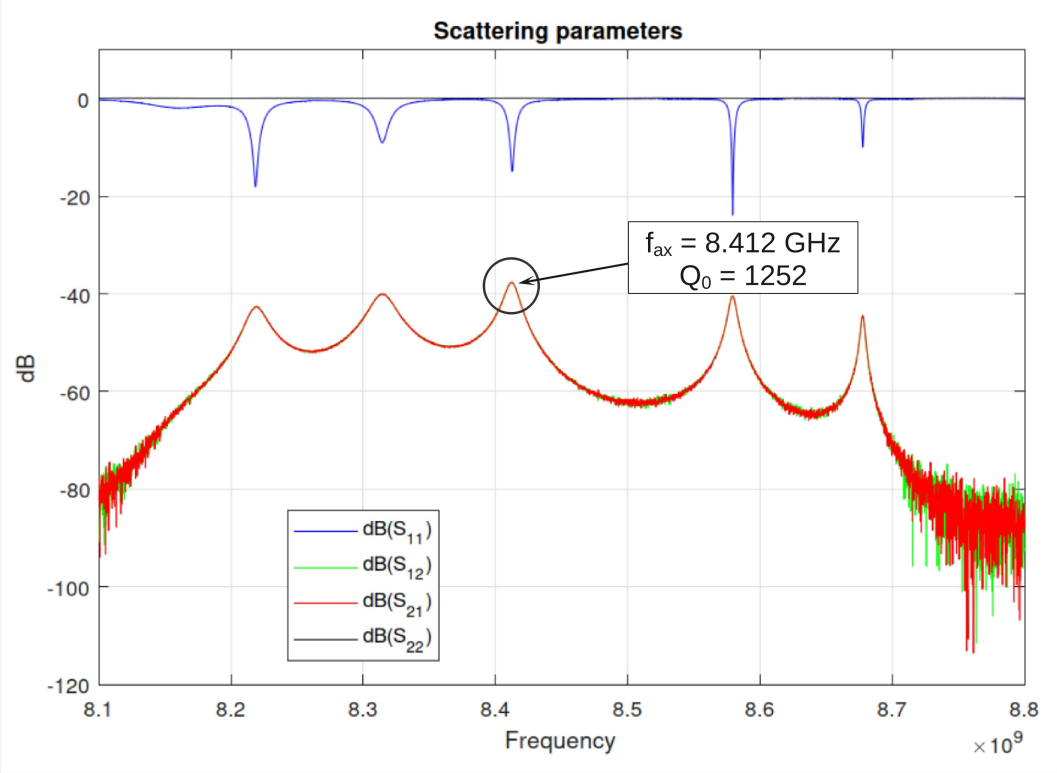

Figure 8.12.: Scattering parameters of the alternated irises prototype measured at cryogenic temperature (2 K).

While it was not possible to find quantitative results with the desired accuracy, a clear influence of micro metric air gaps in specific areas, specially around the irises.

The simplest explanation for this effect can be given in terms of surface currents. As argued in section 3.3.3 when discussing the modes of a multi cavity structure, for the six coherent modes shown in 8.11 the electric field inside of the sub cavities is oriented along the vertical axis and oscillates on time. The difference between those modes are relative phases for the oscillations among different sub cavities. All of those modes, because of the vertical alignment of the E-field, have surface currents over the top and bottom surfaces of each sub cavity and, therefore, this horizontal cut that separates the lid from the bottom half disrupts these currents. Resulting on loses, mostly as electromagnetic radiation along the air gap separating both halves.

In one final test, the upper lid was soldiered onto the lower half using a tin alloy layer [251]. After this step the quality factor almost doubled to a final value of $(Q_0)_{\text{sold}} = 4500$, a 75% of the theoretical value expected from simulations, and a 375% enhancement of the initial value. There is however a 25% loss with respect to the theoretical value for this structure which could be do to other effects, specially deformation of the ideal modes introduced by the gap around the capacitive irises, the effect of which is difficult to mesh properly in simulations. More simulations, outside of the scope of this thesis, are under development for studying this deviations

and finding a way to improve the system performance in future designs.

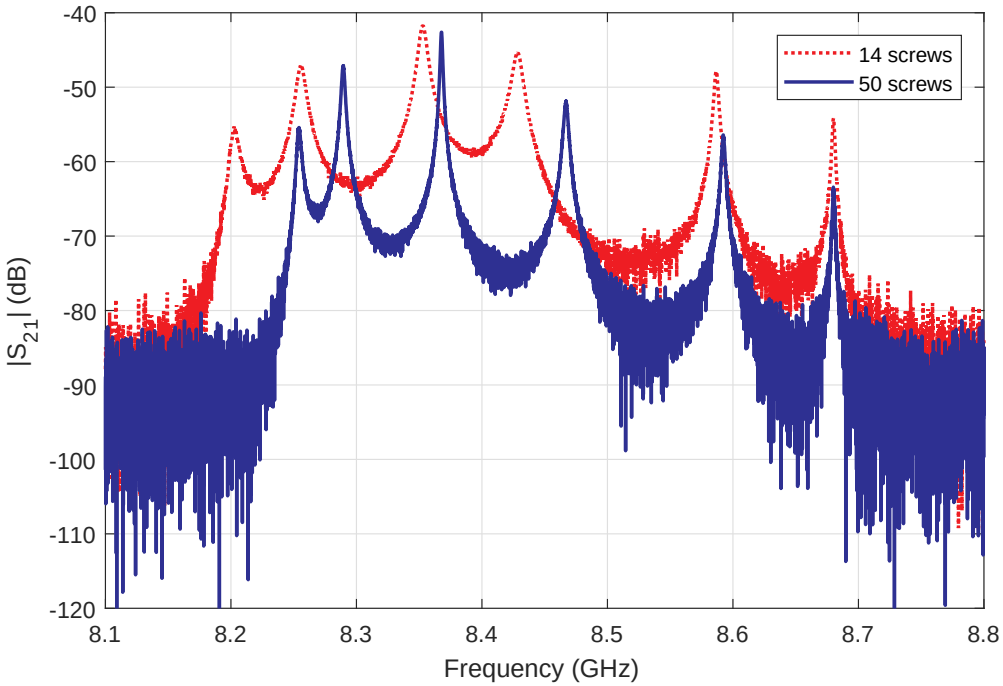

Figure 8.13.: Comparison of the S_{21} scattering parameter for the original prototype with 14 screws on the upper lid and the value measured after adding 36 extra screws for improving electrical contact.

8.3.2. 30 cavities prototype manufacture

We designed and manufactured a 30 sub cavities prototype to be installed inside the CAST magnet for the 2019 data taking campaign. The choice of installing the structure with an array of 30 cavities and not 6 was made because this increase in volume would allow us to go deeper in sensitivity. Gaining a factor of 6 in the sensitivity for $g_{a\gamma}$, in comparison to the 2018 prototype, and allowing us to reach the upper area of the QCD band in a data taking campaign similar as the previous one we had performed at CAST (figure 8.14). However, this decision was taken before we were aware of the misbehavior of the prototype described in the previous section.

For a 30 cavities structure with alternated irises, from our theoretical model we extract that the axion should couple to the central mode, the 16th. This, as in the previous case, can be easily seen to be compatible with simulations performed with a finite element software, see figure 8.15.

The dimensions of the sub cavities where chosen to fix the prototype to be sensitive for an axion mass, $m_a = 34.74\,\mu\text{eV}$, similar to the case of the 6 cavities prototype and the same value for the coupling k was also chosen. This, as argued before, fixed

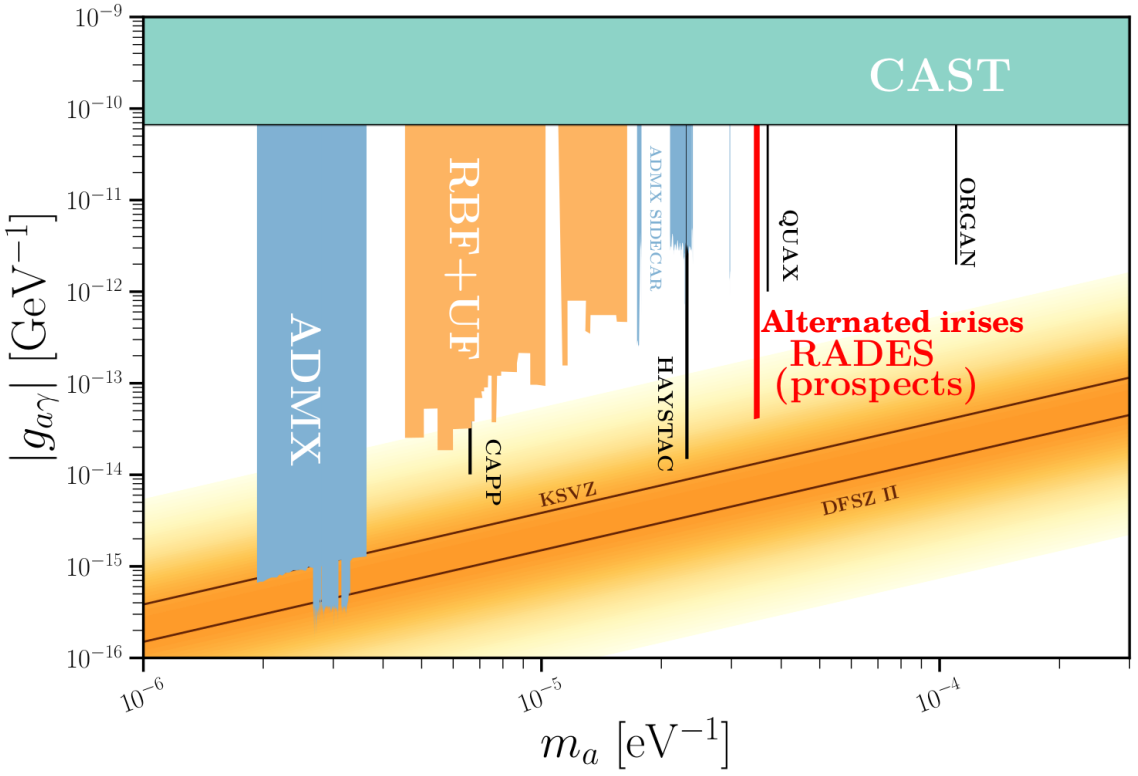

Figure 8.14.: Parameter space for axion-photon coupling vs axion mass. The sensitivity prospects of a 30 cavities prototype with alternated irises are plotted in red, assuming an integration time of 6 months. Current experimental limits set by haloscopes and the CAST experiment are also displayed. The orange region marks the QCD axion band.

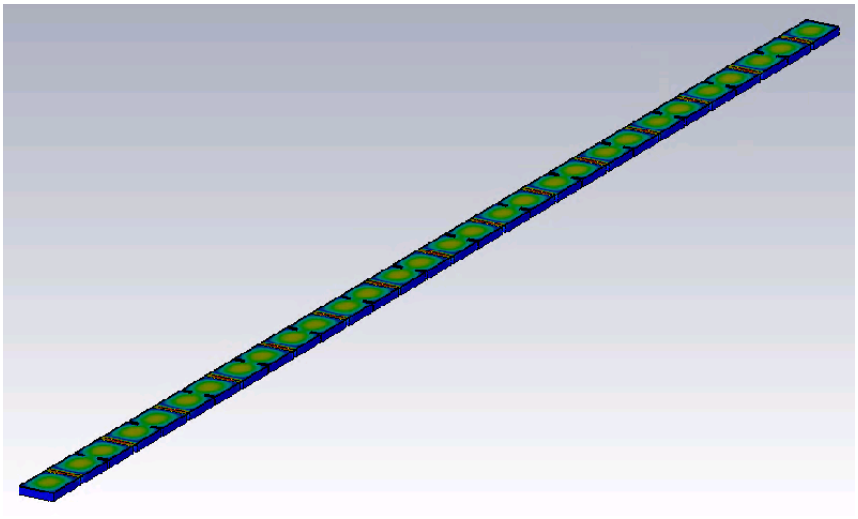

Figure 8.15.: Vertical component of the E-field for the 16th mode of a 30 cavities structure with alternated irises, the homogeneous color gradient along the different sub cavities signals the coherent alignment of the field. The eigenmodes simulations were performed in CST Microwave Studio.

all physical dimensions of the cavities, aside from the irises depth. The result was a structure with dimensions similar to those compiled in table 8.1. Following the same approach taken on the previous prototype, once the structure dimensions were chosen an optimization procedure in CST Microwave Studio with the maximization of the figure of merit, i.e. $\mathcal{G}^2QV$ as the goal function. In this optimization all dimensions were allowed to change, while keeping the proportions fixed for equivalent cavities and irises in order to maintain the periodic arrangement of the structure. The final design dimensions are shown on figure 8.16a.

The cavity was built in stainless steel and a 30μm copper coating was applied, in figure 8.16b we show the final result of the manufacturing process. When the structure was received we assembled the upper lid on top of the cavities and added two coaxial ports, one on top of each of the cavities at the extremes. One of the probes we aimed to have it critically coupled, to maximize the signal output. While the other, the test port, we left it under coupled to minimize the thermal noise introduced in the cavity. After the ports were installed we characterized the cavity at room temperature and found the peak structure to be in accordance with simulations. But the quality factor of the relevant mode, the 16th, at room temperature was measured to be 5 times lower than expected. We obtained an experimental value $Q_{\text{exp}} = 1200$ when, from simulation, we expected a result $Q_{\text{theo}} \approx 6000$.

Next we proceeded with a characterization of the cooling from 300 K down to 5 K, and we saw how the frequency of the 16th mode, was displaced 28MHz higher, due to the contraction of the cavities. Aside from the change in frequency, the coupling factor β and the quality factor both increased during cool down, see figure 8.17. The coupling behavior was simulated at room temperature and at 5 K to account for changes and allow us to be critically coupled at cryogenic temperature, the ideal case would have meant reaching a value of $\beta = 1$. A slightly under coupled value of $\beta = 0.75$ was reached which, even though not ideal, was satisfying. The quality factor, already problematic at room temperature, only increased its value from 1200 to around 2000 when cooling down to 5 K, way below the expected value from simulations of $Q_0 \approx 40000$.

Another important problem derived from the low quality factor for the different modes of the cavity was that the central mode, see figure **??**, was not easy to select any more, as opposed to previous prototypes. Meaning that we could not be sure if the mode we were labeling as the axion mode would indeed be the central one or another, an exhaustive study of the mode identification, the performance and possible ideas for improvement of the 30 sub cavities structure was one of the main parts of the PhD work developed by Dr. Jose María García Barceló [251].

The data taking in 2019 at CAST with this prototype was very complicated, both because of the difficulty of recognizing the mode the antenna was coupled to and because of a drastic reduction of the quality factor that made the sensitivity significantly lower. In [251] a long work was also dedicated to understand and try to analyze the data taken, however in the end the results were inconsistent and we judged them unfit to be published.

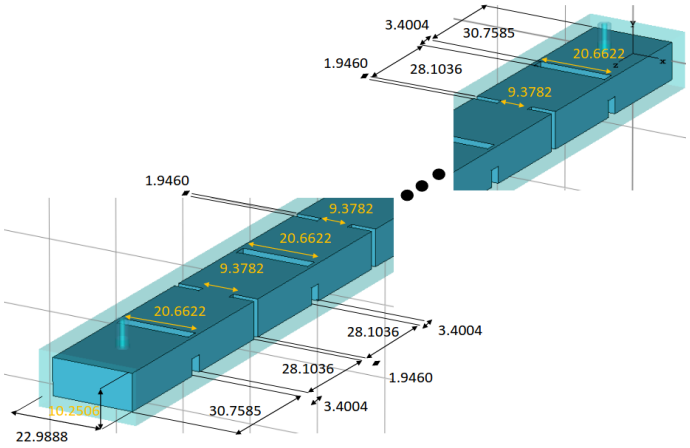

(a) Technical design of the prototype. The central part of the structure has been omitted for keeping the image scale proportioned.

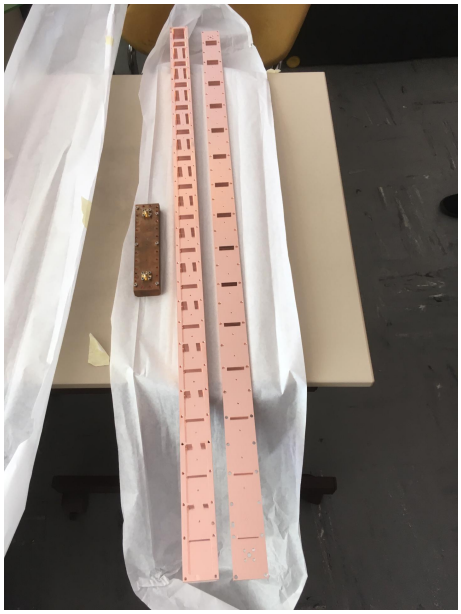

(b) 30 cavities alternated irises structure (right), side-by-side with the original 6 cavities all inductive irises prototype (left) for scale.

Figure 8.16.: 30 cavities alternated irises structure elaborated at Universidad Politécnica de Cartagena by the Electromagnetism and Matter Group, part of the RADES Collaboration.

For the future it was decided to test a new version of the 2018 structure with a vertical cut instead of a horizontal lid, to avoid the low value of the quality factor attributed to cutting the currents at the top-plate discontinuity. However, the discontinuation of the CAST experiment prevented us from having another data taking run.

Another conclusion reached after this results was to approach the construction of bigger cavities modularly, in this sense the cavities would be build independently and then assembled as an array. This way we would be able to avoid compromising

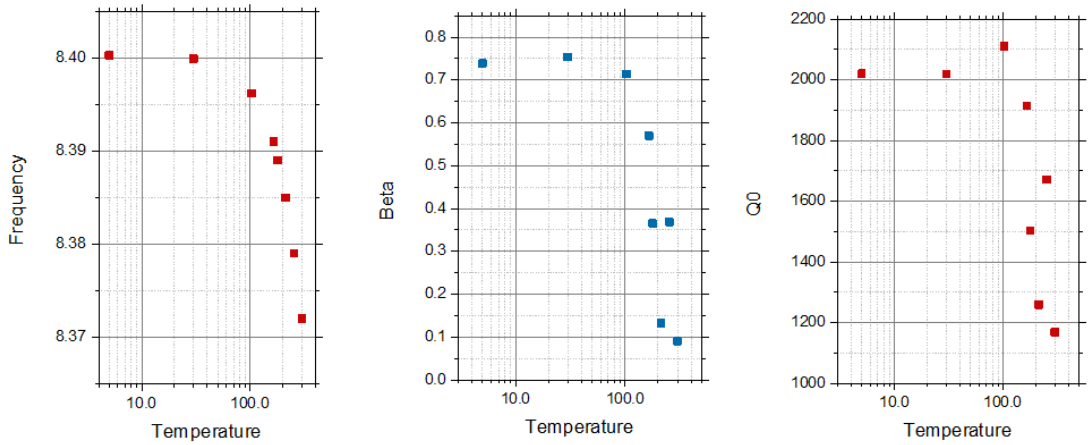

Figure 8.17.: From left to right, evolution of the 16th mode frequency, coupling parameter β and Q_0 when cooling the system from room temperature (300 K down to 5 K.

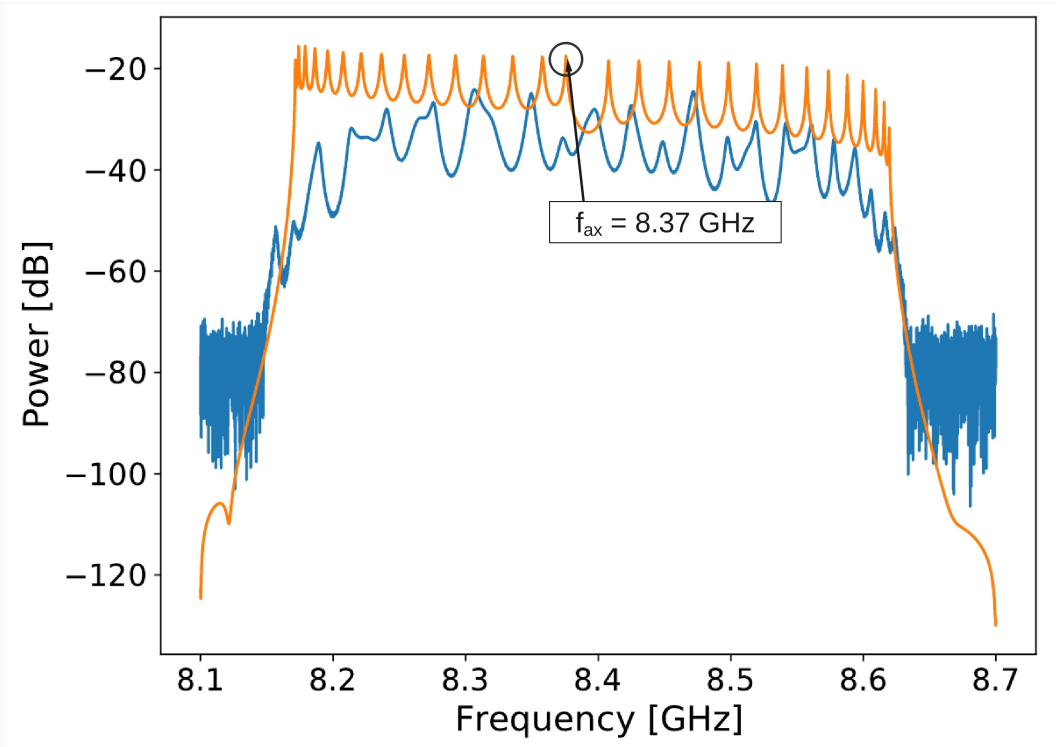

Figure 8.18.: Measurement of the transmission coefficient S_{12} of the 30 sub cavities prototype at room temperature (blue) compared with simulations (orange) [251]. Due to Q factor deterioration and mode overlap, the mode that couples to the axion cannot be properly identified in the measured spectra.

the quality factor of the structure by not cutting through the irises. This manufacturing process also allows us to avoid large tolerance errors on longer structures, and deformations associated to the production of such long steel pieces. Further studies about losses on this kind of structures are still ongoing.

9

Summary and outlook

The CP preservation problem of quantum chromodynamics is one of the main puzzles modern physics has yet to be solved in order to achieve full consistency of the Standard Model of particle physics. Another of the biggest open questions in particle physics is that of explaining the nature of dark matter. It is in this context that the axion appears as one of the most compelling candidates to extend the SM, the introduction of such a particle would easily solve both problems while being a minimal extension of the model. The introduction of an extra U(1) symmetry in the Standard Model (Peccei-Quinn symmetry) and its dynamical breaking explains the preservation of CP in strong interactions, and produces the axion as the pseudo-Nambu Goldstone boson associated to it.

Axions can be produced non-thermally in the very early universe via a production mechanism called misalignment mechanism. Furthermore, if the Peccei-Quinn symmetry is broken after inflation, another considerable source of axions would be from the decay of topological defects such as cosmic strings and domain walls. Independently on the production mechanism, these particles would make an excellent cold dark matter candidate for a certain mass range.

The phenomenology of axion-photon coupling is well defined, except for the exact value of the coupling constant. It predicts a conversion mechanism, inverse Primakoff effect, in which axions under the influence of a strong magnetic field convert into photons, and vice versa. This introduces a new source for axions, axions from the core of stars via plasma photons conversion and it provides us with the most relevant method of direct detection. Axion-photon coupling also lays at the very basis of the two main type of experiments for direct detection. First proposed by Pierre Sikivie [94], these experiments rely on the conversion of axions originated in the core of the Sun (helioscopes) or dark matter axions (haloscopes) by using strong magnetic fields in order to generate a measurable signal.

BabyIAXO is currently projected as an intermediate experimental stage that will be hosted at DESY and test the viability of the full IAXO helioscope. However at the same time it will serve as a new generation helioscope, reaching a region of the parameter space never covered before. The BabyIAXO magnet, which will feature two 10 m long, 70 cm diameter bores makes also for a perfect candidate to host haloscope detectors.

It is in the context of future projects under development, such as the BabyIAXO

experiment, where this PhD thesis proposes a series of technical improvements for experiments looking for axions. The work has been structured in three well differentiated blocks, each one of them dealing with the development of experimental techniques for substantially improving the sensitivity of current and future helioscope and haloscope axion searches, therefore let us summarize them independently in order to have a more clear picture of the reach of the work presented.

Background assessment for BabyIAXO electronics:

Micromegas detectors are extensively used in rare event searches as a readout for gas time projection chambers, due to their potential in terms of low background levels, energy and spatial resolution, gain, and operational stability. The specific case under study in this work has been the BabyIAXO experiment, and more specifically the viability of making front-end cards radiopure enough to be operated close to the detector without increasing the background to a level above the minimum background desired. The need for this background assessment raises from one of the design decisions behind BabyIAXO, where the acquisition electronics is planned to be split between a front-end close to the TPC, inside of the lead shielding and back-end outside of the shielding.

Placing the front-end electronics closer to the detector reduces signal degradation and helps reducing the threshold for events. However, radioactive contamination present on the electronic components could affect notably the background of the detector. This background estimation is part of the full background model where all contributions have to be dissected in order to provide competitive resolution for a solar axion search.

All different components present on the electronic front-end cards where screened at Canfranc Underground Laboratory by using extremely sensitive germanium detectors in order to quantify the activities of different isotopes. With this experimental data in hand a series of simulations were performed by using the REST framework to asses the background in the IAXO-D1 prototype. The IAXO-D1, an optimized prototype with a complex system of muon vetoes is planned as the micromegas detector to be installed in the BabyIAXO experiment for its first solar axion data taking campaign. As a side note, the electronic board where the components will be soldiered was only available recently, and therefore its contribution to the background model was not characterized. However, its activity has been already screened and background simulations are ongoing.

The integrated background found for the front-end electronics was found to be $4.89 \times 10^{-9}\,\mathrm{counts\,keV^{-1}\,cm^{-2}s^{-1}}$, which is substantially below the desired background of $\sim 10^{-7}\,\mathrm{counts\,keV^{-1}\,cm^{-2}s^{-1}}$. It is important to remark that this background takes into account the same analysis cuts imposed for environmental events, leaving plenty of space for future improvements in the analysis. Another important point to take into account is that, due to the difficulty for measuring its activity, the contribution of ^{210}Pb to the background was only modeled as part of the ^{226}Ra decay chain. Future measurements are envisioned with the detector AlphaCAMM [240] which would allow to quantify the activity of the ^{210}Pb partial chain to ensure a

consistent background model.

Studies on haloscope implementations in BabyIAXO:

The BabyIAXO experiment will feature one of the biggest magnetised volumes dedicated for axion searches in the next decade, it is only natural to ask about the impact on axion searches it could have, beyond its original purpose, i.e. the search for solar axions. With that idea in my mind we have put forward a possible strategy for the re-purposing of the power of the BabyIAXO magnet as an axion haloscope. By the use of four differently dimensioned 5-meter-long cavities, equipped with a tuning mechanism based on inner turning plates after a total effective exposure of 440 days, a large region of the QCD band below the current ADMX mass range could be explored over the next decade. Specifically in the mass range between 1 and 2 µeV. The QCD band in this mass range is difficult to reach due to the need of big magnetic volumes, usually not available for smaller experiments, it is in this context that taking advantage of the BabyIAXO infrastructure would open the path for a search otherwise unfeasible. The work covered in this thesis comprised the computation of the sensitivity estimates and the coordination and edition of the paper.

One of the novelties in our proposal is that the radio-frequency (RF) cavities suited for BabyIAXO magnetic field topology have to be conceived for a magnetic dipole, contrary to most haloscope experiments where the magnets are solenoidal. With this in mind, studies have been initiated within the RADES project in the past years, to develop suitable resonant structures with a tuning mechanism. In view of future haloscope installations at BabyIAXO, it is planned to take measurements with prototype cavities that scrutinize the concepts presented here. A mid-scale demonstrator has been already designed and manufactured in the Polytechnic University of Cartagena in Spain and its mechanical tunability is being tested currently.

Development of novel multicavity prototypes:

The RADES project started with the development of multicavity microwave resonators for the search of axion dark matter. These structures allow for higher frequency resonators without compromising detection volume. However, mode crowding and field pattern instability can easily become a problems that compromise the sensitivity of such resonators.

Part of the work developed in this thesis deal with the concept and realization of new cavity designs useful in the search for axions above $> 30\,\mu$eV expanding the microwave filter resonator idea. Such filters can be used in dipole magnetic fields for axion searches, as it was already shown in the 2018 data taking performed by the RADES collaboration at CAST. The development of such structures could also play a role for searches in future dipole magnets, such as the one used by the aforementioned BabyIAXO experiment.

In this PhD, as an extension to the multicavities formalism developed for the first RADES prototype, we have theoretically shown that a structure of alternating

capacitive and inductive irises couples to the axion at a higher order resonance, alleviating the problem of mode-mixing of previous designs. This mathematical formalism is a generalization of the original we developed for our first prototype in 2018, which allows us to cover multicavity structures with more general couplings. We implemented a consistent set of analysis tools to connect the effects of mechanical tolerances with perturbations of the eigennmodes of the system under consideration. This novel framework that abstracts the dimensions of filter structures into a handful of parameters, allows the estimation of electromagnetic mode stability without the need of computationally challenging simulations.

We also built and experimentally characterized a prototype that demonstrated the feasibility of these structures in practice, composed of 6 subcavities, slightly increasing the volume of the previous 5 cavities prototype while increasing mode separation by a factor of 4, around the resonance that couples to the axion field. On the other hand, the quality factor suffered a substantial decrease in comparison to the all-inductive irises prototype. Soldiering the two halves together appears to solve this issue, but a more detailed understanding of this Q_0 degradation is needed to advance in the alternated irises technology. The proposed improvements potentially allow to produce much longer cavities for axion search than previously reported prototypes.

In parallel to these studies a $\sim$ 1 m long cavity of this type was manufactured and installed in the CAST magnet for taking physics data in 2019. Unfortunately this longer prototype also showed a severe decrease in the quality factor and some mode mixing appeared, it was not possible to react on time and try soldiering it like the 6 sub cavities prototype, and thus the axion search planned did not produce results worth publishing. The reason for the low sensitivity of the resonator was found to be, similar as to that for the other structure: the manufacturing and assembly process in which the top plate and the lower volume were produced and fixed together. The discontinuity between the upper lid and the body of the resonator had a strong influence in the electromagnetic currents of the structure and therefore severely reduced its performance. There could have been extra effects, like the deformation of the modes induced by the gaps on the sides of the capacitive irises but simulations of those effects were inconclusive. Despite this shortcoming, the RADES collaboration is still working on the idea of alternating irises structures and their tuning mechanisms, since this approach could produce competitive limits in mass windows otherwise difficult to reach.

Outlook:

In the last decade the amount of publications connected to dark matter axion phenomenology and detection has increased to levels never seen before. It is fair to say that one of the main reasons that motivates this strong comeback of axions as dark matter candidates is the relative stagnation of searches for supersymmetry and beyond standard model particles in colliders which are naturally connected to WIMP candidates. However, there is another strong reason for this increase and it is the

growth of a big network of small to mid-size axion searching experiments. Inside of these fruitful collaborations, technical and theoretical developments will allow to reach regions of the axion parameter space that have been not accessible so far.

Haloscope and helioscope experiments share a common set of challenging technologies, specifically: high field magnets, cryogenics infrastructure and advanced signal analysis techniques. Based on experience while working in the CAST experiment, we believe the best approach to solving problems in these areas is by working in a common front. With this in mind, the development of solid collaborations in research institutes with a diverse axion search program feels like the right environment for future experiments to come. One of the most promising centers in this regards is DESY, where currently BabyIAXO is projected to be installed, as it is the MADMAX dielectric haloscope, and where ALPS-II (the main light-shinning-through-the-wall experiment nowadays) is already under operation.

In this thesis work some advances in the background for the BabyIAXO helioscope have been developed, however the full characterization of the background of the detector is still a work under development with advances on active vetoing and discrimination of cosmic background yet to be concluded. The simulation work presented here could also be easily re-implemented for the background assessment of other detectors envisioned for BabyIAXO, such as SDD or TES.

With our proposal for the installation of haloscope detectors in the BabyIAXO we continue the natural evolution of the successful CAST-RADES axion search performed in 2018. However, in this case targeting a low mass region complementary to other searches. In the coming years we should also see the installation of the FLASH experiment [252], a haloscope to be installed in Frascati with the idea of covering low masses.

Important research lines currently under development in the RADES collaboration include the refining of filter structures, as the ones presented in chapter 8, and the possibility of implementing tuning mechanisms on them, with the use of ferroelectric materials or tuning the dielectric of an inner gas via pressure variations.

I believe the next decade will continue to amaze us, axion hunters, with revolutionary experimental approaches, parameter space hints, and/or even an axion discovery!

A

Units and discrete expressions

A.1. Mathematical notation and units.

- For Minkowski metric we adopt the convention $\eta^{\mu\nu} = (1, -1, -1, -1)$.
- For the electromagnetism parts we use the Heaviside-Lorentz system
- Unless said otherwise, e.g. displaying SI units explicitly, all the expressions on this document are given in natural units[1], i.e. $\hbar = c = 1$.

A.2. Discrete expressions

Most of the expressions used in Chapter 3 deal with a discrete volume V occupying a finite grid of points, to which we associate a discrete momentum space. The general volume we take into consideration is a box of size $V = L_x \times L_y \times L_z$, occupying a grid of $N_x \times N_y \times N_z$ points.

A.2.1. Position and momentum vectors

In this space, position vectors for the nodes of the grid are constructed then as

$$\mathbf{r} = \left(n_x \frac{L_x}{N_x}\hat{\mathbf{x}} + n_y \frac{L_y}{N_y}\hat{\mathbf{y}} + n_z \frac{L_z}{N_z}\hat{\mathbf{z}} \right) \ , \ n_i \in [0, N_i] \, . \tag{A.1}$$

The momentum modes of the Fourier space associated to this grid are then infinite but countable

$$\mathbf{p} = \left(n_x \frac{2\pi}{L_x}\hat{\mathbf{x}} + n_y \frac{2\pi}{L_y}\hat{\mathbf{y}} + n_z \frac{2\pi}{L_z}\hat{\mathbf{z}} \right) \ , \ n_i \in 0, \pm 1, \pm 2, ... \tag{A.2}$$

For the particular case of a squared box with equally spaced points in the three spatial directions, these expressions can be easily expressed in terms of $\mathbf{n}_i = \left(n_x, n_y, n_z\right)$ as

$$\mathbf{r} = \frac{L}{N}\mathbf{n}_i \ , \ \mathbf{p} = \frac{2\pi}{L}\mathbf{n}_i \tag{A.3}$$

[1] The reason being obvious: it is what is natural.

where L is the length of each side of the box and N is the amount of points on each direction.

A.2.2. Discrete sums and continuum limit

Instead of integrating over a continuous variable $\mathbf{p}$, we will consider sums over an infinite countable number of modes. And therefore perform the following substitution when adapting most integral expressions for fields to our discrete grid

$$\int \frac{\mathrm{d}^3\mathbf{p}}{(2\pi)^3} \sim \sum_{\mathbf{p}_i} \frac{\mathrm{d}^3\mathbf{p}_i}{(2\pi)^3} = \frac{1}{(2\pi)^3} \sum_{\mathbf{n}_i} \frac{(2\pi)^3}{V} \mathrm{d}^3\mathbf{n}_i = \frac{1}{V} \sum_{\mathbf{n}_i} \tag{A.4}$$

It is also useful to adapt the orthogonality relation to the discrete case, which implies replacing Dirac delta distributions by Kronecker delta functions

$$\delta_{\mathbf{p},\mathbf{q}} = \frac{1}{N^3} \sum_{\mathbf{x}_i} e^{i(\mathbf{p}-\mathbf{q})\cdot\mathbf{x}_i} = \frac{1}{N^3} \sum_{\mathbf{n}_i} e^{\frac{iL}{N}(\mathbf{p}-\mathbf{q})\cdot\mathbf{n}_i} \tag{A.5}$$

B

REST Codes

Here we compile the main codes used on the generation and analysis of the radiopurity simulations performed with REST. This codes act as configuration files for the simulations and are written in GDML. A general description of the REST framework is found on Section 4.2, for a more detailed account the reader is refereed to the review published in 2021 [141] and to the general documentation of the public code repository [158].

B.1. REST Processes

```
<TRestProcessRunner name="restSimAnalysis" title="restSimAnalysis">

  <parameter name="firstEntry"         value="0" >
  <parameter name="lastEntry"          value="0" >
  <parameter name="eventsToProcess"    value="" >
  <parameter name="pureAnalysisOutput" value="OFF" >

<!-- Adding processes -->

<!-- Geant4 Analysis -->
  <addProcess type="TRestGeant4AnalysisProcess" name="g4Ana"
              value="ON" file="G4Processes.rml"/>

<!-- Hits Analysis -->
  <addProcess type="TRestG4toHitsProcess"          name="G4ToHits"
              value="ON" file="G4Processes.rml" >
  <addProcess type="TRestElectronDiffusionProcess" name="IAXOD0_Ar2Iso_1.4bar"
              value="ON" file="G4Processes.rml" >
  <addProcess type="TRestHitsReductionProcess"     name="hitsReduction-IAXOD0"
              value="ON" file="G4Processes.rml" >
  <addProcess type="TRestHitsAnalysisProcess"      name="hitsAna"
              value="ON" file="G4Processes.rml" >

<!-- Tracks Analysis -->
  <addProcess type="TRestHitsToTrackProcess"           name="hitsToTrack"
```

```
              value="ON" file="G4Processes.rml" >
  <addProcess type="TRestTrackReductionProcess"        name="trackReduction-IAXOD0"
              value="OFF" file="G4Processes.rml" >
  <addProcess type="TRestTrackPathMinimizationProcess" name="trackPathMinimization"
              value="OFF" file="G4Processes.rml" >
  <addProcess type="TRestTrackReconnectionProcess"     name="trackReconnection"
              value="OFF" file="G4Processes.rml" >
  <addProcess type="TRestTrackAnalysisProcess"         name="tckAna"
              value="ON" file="G4Processes.rml" >

</TRestProcessRunner>
```

B.2. TRestRun

```
<TRestRun name="Electronics BG Model"
          title="Simulations ${EXP}. Version ${VERSION}.">

  <parameter name="experiment"     value="${EXP}"/>
  <parameter name="runType"        value="simulation"/>
  <parameter name="runNumber"      value="auto"/>
  <parameter name="runTag"         value="${REST_ISO}_${COMP}${POS}"/>
  <parameter name="runDescription" value="${REST_ISO} decays from ${COMP}${POS}."/>
  <parameter name="user"           value="${USER}"/>
  <parameter name="verboseLevel"   value="3"/>
  <parameter name="overwrite"      value="off"/>
  <parameter name="outputFile"
             value="Run_[fRunType]_[fRunTag]_[fRunNumber]_[VERSION].root"/>

</TRestRun>
```

B.3. TRestG4Metadata

```
<TRestG4Metadata name="restG4 Simulation run"
                 title="${REST_ISO} from ${COMP}${POS}">

  <parameter name="geometryPath"      value="${IAXOD0_GEOPATH}/${IAXOD0_GEO}"/>
  <parameter name="gdml_file"         value="IAXOD0_Setup_AGET.gdml"/>
  <parameter name="maxTargetStepSize" value="200" units="um"/>
  <parameter name="subEventTimeDelay" value="100" units="us"/>
  <parameter name="Nevents"           value="$REST_NEVENTS"/>
```

```
  <generator type="volume" from="${REST_VOL}" >

    <source particle="${REST_ISO}" fullChain="on">
      <angularDist type="isotropic" />
      <energyDist  type="mono" energy="0" units="keV" />
    </source>

  </generator>

  <storage sensitiveVolume="gas">

    <parameter name="energyRange" value="(0,5)" units="GeV" />

    <activeVolume name="gas"               chance="1"/>  <!-- Volume 0 -->
    <activeVolume name="vetoFront"         chance="1"/>  <!-- Volume 1 -->
    <activeVolume name="vetoBack"          chance="1"/>  <!-- Volume 2 -->
    <activeVolume name="vetoTop"           chance="1"/>  <!-- Volume 3 -->
    <activeVolume name="vetoBottom"        chance="1"/>  <!-- Volume 4 -->
    <activeVolume name="vetoEast"          chance="1"/>  <!-- Volume 5 -->
    <activeVolume name="vetoWest"          chance="1"/>  <!-- Volume 6 -->
    <activeVolume name="LeadShielding"     chance="1"/>  <!-- Volume 7 -->
    <activeVolume name="mylarCat"          chance="1"/>  <!-- Volume 8 -->
    <activeVolume name="CuCathodePattern"  chance="1"/>  <!-- Volume 9 -->

  </storage>

</TRestG4Metadata>
```

B.4. TRestPhysicsLists

```
<TRestPhysicsLists name="default" title="Physics list implementation."
                   verboseLevel="debug" >

  <parameter name="cutForGamma"    value="10" units="um" />
  <parameter name="cutForElectron" value="1"  units="mm" />
  <parameter name="cutForPositron" value="1"  units="mm" />

  <!-- EM Physics lists -->
  <physicsList name="G4EmLivermorePhysics"> </physicsList>

  <!-- Decay physics lists -->
  <physicsList name="G4DecayPhysics"> </physicsList>
  <physicsList name="G4RadioactiveDecayPhysics"> </physicsList>
  <physicsList name="G4RadioactiveDecay">
```

```
    <option name="ICM" value="true" />
    <option name="ARM" value="false" />
  </physicsList>

  <!-- Hadron physics lists -->
  <physicsList name="G4HadronElasticPhysicsHP"> </physicsList>
  <physicsList name="G4IonBinaryCascadePhysics"> </physicsList>
  <physicsList name="G4HadronPhysicsQGSP_BIC_HP"> </physicsList>
  <physicsList name="G4NeutronTrackingCut"> </physicsList>
  <physicsList name="G4EmExtraPhysics"> </physicsList>

</TRestPhysicsLists>
```

B.5. Globals

```
<globals>

  <variable name="REST_DATAPATH"   value="${HOME}/RPE_IAXO_REST/data"
            overwrite="true"/>
  <variable name="EXP"             value="IAXOD0" overwrite="false"/>
  <variable name="VERSION"         value="2.29"   overwrite="false"/>
  <variable name="IAXOD0_PATH"     value="${HOME}/RPE_IAXO_REST/IAXOD0_AGET-REST"
            overwrite="true"/>
  <variable name="IAXOD0_DATAPATH" value="${REST_DATAPATH}/IAXOD0"
            overwrite="true"/>
  <variable name="IAXOD0_G4PATH"   value="${IAXOD0_PATH}/G4sims"
            overwrite="true"/>
  <variable name="IAXOD0_GEOPATH"  value="${IAXOD0_G4PATH}/geometry"
            overwrite="true"/>
  <variable name="IAXOD0_GEO"      value="Argon_AGET"
            overwrite="true"/>

  <variable name="REST_NEVENTS" value="1000000"   overwrite="true"/>
  <variable name="REST_ISO"     value="U238"      overwrite="true"/>
  <variable name="COMP"         value="Cap"       overwrite="true"/>
  <variable name="POS"          value="TopCentre" overwrite="true"/>
  <variable name="REST_VOL"     value="${COMP}${POS}PhysVolume"
            overwrite="true"/>
  <variable name="DIR_DATA"     value="${REST_ISO}_${COMP}${POS}"
            overwrite="true"/>

  <parameter name="mainDataPath"
```

```
            value="${IAXOD0_DATAPATH}/${IAXOD0_GEO}/${DIR_DATA}"/>
  <parameter name="gasDataPath"  value="${REST_PATH}/data/gasFiles"/>
  <parameter name="verboseLevel" value="warning"/>

</globals>
```

Glossary

ABC Atomic recombination and de-excitation, Bremsstrahlung, and Compton. 41, 42

ADC Analog to Digital Converter. 98

ADMX Axion Dark Matter eXperiment. 33, 61, 93

AGET ASIC for Generic Electronic system for TPCs. 98, 99, 119

ALP Axion Like Particles. 3, 7, 12–15, 17, 22, 24, 41, 59, 61–63, 65, 72

ALPS Any Light Particle Search. 73, 149

BASE Baryon Antibaryon Symmetry Experiment. 81

BEC Back-End Card. 98, 99

BSM Beyond Standard Model. 1, 7, 12, 13

CAPP Center for Axion and Precision Physics research. 60–62

CAST Cern Solar Axion Telescope. v, 37–40, 43, 44, 59–64, 66–68, 70–73, 76, 78, 81, 97, 98, 108, 121, 124, 138–141, 147–149

CCD Charge Coupled Device. 60

CDM Cold Dark Matter. 1, 4, 14, 23–25, 40

CERN Conseil Européen pour la Recherche Nucléaire. 40, 43, 49, 53, 59, 63, 113, 134–136

CMB Cosmic Microwave Background. 5, 6

CP Charge-Parity. v, 3, 4, 6, 8–10, 12, 14, 145

CRESST Cryogenic Rare Event Search with Superconducting Thermometers. 72

CTA Cherenkov Telescope Array. 66

DAQ Data AcQuisition system. 39, 98, 124

DESY Deutsches Elektronen-SYnchrotron. 64, 113, 145, 149

DFSZ Dine-Fischler-Srednicki-Zhitnitsky. 11, 12, 41

DM Dark Matter. vi, 1, 5, 7, 8, 14, 28, 33, 81, 121, 122, 124, 126, 128, 130, 132, 134, 136, 138, 140, 142

EDM electric dipole moment. 23

ESA European Space Agency. 68

EW electro-weak. 7

FEC Fron-End Card. 97, 117

FFT Fast Fourier Transform. 39

FLASH FINUDA magnet for Light Axion SearcH. 149

FPGA Field Programmable Gate Array. 39, 98

FtF Face-to-Face. 99

GDML Geometry Description Markup Language. 53, 54, 153

GR General Relativity. 3

HAYSTAC Haloscope At Yale Sensitive To Axion CDM. 39, 61

HE High Energy. 64, 65

IAXO International Axion Observatory. v, 45, 52, 59, 60, 62–68, 70, 72–74, 76, 78, 81, 97, 107, 108, 114, 116, 119, 145

KSVZ Kim-Shifman-Vainshtein-Zakharov. 11, 12, 62

KWISP Kinetic WISP detection. 61, 62

LHC Large Hadron Collider. 59

LOI Letter of Intent. 63

MADMAX MAgnetized Disk and Mirror Axion eXperiment. 149

MFOM Magnet Figure Of Merit. 66

MLI Multi-Layer Insulation. 82, 83

MM MicroMegas. 51, 52, 59, 97

MMC Metallic Magnetic Calorimeter. 71, 119

MST Medium-Sized Telescope. 66

MWPC Multi-wire proportional chamber. 49, 50

NAF National Analysis Facility. 113

NEXT Neutrino Experiment with a Xenon TPC. 105, 106, 114

NTD Neutron Transmutation doped Detector. 71

ORGAN Oscillating Resonant Group AxioN. 61

OSQAR Optical Search of QED vacuum magnetic birefringence, Axion and photon Regeneration. 73

PCB Printed Circuit Board. 99, 103

PQ Peccei-Quinn. 10, 11

PRC Physics Review Committee. 64

PVLAS Polarizzazione del Vuoto con LASer. 73

QCD Quantum Chromodynamics. v, 3, 9, 10, 12, 13, 23, 24, 26, 33, 41, 63, 72, 73, 138, 139, 147

QFT Quantum Field Theory. 4, 18, 19

QUAX QUaerere AXion. 61

RADES Relic Axion Exploratory Detector Setup. v, 1, 30, 34, 37, 39, 40, 60, 61, 72, 81, 89, 92–96, 121, 122, 124, 125, 128, 132, 141, 147–149

RBF Rochester-Brookhaven-Fermilab. 60, 61

REST Rare Event Searches Toolkit. v, vii, 45, 52–55, 57, 74, 109, 110, 113, 119, 146, 153, 154, 156

RF Radio Frequency. 82, 83, 135

ROOT Rapid Object-Oriented Technology. 45, 53

RRR Residual Resistivity Ratio. 86

SAFEC STAGE Front-End Card. 98–100, 103, 105, 109–111, 116–119

SDD Silicon Drift Detector. 62, 71, 119, 149

SHM Standard Halo Model. 8

SM Standard Model. 3, 4, 7, 8, 10–14, 22, 32, 41

SMASH Standard Model - Axion – Seesaw – Higgs Portal Inflation. 12

SNR Signal to Noise Ratio. 31

SSB Spontaneous Symmetry Breaking. 10, 12

STAGE Second sTep AGEt. vi, 98–101, 103, 109, 111, 115, 117

TCM Trigger and Clock Module. 98

TES Transition Edge Sensor. 72, 149

TPC Time Projection Chamber. 45, 48–51, 59, 77, 98, 146

TREX-DM TPC for Rare Event eXperiments-Dark Matter. 98, 105, 114

UF University of Florida. 61

UV Ultraviolet. 11, 17

WIMP Weakly Interacting Massive Particle. 7, 148

XMM X-ray Multi-Mirror. 68, 69

Bibliography

[1] The ATLAS Collaboration, "Observation of a new particle in the search for the Standard Model Higgs boson with the ATLAS detector at the LHC," *Phys. Lett. B*, vol. 716, pp. 1–29, 2012. 4

[2] H. M. Lee, "Lectures on physics beyond the standard model," *Journal of the Korean Physical Society*, vol. 78, p. 985–1017, May 2021. 4

[3] V. A. Rubakov and D. S. Gorbunov, *Introduction to the Theory of the Early Universe: Hot big bang theory*. Singapore: World Scientific, 2017. 4

[4] The Planck Collaboration, "Planck2018 results: I. overview and the cosmological legacy ofplanck," *Astronomy & Astrophysics*, vol. 641, p. A1, Sept. 2020. 4

[5] The Planck Collaboration, "Planck 2018 results. VI. Cosmological parameters," *Astron. Astrophys.*, vol. 641, p. A6, 2020. [Erratum: Astron.Astrophys. 652, C4 (2021)]. 4, 5, 6, 23

[6] A. Arbey and F. Mahmoudi, "Dark matter and the early universe: A review," *Progress in Particle and Nuclear Physics*, vol. 119, p. 103865, July 2021. 4

[7] S. Cebrián, "Review on dark matter searches," *Journal of Physics: Conference Series*, vol. 2502, May 2023. 4

[8] D. Huterer and D. L. Shafer, "Dark energy two decades after: observables, probes, consistency tests," *Reports on Progress in Physics*, vol. 81, p. 016901, Dec. 2017. 4

[9] P. J. E. Peebles and B. Ratra, "The cosmological constant and dark energy," *Reviews of Modern Physics*, vol. 75, p. 559–606, Apr. 2003. 4

[10] T. Clifton *et al.*, "Modified gravity and cosmology," *Physics Reports*, vol. 513, no. 1, pp. 1–189, 2012. 5

[11] F. Zwicky, "On the Masses of Nebulae and of Clusters of Nebulae," *Astrophysical Journal*, vol. 86, p. 217, Oct. 1937. 5

[12] V. C. Rubin, J. Ford, W. K., and N. Thonnard, "Extended rotation curves of high-luminosity spiral galaxies. IV. Systematic dynamical properties, Sa -> Sc.," *Astrophysical Journal Letters*, vol. 225, pp. L107–L111, Nov. 1978. 5, 6, 8

[13] Y. Sofue and V. Rubin, "Rotation Curves of Spiral Galaxies," *Ann. Rev. Astron. Astrophys.*, vol. 39, pp. 137–174, Jan. 2001. 5

[14] F. Iocco, M. Pato, and G. Bertone, "Evidence for dark matter in the inner

Milky Way," *Nature Phys.*, vol. 11, pp. 245–248, 2015. 5, 8

[15] D. Clowe *et al.*, "A direct empirical proof of the existence of dark matter," *Astrophys. J. Lett.*, vol. 648, pp. L109–L113, 2006. 5

[16] J. A. Tyson, F. Valdes, and R. A. Wenk, "Detection of Systematic Gravitational Lens Galaxy Image Alignments: Mapping Dark Matter in Galaxy Clusters," *Astrophysical Journal Letters*, vol. 349, p. L1, Jan. 1990. 5

[17] A. A. Penzias and R. W. Wilson, "A Measurement of Excess Antenna Temperature at 4080 Mc/s.," *Astrophysical Journal*, vol. 142, pp. 419–421, July 1965. 6

[18] L. A. Kofman, N. Y. Gnedin, and N. A. Bahcall, "Cosmological Constant, COBE Cosmic Microwave Background Anisotropy, and Large-Scale Clustering," *Astrophysical Journal*, vol. 413, p. 1, Aug. 1993. 6

[19] D. Spergel *et al.*, "Wilkinson Microwave Anisotropy Probe (WMAP) three year results: Implications for cosmology.," *Astrophys. J. Suppl.*, vol. 170, no. 377, 2007. 6

[20] L. D. Duffy and K. van Bibber, "Axions as dark matter particles," *New Journal of Physics*, vol. 11, 2009. 7, 11

[21] A. Á. Gonzalo *et al.*, "On the wondrous stability of ALP dark matter," *JCAP*, vol. 2020, p. 052, Mar. 2020. 7

[22] L. Roszkowski, E. M. Sessolo, and S. Trojanowski, "WIMP dark matter candidates and searches—current status and future prospects," *Rept. Prog. Phys.*, vol. 81, no. 6, p. 066201, 2018. 7

[23] The XENON Collaboration, "The XENONnT Dark Matter Experiment," 2024. 7

[24] The CRESST Collaboration, "Light dark matter search using a diamond cryogenic detector," 2023. 7

[25] The COSINUS Collaboration, "Deep-underground dark matter search with a COSINUS detector prototype," 2023. 7

[26] A. E. Nelson and J. Scholtz, "Dark Light, Dark Matter and the Misalignment Mechanism," *Phys. Rev. D*, vol. 84, p. 103501, 2011. 7

[27] P. Villanueva-Domingo, O. Mena, and S. Palomares-Ruiz, "A brief review on primordial black holes as dark matter," *Front. Astron. Space Sci.*, vol. 8, p. 87, 2021. 7

[28] V. Domcke, C. Garcia-Cely, and N. L. Rodd, "Novel search for high-frequency gravitational waves with low-mass axion haloscopes," *Physical Review Letters*, vol. 129, July 2022. 7

[29] A. Berlin *et al.*, "Detecting high-frequency gravitational waves with microwave cavities," *Physical Review D*, vol. 105, June 2022. 7

[30] X. Shi and G. M. Fuller, "New dark matter candidate: Nonthermal sterile neutrinos," *Physical Review Letters*, vol. 82, p. 2832–2835, Apr. 1999. 8

[31] S. Dodelson and L. M. Widrow, "Sterile-neutrinos as dark matter," *Phys. Rev. Lett.*, vol. 72, pp. 17–20, 1994. 8

[32] A. Boyarsky *et al.*, "Sterile neutrino dark matter," *Progress in Particle and Nuclear Physics*, vol. 104, p. 1–45, Jan. 2019. 8

[33] B. Dasgupta and J. Kopp, "Sterile neutrinos," *Physics Reports*, vol. 928, p. 1–63, Sept. 2021. 8

[34] A. Datta, R. Roshan, and A. Sil, "Imprint of the seesaw mechanism on feebly interacting dark matter and the baryon asymmetry," *Physical Review Letters*, vol. 127, Dec. 2021. 8

[35] M. R. Lovell *et al.*, "The spatial distribution of milky way satellites, gaps in streams, and the nature of dark matter," *Monthly Notices of the Royal Astronomical Society*, vol. 507, p. 4826–4839, Aug. 2021. 8

[36] Y. Sofue, "Rotation curve of the milky way and the dark matter density," 2020. 8

[37] E. J. Gonzalez *et al.*, "New catalogue of dark-matter halo properties identified in mice-gc – i. analysis of density profile distributions," 2022. 8

[38] N. G. de Oliveira *et al.*, "Dark matter distribution in milky way-analog galaxies," 2024. 8

[39] A. K. Drukier, K. Freese, and D. N. Spergel, "Detecting cold dark-matter candidates," *Phys. Rev. D*, vol. 33, pp. 3495–3508, Jun 1986. 8

[40] G. R. Knapp, S. D. Tremaine, and J. E. Gunn, "The global properties of the Galaxy. I. The H I distribution outside the solar circle.," *Astronomical Journal*, vol. 83, pp. 1585–1593, Dec. 1978. 8

[41] C. A. J. O'Hare *et al.*, "Velocity substructure from gaia and direct searches for dark matter," *Phys. Rev. D*, vol. 101, p. 023006, Jan 2020. 8

[42] N. W. Evans, C. A. J. O'Hare, and C. McCabe, "Refinement of the standard halo model for dark matter searches in light of the Gaia Sausage," *Phys. Rev. D*, vol. 99, no. 2, p. 023012, 2019. 8

[43] C. W. Purcell, A. R. Zentner, and M.-Y. Wang, "Dark matter direct search rates in simulations of the Milky Way and Sagittarius stream," *Journal of Cosmology and Astroparticle Physics*, vol. 2012, p. 027–027, Aug. 2012. 9

[44] M. Vogelsberger and S. D. M. White, "Streams and caustics: the fine-grained

structure of λ cold dark matter haloes," *Monthly Notices of the Royal Astronomical Society*, vol. 413, pp. 1419–1438, feb 2011. 9

[45] V. Springel *et al.*, "The Aquarius Project: the subhaloes of galactic haloes," *Monthly Notices of the Royal Astronomical Society*, vol. 391, pp. 1685–1711, 12 2008. 9

[46] I. I. Bigi and A. I. Sanda, *The Strong CP Problem*, p. 314–332. Cambridge University Press, 2009. 9

[47] R. D. Peccei, *The Strong CP Problem and Axions*, p. 3–17. Springer Berlin Heidelberg, 2008. 9

[48] L. D. Duffy and K. van Bibber, "Axions as dark matter particles," *New Journal of Physics*, vol. 11, 2009. 9

[49] M. Pospelov and A. Ritz, "Theta vacua, qcd sum rules, and the neutron electric dipole moment," *Nuclear Physics B*, vol. 573, p. 177–200, May 2000. 9

[50] N. F. Ramsey, "Electric dipole moment of the neutron," *Ann. Rev. Nucl. Part. Sci.*, vol. 40, pp. 1–14, 1990. 9

[51] C. Abel *et al.*, "Measurement of the Permanent Electric Dipole Moment of the Neutron," *Phys. Rev. Lett.*, vol. 124, no. 8, p. 081803, 2020. 9

[52] S. M. Barr, D. Chang, and G. Senjanović, "Strong CP Problem and parity," *Phys. Rev. Lett.*, vol. 67, pp. 2765–2768, Nov 1991. 10

[53] A. Nelson, "Naturally weak CP violation," *Physics Letters B*, vol. 136, no. 5, pp. 387–391, 1984. 10

[54] A. Hook, "Anomalous solutions to the Strong CP Problem," *Physical Review Letters*, vol. 114, Apr. 2015. 10

[55] R. D. Peccei and H. R. Quinn, "CP conservation in the presence of pseudoparticles," *Physical Review Letters*, vol. 38, no. 25, 1977. 10, 11

[56] R. D. Peccei and H. R. Quinn, "Constraints imposed by CP conservation in the presence of pseudoparticles," *Physical Review D*, vol. 16, no. 6, 1977. 10, 11

[57] F. Wilczek, "Problem of strong P and T invariance in the presence of instantons," *Physical Review Letters*, vol. 40, pp. 279–282, 1 1978. 10

[58] S. Weinberg, "A new light boson?," *Physical Review Letters*, vol. 40, pp. 223–226, 1 1978. 10

[59] C. Vafa and E. Witten, "Parity conservation in quantum chromodynamics," *Phys. Rev. Lett.*, vol. 53, pp. 535–536, Aug 1984. 10

[60] J. E. Kim, "Weak-interaction singlet and strong CP invariance," *Phys. Rev. Lett.*, vol. 43, pp. 103–107, Jul 1979. 11

[61] M. Shifman, A. Vainshtein, and V. Zakharov, "Can confinement ensure natural cp invariance of strong interactions?," *Nuclear Physics B*, vol. 166, no. 3, pp. 493–506, 1980. 11

[62] M. Dine, W. Fischer, and M. Srednicki, "A simple solution to the strong CP problem with a harmless axion," *Physics Letters*, vol. 104B, August 1981. 11

[63] A. R. Zhitnitsky, "On Possible Suppression of the Axion Hadron Interactions. (In Russian)," *Sov. J. Nucl. Phys.*, vol. 31, p. 260, 1980. 11

[64] L. D. Luzio *et al.*, "Probing the axion-nucleon coupling with the next generation of axion helioscopes," *Eur. Phys. J. C*, 11 2021. 12, 22

[65] G. G. di Cortona *et al.*, "The QCD axion, precisely," *Journal of High Energy Physics*, vol. 2016, Jan. 2016. 12

[66] J. Diehl and E. Koutsangelas, "Dine-fischler-srednicki-zhitnitsky-type axions and where to find them," *Physical Review D*, vol. 107, May 2023. 12

[67] I. G. Irastorza and J. Redondo, "New experimental approaches in the search for axion-like particles," *Prog. Part. Nucl. Phys.*, vol. 102, pp. 89–159, 2018. 12, 22

[68] C. O'Hare, "cajohare/axionlimits: Axionlimits." `https://cajohare.github.io/AxionLimits/`, July 2020. 13, 25, 94, 95, 96

[69] P. Arias *et al.*, "Wispy cold dark matter," 2012. 12, 13, 14, 32, 33

[70] Y. Chikashige, R. N. Mohapatra, and R. D. Peccei, "Are There Real Goldstone Bosons Associated with Broken Lepton Number?," *Phys. Lett. B*, vol. 98, pp. 265–268, 1981. 12

[71] F. Wilczek, "Axions and family symmetry breaking," *Phys. Rev. Lett.*, vol. 49, pp. 1549–1552, Nov 1982. 12

[72] M. Cicoli, M. Goodsell, and A. Ringwald, "The type IIB string axiverse and its low-energy phenomenology," *JHEP*, vol. 10, p. 146, 2012. 12

[73] S. Centelles Chuliá and otters, "Natural axion model from flavour," *JHEP*, vol. 09, p. 137, 2020. 12

[74] G. Ballesteros *et al.*, "Standard model—axion—seesaw—higgs portal inflation. five problems of particle physics and cosmology solved in one stroke," *Journal of Cosmology and Astroparticle Physics*, vol. 2017, Aug. 2017. 12

[75] M. Fabbrichesi, E. Gabrielli, and G. Lanfranchi, *The Physics of the Dark Photon: A Primer*. Springer International Publishing, 2021. 13

[76] A. Caputo *et al.*, "Dark photon limits: a handbook," *Physical Review D*, 5 2021. 13, 14, 32, 33, 94

[77] T. Schneemann, K. Schmieden, and M. Schott, "First results of the supax experiment: Probing dark photons," 2023. 13

[78] R. Cervantes *et al.*, "Deepest sensitivity to wavelike dark photon dark matter with superconducting radio frequency cavities," *Physical Review D*, vol. 110, Aug. 2024. 13

[79] V. Flambaum *et al.*, "Searching for scalar field dark matter using cavity resonators and capacitors," *Physical Review D*, vol. 106, Sept. 2022. 13

[80] P. Agrawal *et al.*, "Relic abundance of dark photon dark matter," *Physics Letters B*, vol. 801, Feb. 2020. 14

[81] M. A. Amin *et al.*, "Small-scale structure in vector dark matter," *Journal of Cosmology and Astroparticle Physics*, vol. 2022, Aug. 2022. 14

[82] The CMS Collaboration, "Search for new physics in final states with an energetic jet or a hadronically decaying W or Z boson using 35.9 fb^{-1} of data at $\sqrt{s} = 13$ TeV," 2017. 14

[83] N. Okada and O. Seto, "Inelastic extra U(1) charged scalar dark matter," *Physical Review D*, vol. 101, Jan. 2020. 14

[84] K. Harigaya, Y. Nakai, and M. Suzuki, "Inelastic dark matter electron scattering and the XENON1T excess," *Physics Letters B*, vol. 809, p. 135729, Oct. 2020. 14

[85] B. A. Dobrescu, "Massless gauge bosons other than the photon," *Phys. Rev. Lett.*, vol. 94, p. 151802, Apr 2005. 14

[86] S. Biswas *et al.*, "Dark-photon searches via higgs-boson production at the lhc," *Phys. Rev. D*, vol. 93, p. 093011, May 2016. 14

[87] E. Gabrielli and M. Raidal, "Exponentially spread dynamical yukawa couplings from nonperturbative chiral symmetry breaking in the dark sector," *Phys. Rev. D*, vol. 89, p. 015008, Jan 2014. 14

[88] S. D. McDermott and S. J. Witte, "Cosmological evolution of light dark photon dark matter," *Physical Review D*, vol. 101, Mar. 2020. 14

[89] P. W. Graham, J. Mardon, and S. Rajendran, "Vector Dark Matter from Inflationary Fluctuations," *Phys. Rev. D*, vol. 93, no. 10, p. 103520, 2016. 14

[90] R. T. Co *et al.*, "Dark Photon Dark Matter Produced by Axion Oscillations," *Phys. Rev. D*, vol. 99, no. 7, p. 075002, 2019. 15

[91] A. J. Long and L.-T. Wang, "Dark Photon Dark Matter from a Network of Cosmic Strings," *Phys. Rev. D*, vol. 99, no. 6, p. 063529, 2019. 15

[92] P. Adshead and K. D. Lozanov, "Self-gravitating vector dark matter," *Physical Review D*, vol. 103, May 2021. 15

[93] D. Cyncynates and Z. J. Weiner, "Detectable, defect-free dark photon dark matter," 2023. 15

[94] P. Sikivie, "Experimental tests of the invisible axion," *Physical Review Letters*, 1983. 17, 24, 41, 145

[95] D. Kim *et al.*, "Revisiting the detection rate for axion haloscopes," *Journal of Cosmology and Astroparticle Physics*, vol. 2020, mar 2020. 17

[96] M. D. Schwatrz, *Quantum field theory and the standard model.* Cambridge university press, 2014. 18, 19, 20

[97] M. E. Peskin and D. V. Schroeder, *An Introduction to quantum field theory.* Reading, USA: Addison-Wesley, 1995. 18

[98] L. D. Landau, *Textbook on theoretical physics. Vol. 2: Classical field theory.* Akademie Verlag, 1987. 19

[99] J. Preskill, M. B. Wise, and F. Wilczek, "Cosmology of the invisible axion," *Physics Letters B*, vol. 120, no. 1, pp. 127–132, 1983. 22

[100] L. Abbott and P. Sikivie, "A cosmological bound on the invisible axion," *Physics Letters B*, vol. 120, no. 1, pp. 133–136, 1983. 22

[101] A. Vilenkin and A. E. Everett, "Cosmic strings and domain walls in models with goldstone and pseudo-goldstone bosons," *Phys. Rev. Lett.*, vol. 48, pp. 1867–1870, Jun 1982. 22

[102] J. I. Read, "The Local Dark Matter Density," *J. Phys. G*, vol. 41, p. 063101, 2014. 23

[103] P. Fox, A. Pierce, and S. D. Thomas, "Probing a QCD string axion with precision cosmological measurements," 9 2004. 23

[104] K. Saikawa *et al.*, "Spectrum of global string networks and the axion dark matter mass," 1 2024. 24, 25

[105] S. Borsanyi *et al.*, "Lattice QCD for Cosmology," 2016. 24

[106] M. J. Stott and D. J. E. Marsh, "Black hole spin constraints on the mass spectrum and number of axionlike fields," *Physical Review D*, vol. 98, Oct. 2018. 25

[107] A. Notari, F. Rompineve, and G. Villadoro, "Improved Hot Dark Matter Bound on the QCD Axion," *Phys. Rev. Lett.*, vol. 131, no. 1, p. 011004, 2023. 25

[108] P. M. Morse and H. Feshbach, *Methods of theoretical physics. Part I.* Mc.

Graw-Hill Book Company, 1953. 27

[109] J. M. Wrobel and R. C. Walker, *Synthesis Imaging in Radio Astronomy II*, ch. Sensitivity. Astronomical Society of the Pacific, 1999. 31

[110] B. F. Burke and F. Graham-Smith, *An Introduction to Radio Astronomy*. Cambridge University Press, third ed., 2010. 31

[111] S. Chaudhuri *et al.*, "A radio for hidden-photon dark matter detection," *Physical Review D*, 11 2014. 32

[112] R. Khatiwada *et al.*, "Axion Dark Matter Experiment: Detailed design and operations," *Rev. Sci. Instrum.*, vol. 92, no. 12, 2021. 33

[113] The MADMAX Collaboration, "A new experimental approach to probe QCD axion dark matter in the mass range above 40 μeV," *The European Physical Journal C*, vol. 79, Mar. 2019. 33

[114] D. Horns *et al.*, "Searching for wispy cold dark matter with a dish antenna," *Journal of Cosmology and Astroparticle Physics*, vol. 2013, p. 016–016, Apr. 2013. 33

[115] A. A. Melcón *et al.*, "Axion Searches with Microwave Filters: the RADES project," *JCAP*, vol. 05, p. 040, 2018. 34, 35, 38, 40

[116] J. Jeong *et al.*, "Concept of multiple-cell cavity for axion dark matter search," *Physics Letters B*, vol. 777, pp. 412–419, 2018. 34

[117] M. Goryachev, B. T. McAllister, and M. E. Tobar, "Axion detection with negatively coupled cavity arrays," *Physics Letters A*, vol. 382, no. 33, pp. 2199–2204, 2018. Special Issue in memory of Professor V.B. Braginsky. 34

[118] R. Cameron, *Design and Physical Realization of Coupled Resonator Filters*, ch. 14, pp. 457–484. John Wiley&Sons, Ltd, 2018. 35

[119] A. A. Melcón *et al.*, "First results of the CAST-RADES haloscope search for axions at 34.67 μeV," *JHEP*, vol. 21, p. 075, 2020. 37, 40, 60, 61

[120] B. M. Brubaker *et al.*, "HAYSTAC axion search analysis procedure," *Phys. Rev. D*, vol. 96, no. 12, p. 123008, 2017. 40

[121] S. Arguedas Cuendis, "Dark matter axion search using novel RF resonant cavity geometries in the CAST experiment.," 2021. 40

[122] G. G. Raffelt, "Plasmon decay into low-mass bosons in stars," *Phys. Rev. D*, vol. 37, pp. 1356–1359, Mar 1988. 41

[123] J. N. Bahcall and M. H. Pinsonneault, "What do we (not) know theoretically about solar neutrino fluxes?," *Phys. Rev. Lett.*, vol. 92, p. 121301, 2004. 41

[124] The CAST Collaboration, "An Improved limit on the axion-photon coupling

from the CAST experiment," *JCAP*, vol. 04, p. 010, 2007. 41, 60

[125] J. Redondo, "Solar axion flux from the axion-electron coupling," *JCAP*, vol. 12, p. 008, 2013. 41, 42

[126] T. Dafni *et al.*, "Weighing the solar axion," *Phys. Rev. D*, vol. 99, p. 035037, Feb 2019. 41, 42

[127] J. Jaeckel and L. J. Thormaehlen, "Distinguishing Axion Models with IAXO," *JCAP*, vol. 03, p. 039, 2019. 41

[128] E. Armengaud *et al.*, "Physics potential of the international axion observatory (iaxo)," *Journal of Cosmology and Astroparticle Physics*, 4 2019. 43

[129] K. van Bibber *et al.*, "Design for a practical laboratory detector for solar axions," *Phys. Rev. D*, vol. 39, pp. 2089–2099, Apr 1989. 42

[130] E. Arik *et al.*, "Probing eV-scale axions with CAST," *JCAP*, vol. 02, p. 008, 2009. 43, 60

[131] M. Arik *et al.*, "Search for sub-ev mass solar axions by the cern axion solar telescope with ^{3}He buffer gas," *Phys. Rev. Lett.*, vol. 107, p. 261302, Dec 2011. 43, 60, 72

[132] M. Arik *et al.*, "Search for solar axions by the cern axion solar telescope with ^{3}He buffer gas: Closing the hot dark matter gap," *Phys. Rev. Lett.*, vol. 112, p. 091302, Mar 2014. 43, 60, 72

[133] M. Arik *et al.*, "New solar axion search using the cern axion solar telescope with ^{4}He filling," *Phys. Rev. D*, vol. 92, p. 021101, Jul 2015. 43, 60

[134] V. Anastassopoulos *et al.*, "New CAST Limit on the Axion-Photon Interaction," *Nature Phys.*, vol. 13, pp. 584–590, 2017. 44, 60, 68, 70, 72, 76, 97

[135] A. Abeln *et al.*, "Conceptual design of BabyIAXO, the intermediate stage towards the International Axion Observatory," *JHEP*, vol. 05, p. 137, 2021. 45, 66, 69, 70, 72, 81, 109

[136] J. Amaré *et al.*, "Annual modulation results from three-year exposure of anais-112," *Phys. Rev. D*, vol. 103, p. 102005, May 2021. 45

[137] G. Angloher *et al.*, "The COSINUS project - perspectives of a NaI scintillating calorimeter for dark matter search," *Eur. Phys. J. C*, vol. 76, no. 8, p. 441, 2016. 45

[138] H. Kluck *et al.*, "DANAE: A new effort to directly search for dark matter with DEPFET-RNDR detectors," *Nuclear Instruments and Methods in Physics Research Section A: Accelerators, Spectrometers, Detectors and Associated Equipment*, vol. 958, p. 162155, 2020. Proceedings of the Vienna Conference on Instrumentation 2019. 45

[139] D. Akerib *et al.*, "The LUX-ZEPLIN (LZ) experiment," *Nuclear Instruments and Methods in Physics Research Section A: Accelerators, Spectrometers, Detectors and Associated Equipment*, vol. 953, Feb. 2020. 45

[140] S. Cebrian, "Low radioactivity techniques for Large TPCs in rare event searches," in *11th Symposium on Large TPCs for low-energy rare event detection*, 3 2024. 45

[141] K. Altenmüller *et al.*, "REST-for-Physics, a ROOT-based framework for event oriented data analysis and combined Monte Carlo response," *Computer Physics Communications*, vol. 273, p. 108281, apr 2022. 45, 52, 153

[142] C. Grupen and B. Shwartz, *Particle Detectors*. Cambridge Monographs on Particle Physics, Nuclear Physics and Cosmology, Cambridge University Press, 2 ed., 2008. 45

[143] F. Sauli, *Gaseous Radiation Detectors: Fundamentals and Applications*. Cambridge Monographs on Particle Physics, Nuclear Physics and Cosmology, Cambridge University Press, 2023. 45, 46

[144] E. Rutherford and H. Geiger, "An electrical method of counting the number of -particles from radio-active substances," *Proceedings of the Royal Society of London. Series A, Containing Papers of a Mathematical and Physical Character*, vol. 81, no. 546, 1908. 46

[145] H. Geiger and W. Müller, "Elektronenzählrohr zur messung schwächster aktivitäten," *Naturwissenschaften*, vol. 16, no. 31, 1928. 47

[146] T. Ferbel, *Experimental Techniques in High Energy Physics*, vol. 64. Calif.: Addison-Wesley, 1987. 47

[147] S. Biagi, "Monte carlo simulation of electron drift and diffusion in counting gases under the influence of electric and magnetic fields," *Nuclear Instruments and Methods in Physics Research Section A: Accelerators, Spectrometers, Detectors and Associated Equipment*, vol. 421, no. 1, 1999. 47

[148] W. Shockley, "Currents to conductors induced by a moving point charge," *J. Appl. Phys.*, vol. 9, no. 10, pp. 635–636, 1938. 48

[149] S. Ramo, "Currents induced by electron motion," *Proceedings of the IRE*, vol. 27, no. 9, 1939. 48

[150] D. Autiero *et al.*, "The CAST time projection chamber," *New Journal of Physics*, vol. 9, pp. 171–171, jun 2007. 48, 60

[151] G. Charpak and et al., "The use of multiwire proportional counters to select and localize charged particles," *Nuclear Instruments and Methods*, vol. 62, no. 3, pp. 262–268, 1968. 49

[152] P. Catapano, "Georges Charpak: hardwired for science," *CERN Courier*,

vol. 49, no. 2, pp. 24–28, 2009. 49

[153] M. Hamid and S. Bri, "Micromegas detector using 55 fe x-ray source," *International Journal of Advanced Research*, vol. 1, 01 2013. 49

[154] "FLC - Forschung mit Lepton Collidern : TPC Basics." `https://flc.desy.de/tpc/basics/tpc/index_eng.html`. Accessed: 2024-05-19. 50

[155] Y. Giomataris *et al.*, "Micromegas: a high-granularity position-sensitive gaseous detector for high particle-flux environments," *Nuclear Instruments and Methods in Physics Research Section A: Accelerators, Spectrometers, Detectors and Associated Equipment*, vol. 376, no. 1, pp. 29–35, 1996. 51

[156] S. Cebrián *et al.*, "Radiopurity of micromegas readout planes," *Astroparticle Physics*, vol. 34, no. 6, pp. 354–359, 2011. 52

[157] The XENON Collaboration and M. Laubenstein, "Lowering the radioactivity of the photomultiplier tubes for the XENON1T dark matter experiment," *The European Physical Journal C*, vol. 75, no. 11, 2015. 52

[158] J. Galan and et al., "rest-for-physics/framework," July 2021. 52, 113, 153

[159] J. Castel *et al.*, "Background assessment for the TREX dark matter experiment," *Eur. Phys. J. C*, vol. 79, p. 782, 2019. 52

[160] J. Galan *et al.*, "Topological background discrimination in the PandaX-III neutrinoless double beta decay experiment," *Journal of Physics G: Nuclear and Particle Physics*, vol. 47, Mar. 2020. 52

[161] "Geant4." `https://geant4.web.cern.ch/`. Accessed: 2024-06-06. 53

[162] "ROOT: analyzing petabytes of data, scientifically.." `https://root.cern/`. Accessed: 2024-06-06. 53

[163] R. Chytracek *et al.*, "Geometry description markup language for physics simulation and analysis applications," *IEEE Transactions on Nuclear Science*, vol. 53, no. 5, pp. 2892–2896, 2006. 53

[164] D. M. Lazarus *et al.*, "Search for solar axions," *Phys. Rev. Lett.*, vol. 69, pp. 2333–2336, Oct 1992. 59

[165] S. Moriyama *et al.*, "Direct search for solar axions by using strong magnetic field and x-ray detectors," *Phys. Lett. B*, vol. 434, p. 147, 1998. 59

[166] Y. Inoue *et al.*, "Search for sub-electronvolt solar axions using coherent conversion of axions into photons in magnetic field and gas helium," *Physics Letters B*, vol. 536, no. 1, pp. 18–23, 2002. 59

[167] Y. Inoue *et al.*, "Search for solar axions with mass around 1 eV using coherent conversion of axions into photons," *Phys. Lett. B*, vol. 668, pp. 93–97, 2008. 59

[168] K. Zioutas *et al.*, "A Decommissioned LHC model magnet as an axion telescope," *Nucl. Instrum. Meth. A*, vol. 425, pp. 480–489, 1999. 59

[169] The CAST Collaboration, "First results from the CERN Axion Solar Telescope (CAST)," *Phys. Rev. Lett.*, vol. 94, p. 121301, 2005. 59

[170] P. Abbon *et al.*, "The Micromegas detector of the CAST experiment," *New J. Phys.*, vol. 9, p. 170, 2007. 59, 60, 98

[171] M. Kuster *et al.*, "The x-ray mirror telescope and the pn-CCD detector of CAST," *Proc. SPIE Int. Soc. Opt. Eng.*, vol. 5500, pp. 139–146, 2004. 60

[172] M. Kuster *et al.*, "The X-ray Telescope of CAST," *New Journal of Physics*, 2 2007. 60

[173] The CAST Collaboration, "Search for 14.4-keV solar axions emitted in the M1-transition of Fe-57 nuclei with CAST," *JCAP*, vol. 12, p. 002, 2009. 60

[174] The CAST Collaboration, "Search for solar axion emission from ^7Li and $D(p,\gamma)^3He$ nuclear decays with the CAST γ-ray calorimeter," *JCAP*, vol. 03, p. 032, 2010. 60

[175] The CAST Collaboration, "New Upper Limit on the Axion-Photon Coupling with an Extended CAST Run with a Xe-Based Micromegas Detector," *Phys. Rev. Lett.*, vol. 133, no. 22, p. 221005, 2024. 60

[176] The CAST Collaboration, "CAST - Status Report to the SPSC for the 127th Meeting and Planning for 2018," tech. rep., CERN, Geneva, 2017. 60

[177] C. M. Adair *et al.*, "Search for Dark Matter Axions with CAST-CAPP," *Nature Commun.*, vol. 13, no. 1, p. 6180, 2022. 61, 62

[178] S. Arguedas Cuendis *et al.*, "First Results on the Search for Chameleons with the KWISP Detector at CAST," *Phys. Dark Univ.*, vol. 26, p. 100367, 2019. 61, 62

[179] The ADMX Collaboration, "A Search for Invisible Axion Dark Matter with the Axion Dark Matter Experiment," *Phys. Rev. Lett.*, vol. 120, no. 15, p. 151301, 2018. 61

[180] C. Boutan *et al.*, "Piezoelectrically Tuned Multimode Cavity Search for Axion Dark Matter," *Phys. Rev. Lett.*, vol. 121, no. 26, p. 261302, 2018. 61

[181] The ADMX Collaboration, "Extended Search for the Invisible Axion with the Axion Dark Matter Experiment," *Phys. Rev. Lett.*, vol. 124, no. 10, p. 101303, 2020. 61

[182] S. DePanfilis *et al.*, "Limits on the abundance and coupling of cosmic axions at $4.5 < m_a < 5.0\mu$ev," *Phys. Rev. Lett.*, vol. 59, pp. 839–842, Aug 1987. 61

[183] C. Hagmann *et al.*, "Results from a search for cosmic axions," *Phys. Rev. D*,

vol. 42, pp. 1297–1300, Aug 1990. 61

[184] S. Lee *et al.*, "Axion Dark Matter Search around 6.7 μeV," *Phys. Rev. Lett.*, vol. 124, no. 10, p. 101802, 2020. 61

[185] J. Jeong *et al.*, "Search for Invisible Axion Dark Matter with a Multiple-Cell Haloscope," *Phys. Rev. Lett.*, vol. 125, no. 22, p. 221302, 2020. 61

[186] L. Zhong *et al.*, "Results from phase 1 of the HAYSTAC microwave cavity axion experiment," *Phys. Rev. D*, vol. 97, no. 9, p. 092001, 2018. 61

[187] K. M. Backes *et al.*, "A quantum-enhanced search for dark matter axions," *Nature*, vol. 590, no. 7845, pp. 238–242, 2021. 61

[188] D. Alesini *et al.*, "Galactic axions search with a superconducting resonant cavity," *Phys. Rev. D*, vol. 99, no. 10, p. 101101, 2019. 61

[189] D. Alesini *et al.*, "Search for invisible axion dark matter of mass $m_a = 43$ μeV with the QUAX–$a\gamma$ experiment," *Phys. Rev. D*, vol. 103, no. 10, p. 102004, 2021. 61

[190] B. T. McAllister *et al.*, "The ORGAN Experiment: An axion haloscope above 15 GHz," *Phys. Dark Univ.*, vol. 18, pp. 67–72, 2017. 61

[191] P. Brax, "Chameleon dark energy," in *AIP Conference Proceedings*, AIP, 2004. 61

[192] J. Khoury and A. Weltman, "Chameleon fields: Awaiting surprises for tests of gravity in space," *Physical Review Letters*, vol. 93, Oct. 2004. 61

[193] P. Brax *et al.*, "Testing chameleon theories with light propagating through a magnetic field," *Phys. Rev. D*, vol. 76, p. 085010, Oct 2007. 61

[194] V. Anastassopoulos *et al.*, "Search for chameleons with cast," *Physics Letters B*, vol. 749, p. 172–180, Oct. 2015. 62

[195] The CAST Collaboration, "Improved Search for Solar Chameleons with a GridPix Detector at CAST," *JCAP*, vol. 01, p. 032, 2019. 62, 71

[196] I. G. Irastorza *et al.*, "The International Axion Observatory IAXO. Letter of Intent to the CERN SPS committee," tech. rep., CERN, Geneva, 2013. 63, 64, 70

[197] F. A. Harrison *et al.*, "The Nuclear Spectroscopic Telescope Array (NuSTAR)," 8 2010. 63

[198] T. Takahashi *et al.*, "Astro-h white paper - introduction," 2014. 63

[199] L. Di Luzio *et al.*, "The landscape of QCD axion models," *Phys. Rept.*, vol. 870, pp. 1–117, 2020. 63

[200] E. Armengaud *et al.*, "Physics potential of the International Axion Observatory (IAXO)," *JCAP*, vol. 06, p. 047, 2019. 63, 64, 72

[201] R. Daido, F. Takahashi, and W. Yin, "The ALP miracle: unified inflaton and dark matter," *JCAP*, vol. 05, p. 044, 2017. 64

[202] M. Giannotti *et al.*, "Cool WISPs for stellar cooling excesses," *JCAP*, vol. 05, p. 057, 2016. 64

[203] A. De Angelis, M. Roncadelli, and O. Mansutti, "Evidence for a new light spin-zero boson from cosmological gamma-ray propagation?," *Phys. Rev. D*, vol. 76, p. 121301, 2007. 64

[204] T. I. collaboration, "BabyIAXO proposal review report," tech. rep., DESY, Hamburg, 2019. 64

[205] M. Garczarczyk *et al.*, "Status of the Medium-Sized Telescope for the Cherenkov Telescope Array," *arXiv e-prints*, p. arXiv:1509.01361, Sept. 2015. 66

[206] The IAXO Collaboration, "Conceptual design of babyiaxo, the intermediate stage towards the international axion observatory," 10 2020. 67, 68

[207] F. Aznar *et al.*, "A Micromegas-based low-background x-ray detector coupled to a slumped-glass telescope for axion research," *JCAP*, vol. 12, p. 008, 2015. 68, 108

[208] T. Döhring *et al.*, "The challenge of developing thin mirror shells for future x-ray telescopes," in *Optical Systems Design 2015: Optical Fabrication, Testing, and Metrology V* (A. Duparré and R. Geyl, eds.), vol. 9628, p. 962809, International Society for Optics and Photonics, SPIE, 2015. 69

[209] F. A. Harrison *et al.*, "Development of the HEFT and NuSTAR focusing telescopes," *Experimental Astronomy*, vol. 20, pp. 131–137, Dec. 2005. 68

[210] M. Civitani *et al.*, "Cold and Hot Slumped Glass Optics with interfacing ribs for high angular resolution x-ray telescopes," in *Space Telescopes and Instrumentation 2016: Ultraviolet to Gamma Ray* (J.-W. A. den Herder, T. Takahashi, and M. Bautz, eds.), vol. 9905, p. 99056U, International Society for Optics and Photonics, SPIE, 2016. 68

[211] F. Jansen *et al.*, "Xmm-newton observatory," *Astronomy&Astrophysics*, vol. 365, pp. L1–L6, 1 2001. 68

[212] Krieger, Christoph *et al.*, "Operation of an ingrid based x-ray detector at the cast experiment," *EPJ Web Conf.*, vol. 174, p. 02008, 2018. 70

[213] P. Lechner *et al.*, "Silicon drift detectors for high count rate x-ray spectroscopy at room temperature," *Nuclear Instruments and Methods in Physics Research Section A: Accelerators, Spectrometers, Detectors and Associated Equipment*,

vol. 458, no. 1, pp. 281–287, 2001. Proc. 11th Inbt. Workshop on Room Temperature Semiconductor X- and Gamma-Ray Detectors and Associated Electronics. 71

[214] A. Fleischmann *et al.*, "Metallic magnetic calorimeters," *AIP Conference Proceedings*, vol. 1185, pp. 571–578, 12 2009. 71

[215] E. Haller, "Advanced far-infrared detectors," *Infrared Physics&Technology*, vol. 35, no. 2, pp. 127–146, 1994. 71

[216] D. Poda and A. Giuliani, "Low background techniques in bolometers for double-beta decay search," *Int. J. Mod. Phys. A*, vol. 32, no. 30, p. 1743012, 2017. 72

[217] E. Armengaud *et al.*, "The CUPID-Mo experiment for neutrinoless double-beta decay: performance and prospects," *Eur. Phys. J. C*, vol. 80, no. 1, p. 44, 2020. 72

[218] B. Cabrera, "Introduction to TES Physics," *Journal of Low Temperature Physics*, vol. 151, pp. 82–93, 12 2008. 72

[219] J. Rothe *et al.*, "TES-Based Light Detectors for the CRESST Direct Dark Matter Search," *J. Low Temp. Phys.*, vol. 193, no. 5-6, pp. 1160–1166, 2018. 72

[220] M. Giannotti, "Hints of new physics from stars," *PoS*, vol. ICHEP2016, p. 076, 2016. 72

[221] E. Armengaud *et al.*, "Conceptual design of the international axion observatory (iaxo)," 1 2014. 73, 114

[222] E. Ruiz Chóliz, "Ultra-low background Micromegas X-ray detectors for Axion searches in IAXO and BabyIAXO," 2019. 74, 75, 78

[223] K. Altenmüller *et al.*, "Background discrimination with a micromegas detector prototype and veto system for babyiaxo," *Frontiers in Physics*, vol. 12, 2024. 75, 78

[224] C. Margalejo Blasco, "Modelo de fondo para IAXO-D0, prototipo del experimento IAXO (International Axion Observatory)," 2018. 77

[225] S. Aune *et al.*, "Low background x-ray detection with Micromegas for axion research," *JINST*, vol. 9, no. 01, p. P01001, 2014. 77

[226] P. Benetti *et al.*, "Measurement of the specific activity of ar-39 in natural argon," *Nucl. Instrum. Meth. A*, vol. 574, pp. 83–88, 2007. 77

[227] S. Ahyoune *et al.*, "A Proposal for a Low-Frequency Axion Search in the 1–2 μeV Range and Below with the BabyIAXO Magnet," *Annalen der Physik*, vol. 535, Oct. 2023. 81, 82

[228] Smorra, C. *et al.*, "Base – the baryon antibaryon symmetry experiment," *Eur. Phys. J. Special Topics*, vol. 224, no. 16, 2015. 81

[229] M. Siodlaczek, "Thermodynamic Design of a Cryostat for a Radiofrequency Cavity Detector in BabyIAXO in Search of Dark Matter.," 2022. Presented 22 Mar 2022. 81, 83

[230] G. Riddone, "Theoretical modeling and experimental investigation of the thermal performance of the LHC prototype lattice cryostats.," 1997. 82

[231] "Cryomech, 'PT420 Cryocoolers' ." `https://www.cryomech.com/products/pt420/`. 83

[232] "Stirling Cryogenics BV." `https://www.stirlingcryogenics.eu/`. 83

[233] R. E. Collin, *Foundations for Microwave Engineering*. Wiley-IEEE Press, 2001. 85

[234] N.J.Simon, E.S.Drexler, and R.P.Reed, *Properties of Copper and Copper Alloys at Cryogenic Temperature*. 1992. 86

[235] K. Altenmueller *et al.*, "Using micromegas detectors for direct dark matter searches: challenges and perspectives," 2024. 98

[236] S. Anvar *et al.*, *AGET, the GET Front-End ASIC, for the readout of the Time Projection Chambers used in Nuclear Physic Experiments*. 2011. 98

[237] A. Ianni, "Canfranc underground laboratory," *Journal of Physics: Conference Series*, vol. 718, p. 042030, may 2016. 100

[238] L. A. Currie, "Limits for qualitative detection and quantitative determination. application to radiochemistry," *Analytical Chemistry*, vol. 40, no. 3, pp. 586–593, 1968. 100

[239] C. Hurtgen, S. Jerome, and M. Woods, "Revisiting currie — how low can you go?," *Applied Radiation and Isotopes*, vol. 53, no. 1, pp. 45–50, 2000. 100

[240] K. Altenmüller *et al.*, "Alphacamm, a micromegas-based camera for high-sensitivity screening of alpha surface contamination," *Journal of Instrumentation*, vol. 17, p. P08035, aug 2022. 101, 146

[241] F. Aznar *et al.*, "Assessment of material radiopurity for Rare Event experiments using Micromegas," *JINST*, vol. 8, p. C11012, 2013. 105

[242] S. Cebrián *et al.*, "Radiopurity assessment of the tracking readout for the NEXT double beta decay experiment," *JINST*, vol. 10, no. 05, p. P05006, 2015. 105, 106, 107

[243] S. Cebrián *et al.*, "Radiopurity assessment of the energy readout for the NEXT double beta decay experiment," *JINST*, vol. 12, no. 08, p. T08003, 2017. 105, 106, 107

[244] CERN, "Lxplus service - abp computing @ cern." 113

[245] DESY, "Naf - national analysis facility - computing - desy confluence." 113

[246] E. Ferrer-Ribas *et al.*, "Ultra low background micromegas detectors for babyiaxo solar axion search," 2023. 118, 119

[247] J. M. García-Barceló *et al.*, "Methods and restrictions to increase the volume of resonant rectangular-section haloscopes for detecting dark matter axions," *Journal of High Energy Physics*, 2 2023. 121

[248] J. Golm *et al.*, "Split-cavity tuning of a rectangular axion haloscope operating around 8.4 GHz," *Front. in Phys.*, vol. 12, p. 1372846, 2024. 125

[249] A. Álvarez Melcón *et al.*, "Scalable haloscopes for axion dark matter detection in the 30μeV range with RADES," *JHEP*, vol. 07, p. 084, 2020. 126, 127, 128

[250] D. Pozar, *Microwave Engineering*. Wiley, 2012. 135

[251] C. Margalejo Blasco, "Development of resonant cavity-based microwave filters for axion detection," 2023. 137, 140, 142

[252] D. Alesini *et al.*, "The future search for low-frequency axions and new physics with the FLASH resonant cavity experiment at Frascati National Laboratories," *Phys. Dark Univ.*, vol. 42, p. 101370, 2023. 149

Tengo todo bajo control.
Puedo hacerlo mucho peor, debes entenderlo.

Monteperdido. *Me Tumbas, Me Matas*

Acknowledgments

And so, here we are. One of the main motivations that kept me going through every single sleepless night in the last years[1], was imagining this exact same moment and how good it will feel to sit down to remember and thank all the people that have made this work possible, one way or another. However, when facing this task right now my feeling is not only that of deep happiness but also of serious concern of not making it up to all the people that, one way or another, have helped me through this restless trip.

First, I would like to express my heartfelt gratitude to Edu for his guidance and support as my supervisor over the years. It wasn't easy, but we made it! My thanks also go to Babette for her scientific supervision and for being one of the finest examples I have encountered in academia—a truly remarkable scientist and, above all, a wonderful human being. I cherish my time as part of the SiUB and miss the lunch and *Exploding Kittens* breaks with the CDP Team.

The diverse topics covered in this thesis allowed me to learn from a wide range of experts. Igor Irastorza has exemplified organization and scientific direction like few others I have encountered during these years. Javier Redondo has been, without a doubt, my greatest teacher regarding axion theory and phenomenology. I hope to honor him someday by developing some of the detection ideas we've discussed, though I didn't manage to mature them enough for this work. Javier Galń, Gloria Luzón, and Susana Cebrián were invaluable in helping me understand the radioactive background in IAXO and in dealing with its simulation in REST. My time at CERN allowed me to become a better and more reliable scientist, mainly thanks to Theodoros, Bjliana, and Jean Michel. I owe much of my understanding of RF theory and technologies to Juan Daniel, Benito, Walter, and Alejandro.

This PhD thesis would not have been possible without the foundational work of several other PhD and master's students. The contributions of Sergio, José María

[1] And, believe me, there were **A LOT**

and Jessica in the RADES group are closely linked to mine; without their simulations and measurements, a significant part of this thesis would not have been feasible. Similarly, the efforts of Elisa, Cristina, and Luis in characterizing the IAXO background were crucial for developing the electronics background model.

I would also like to thank Javier Sieiro for his commitment to proposing an experimental RF component to the original project, though sadly, the *COVID times* led us to very different plans. I hope that one day we can revive some of those original ideas and prepare our own haloscope search!

I am incredibly grateful for the unwavering confidence Lluís Garrido has placed in me, helping me secure the APIF grant that made this work possible and handling the paperwork unconditionally throughout these years. The assistance of Assumpta Parreño, SÍvia Boquer and the postgraduate secretariat of the physics faculty at UB was also crucial for the completion of this work.

The final part of my PhD journey was marked by my move to the Max Planck Institue for Physics in Munich, where I met incredible people who became both colleagues and friends. A special place in my heart goes to the Cosinus team, who quickly welcomed me into the *container crew*. The MADMAX team at MPP has also been a fantastic group with whom I've enjoyed working (and partying).

These acknowledgments would not be complete without recognizing the invaluable support of those outside academia. Their help, encouragement, and companionship have been equally, if not more, important during these generally challenging years.

In one way or another, my family has played an essential role in helping me achieve this goal, believing in me even when they couldn't fully grasp the complexities of this physics endeavor. A significant part of this adventure stems from the seed of scientific curiosity and skepticism that my grandfather planted in me as a child. Though he didn't live long enough to witness the completion of this work, I know he didn't need to see it to believe in me; as for this he was certainly no skeptic.

If there's one thing I've learned from my *PhD years*, far more relevant than anything about axions, it's the importance of having a strong support network. In this regard, I count myself incredibly fortunate. My deepest thanks go to Dani and Anna, who supported me through some of the most complex and challenging times of my life while having as much fun as possible. A part of me will always remain in Valencia, with the wonderful people from Osadía, especially the official and unofficial inhabitants of Siveria.

I'm equally grateful for the amazing people I met in Zaragoza. Even after more than two years, I still fondly remember pizza-and-movie nights with Bea as if they were just last week. I also want to thank the Arrebato crew, especially Rosa, who made me feel at home—long live the underground!

Finally, I would like to thank Franzi and Jonas for their friendship and for helping me adjust to life in Munich.

Last and not least, my most profound gratitude goes to Vera, Tofu and all other cats, bands and underground concert venues that- literally- kept me alive during the last few years. To all of you, and from the bottom of my heart:

GRACOAS.